MOCVD and electrochemical polymeric thin films : elaboration, characterization, properties ans applications

Claudiu Constantin Manole

Université de Toulouse

THÈSE

En vue de l'obtention du

DOCTORAT DE L'UNIVERSITÉ DE TOULOUSE

Délivré par :
Institut National Polytechnique de Toulouse (INP Toulouse)

Discipline ou spécialité :

Sciences et génie des matériaux

Présentée et soutenue par :
Claudiu Constantin MANOLE

le : vendredi 7 décembre 2012

Titre :
MOCVD and electrochemical polymeric thin films : elaboration, characterization, properties ans applications
FIlms minces polymères par CVD et électrodeposition : élaboration, caractérisation, propriétes et applications

---

Ecole doctorale :
Sciences de la Matière (SDM)

Unité de recherche :
CIRIMAT UMR 5085

Directeur(s) de Thèse :
Francis MAURY, Directeur de recherche CNRS, INP Toulouse
Ioana DEMETRESCU, Prof. des Universités, Université Polytechnique de Bucarest

Rapporteurs :
Michael PONS, Directeur de recherche CNRS
Horia IOVU, Prof. étranger, Université Polytechnique de Bucarest
Laura TUGULEA, Prof. étranger, Université Polytechnique de Bucarest

Membre(s) du jury :
Mircea Teodorescu, Prof. étranger, Université Polytechnique de Bucarest, Président
Francis MAURY, Directeur de recherche CNRS, INP Toulouse, Membre
Ioana DEMETRESCU, Prof. des Universités, Université Polytechnique de Bucarest, Membre
Michael PONS, Directeur de recherche CNRS, Rapporteur
Horia IOVU, Prof. étranger, Université Polytechnique de Bucarest, Rapporteur
Laura TUGULEA, Prof. étranger, Université Polytechnique de Bucarest, Rapporteur

INSTITUT NATIONAL **POLYTECHNIQUE** DE TOULOUSE
Ecole doctorale Sciences de la Matière
Centre Interuniversitaire de Recherche Ingénierie Matériaux
UNIVERSITATEA **POLITEHNICA** DIN BUCUREŞTI
Facultatea de Chimie Aplicată si Ştiinţa Materialelor
Departamentul de Chimie Generală

THÈSE DE DOCTORAT
(RÉSUMÉ)

FILMS MINCES POLYMERES PAR CVD ET ELECTRODEPOSITION: ELABORATION, CARACTERISATION, PROPRIETES ET APPLICATIONS

CVD AND ELECTROCHEMICAL POLYMERIC THIN FILMS: ELABORATION, CHARACTERIZATION, PROPERTIES AND APPLICATIONS

Auteur
Claudiu Constantin MANOLE

Coordinateurs Scientifiques
Dr. Francis MAURY
Prof. Dr. Ioana DEMETRESCU

2012

Films minces polymères par CVD et électrodéposition: élaboration, caractérisation, propriétés et applications

La thèse traite de deux types de polymères en films minces: poly (méthacrylate de méthyle) (PMMA) et polypyrrole (PPy). Les films minces ont été élaborés par voie sèche et humide.

La voie sèche consiste à déposer less films polymères par un procédé original de Chemical Vapor Deposition (CVD), nommé Photo-CVD. La croissance implique l'activation UV de l'espèce monomère dans la phase gazeuse. Les deux polymères PMMA et PPy ont été obtenus pour la première fois par Photo-CVD. La caractérisation des propriétés a été mise en évidence avec des applications possibles en microélectronique, micro-optique et des appareils générant de la chaleur.

La voie humide est une croissance de films minces par une approche électrochimique. Des films minces organiques PPy et inorganiques TiO_2 nanostructurés ont été obtenus et caractérisés par différentes techniques électrochimiques. Des aspects de croissance de PPy ont été complémentairement mis en évidence par SPR.

Cette thèse est pourrait être divisés en quatre sections principales: *i*) les processus de croissance, *ii*) la caractérisation, *iii*) des propriétés et *iv*) les perspectives d'avenir pour l'applicabilité.

1. Processus de croissance

Une des premières originalités est donné par le moyen de polymérisation par voie sèche. Elle est basée sur l'activation UV du monomère dans la phase gazeuse par le procédé photo-CVD (*Figure 1*). Par rapport aux données de la littérature, cette approche ne nécessite pas l'exposition directe aux UV du substrat et du film en croissance. Il permet la polymérisation à la température ambiante et sur un substrat fragile (sensible aux photons).

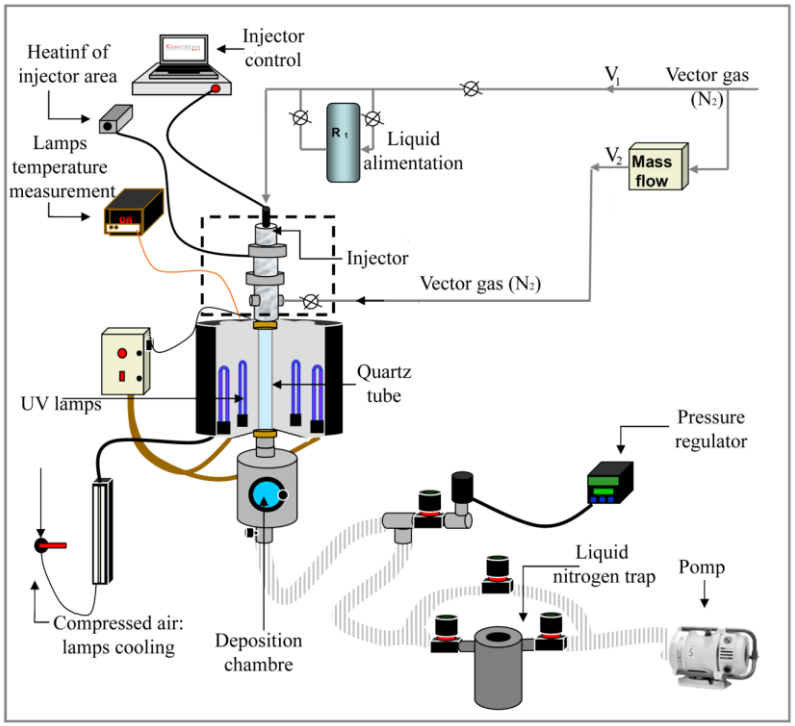

Figure 1: La configuration photo-CVD utiliseé pour les expériences

Un autre aspect de l'originalité en termes de dépôt est le procédé d'élaboration de composites de TiO_2 et PPy. Ce processus de croissance voie humide est conçu pour offrir une à deux étapes électrochimique de contrôle: (*i*) une croissance auto-ordonnée des nanostructures de TiO_2 et (*ii*) une polymérisation ultérieure d'un film mince PPy sur les nanotubes TiO_2. La croissance électrochimique des films et leurs paramètres électrochimiques sont représentés en *Figure 2*.

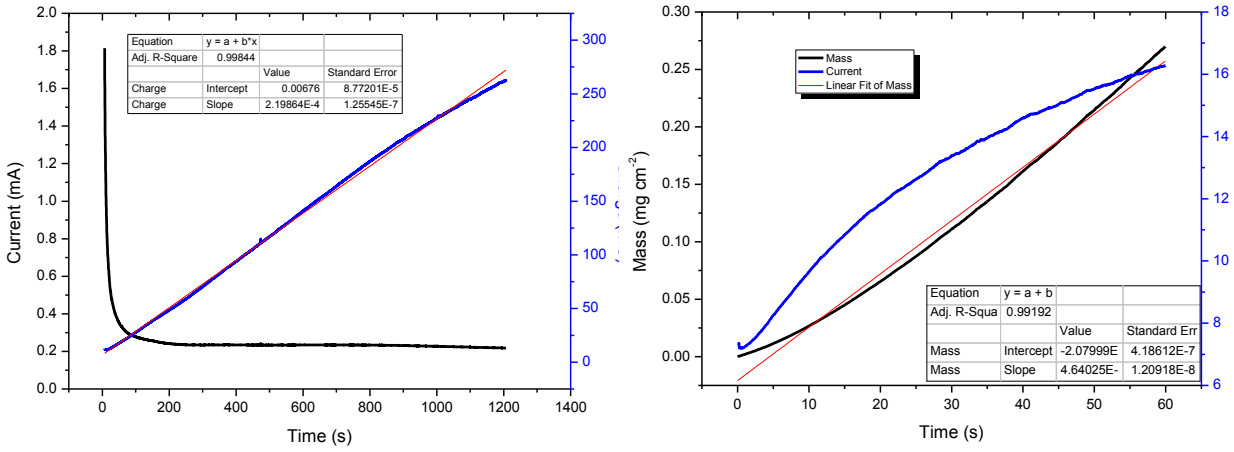

a) *b)*

Figure 2: variation temporelle de la croissance chronoampérométrique de TiO2 et de la charge calculée des nanotubes (a) et de PPy et de la masse déposée calculé (b). Les résultats de l'ajustement linéaire de la masse sont présentés dans l'encadré.

En outre, l'utilisation des paramètres expérimentaux et l'efficacité de la consommation d'énergie a également été poursuivie. Les films minces ont été caractérisé dans le détail afin d'étudier les aspects liés à leur nature et les propriétés.

2. Caractérisation

Une originalité est donné par l'approche du processus de caractérisation à partir d'une perspective unitaire d'un modèle mathématique. Le modèle met en mouvement harmonique divers moyens de caractérisation physique (*Figure 3*).

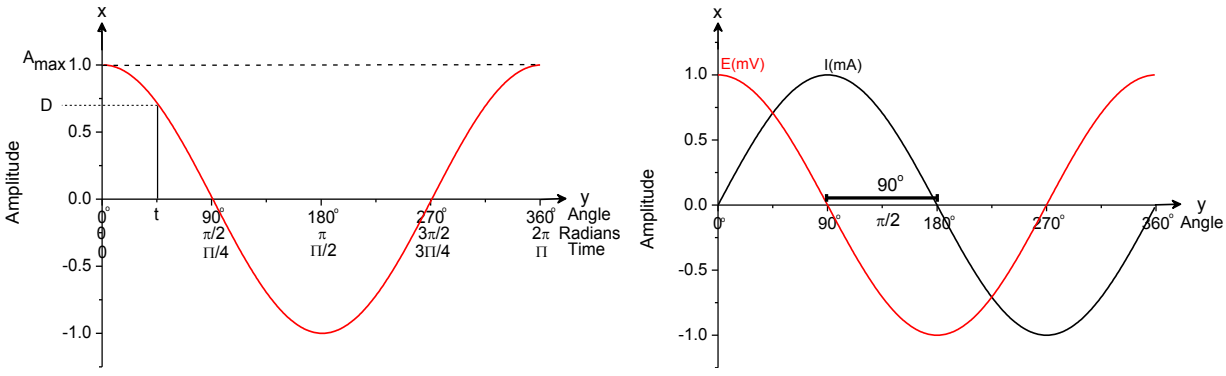

a) *b)*

Figure 3: Simple harmonic motion (a) and the shift between two harmonics (b)

Ainsi, les méthodes d'investigation utilisées pour caractériser les films minces, tels que la Microscopie à force atomique (AFM), la Spectroscopie d'impédance électrochimique (EIS)

et de la Résonance des Plasmons de Surface (SPR), trouvent des dénominateurs communs en ce qui concerne l'approche mathématique.

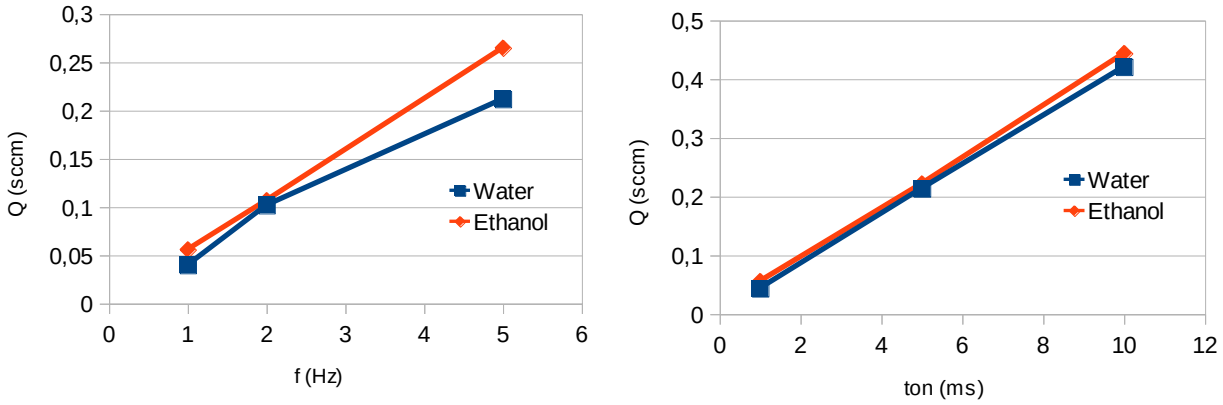

a) *b)*

Figure 4: L'influence sur les paramètres d'injection sur le débit de l'eau et de l'éthanol: a) la fréquence (f) en fonction du débit de liquide (Q) à ton = 1 ms et P_M = 2,8 bar et b) temps d'ouverture (ton) en fonction du débit de liquide (Q) à f = 1 Hz et P_M = 2.8 bar. Les essais effectués à la pression (P_C) et la température (T = 18 °C) ambiante

L'utilisation de l'Injection Liquide Directe (DLI) pour obtenir la phase vapeur requise pour la polymérisation est une nouveauté dans la littérature. Le principe de la DLI (pas couplé à une CVD) est utilisé sur une grande échelle dans l'industrie de l'automobile. Ses paramètres ne sont cependant pas définis pour des liquides ayant des propriétés différentes et, dans ces cas particuliers de conditions de fonctionnement.

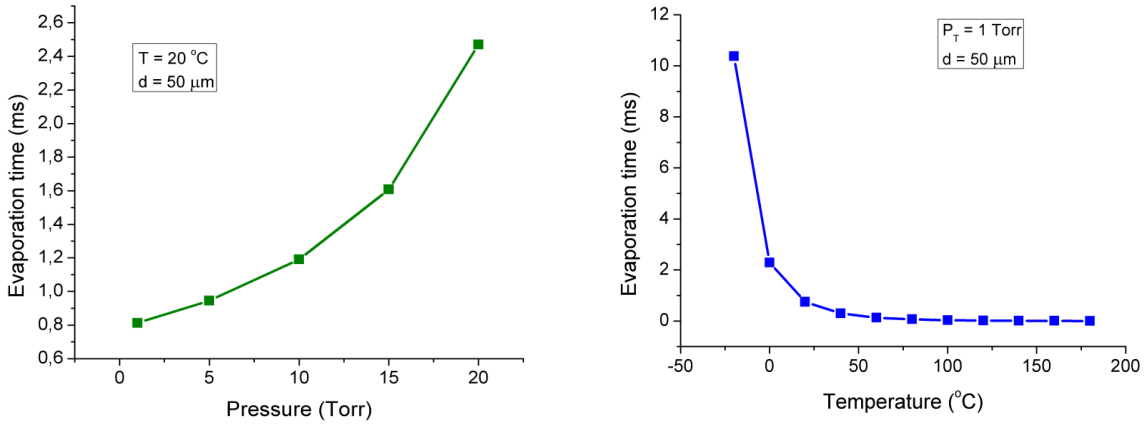

a) *b)*

Figure 5: Taux d'évaporation théorique d'une goutte de liquide de monomère avec diamatre d = 50 µm a) en fonction de la pression à température constante (T = 20 °C) et b) en fonction de la température à pression constante (P_T = 1 Torr)

Par conséquent, une étude pratique a été de caractériser les paramètres d'injection de liquide en relation avec une étude théorique concernant l'obtention d'une phase vapeur dans les conditions de basse pression.

Le processus photo-CVD conduit à l'encapsulation d'une phase fluide du monomère dans une membrane solide constitué de son polymère. La Spectroscopie de Force Atomique a souligné le revêtement de surface d'une fine membrane de polymère (*Figure 6*) et la technique Raman a mis en évidence la présence du monomère liquide (*Figure 7*).

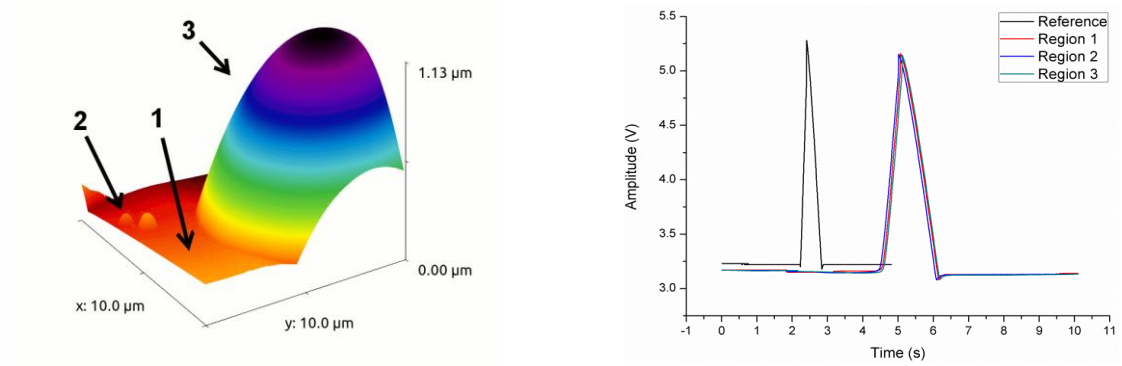

a) *b)*

Figure 6: La topographie 3D sur Si (111) substrat
avec a) les zones marquées où b) la spectrométrie de force a été effectuée

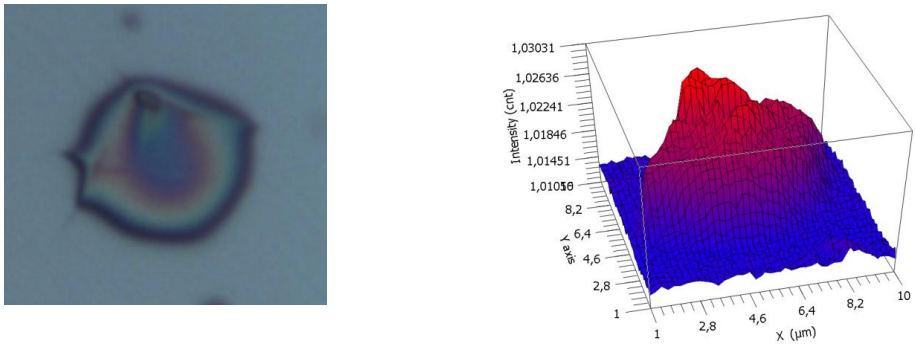

a) *b)*

Figure 7: La structure alvéolaire vue par le Microscope Cofocal Raman a) et la représentation du rapport 1640cm^{-1}/1660cm^{-1} des spectres Raman pour révéler la présence de monomer.

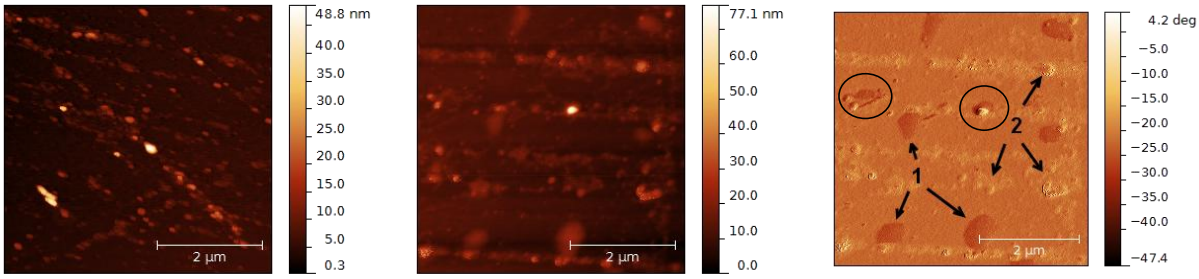

a) *b)* *c)*

Figure 8: AFM topographie d'une zone masquée (a) et une zone de dépôt (b), la phase de l'image de la zone recouverte est également présentée (c). L'encapsulation de liquide est possible dans les bulles (1) et des hétérogénéitéssont recouvertes (2); des sites de nucléation possibles sont encerclés.

Dans le processus de caractérisation, la présence des centres de nucléation pour le monomère liquide a été étudié (*Figure 8*). Une interprétation fondamentale des études scientifiques récentes souligne l'originalité de l'obtention d'une phase liquide du monomère qui est recouverte d'une fine membrane de son polymère.

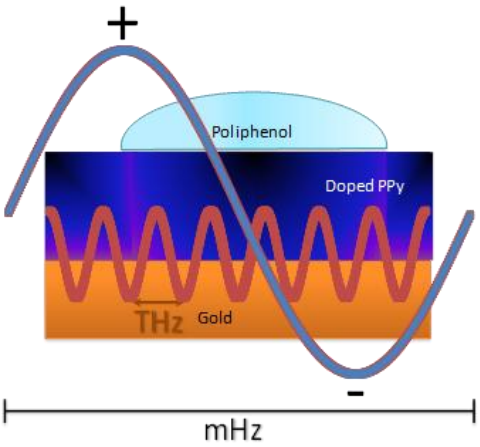

Figure 9: Schéma du dispositif expérimental, en MHz est représentée la fréquence de variation de potentiel au cours de l'EIS et dans le domaine THz est représentée la fréquence de perturbation des électrons dans SPR

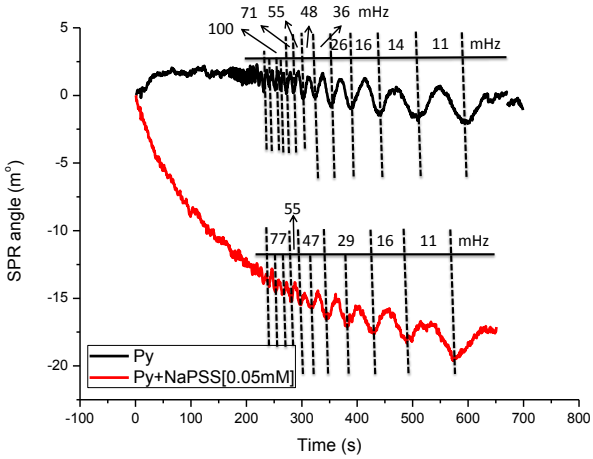

Figure 10: SPR angle réponse pendant les expériences relatives à l'EIS; dans la gamme mHz la SPR commence à réagir à la perturbation visible appliqué pendant EIS

En ce qui concerne la voie humide par lequel la caractérisation de certains films minces a été atteinte, une étude originale a été réalisée qui implique le couplage entre l'EIS et la technique SPR (*Figure 9*). Par l'utilisation de polyphénols, le suivi en parallèle de la réponse SPR avec celle de l'EIS a été réussi, mettant l'accent sur les aspects liés à l'arrangement de réseau du polymère dans les conditions d'application d'une différence de potentiel perturbateur périodique (*Figure 10*).

Une autre façon originale de caractérisation a été mies en évidence dans le cas des nanotubes de TiO_2 par voie électrochimique. Ce type de caractérisation a été réalisée en appliquant un traitement aux ultrasons qui conduit à une élimination des nanotubes en couches. L'originalité de cette caractérisation a été décrite aussi dans une série d'articles publiés dans des revues scientifiques [1–3].

Suite à la caractérisation, une série de propriétés avec un point important de l'originalité a été définis pour les films minces obtenus.

3. Propriétés

Une série de dépôts par voie photo-CVD sec ont été réalisés en faisant varier la température du substrat. La caractérisation de la surface a souligné la possibilité de libérer le monomère liquide à l'intérieur des vésicules par la rupture de la membrane polymère enveloppante. Ceci a été réalisé in situ par des changements de volume pendant la croissance induits par la diffférence des coefficients de dilatation thermique. Ce procédé a été décrit comme une libération sous activation thermique de la phase interne (TI-RIP) [4] (*Figure 11*).

Un autre effet thermique a été observé également dans le cas de l'irradiation avec le laser VIS du Microscopie Confocale Raman. Une étude a été présentée qui étudie l'influence du laser sur la transition de phase du monomère MMA en fonction de la température, mais aussi la température estimée générée par le laser dans le domaine d'analyse. Cet effet s'est révélé présenter des propriétés originales d'auto-guérison des vésicules obtenues par voie sèche (*Figure 12*).

Les aspects originaux présentés ci-dessus ont été obtenus par l'étude (à la fois théorique et expérimentale) du comportement du matériau en fonction de la température. Des aspects originaux ont également été mis en évidence par des études sur les propriétés des matériaux

qui décrivent la résistance que l'on rencontre lors de la formation d'un champ électrique, également appelée permittivité.

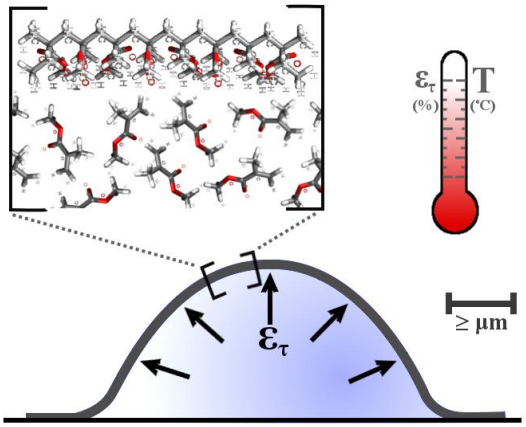

Figure 11: Description schématique du procédé TI-RIP; Il est souligné le caractère proportionné de la différence de température (T) et la souche induite thermiquement élastique (ετ)

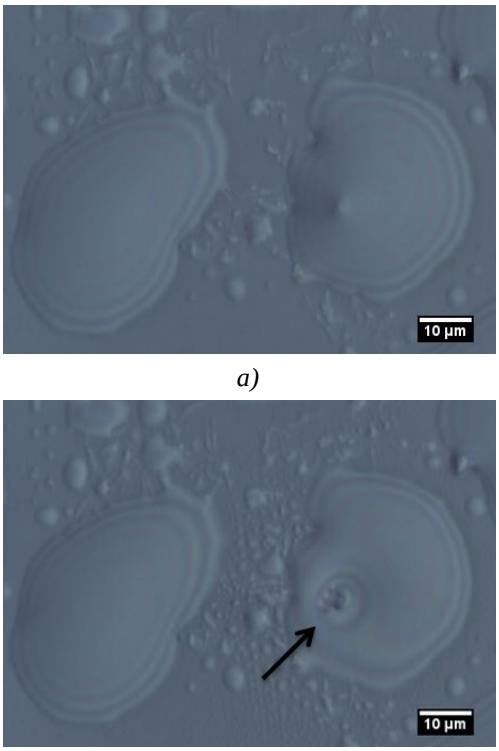

a)

b)

Figure 12: L'évolution du film sur le substrat de verre avec la région in-situ d'analyset (a) avant et (b) après la mesure Raman (la flèche pointe vers la morphologie en forme de cratère avec une hétérogénéité au centre)

La permittivité a été étudiée à la fois par l'EIS et SPR (*Figure 10*). En outre, les aspects de nouveauté ont été soulignés par l'étude électrochimique de la Neutralisation d'ion assisté par Plasmon. Ainsi, la réponse SPR a été étudiée dans deux plaines qui décrivent deux phénomènes différents: *i*) l'approche classique de contrôle des changements de masse à l'interface qui sont dues à l'évolution de la permittivité (*Figure 13 a*) et *ii*) une nouvelle approche liée à la neutralisation électrochimique des plasmons produisant le signal SPR (*Figure 13 b*).

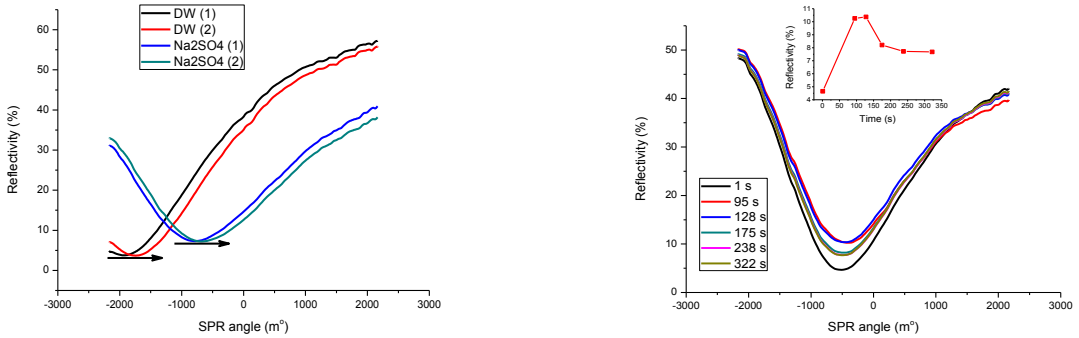

a) b)

Figure 13: SPR réponse pour l'eau déminéralisée (DW) et DW avec Na_2SO_4 50 mM pendant un cyclage entre 0 et 1 V (vs AgAgCl) (a). SPR réponse pour DW avec de l'acide oxalique 50 mM durant 322 s pour un potentiel appliqué de 0,8 V (vs Ag / AgCl) avec le minimum de réflectivité.

Ces propriétés présentées ci-dessus, mais aussi d'autres aspects mis en évidence dans les chapitres précédents, posent des bases pour des applications des matériaux préparés. Ces propriétés seront ensuite présentées en vue de leur applicabilité et des perspectives pour de futurs développements après l'optimisation de certains paramètres.

4. *Perspectives pour le développement ultérieur*

La croissance des couches minces, la caractérisation et l'étude des propriétés ont souligné leur applicabilité. La thèse traite les contributions scientifiques originales à la fois du point de vue expérimental et un problème théorique. Les propriétés des matériaux définir le fondement de leur applicabilité.

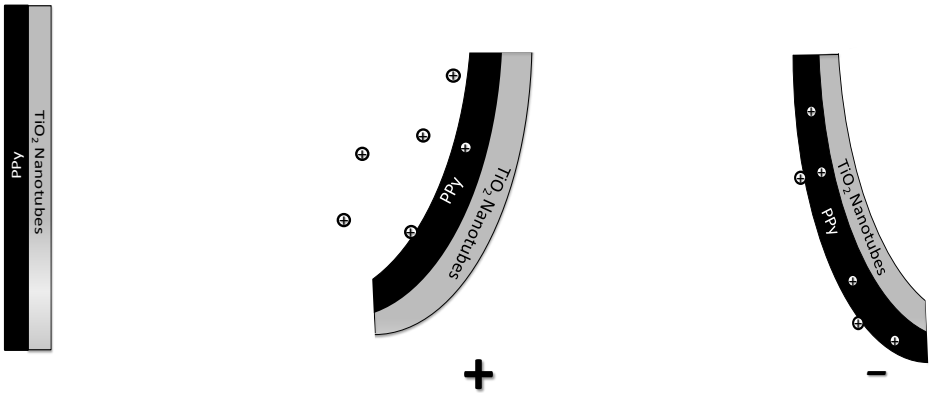

a) *b)* *c)*

Figure 14: PPy/TiO_2 nanotube bicouches (a) avec le compression de volume du film de PPy dans des conditions oxydantes (b) et la dilatation du film PPy dans des conditions de réduction (c)

De cette manière, les films minces obtenus (soit par voie sèche de la photo-CVD ou par voie électrochimique humide) ont été caractérisés afin de mettre en évidence leurs propriétés essentielles en ce qui concerne les applications. Ces propriétés décrivent un large éventail d'applications possibles.

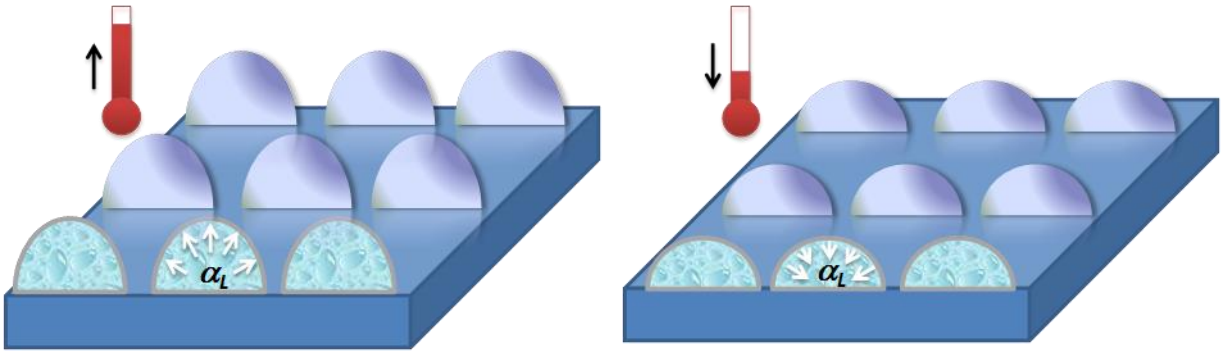

a) *b)*

Figure 15: La dilatation thermique (α_L) du liquide qui provoque le changement de convergence a) lorsque la température augmente et b) lorsque la température diminue

Les propriétés étudiées par les films minces obtenu par la voie humide soulignent des applications telles que des détecteurs pour Réactions Interfaciales de Réduction / Ionisation, par la technique SPR, actionneurs PPy formés par les PPy/TiO_2 films minces (*Figure 14*) ou de la chaleur générant films de PPy.

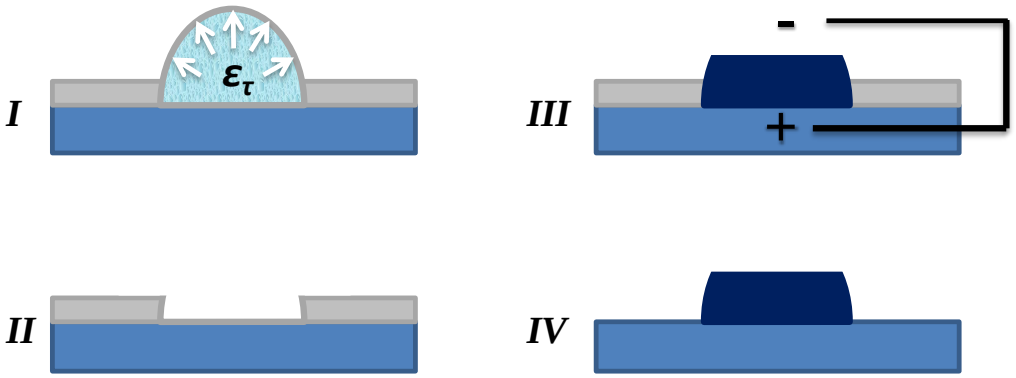

Figure 16 : nanostructuration de surface par libération de phase interne par activation thermique (I et II) combiné à la croissance électrochimique ultérieure (III) et de la dissolution de film mince (IV).

Les films obtenus par voie sèche ont révélé des propriétés qui les prédestinent comme matrice de micro-lentilles focales (*Figure 15*), ou en tant que solution de rechange pour la lithographie par faisceaux d'électrons (*Figure 16*).

Dans les perspectives futures, une optimisation des propriétés peut suivre avec comme objectif l'augmentation de l'efficacité pour une application spécifique.

Sélection de Bibliographié

[1] C.C. Manole, C. Pirvu, I. Demetrescu, Evaluation of TiO2 Nanotubes Changes after Ultrasonication Treatment, Molecular Crystals and Liquid Crystals. 521 (2010) 84–92.

[2] C.C. Manole, C. Pirvu, Surface and electrochemical analysis for the understanding of TiO2 nanopores/nanotubes changes in post-elaboration treatment, Surface and Interface Analysis. 43 (2011) 1022–1029.

[3] C.C. Manole, A.B. Stoian, C. Pirvu, Surface Perspective of a TiO2 Nanoarchitecture, U.P.B. Sci. Bull. 72 (2010) 91–98.

[4] C.C. Manole, F. Maury, Ioana Demetrescu, Thermally Induced Release of Internal Liquid Phase Encapsulated in a Polymer Membrane Grown by Photoactivated DLICVD, Chemical Vapor Deposition. DOI:10.1002/cvde.201206987

FONDUL SOCIAL EUROPEAN
Investeşte în oameni!
Programul Operaţional Sectorial pentru Dezvoltarea Resurselor Umane 2007 – 2013
Proiect POSDRU/88/1.5/S/61178 – *Competitivitate şi performanţă în cercetare prin programe doctorale de calitate (ProDOC)*

UNIVERSITATEA **POLITEHNICA** DIN BUCUREŞTI
Facultatea de Chimie Aplicată și Știința Materialelor
Departamentul de Chimie Generală

INSTITUT NATIONAL **POLYTECHNIQUE** DE TOULOUSE
Ecole Nationale Supérieure des Ingénieurs en Arts Chimiques Et Technologiques
Centre Interuniversitaire de Recherche Ingénierie Materiaux

Senate Decision Nr. 219 / 28.09.2012

DOCTORATE THESIS

CVD and electrochemical polymeric thin films: elaboration, characterization, properties and applications

Filme polimerice subțiri depuse prin tehnici electrochimice și CVD: elaborare, caracterizare proprietăți și aplicații

Author: Claudiu Constantin MANOLE

DOCTORATE COMMITEE

President	Prof. Dr. Mircea Teodorescu	from	Universitatea Politehnică București
PhD Coordinator-1	Dr. Francis MAURY	from	Institut National Polytechnique de Toulouse
PhD Coordinator -2	Prof. Dr. Ioana DEMETRESCU	from	Universitatea Politehnică București
Referent	Dr. Michael PONS	from	Science et Ingénierie des Matériaux et Procédés
Referent	Prof. Dr. Eng. Horia IOVU	from	Universitatea Politehnică București
Referent	Prof. Dr. Laura ȚUGULEA	from	Universitatea București

Bucureşti 2012

Abstract

The thesis deals with the growth, characterization and the properties of two types of polymeric thin films: poly (methyl methacrylate) (PMMA) and polypyrrole (PPy). These thin films were obtained by a dry and a wet route.

The dry route involved the growth of the polymeric films by an original process of Chemical Vapor Deposition, namely Photo-CVD. The growth process includes an aspect of originality by the UV activation of the monomer species in the gas phase. Both PMMA and PPy were obtained for the first time by this Photo-CVD. The characterization highlighted properties with possible applications in microelectronics, micro-optics and functional coating on fabrics.

The wet route involved the growth of polymeric and hybrid organic/inorganic thin films by an electrochemical approach. Organic PPy and inorganic TiO_2 nanostructures were obtained and characterized particularly by various electrochemical techniques. The growth aspects of PPy were supplementary highlighted by the Surface Plasmon Resonance (SPR). The properties for the films obtained and characterized by the electrochemical techniques recommend them for actuating devices and also as heat generating films.

GRATITUTO

I address worm thanks to Prof. Dr. Ioana DEMETRESCU, the scientific coordinator of this doctorate work from Universitatea Politehnică București, for the guidance and the valuable advices that which led me to a continuous evolution during the doctorate years. I would also like to address thanks to Dr. Francis MAURY, the scientific coordinator of this doctorate thesis from Institut National Polytechnique de Toulouse, for the support and the guidance that proved to be a valuable help in following the scientific objectives.

I would also like to thank Conf. Dr. Cristian PÎRVU for the discussions and the support during the whole period of theoretic and practical research. I would also like to thank Dr. Francois SENOCQ for the discussions and the exceptional help offered in designing and conducting the experiments made by the dry route.

I would like to thank especially to the whole collective of the Department of General Chemistry from Facultea de Chimie Aplicată și Știința Materialelor and to the SURF team from Centre Interuniversitaire de Recherche Ingénierie Materiaux that offered me their support along the doctorate years.

I would like to thank to the collegues from Centre Interuniversitaire de Recherche Ingénierie Materiaux, Ana-Maria CIUBOTARU, Diane SAMELOR, Daniel SADOWSKY and Guilhaume BOISSELIER for the help given to for the adaptation to the working atmosphere in Toulouse.

I give special thanks to Mr. Yves MILLE and Mrs. Hélèn MILLE for offering me the occasion of reflecting on the scientific objectives from a charming location. I am also grateful to Prof Alain GLEIZES for introducing me to these remarkable persons.

Last, but not least, I would like to thank to Prof. Dr. Laura ȚUGULEA for offering me the opportunity to work in the Prof. Dr. Ioana DEMETRESCU group during the master's thesis, as this doctorate thesis would not have been written without this opportunity.

List of abbreviations

AC	Acoustic Mode of the Atomic Force Microscope
AFM	Atomic Force Microscopy
BC	Before Christ
CVD	Chemical Vapor Deposition
DLI	Direct Liquid Injection
EDL	Electrical Double Layer
ESPR	Electrochemical Surface Plasmon Resonance
FTIR	Fourier Transform Infrared
HCPK	1-hydroxycyclohexyl-phenil ketone
HWCVD	Hot Wire Chemical Vapor Deposition
MFC	Mass Flow Controller
MFM	Mass Flow Meter
MMA	methyl methacrylate
NO	Numerical Aperture
NPs	Nanoparticles
oCVD	Oxidative Chemical Vapor Deposition
PE	Polyethylene
PET	Polyethylene terephthalate
Photo-CVD	Photon Assisted-Chemical Vapor Deposition
piCVD	Photo Initiated Chemical Vapor Deposition
PMMA	Poly (methyl methacrylate)
PP	Polypropylene
PPy	Polypyrrole
PS	Polystyrene
PVC	Polyvinylchloride
Py	Pyrrole
TCM	Transparent Conducting Materials
QCM	Quartz Crystal Microbalance
SEM	Scanning Electron Microscopy
SPR	Surface Plasmon Resonance
TI-RIP	Thermally Induced-Release of Internal Phase
A	area

A_p	pizoelectrically active area
c	speed of light
D_Z	normal of the electric field in the dielectric
E	Young modulus of elasticity
E_Z	normal of the electric field in the metal
F	force
F_{ct}	Faraday constant
f	frequency – continuous variable
f_{gas}	gas injector frequency
f_{liq}	liquid injector frequency
h	Planck's constant
k_0	wavevector of light in free space
k_{spr}	Surface Plasmon Resonance wavevector
K_a	equilibrium constant
M_{eq}	equivalent weight
M_W	molecular weight
m	mass
m_{pe}	photoelectron mass
P	pressure
P_C	chamber pressure
P_M	motive pressure
P_{N2}	N_2 gas pressure
P_T	total pressure
P_V	vapor pressure
p	work
Q	flow rate
Q_C	charge; electron flow rate
Q_J	Joule heat
Q_{N2}	flow rate of N_2
R	universal constant of gases
r	radius
T	temperature
T_{inj}	temperature below the injector
$T_{substrate}$	substrate holder temperature

T_{UV}	UV chamber temperature
t	time
t_{off}	close time of the injector aperture
t_{on}	opening time of the injector aperture
V	volume
V_P	position-sensitive photodiode response
v_{pe}	photoelectron speed
x	displacement distance
ϵ_f	strain-at-break point
ϵ_t	thermal strain
ϵ_T	total strain
ϵ_τ	thermal-induced strain
ΔG_{hmo}	Gibbs free energy needed for homogenous nucleation
ΔG_{hto}	Gibbs free energy needed for heterogeneous nucleation
ΔH_{vap}	molar heat of vaporization
K	sensitivity factor of the Quartz Crystal Microbalance
Π	period
Θ	critical angle of reflection
α	thermal expansion
α_L	thermal expansion of the liquid
α_S	thermal expansion of the solid
α_{MMA}	thermal expansion of methyl methacrylate
α_{PMMA}	thermal expansion of Poly (methyl methacrylate)
δ	deflection sensitivity
ε_1	permittivity of the metal
ε_2	permittivity of the dielectric medium
ε_r	relative permittivity
φ	angle between x axis and the projection of the normal to the a xy plane
κ	spring constant
λ	wavelength
μ	viscosity
η	chemical reaction efficiency

ν	kinematic viscosity
θ	angle between the vertical direction (z axis) and the normal to the a horizontal (x and y axis) plane; it has physical significations related to phase shift and contact angle
ρ	density
υ	frequency – discrete variable
υ_0	fundamental resonance frequency
ω	angular speed
ξ	extinction coefficient

SUMMARY

CHAPTER 1 - INTRODUCTION

The pages of this thesis contain the elaboration, characterization and applications of various materials under the form of thin films. The thin films are both from the organic (polymers) and inorganic (metals and metal oxides) category, treating aspects that involve the micro-technology and nano-technology areas.

Materials have specific properties which recommend them for various applications. The scientific contributions further expand the applicability of some materials, or enhance the properties for the applications already consecrated.

This chapter treats the production of materials related to the studies done in this thesis and discusses it based on their usage. As source of further development, the today's context of the expanding world of scientific information is also presented. Starting from this general overview of the scientific context (both as informational and applicative), the elements of originality in this thesis will be presented.

1.1. Worldwide Demand for Materials

An overview on the production and use of the most important materials as primary basis for the scientific research is further detailed. They include the metals (gold, silver and titanium) but also the wide class of polymers, both from a worldwide perspective.

1.1.1. Metals

The most appreciated metal from the ancient times until now, gold, had and still has a big impact on the today's society. The history of gold is found to begin in the human society since the remote antiquity. Fossil study revealed pieces of gold in Spanish caves which were used by the Paleolithic Man around 40 000 BC [1]. Later, in around 3 000 BC, the Egyptian priests and pharaohs used it for adornment [1]. Gold was used for trading as gold coins at around 600 BC [2]. The gold standard for the monetary system was ended firstly in Argentina and Australia in 1929, Romania left the gold standard in 1932 for the Leu while in 1936 France renounced the gold standard for the Franc [3]. In the last decades, the gold production had two steep increases from 1986 to 1990 and 1996 to 1999, with a significant part used in industry. The recent economic difficulties of the global markets are observed in 2009 as the gold production decreased (*Figure 1.1 a*).

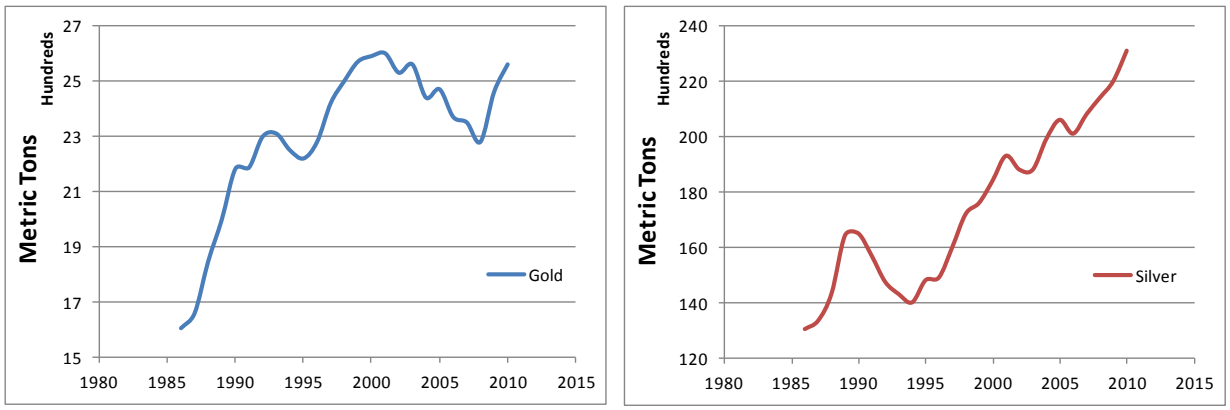

a) *b)*

Figure 1.1: World mine production of a) gold and b) silver; data compiled from [4–15]

In 2010 the gold production recovered and increased with 4%, after 10 years of decrease. From the total production of gold, 2020 metric tons (t) were used for jewelry

fabrication [8]. Another important use of gold was the one allocated to the coins fabrication, with 207 t of gold [8]. The electronic industry in 2010 used 327 t of gold, marking a 19% increase with respect to 2009 [2]. The gold is the material capable of producing a phenomenon called Surface Plasmon Resonance which is used as a scientific tool in investigating the behavior of various materials. *Chapter 5* presents a series of studies that reveal original aspects of such a SPR system coupled with an electrochemical system.

The price increase of gold in 2009 resulted in the increase of silver consumption in the same period, as reflected in *Figure 1.1 b)*. The jewelry and silverware consumption of silver a decade ago was of 33 %, while in 2010 it accounts for 25 % of fabrication demand [13]. This is indicative for an increase of silver demand for other fabrication routes. From the total of silver produced in 2010, 3570 t were used in industry, accounting for a 19% increase with respect to the previous year [15]. In the context of the global economic recovering and the need for renewable energy, the silver use for photovoltaic cells increased with 27% from 2010 to 2009 with a silver consumption of 1500 t [13].

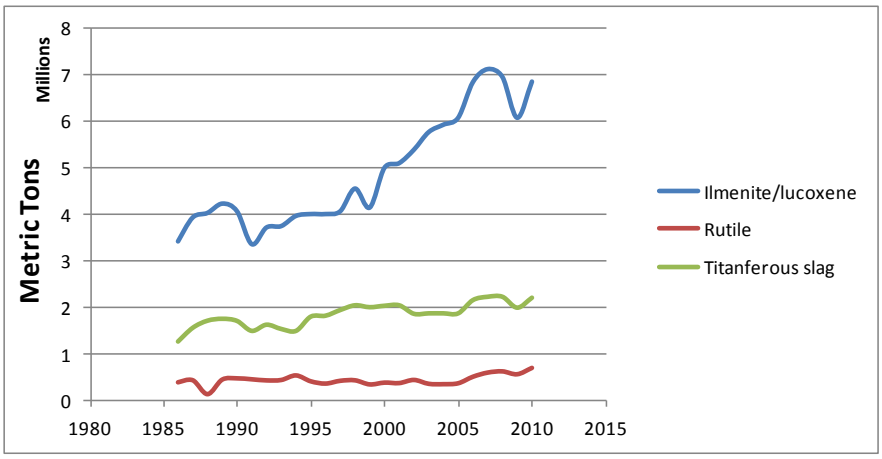

Figure 1.2: World mine production of titanium concentrates; data compiled from [16–21]

The photovoltaic cells can be divided in two categories with respect to silver consumption: thick film cells and thin film cells. The thick film cells require a quantity of silver ranging from 0.15 to 0.25 g/cell, while the thin film cells have a negligible use of silver [13]. This thesis focuses on the fabrication of thin films, as from a material consumption perspective is a more economically efficient approach. Also, the scientific community focused on the alternative materials for the use in photovoltaic cells. Such a material is titanium under the form of titanium dioxide (TiO_2) [22]. In this thesis TiO_2 thin films under the form of nanostructured matrix are obtained over titanium (Ti) substrates. Subsequent versatility was added by the controlled growth of a conductive thin film facet (*Chapter 5*). Titanium substrate has a great advantage with respect to the material availability, as it has a presence of 0.5% in Earth's crust [23].

In 1791, William Gregor discovered titanium in an ilmenite (crystalline iron titanium oxide - $FeTiO_3$) deposit. Subsequently, the natural-occuring TiO_2 rutile mineral (composed primarily by impure TiO_2) was discovered by Martin H. Klaproth in 1795. From its discovery, the production of the titanium concentrates reached the total quantity of 9 790 000 t in 2010 [20]. The full evolution of the mine production of the titanium concentrates in the last decades can be seen in *Figure 1.2*. After the economic turning point in 2009, the titanium concentrates production starts to recover. From the total quantity of the produced Ti mineral concentrates, 95% was used in 2010 to produce pigments (mainly paint and coatings, plastics, rubber, and paper) [20]. The mill product for Ti alloys increases in 2010 with 62% [20]. From the total mill production, 67% is used in the aerospace industry [20]. Also a significant amount of Ti is consumed in the steel and nonferrous alloy industries. The steel is considered as the basis for

the metal industry. It is an iron-based alloy. It usually contains a minimum of around 12% Cr required to prevent the rust in unpolluted atmospheres (hence the naming of *stainless*) [24].

In the late 1980 the steel production was exceeded by the plastics production. In 2011, the steel production (8 kg crude steel = 1 liter polymer [25][1]) of 186 milliard liters[2] is surpassed by the plastics industry that has an estimated production of around 280 milliard liters[3]. The plastic industry will be further treated from the perspective of the polymers use for various applications. The context of the plastics, and widely the one of polymer industry is relevant as this thesis deals significantly with processes of producing polymers for various application.

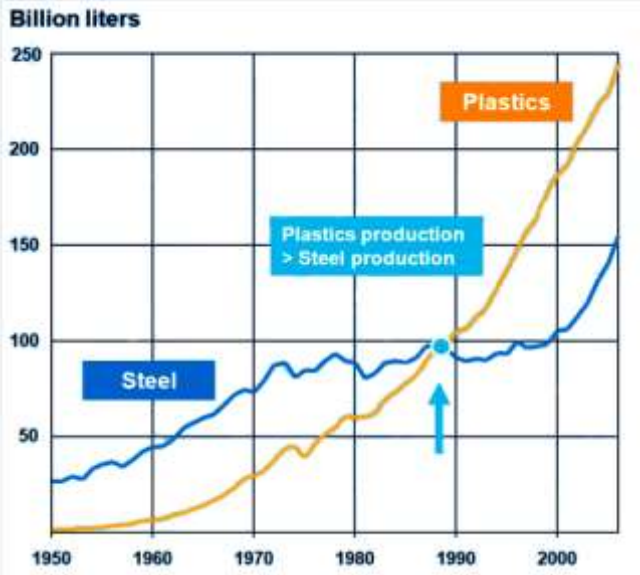

Figure 1.3: World production of plastics and steel; data from [26]

1.1.2. Polymers

The plastic industry is dominated by the production of the "*big five*" plastic types: Polyethylene (PE), Polypropylene (PP), Polyvinylchloride (PVC), Polystyrene (PS) and Polyethylene terephthalate (PET). As observed in *Figure 1.4 a)* the top three resin types in the market share are PE with 29%, PP with 19% and PVC with 12%. In the class of other plastics, in 2011 Poly (methyl methacrylate) (PMMA) accounted for 2.3% of total plastics production4 [27]. In 2009, 80% of the PMMA production was used in constructions and automotive industry[5]. In 2011, an estimated 40% of total PMMA production was oriented towards the electronic sector[6]. This fast growing PMMA demand in the electronic sector can be divided in two categories: light-guided panels and transparent acrylonitrile-butadiene-styrene/methyl methacrylate casings[7]. Chapter 2 and 3 will treat the obtainment and characterization of the PMMA thin films, with its final applicability concluded in Chapter 6.

As observed in *Figure 1.4 b)*, the highest demand for plastics was recorded in packing with 39%, construction with 21% followed by the electrical and electronic industry with 6%. The electronic industry through the micro and nano-technology strives to achieve better performance by streamlining the use of materials. This leads to the decrease in material usage and to increases in performances. Aspects that implicate the applicability in the

[1] Approximated from the steel density of around 8 g/cm3
[2] Source: *worldsteel.org*
[3] Source: *plasticseurope.org*
[4] Source: ICB via *ICIS.com*
[5] Source: *marketpublishers.com*
[6] Source: ICB via *ICIS.com*
[7] Source: ICB via *ICIS.com*

microelectronic production processes will be highlighted in this thesis along with the experimental studies (Chapter 6).

Furthermore, intrinsically conducting polymers are a different class of polymers that have properties recommended for electronics, but generally do not belong to the plastics class. The class of plastics (defined by the moldable polymers) does not have conductive properties. However, by the addition of a non-plastic polymer, namely Polypyrrole (PPy), to form a plastic composite gives electrical conductivity to the final plastic [28]. Such PPy films are obtained in this thesis by dry routes (Chapter 4) and wet routes (Chapter 5). Their resulting properties are set in perspective along with the applicability in Chapter 6.

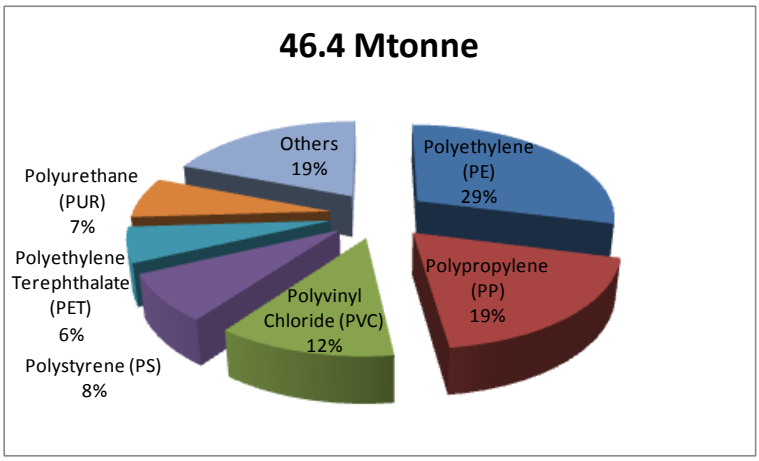

a)

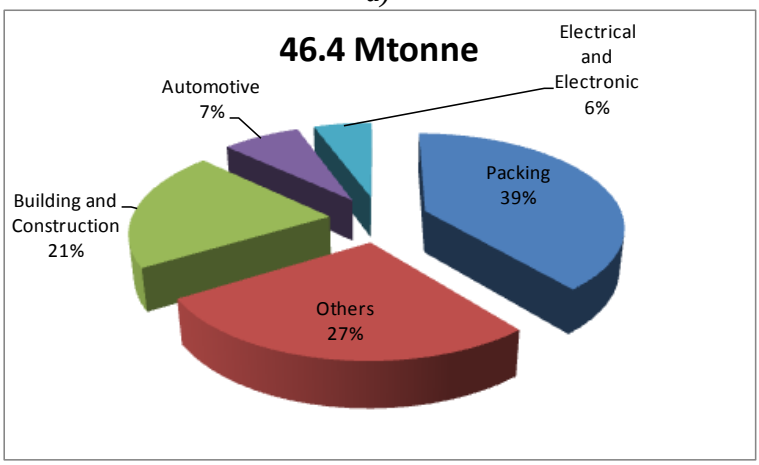

b)

Figure 1.4: European plastic demand in 2010 by a) resin type and b) market segment; data from [27]

The material properties define the use of materials for various applications and are a direct result of the characterization process. The approach of dealing with the information interpretation obtained by the characterization techniques is further presented.

1.2. Scientific Approach

The scientific approach in synthesizing the aspects observed during the steps of film growth and characterization is made by a scientific inquiry over the obtained results. The source of answers for such inquiries is found in scientific publications, such as scientific papers, books or reports. This leads essentially to a unitary overview of the obtained results that are discussed with respect to the representative scientific knowledge. Such discussions will highlight the properties of materials and will define their applicability.

1.2.1. The Scientific Inquiry Strategy

The raw experimental results presented in this thesis require specific fundamental tools for interpretation. These tools can be enveloped by the knowledge of one discipline (such as physics, chemistry or biology).

Bridges between disciplines are attested to emerge at the middle of the 20th century [29,30]. These bridges are defined by the emergence of the multidisciplinarity and the interdisciplinarity approaches [29,30]. The multidisciplinarity can be described as the use of the knowledge from more than one discipline (such as physics and chemistry or chemistry and biology) with a framework limited to a disciplinary research [27]. A further step in strengthening the bridge is given by the interdisciplinarity, which makes transfers of methods specific to one discipline into another [27]. Such aspects can deal with the understanding of the experimental data obtained in this thesis.

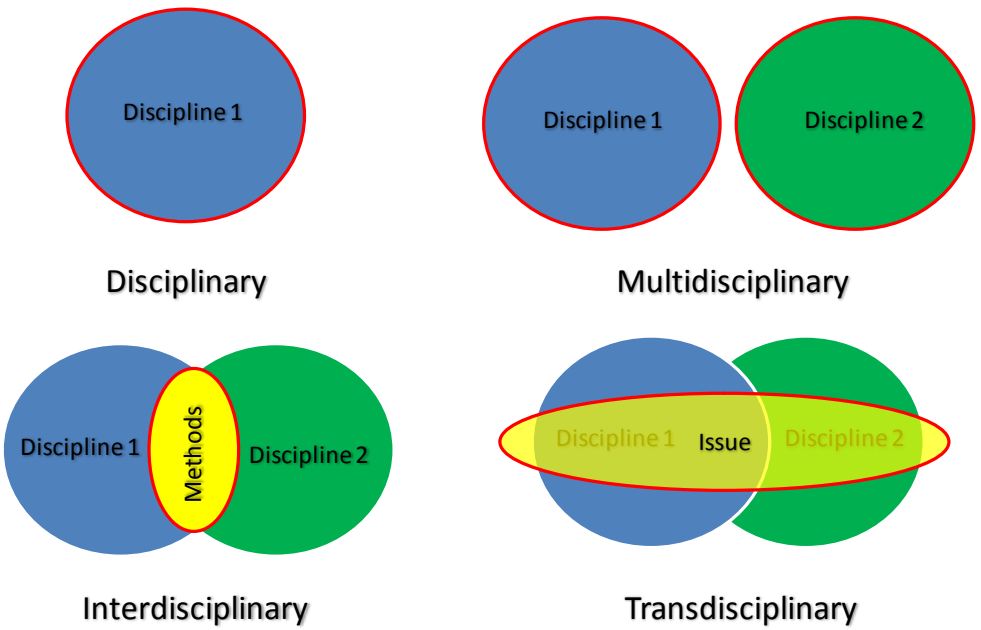

Figure 1.5: Scientific inquiry types with respect to disciplines

However, in the actual research the main drive is the economic need for more efficient, environmentally friendly and renewable technologies. The research needs to respond to the modern world demands. The latest economic state was previously presented in a manner related to aspects presented in this thesis. The economic reasoning requires an approach that is not found relative to the scientific disciplines, but rather to the issue of applicability. The focus on the issue in question and the use of tools specific to various disciplines for addressing it can describe the transdisciplinary approach [27]. The diagram of the pluridisciplinarity as previously discussed can be seen in *Figure 1.5*.

The multidisciplinarity approach is reflected in the use of the scientific knowledge for the interpretation of the results. Also the interdisciplinarity is observed, as aspects of physico-chemistry are treated unitary with respect to the results. The results can also be enveloped in separate branches, such as material sciences and engineering sciences.

The polidiciplinarity is also expressed in the scientific context of article publications. Studies have been made to analyze and synthesize the aspects of the scientific articles with respect to the scientific branches [31–33] but also by focusing on specific domains research groups [34].

1.2.2. Multidisciplinary Research in the Scientific Context

The expanding world of scientific research and its interconnectivity leads to the need of an efficient synthesis of the disciplines. R. Klavans and K. W. Boyack studied 20 maps of sciences classifications to determine a consensus ordering for the disciplines. They observed that the maps can be classified in three basic forms: linear, centric and noncentric (as detailed in *Figure 1.6*) and recommended various patterns for different purposes (such as navigation or education) [37].

The weighing is given by the citations factors which interconnect various scientific areas. L. Leydesdorff and I. Rafols presented a global map of science using the Thomson Reuters citations indexes (formerly known as ISI) for subject categories in 2009 [35]. Based on their data, the overall scientific map of sciences considering the 2009 citations is presented in *Figure 1.7 a)*. The thicknesses of the connecting arrows describe the citation factors between the various disciplines and the citation factor per domain is described by the size and color of the dots. The biomedical sciences have the highest citation factors for the 2009 year.

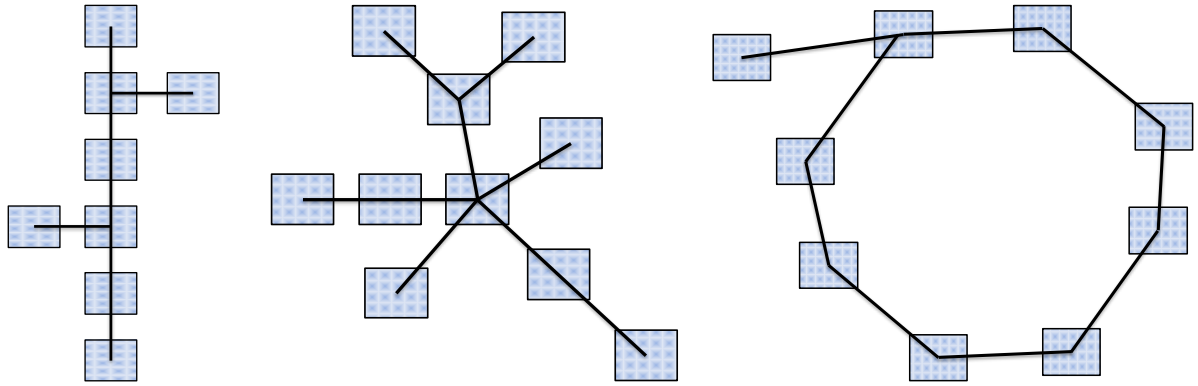

a) *b)* *c)*

Figure 1.6: Examples of a) hierarchical (or linear), b) centric, and c) noncentric (or circular) map forms; classification made by [37]

The scope of this thesis is focused on the scientific area described by the physics, chemistry, material sciences and engineering. An expanded view on the discipline area representative for this thesis and their designated categories are shown in *Figure 1.7 b)*. It can be observed that chemistry has the highest citation factor, preceded by the material sciences. Physics is on the third place with respect to the citation factors, separating the engineering sciences with the lowest citation factor. This reveals the fact that the scientific production has a powerful contribution dictated by the research related to economic applicability. The increased importance of chemistry is given by the contributions to the material chemistry but also to the biomedical sciences (*Figure 1.7 a* and *b*).

The scientific map is designed to reflect the dynamic context of the scientific publications. This thesis contains 260 unique references. From these, 70% are scientific articles. The scientific articles are a good reference for weighing the interrelations between disciplines.

A grasp of the scientific context also allowed identifying the aspects of originality with respect to the experimental routes. Such aspects will be further highlighted in the description of the methodology.

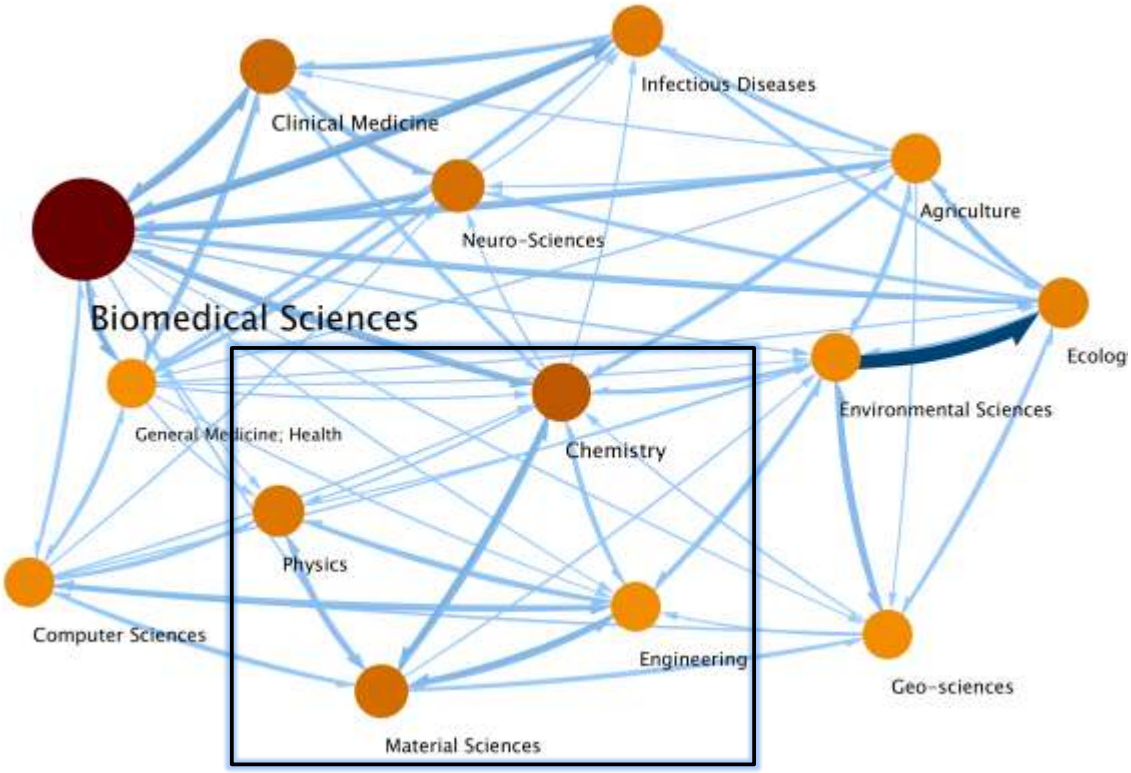

a)

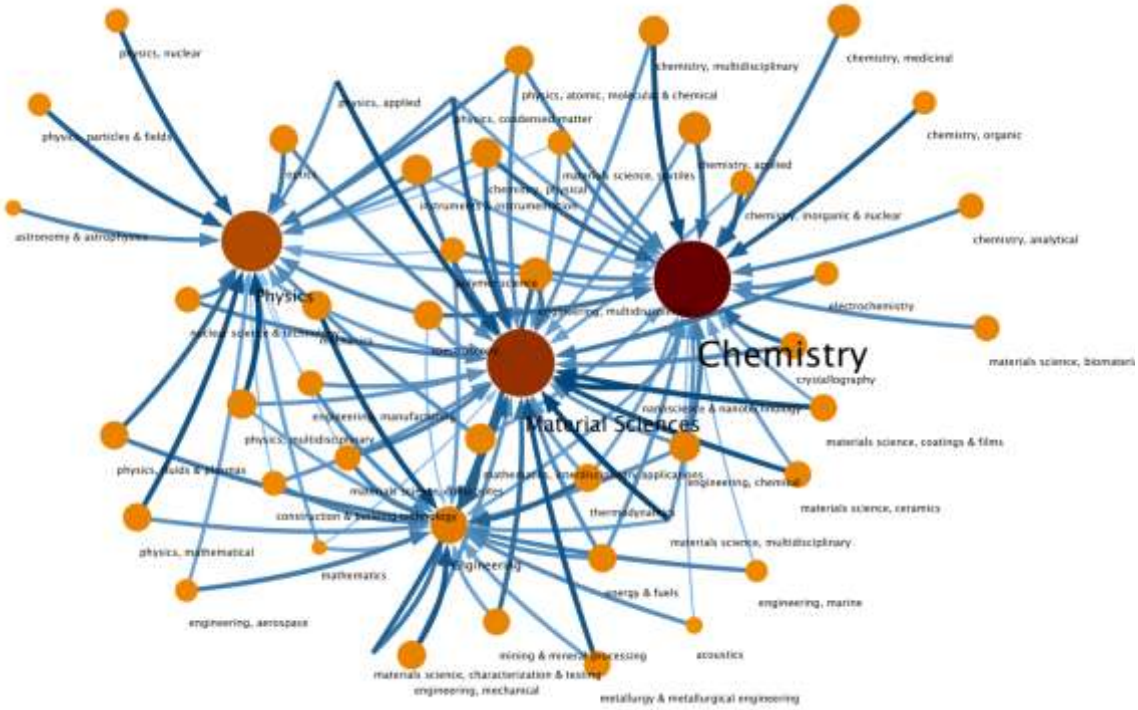

b)

Figure 1.7: The map of citing factors 2009 a) over 14 main ISI Subject Categories (estimate based on the data from [35]) and particularly b) over material science, chemistry, physics and engineering sciences; the maps were made with [36]

1.3. Methodology

In the thesis the thin films are obtained either by consecrated methods such as the wet route of the electrochemical depositions or original methods such as the dry route of the Photon-Assisted Chemical Vapor Deposition (Photo-CVD). The wet route also marks aspects of originality with respect to the scientific approach, as the Surface Plasmon Resonance (SPR) technique, generally used for bio-sensing, is studied in conjunction with the electrochemical processes.

1.3.1. Chemical Vapor Deposition

One of the means of obtaining polymeric thin films in this thesis is the dry route of the Chemical Vapor Deposition (CVD). A synthetic diagram of the CVD process is presented in *Figure 1.8.*

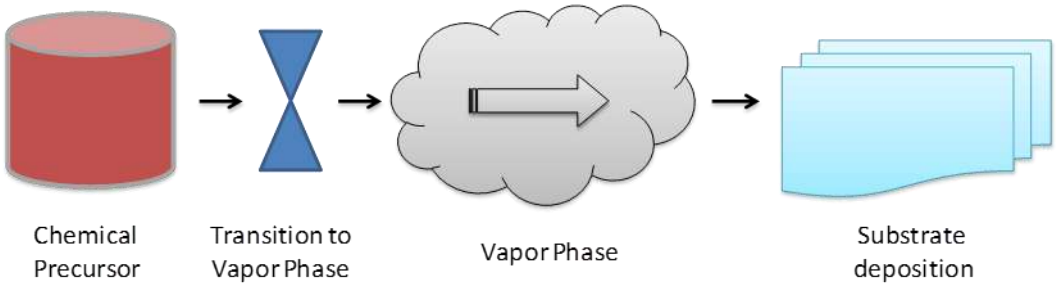

Figure 1.8: General diagram of the Chemical Vapor Deposition process

It involves the use of chemical species, called precursors, which can be generally in liquid or solid state. These precursors are further transformed in a vapor phase. The whole CVD process can be classified by the method of obtaining the vapor phase as:

- *Aerosol assisted* technique which generates the vapor phase ultrasonically; it is useful for non-volatile precursors [38–41];
- *Sublimation* technique in which the obtains the vapor phase from a solid without passing through the intermediary liquid phase, such as the case of parylene deposition by CVD [42];
- *Bubbling* technique which obtains the vapor phase is obtained by passing an inert gas through a glass jar filled with a liquid precursor [43].
- *Direct Liquid Injection* (DLI) technique which uses a liquid injector (usually based on the car injection technology) to vaporize the liquid; this technique can facilitate relatively high growth rates due to the high flow rates of the precursor [44–46].

In this thesis the DLI technique is used to obtain the vapor phase required to grow the polymeric thin films.

The vapor phase obtained using one of the techniques previously described is then directed to the substrate by a flux of inert gas named carrier gas. When gas phase reaches at the substrate a heterogeneous reaction occurs leading to the growth of a solid phase, thus describing the deposition. The deposition process is the result that is aimed to be achieved.

Aside from the overall steps involved in CVD, a significant aspect can be addresses by considering the factors involved in the final deposition on the substrate level. In the case of polymers, the deposition onto the substrate is governed by the process of polymerization.

The polymerization occurs by the chemical binding of a series of single molecular units called monomers. The monomers need to be brought in a reactive state in order to bind. With respect to CVD, in literature there are several techniques that are used to obtain the reactive species of the monomer, such as:

- Physical activation of the gas phase of monomers by thermal energy, with techniques such as Hot wire CVD (HWCVD) [47,48].
- Chemical assisted by the addition of oxidant compounds; they can be created by a heated crucible in the oxidative CVD (oCVD) [47].
- Physico-chemicaly assisted by parallel introduction of the additive with the monomer (if such an additive is volatile) and with a UV irradiation of the substrate in the photo initiated CVD (piCVD) [49,50].

The main focus in this thesis is on the UV activation of the gas phase by the Photo-CVD. This offers originality to the CVD process, as the substrate is not under direct UV irradiation, such as the case of piCVD. Furthermore, the deposition can be obtained at room temperature if desired and permits the use of additives that are not volatile. Particular aspects of the experimental parameters will be further treated with respect to this original approach to CVD process.

1.3.2. Electrochemical Surface Plasmon Resonance

The previously described CVD process describes the dry route used to obtain the thin film. The wet route involves the growth of polymers by electrochemical technique. This is comprised by a unified physical and chemical overview of processes involved in wet environment.

From a chemical point of view, the chemical bonds can be grouped as [51]:

- *Ionic bond* that describes the chemical bond between two atoms caused by the electrostatic force between oppositely charged ions;
- *Covalent bond* that describes the chemical bond of two atoms which share between them two electrons;
- *Metallic bond* where the electrons are shared over many atoms; it can be described as lattices of metal cations immersed in a fluid "sea" of electrons.

The electrochemical processes involve the reaction at the interface of two environments: the electrolyte and the working electrode.

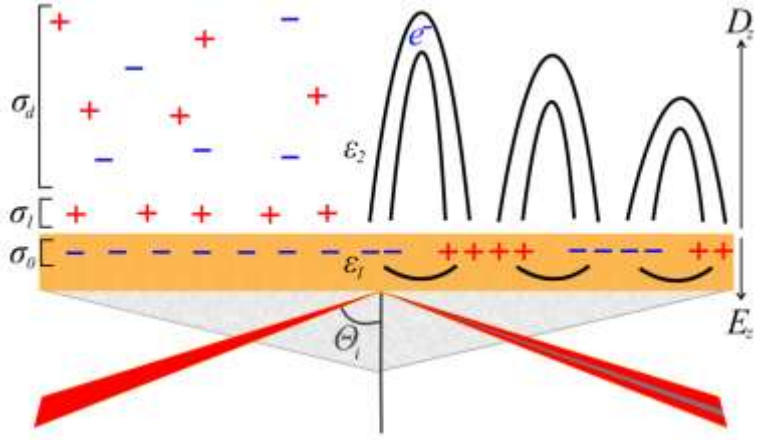

Figure 1.9: Schematic representations of Electrical Double Layer (EDL) to the left and Surface Plasmon Resonance (SPR) to the right

The salts held together by ionic bonds usually suffer dissolution in the polar environment of water. Through this process an electrolyte solution that contains a certain amount of ions is obtained. The electrolyte can participate at the chemical reactions that occur at the interface with the working electrode. The working electrode is usually a metal electrode characterized by the metallic bonds.

In *Figure 1.9* to the left, the charge of the metal is noted as σ_0 and represented as negative due to the free electrons in the metal network. In the electrolyte, a positive charged

compact layer next to the metal is formed to compensate the negative charge of the metal. This is called the Stern layer and its charge is noted with σ_1. On top of the Stern layer, a diffusion layer is described by coulomb interactions of the ions with the total charge noted as σ_d.

The electro-neutrality of the two electrical double layers (EDL) in the solution (σ_1 and σ_d) in the metastable conditions needs to be preserved with respect to the metal charge (σ_0), gold for instance [52]:

$$\sigma_0 + \sigma_1 + \sigma_d = 0 \qquad (1.1)$$

The Electrochemical Surface Plasmon Resonance (ESPR) system involves both of the sides of the gold as working electrode. As observed in *Figure 1.9* the upper side of gold is the place where the ionic charges act. If on the lower side a light is reflected (necessarily below a critical angle, Θ), the light's photons interact with the gold and, more precisely, with the free electrons in the gold network. By this interaction the photon energy is given to the electrons (absorbed), and as a consequence, on the reflected side a reflection minimum is observed. When the electrons receive the electromagnetic energy of the photons, they oscillate in and out of the gold lattice (described by the harmonic motion treated in Chapter 5). The property of the material that describes the resistance to an applied electric field (such as the one of the oscillating electrons) is named permittivity (described in Chapter 5).

The collective oscillation of the electrons onto a planar surface is called Surface Plasmon Resonance. The Surface Plasmon Resonance wavevector (k_{SPR}) is described by the wavevector of light in free space (k_0) and the permittivities of the gold (ε_1) and the electrolyte (ε_2) [53]:

$$k_{sp} = k_0 \sqrt{\frac{\varepsilon_1 \varepsilon_2}{\varepsilon_1 + \varepsilon_2}} \qquad (1.2)$$

This shows that the Surface Plasmon Resonance (SPR) wavevector is related to the permittivity at the electrolyte interface. In order to obtain the SPR wavevector, the normal of the electric field in the metal (E_z) needs to be of opposite sign to the normal of the electric field in the dielectric (D_z) [53,54]:

$$D_Z = \varepsilon_1 E_Z \qquad (1.3)$$

To sustain the electric field change, it results that $\varepsilon_1 < \varepsilon_2$. The gold responds to this requirement with a negative value for the permittivity [53].

The theoretical aspects treated above with respect to the EDL and SPR are treated for metastable conditions. The dynamic conditions where increasing potential differences are applied to the ESPR system will be further treated in Chapter 5.

The results treated in this thesis involve aspects that occur by various steps of phase changes. An overview over them is set in the next subchapter.

1.3.3. Overview

The most common tree matter phases are solid, liquid and gas. The particles in the solid phase are closely packed, with fixed volume and shapes.

In liquid the particles are close together and although they have fixed volume, they have no fixed shape. In gas the particles are widely spaced and occupy only a small fraction of the volume of the gas (1 cm^3 of water boils to make 1700 cm^3 of steam) [55].

Plasma is considered as the fourth state of matter [56]. It consists of ionized gas where at least one electron is not bound to an atom or a molecule [56]. This is the case of the SPR phenomenon in gold.

The transitions that can occur from one state of matter to another are schematically presented in *Figure 1.10*. As previously discussed, the CVD can use the sublimation to obtain

the phase transition from the solid to the gas phase of the precursor. However, for the experiments presented in this thesis the use of the liquid precursor required the vaporization into the vapor phase. During the process presence of both liquid and solid on the substrate can observed after the Photo-CVD growth (Chapters 2, 3 and 4). This indicates also a physical condensation onto the substrate but also a chemical polymerization at the substrate level. This offers specific conditions for applications that will be concluded based on a synthesis of properties in Chapter 6.

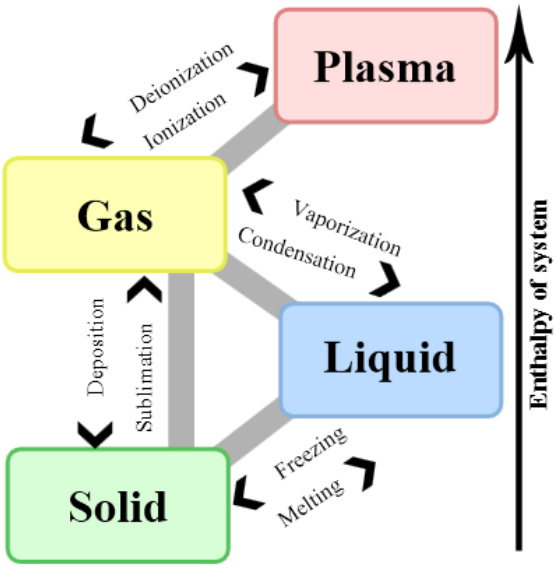

Figure 1.10: The diagram of the phase transitions and their nomenclature

The physical transition from liquid to solid is called freezing. From a chemical perspective, the transition from the liquid phase of the monomer to the solid phase of the polymer is called polymerization. The polymerization is obtained in this thesis both by a dry route (Chapters 2, 3 and 4) but also by a wet route (Chapter 5).

All of the original contributions presented in the following chapters are treated along with a fundamental insight onto the processes involved in the experimental studies. The fundamental insight also treats aspects of state of the art in today's science with respect to material characterization but also some aspects of the classical sciences.

Bibliography

[1] A. Pryor, California's Hidden Gold: Nuggets from the State's Rich History, Stagecoach Pub., 2002.
[2] S. Dalmia, Financial Supply Chain, Tata McGraw-Hill Education, 2009.
[3] T.J. Hatton, K.H. O'Rourke, A.M. Taylor, The New Comparative Economic History: Essays in Honor of Jeffrey G. Williamson, MIT Press, 2007.
[4] Earle B. Amey, Gold, U.S. Geological Survey, 1998.
[5] Earle B. Amey, Gold, U.S. Geological Survey, 2002.
[6] John M. Lucas, Gold, U.S. Geological Survey, 1994.
[7] Micheal W. George, Gold, U.S. Geological Survey, 2006.
[8] Micheal W. George, Gold, U.S. Geological Survey, 2010.
[9]Minerals yearbook minerals in the world economy, Bureau of Mines. 3 (1990).
[10]Minerals yearbook minerals in the world economy, Bureau of Mines. 3 (1993).
[11] Henry E. Hilliard, Silver, U.S. Geological Survey, 1998.
[12] Henry E. Hilliard, Silver, U.S. Geological Survey, 2002.
[13] Robert G. Reese Jr., Silver, U.S. Geological Survey, 1994.
[14] William E. Brooks, Silver, U.S. Geological Survey, 2006.
[15] William E. Brooks, Silver, U.S. Geological Survey, 2010.
[16] Joseph Gambogi, Titanium, U.S. Geological Survey, 1994.
[17] Joseph Gambogi, Titanium, U.S. Geological Survey, 1998.
[18] Joseph Gambogi, Titanium, U.S. Geological Survey, 2002.
[19] Joseph Gambogi, Titanium, U.S. Geological Survey, 2008.
[20] Joseph Gambogi, Titanium, U.S. Geological Survey, 2010.
[21] U.S. Geological Survey, Titanium Statistical Compendium, (1990).
[22] U. Diebold, The surface science of titanium dioxide, Surface Science Reports. 48 (2003) 53–229.
[23] W.L. Pohl, Economic Geology: Principles and Practice, John Wiley and Sons, 2011.
[24] J.R. Davis, Alloy Digest Sourcebook: Stainless Steels, ASM International, 2000.
[25] R. Baboian, Corrosion Tests And Standards: Application And Interpretation, ASTM International, 2005.
[26]PlasticsEurope - Plastic statistics, (2011).
[27]Plastics Europe. Plastics - the Facts 2011. An analysis of European plastics production, demand and recovery for 2010, PlasticsEurope Market Research Group, 2011.
[28] M.-A. De Paoli, R.J. Waltman, A.F. Diaz, J. Bargon, An electrically conductive plastic composite derived from polypyrrole and poly(vinyl chloride), Journal of Polymer Science: Polymer Chemistry Edition. 23 (1985) 1687–1698.
[29] T.A. Osborn, Beyond the Boundaries: A Transdisciplinary Approach to Learning and Teaching, Greenwood Publishing Group, 2003.
[30] Basarab N., Basarab Nicolescu : Transdisciplinarity and Complexity - Levels of Reality as Source of Indeterminacy, (n.d.).
[31] J.T. Klein, Evaluation of Interdisciplinary and Transdisciplinary Research: A Literature Review, American Journal of Preventive Medicine. 35 (2008) S116–S123.
[32] M. O'Brien, New Pedagogies in the Knowledge Society: Teaching for deep learning, conceptual understanding and generative thinking, in: Teaching Education 2010: ATEA Forum 2002: Proceedings of the 30th Annual Australian Teacher Education Association Conference, Brisbane, July 2002, Toowoomba Education Centre, Mercure Hotel, Brisbane, 2002.
[33] Basarab N., The transdisciplinary evolution of learning, Paris, France: CIRET. Office of P-16: The University System of Georgia P-16 Department. Retrieved March. 13 (1999) 2009.
[34] B. Nicolas, Convergence and multidisciplinarity in nanotechnology: Laboratories as technological hubs, Technovation. 32 (2012) 234–244.
[35] L. Leydesdorff, I. Rafols, A global map of science based on the ISI subject categories, Journal of the American Society for Information Science and Technology. 60 (2009) 348–362.
[36] D. Edler, M. Rosvall, The Map Generator software package, online at http://www.mapequation.org, (2010).
[37] R. Klavans, K.W. Boyack, Toward a consensus map of science, Journal of the American Society for Information Science and Technology. 60 (2009) 455–476.

[38] A.Y. Shah, A. Wadawale, V.S. Sagoria, V.K. Jain, C.A. Betty, S. Bhattacharya, Aerosol assisted chemical vapour deposition of germanium thin films using organogermanium carboxylates as precursors and formation of germania films, Bulletin of Materials Science. 35 (2012) 365–368.
[39] S.A. Bakar, S.T. Hussain, M. Mazhar, CdTiO3 thin films from an octa-nuclear bimetallic single source precursor by aerosol assisted chemical vapor deposition (AACVD), New J. Chem. 36 (2012) 1844–1851.
[40] C.R. Crick, J.C. Bear, A. Kafizas, I.P. Parkin, Superhydrophobic Photocatalytic Surfaces through Direct Incorporation of Titania Nanoparticles into a Polymer Matrix by Aerosol Assisted Chemical Vapor Deposition, Advanced Materials. 24 (2012) 3505–3508.
[41] C. Edusi, G. Sankar, I.P. Parkin, The Effect of Solvent on the Phase of Titanium Dioxide Deposited by Aerosol-assisted CVD, Chemical Vapor Deposition. 18 (2012) 126–132.
[42] V. Santucci, F. Maury, F. Senocq, Vapor phase surface functionalization under ultra violet activation of parylene thin films grown by chemical vapor deposition, Thin Solid Films. 518 (2010) 1675–1681.
[43] K. Chan, L.E. Kostun, W.E. Tenhaeff, K.K. Gleason, Initiated chemical vapor deposition of polyvinylpyrrolidone-based thin films, Polymer. 47 (2006) 6941–6947.
[44] J. Mungkalasiri, L. Bedel, F. Emieux, J. Doré, F.N.R. Renaud, F. Maury, DLI-CVD of TiO2–Cu antibacterial thin films: Growth and characterization, Surface and Coatings Technology. 204 (2009) 887–892.
[45] G. Boisselier, F. Maury, F. Schuster, Growth of chromium carbide in a hot wall DLICVD reactor, J Nanosci Nanotechnol. 11 (2011) 8289–8293.
[46] A. Douard, C. Bernard, F. Maury, Thermodynamic simulation of atmospheric DLI-CVD processes for the growth of chromium-based hard coatings using bis(benzene)chromium as molecular source, Surface and Coatings Technology. 203 (2008) 516–520.
[47] M.E. Alf, A. Asatekin, M.C. Barr, S.H. Baxamusa, H. Chelawat, G. Ozaydin-Ince, et al., Chemical vapor deposition of conformal, functional, and responsive polymer films., Advanced Materials. 22 (2010) 1993–2027.
[48] R.E.I. Schropp, B. Stannowski, A.M. Brockhoff, P. Van Veenendaal, J.K. Rath, Hot wire CVD of heterogeneous and polycrystalline silicon semiconducting thin films for application in thin film transistors and solar cells, PDF). Materials Physics and Mechanics. (2000) 73–82.
[49] K. Chan, K.K. Gleason, Photoinitiated Chemical Vapor Deposition of Polymeric Thin Films Using a Volatile Photoinitiator, Langmuir. 21 (2005) 11773–11779.
[50] W.S. O'Shaughnessy, S. Baxamusa, K.K. Gleason, Additively Patterned Polymer Thin Films by Photo-Initiated Chemical Vapor Deposition (piCVD), Chem. Mater. 19 (2007) 5836–5838.
[51] P.J.M. PhD, M.R. Gilman, K. Brutlag, AP Chemistry For Dummies, John Wiley & Sons, 2008.
[52] J. Lyklema, Fundamentals of Interface and Colloid Science - Volume II: Solid-Liquid Interfaces, Academic Press, 1995.
[53] A. Abbas, M.J. Linman, Q. Cheng, New trends in instrumental design for surface plasmon resonance-based biosensors., Biosensors & Bioelectronics. 26 (2011) 1815–24.
[54] W.L. Barnes, Surface plasmon–polariton length scales: a route to sub-wavelength optics, Journal of Optics A: Pure and Applied Optics. 8 (2006) S87–S93.
[55] C. Taylor, The Kingfisher Science Encyclopedia, Oxford University Press, 2000.
[56] A. Fridman, Plasma Chemistry, Cambridge University Press, 2008.

CHAPTER 2 - PMMA THIN FILMS OBTAINED BY DRY ROUTE - KEMSTREAM G1.5 DLI

2.1. Experimental Approach

Although the PMMA polymer is intensively studied, the UV polymerization of its monomer was not extensively investigated. The photo-initation of the MMA was used to obtain intraocular lenses, using direct irradiation in condensed phase by sunlight and UV light at a wavelength of 280nm. For the designed lens dimensions of 13.5 mm in diameter and a thickness of 5mm a 15 hours exposure was used [1]. By the original approach of the present work, the polymerization is made in a CVD reactor, where the monomer activation is achieved in the vapor phase, in a UV chamber Separated from the deposition zone. The polymerization principle of PMMA by this Photon Assisted-Chemical Vapor Deposition (Photo-CVD) is schematically shown in Figure 2.1 *a)*. The polymerization can occur on the surface of the substrate at room temperature without the direct influence of the UV radiation.

To enhance the polymerization process, the monomer was mixed with 2% 1-hydroxycyclohexyl-phenil ketone photo-initiator (HCPK) (see *Figure 2.2*) as an electron donor.

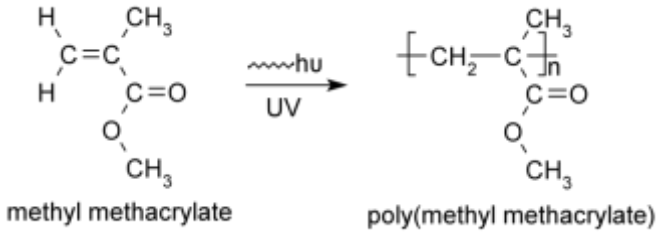

Figure 2.1: The UV polymerization principle of methyl metacrylate into poly(methyl metacrylate)

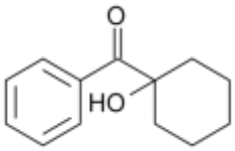

Figure 2.2: Chemical formula of 1-hydroxycyclohexyl-phenil ketone

With respect to the experimental setup, the Direct Liquid Injection (DLI) system used to deposit PMMA thin films was a Kemstream *G1.5* injector.

2.1.1. Experimental Setup and Parameters

2.1.1.1. Overview of the Photo-CVD Setup

The Photo-CVD setup that was used is presented in *Figure 2.3*. It presents 4 key components:

1. The **liquid alimentation** from a reservoir which provides the required amount of monomer for the injection into the system
2. The **injector**, the device that ensures the vaporization of the monomer
3. The **UV chamber**, where the monomer is excited by a series of 254 nm UV lamps
4. The **deposition chamber**, where the monomers polymerize.

The liquid alimentation is made under a nitrogen gas pressure. Also, a certain flow rate of gaseous nitrogen is inserted in a heated area below the injector to control the mole fraction of the monomer and its transportation towards the UV chamber (carrier gas).

The N_2 vector gas ($\boldsymbol{P_{N2}}$) was set at a pressure of 2.8 bar for the next experiments. This vector gas pressure was also directed to the injector, to help vaporize the monomer into the Photo-CVD UV chamber. Studies were made on the influence of the N_2 vector gas pressure over the monomer flowrate through the injector (Anneses 4 and 6). They indicated that the

vector gas pressure (named carrier gas - V_1 in *Figure 2.3*) is dependent to the N_2 flowrate (V_2 in *Figure 2.3*).

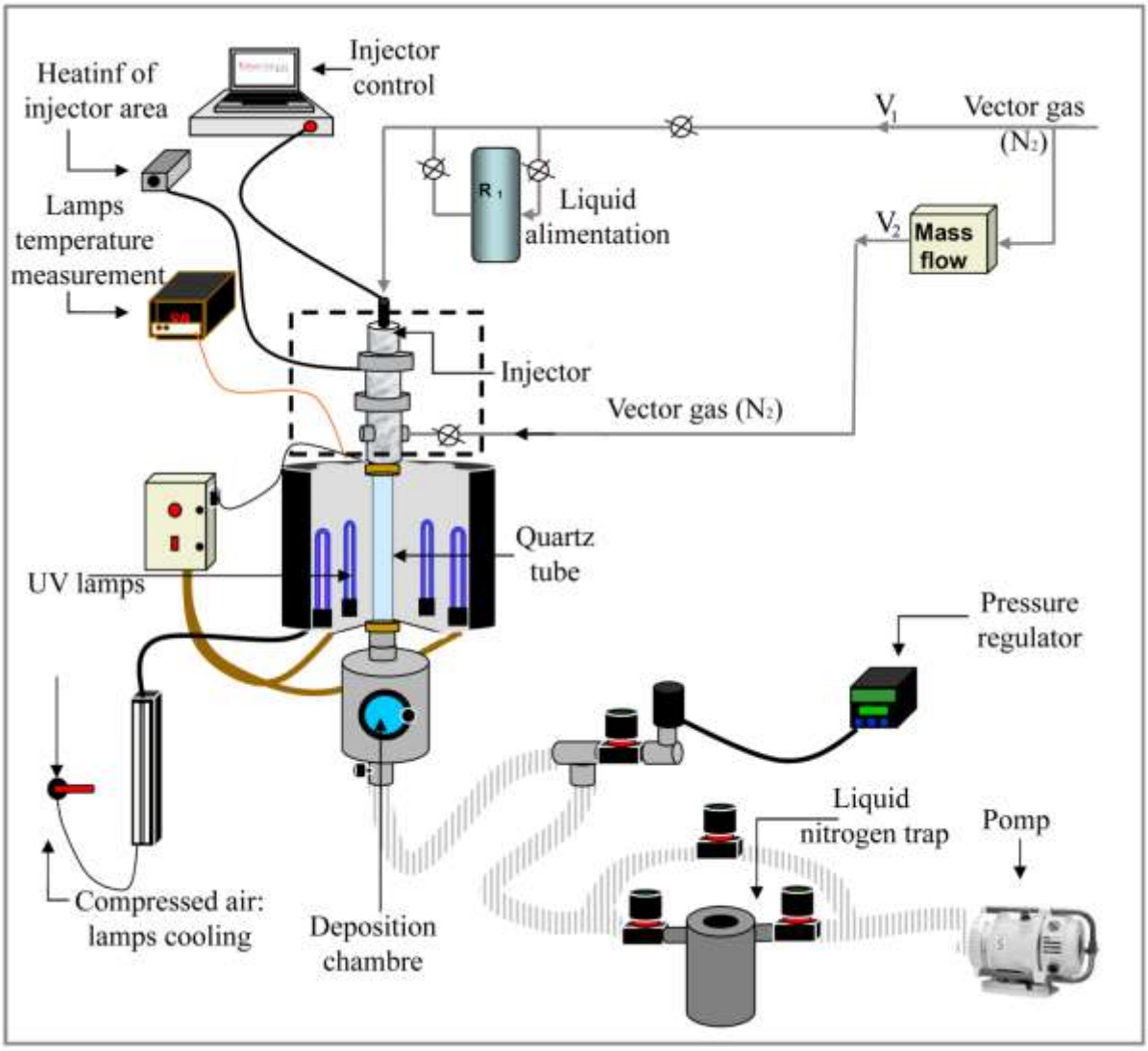

Figure 2.3: The Photo-CVD setup used for the experiments

The mixed area below the injector (where the monomer is further carried by the N_2 gas stream) was also heated at a certain $\boldsymbol{T_{inj}}$ temperature to avoid condensation. The UV chamber was kept all the time at $\boldsymbol{T_{uv}}$ = 80°C by adjusting the compressed air debit to cool the UV lamps.

A pressure regulator monitories and regulates the total pressure ($\boldsymbol{P_T}$) into the Photo-CVD system.

2.1.1.2. Direct Liquid Injection (DLI) System

The DLI system was purchased from Kemstream. The *G1.5* represents an indication of the injector system generation. The generation (G) of which this injector system belongs is 1.5 (1 from the number of injectors – namely one liquid injector – and 5 for the number of apertures at the DLI outlet to the CVD system).

With respect to the injection principle, the liquid is pushed by a motive pressure (P_M) through an injector. When the injector aperture is opened, the liquid is pushed to a chamber pressure (P_C) where the liquid is therefore flash vaporized. The P_C can be the atmospheric pressure or the CVD reactor pressure. The bigger the difference between the P_M and the P_C ($P_M >>> P_C$), the better the vapor phase.

In the particular case of the G1.5 DLI, $P_M = P_{N2}$ (the gaseous nitrogen pressure that pushes the liquid) and $P_C = P_T$ (total pressure at the sample chamber, considered equal into all of the CVD chamber system).

Considering the chamber pressure constant $P_C = P_T = constant$, then according to the square law pressure-flow relationship [2]:

$$\frac{Q_1}{Q_2} = \frac{\sqrt{P_1}}{\sqrt{P_2}} \qquad (2.1)$$

Where P_1 and P_2 are two motive pressures (P_M) of the same system, also Q_1 and Q_2 are their respective liquid flow values.

It can be observed in *Table 2.1* that the calculated values according to *(2.1)* are in concordance to the experimental data. The difference between the experimental and calculated values is likely due to experimental errors.

Table 2.1: The experimental values of the liquid flow (Q) through the G1.5 DLI and the calculated values based on the square-law pressure relationship

Liquid Substance	P_{N2} (bar)	Q (sccm)	Q_{calc} (sccm)
Ethanol	1.8	0.203	-
	2.8	0.265	0.253
Water	1.8	0.176	-
	2.8	0.212	0.219
	3.8	0.240	0.247

The injector can be software controlled by Vapsoft software. It adjusts two main parameters of the injector: the opening time of aperture, namely the time on (***t_{on}***) and the frequency (***f***) of this repeating process. As units of measure, t_{on} is expressed in ms (10^{-3} seconds) and the frequency is expressed in Hz (hertz). The 'time on' represents the opening time of the injector apertures that allows the polymer to be evaporated.

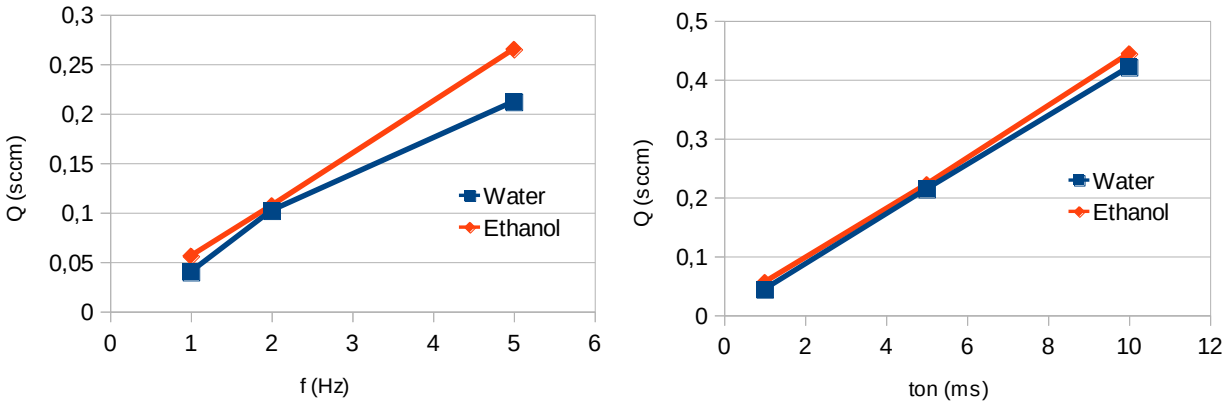

a) *b)*

Figure 2.4: The influence on the injector parameters on the water and ethanol flow: a) frequency (f) as a function of liquid flow (Q) at t_{on} = 1 ms and P_M = 2,8 bar and b) opening time (t_{on}) as a function of liquid flow (Q) at f = 1 Hz and P_M = 2.8 bar. Tests made at room pressure (P_C) and temperature (T = 18 °C) with the G1.5 DLI

The frequency can be defined as the number of occurrences per unit of time. In the international system of units of measure (SI) the measurement unit for frequency is:

$$[f]_{SI} = Hz = \frac{1}{s}.$$

If we name t_{off} the time the injector apertures are closed, then we can describe the frequency as:

$$f = \frac{1}{t_{on} + t_{off}} \qquad (2.2)$$

To address the effect of injector parameters on the liquid flow, a study of the injector parameters was made for G1.5 DLI injector using two different liquids: water and ethanol. The plotted results are shown in *Figure 2.4*.

It can be observed that the change of the liquid injection flow depends linearly to the injector parameters. Experimental error is suspected to be responsible in the case of the deviation from linearity for water at high frequencies observed in *Figure 2.4 a)*. The difference in the flow rates for the two liquids can be associated to the viscosity (μ), density (ρ) or due the ratio of the two under the form of kinematic viscosity:

$$\nu = \frac{\mu}{\rho} \qquad (2.3)$$

The SI the unit of ν is m^2/s. While considering the dynamic nature of the injection, the kinematic viscosity seems to describe well the flow phenomena. The influence of ρ, μ or υ parameters for the two liquids that were used are not enough to extrapolate an estimation of their effect on the flow. In order to have a better control on the DLI parameters further study can be made by adding supplementary values for different liquid substances.

These above parameters (P_{N2}, t_{on}, f, T_{inj}, T_{uv} and P_T) are a characteristic to the Photo-CVD system and will be used to define the experimental conditions. A checklist with the experimental procedure steps is listed in Annex 1.

2.2. Experimental Startup

The first set of experiments will reveal aspects of the surface deposition of a thin film by the Photo-CVD technique. The experimental conditions followed by a surface characterization will be further treated.

2.2.1. First series of deposition experiments

Before use, the substrates were cleaned in a Branson 200 ultrasonic bath for 10 min in acetone and then 10 min in ethanol. Then the samples were dried in a Memmert Model 550 oven at 60 ˚C. The Si(111) substrate presents a negligible native oxide layer while the Si(100) provides a thicker SiO_x layer thermally grown. Two Si(111) substrates were overlapped, one making the other substrate during the deposition. This allows for a direct comparison between a coated and an uncoated area.

Table 2.2: The Photo-CVD experimental parameters

Gas flow		Pressure		Temperature		Injector	
Q_{N2}	291sccm	P_{N2}	2.8bar	T_{inj}	60 ˚C	t_{on}	1 ms
		P_T	5.6Torr	T_{uv}	80 ˚C	f	1 Hz
		-	-	$T_{substrate}$	~ 18ºC	t_{exp}	45 & 150 min

The monomer was mixed with 2% 1-hydroxycyclohexyl-phenil ketone photo-initiator (HCPK) to enlarge the MMA monomer spectral range for the UV activation.

Due to the low signal/noise ratio of the spectroscopic characterization, in this stage only aspects of surface microscopy will be firstly treated.

2.2.2. Scanning Electron Microscopy (SEM) Characterization

The SEM images were difficult to obtain at an angle of 90º due to what seems to be a conformal covering over the surface. The measurements were thus made at a 75º tilt. In these conditions apparently no indication of a film covering is revealed for the 45 min deposition in

the SEM image from *Figure 2.5 a)*. However, in the enhanced inset a conformal coating of heterogeneity is indicated. As the deposition time is increased (150 min), the conformal covering is further attested by the encapsulation of heterogeneity in what seems to be a thin film. This aspect is observed in *Figure 2.5 b)*. Drop-like morphologies are also observed, aspect which leads to the premises of a possible liquid encapsulation.

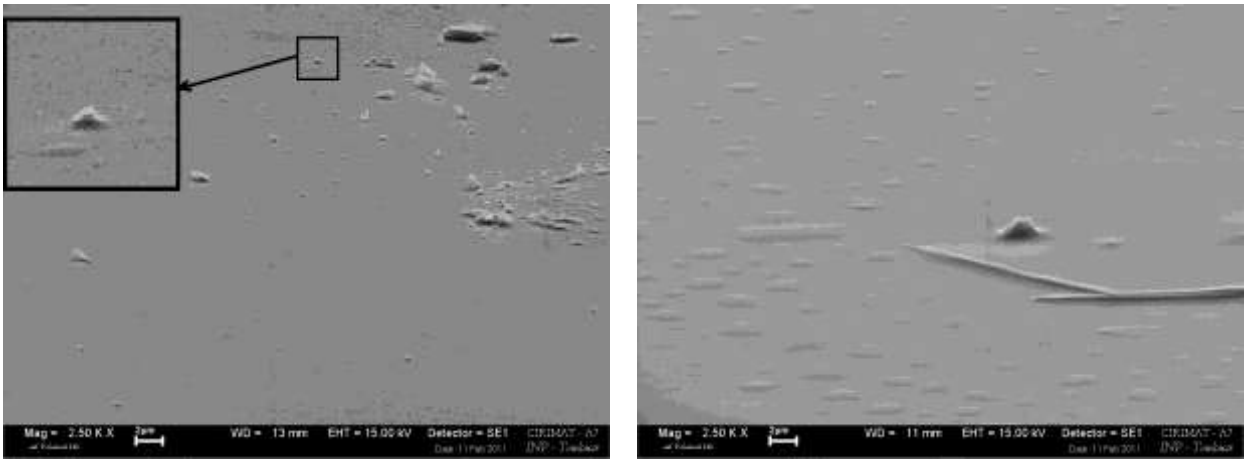

a) *b)*

Figure 2.5: SEM images for a) 45 min of polymerization on Si/SiO_x and b) 150 min polymerization on Si(111)

The complementary AFM technique will be used to investigate the aspects of the possible liquid encapsulation and the presence of the thin films.

2.2.3. Atomic Force Microscopy (AFM) Characterization

The AFM images presented in *Figure 2.6 a)* and *b)* for the uncoated and the coated substrate respectively reveal topographical differences that indicate the presence of a thin deposition. The uncoated substrate presents both oblique and parallel arrangements of sharp heterogeneities (*Figure 2.6 a*) with heights up to 48.8 nm. The coated substrate shows only parallel heterogeneities with heights up to 77.1 nm. The linear arrangement is probably due to preferential nucleation at the steps of the vicinal (111) surface of the Si substrate or at defects originating from the cleaning of the substrate that was notmade in a clean room.

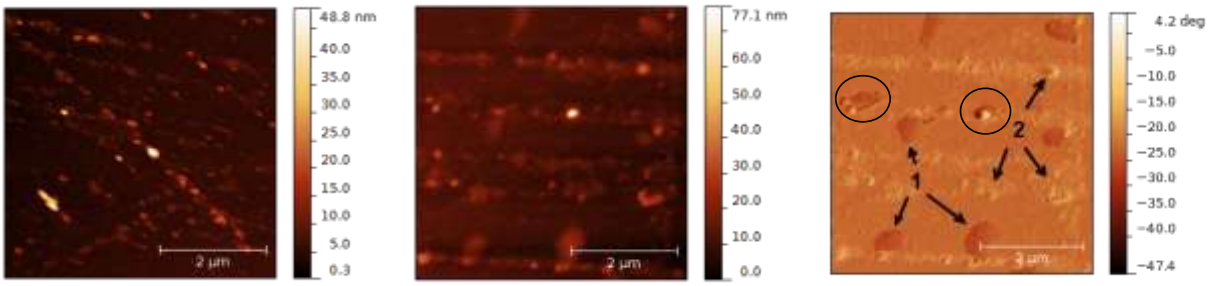

a) *b)* *c)*

Figure 2.6: AFM topography for a masked area (a) and a deposited area for 45 min (b); the phase image of the deposited area is also presented (c) with possible liquid encapsulation as blisters (1) and heterogeneities covering (2); possible nucleation sites are circled

To highlight the heterogeneities and the deposit in more detail the phase image obtained during the simultaneous AFM scanning is shown in *Figure 2.6 c)*. Such a phase measurement responds to changes in the local stiffness, viscoelastic properties and the variation in chemical composition [3]. The presence of heterogeneities is indicated by the arrows noted with 2 in *Figure 2.6 c)*. The species noted with 1 in *Figure 2.6 c)* seem to indicate the liquid presence.

By the phenomenon of condensation, the liquid can nucleate at substrates heterogeneities. The possible presence of such nucleation centers are highlighted in *Figure 2.6 c)*.

2.2.4. Aspects of Surface Nucleation

The surface characterization reveals aspects what seem to indicate nucleation on the surface. The nucleation is at the basis of liquid droplet formation over a solid surface in an environment of saturated vapors. The polymers also start polymerizing from nucleation sites. These aspects were studied both theoretically [4] and in parallel with experimental aspects [5].

The liquid that nucleates at the interface at preferential sites such as phase boundaries or impurities like dust is called heterogeneous nucleation. The nucleation in the absence of such preferential sites is called homogenous nucleation. Heterogeneous nucleation requires less energy than homogeneous nucleation [6] and consenquently it preferentially occurs to the detriment of homogenous nucleation. The Gibbs free energy needed for heterogeneous nucleation (ΔG_{hto}) is equal to the product of the Gibbs energy for homogeneous nucleation (ΔG_{hmo}) and a function of the contact angle (θ) [6]:

$$\Delta G_{hto} = \Delta G_{hmo} \times f(\theta) \tag{2.4}$$

The function of the contact angle in *(2.4)* is:

$$f(\theta) = \frac{1}{2} - \frac{3}{4}\cos\theta + \frac{1}{4}\cos^2\theta \tag{2.5}$$

The contact angle (θ) determines the ease of nucleation by reducing the needed energy [6]. The spectroscopy characterization could not offer indications of the polymerization nucleation, as the signal/noise ratio was low. By changing the Photo-CVD injection system indications of such aspects will be studied (Chapter 3).

2.3. In-depth Investigation

The main focus on the next set of experiments will be mainly on the overall characterization (both spectroscopic and microscopic) of the deposited polymeric film from the methyl-metacrylate (MMA) monomer in the conditions provided by the Photo-CVD system described below.

2.3.1. Experimental Conditions

Previous to the deposition, the substrates were rinsed with acetone and then with ethanol. Subsequently, the ethanol was removed slowly by passing over the sample a soft paper tissue. Then 5 min of ultrasonication treatment was applied to the substrates, first in acetone and then in ethanol. The samples were dried in an oven at 40 ^{o}C.

Table 2.3: The Photo-CVD experimental parameters

Gas flow		Pressure		Temperature		Injector	
Q_{N2}	108 sccm	P_{N2}	2.8 bar	T_{inj}	60˚C	t_{on}	1 ms
		P_T	9.5 Torr	T_{uv}	80˚C	f	1 Hz
		-	-	$T_{substrate}$	~18ºC	t_{exp}	45 & 150 min

In order to increase the residence time of the monomer in the UV activation zone, the total pressure was rised from 5.6 Torr for the previous experimental set, to 9.5 Torr as seen in *Table 2.3*. Also, the temperature of the mixed zone **below** the injector was increased to 60 °C.

Two experiments were made with the polymerization time corresponding to 45 and 150 min. The rest of the parameters were left unchanged, including the model of the injector (G1.5 model).

Changes were observed, both in the microscopy and spectroscopy characterization.

2.3.2. Surface Morphology Characterization

During the sample metallization for SEM by Ag sputtering, a sudden change of the pressure was applied to sample since the sputtering chamber was vacuum purged and then suddenly pressurized with an Ar gas stream. If we assume that there is liquid (monomer) covered by a very thin layer of polymer, a cracking or rupture of the drops is expected at those pressure difference.

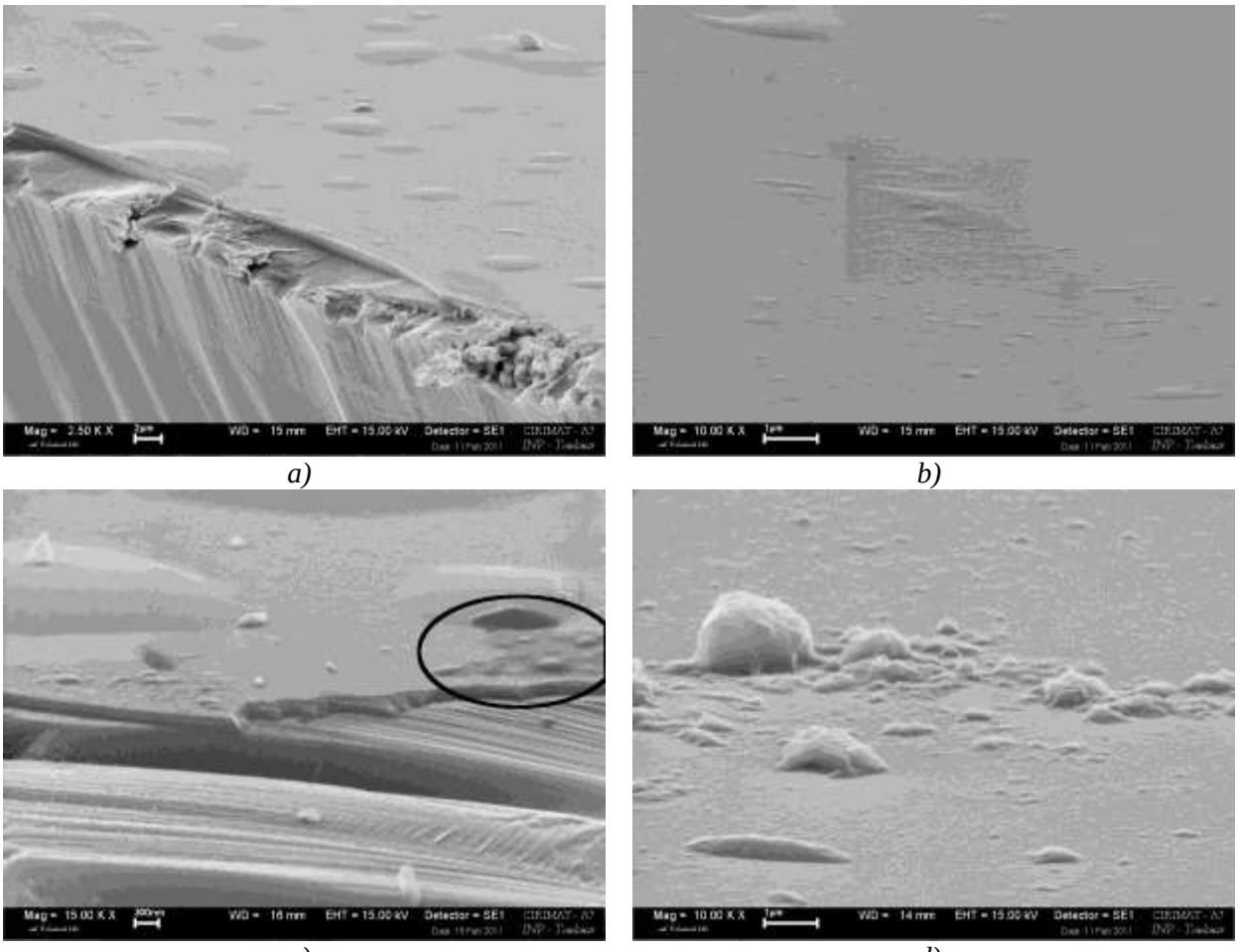

a) *b)* *c)* *d)*

Figure 2.7: SEM micrographs for a deposition of 45 min over a) Si/SiO_x and a) Si/SiO_x and a deposition of 150 min over c) Si/SiO_x and d) Si/SiO_x

In *Figure 2.7 c)*, after 150 min of polymerization over a Si/SiO_x substrate, a possible breakdown of a drop-like structure is observed, with what it seems to be an internal liquid release. On the same substrate, but after 45 min polymerization (*Figure 2.7 a*), the layer shows an ability to successfully cover complex structures up to 1 µm in dimension, embedding them into the grown film. Also, drop-like morphology is observed for Si/SiOx substrates (*Figure 2.7 a, c*), while for Si(111) substrates the liquid is enveloped under different shapes (*Figure 2.7 b*).

Notably, the drop-like structures preserved their distribution over the surface even after 2 months of storage in a dark environment at around 17 ^{o}C. The storing conditions ensured the unwanted effects of polymerization (either by UV or thermal). **The question that arises is to know if inside the drop-like structures there is liquid monomer or solid polymer**. If liquid is present encapsulated inside the thin film, it will form blisters that can find various applications in the microfabrication industry.

A further spectroscopic study was undertaken to investigate the content of the drop-like structures. It was made over 2 months old samples.

2.3.3. In-depth Composition Study

The main aspect that followed in this study is the identification of the monomer species (MMA) presumed encapsulated in the thin film. If liquid MMA is present inside the blisters, the photo-initiator presence is expected also to be present, as a component of the monomer solution.

Subsequent post-treatments are designed to highlight the presence of the two species: the monomer and the photo-initiator. The post-treatments were selected to activate two different properties of the films:

- the photo-initiator responds strongly in the *UV* range (at 290 nm in ethanol), property that was used to aid the *photo*-initiation to polymerize the monomer
- the glass transition temperature of *MMA* is at 105ºC (378 K [7]), allowing a part of the monomer to be polymerized with the aid of the *thermal* energy.

As a consequence, a UV post-treatment of the samples will induce a significant response of the photo-initiator species, acting as a marker in the UV range. On the other side, a thermal post-treatment will induce a preferential response of the MMA species, by further polymerizing a part of the monomers present in the film (without the photo-initiator contribution).

2.3.3.1. UV-VIS Investigation

The *UV-VIS* determinations were made in transmittance mode of the thin film deposited over a glass sample.

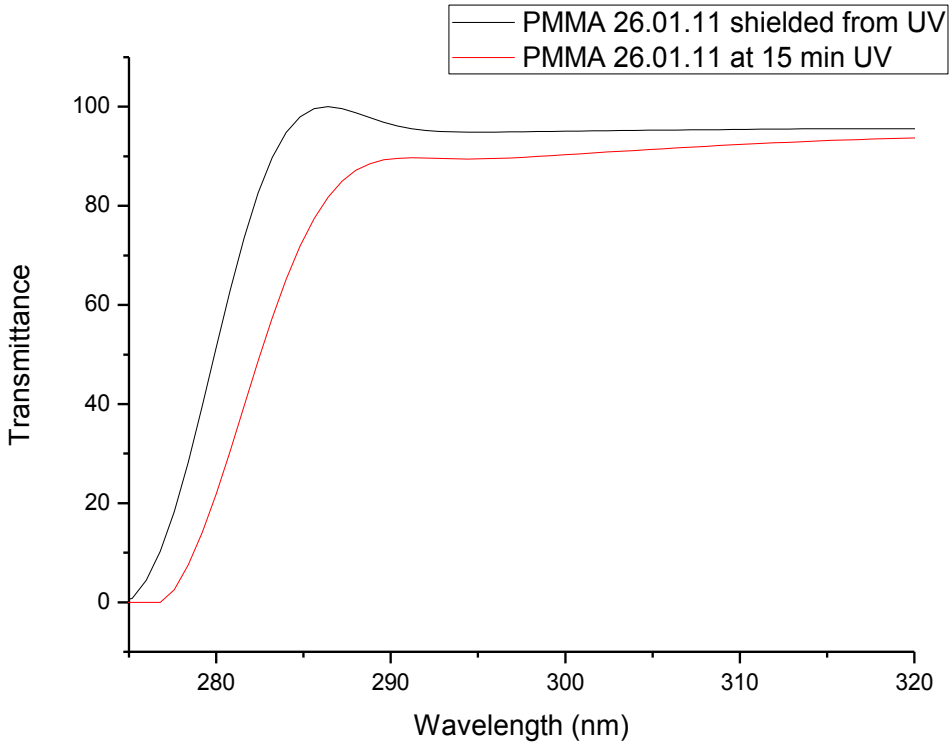

Figure 2.8: UV transmittance spectra of the deposited thin film, exposed or unexposed to a 10 min UV treatment

The samples were exposed to the UV radiation (254 nm in the Photo-CVD reactor) in atmospheric conditions (in air) for 10 min and were half covered with aluminum foil to prevent irradiation. Thus, the UV spectrum was obtained over the same sample, with and

without UV irradiation. The spectra for the treated and untreated samples were simultaneously smoothened. The spectra are presented in *Figure 2.8*. It is likely that the decrease in transmittance is due to the MMA densification in the blisters as a result of the UV polymerization [8].

Thus, after the UV treatment, the spectra show that the sample transmits less in the UV range, indicating the presence of the monomer that is not polymerized. The effect of the UV exposure is further investigated in order to discriminate between the chemical bonds of monomer and photo-initiator.

2.3.3.2. Raman Investigation

The Raman spectra will further help to underline the film composition with respect to the monomer and the photo-initiator species.

Notably, the MMA monomer is described as volatile liquid that releases a strong irritant odor. The samples were prepared two months before Raman analysis and they were stored in a PMMA-derived sample-box whichwas not sealed. Forthis long time any residual monomer on the surface should have been evaporated.

The characterized samples were from the same experiment as those for the UV post-treatment, but deposited on Si(111) instead of glass. The Raman focal area was set for every measurement over the median part of 10 µm the diameter drop-like structures.

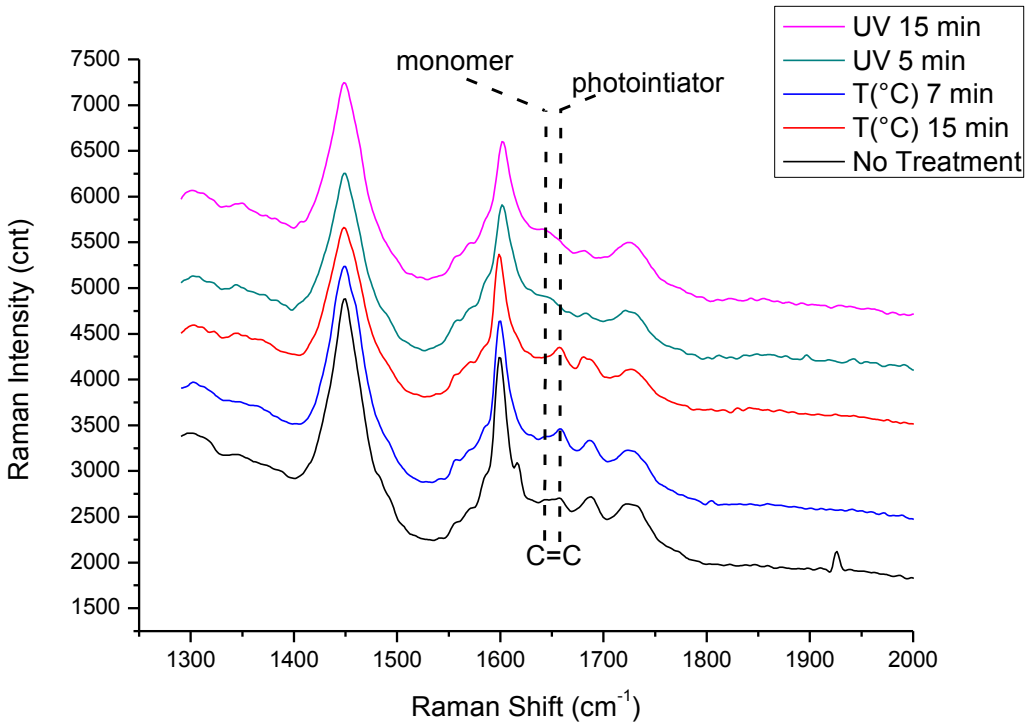

Figure 2.9: Raman spectra of the deposited film after the UV and thermal post-treatment

The UV post-treatment was applied in the same conditions, but in two stages: initial 5 min and subsequent 10 min, which sum a total UV exposure of 15 min. The thermal post-treatment was also applied in two stages: 2x7.5 min totaling to the final 15 min. The temperature for the post-treatment was chosen to be 115ºC, as it was reported to be the most efficient MMA polymerization temperature [7].

The temperature post-treatment is meant to highlight the photo-initiator (by remaining dominant active specie after a thermal induced polymerization of MMA). The UV treatment will highlight aspects related to the monomer (by initiating chemical reactions of the photo-initiator which insolate the monomer species).

The C=C Raman bands present in MMA (not in the polymer) are reported at 1640 cm^{-1} [7] which is close to the photo-initiator C⎓C present in the phenyl aromatic chain. The C=C bond of the monomer for the untreated sample cannot be clearly distinguished because of a wide band in 1620 - 1660 cm^{-1} range where the phenyl also is expressed. However, after the species separation by the thermal post-treatment, the C=C disappearance can be observed for MMA at 1640 cm^{-1} compared with the photo-initiator band at 1660 cm^{-1} (*Figure 2.9* - UV 15 min).

After the UV post-treatment, it is observed that the photo-initiator band at 1660 cm^{-1} strongly decreases as it likely undergoes an oxidation under the atmospheric conditions of the UV post-treatment, reducing the three C=C double bonds per photo-initiator molecule to two C=C bonds per molecule. This is described by the chemical phenil oxidation in quinone methide [9].

After the two post-treatments, the shift of the band at 1690 cm^{-1} in as-deposited film to 1680 cm^{-1} after 15 min of UV or thermal treatment can be observed that can be associated to the C=O stretching of the photonitiator and monomer respectively [10]. The C=O vibration at 1720 cm^{-1} [11] does not indicate a strong distinction between the monomer and photointiator species.

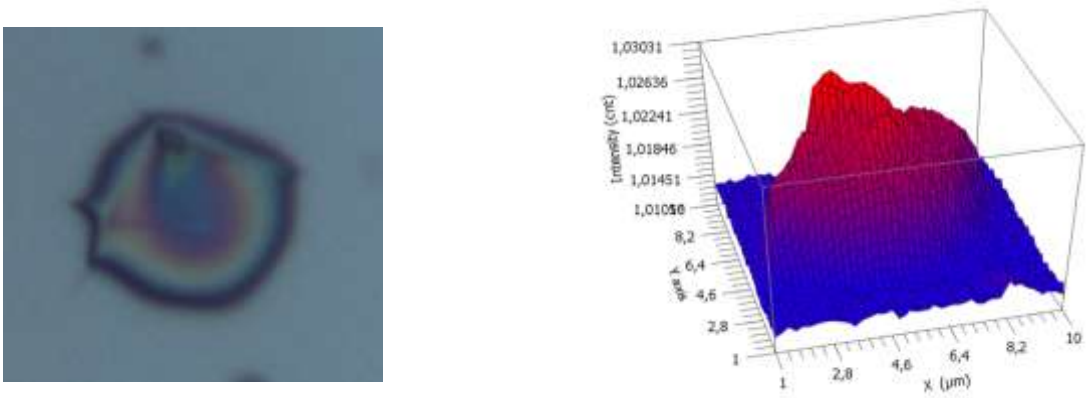

a) *b)*

Figure 2.10: The blister structure as seen by the Raman cofocal microscope a) and the representation of the 1640cm^{-1}/1660cm^{-1} ratio of the Raman spectra for the same surface

A Raman reconstruction of a drop-like surface was achieved in order to determine the composition of the drop-like structures that can be observed by the microscopy techniques over the surface. The ratio of the 1640 cm^{-1} double bond of the carbon found in monomer and the photo-initiator 1660 cm^{-1} carbon double bond in the aromatic ring was used to determine the point-by-point monomer contribution over the drop-like area. It can be observed in *Figure 2.10* that the profile of the Raman intensity ratio corresponds to the one of the blister. This aspect indicates the presence of the MMA monomer as fluid phase.

These experiments allowed the separation between MMA monomer and the photinitiator. Also, the selected post-treatments allowed emphasizing the presence of blisters containing a fluid phase of monomer over the substrate. The liquid content of the blisters, indicated by the microscopy study (subchapter *2.3.2.*) is confirmed by spectroscopy investigation.

As previously discussed, the temperature can influence the MMA polymerization. The next study will investigate the influence of the substrate temperature during the Photo-CVD deposition conditions.

2.4. Influence of the Deposition Temperature

In order to highlight some polymerization aspects, the temperature of the substrate (where the polymerization takes place) was changed. Two main temperature ranges was investigated: around -44ºC with a variation of ± 21ºC (ΔT = 42ºC) and 0ºC with a variation of around ± 4.6ºC (ΔT = 8 ºC). Also, some aspects of film thermal stress due to the difference in temperature have been pointed based on the experimental data.

2.4.1. Substrate Temperature ~ -44ºC ± 21ºC

Prior to the deposition the glass and Si substrates were rinsed and mechanically cleaned with an acetone and subsequently with an ethanol dipped cleanex tissue. Following, an ultrasonic treatment was applied for 5 min in acetone and then for 5 min in ethanol. The final drying of the sample was made under an Ar gas stream. The experimental conditions used for the experiment are presented in *Table 2.4*.

Also, an oil droplet was left on the surface of the substrate in order to investigate the possible encapsulation of a liquid. These aspects will be covered in subchapter *2.5.2*.

Table 2.4: The Photo-CVD experimental parameters

Gas flow		Pressure		Temperature		Injector	
Q_{N2}	108 sccm	P_{N2}	2.8 bar	T_{inj}	45˚C	t_{on}	1 ms
		P_T	9.5T orr	T_{uv}	80˚C	f	1 Hz
		-	-	$T_{substrate}$	-44±21ºC	t_{exp}	45 min

The substrate had a temperature monitored by a *K-type* thermocouple. An oscillation of the temperature around -44ºC was applied. The substrate temperature as a function of time is represented in *Figure 2.11*. It can be observed that there are two main increases and one significant drop in temperature between them leading to a change in temperature with an amplitude of 42ºC. The deposition was made for 45 min (as seen in *Figure 2.11*).

The big differences in temperatures imply a variation in volume. This is given by two expansions and one compression that occur during the thin film deposition.

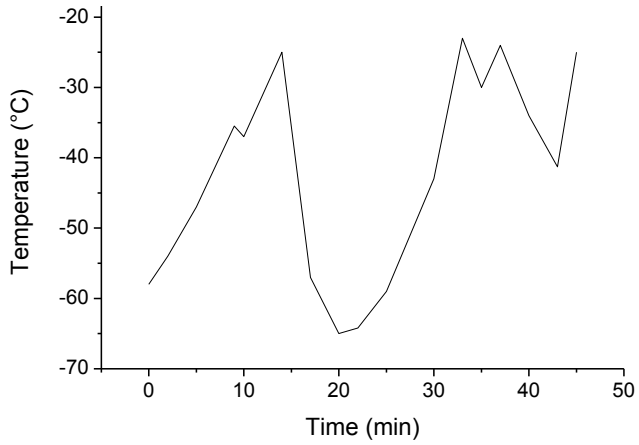

Figure 2.11: The temperature variation of the samples during the 1st deposition experiments (average deposition T = -44 °C)

2.4.1.1. Microscopy Characterization

SEM and *FESEM* determinations were made and highlight two aspects: a) a substrate specificity and b) aspects of the film deposition. The images were obtained at the same 75º tilt in order to achieve improved profile images. The high resolution FESEM images allowed perpendicular scanning with detailed morphology.

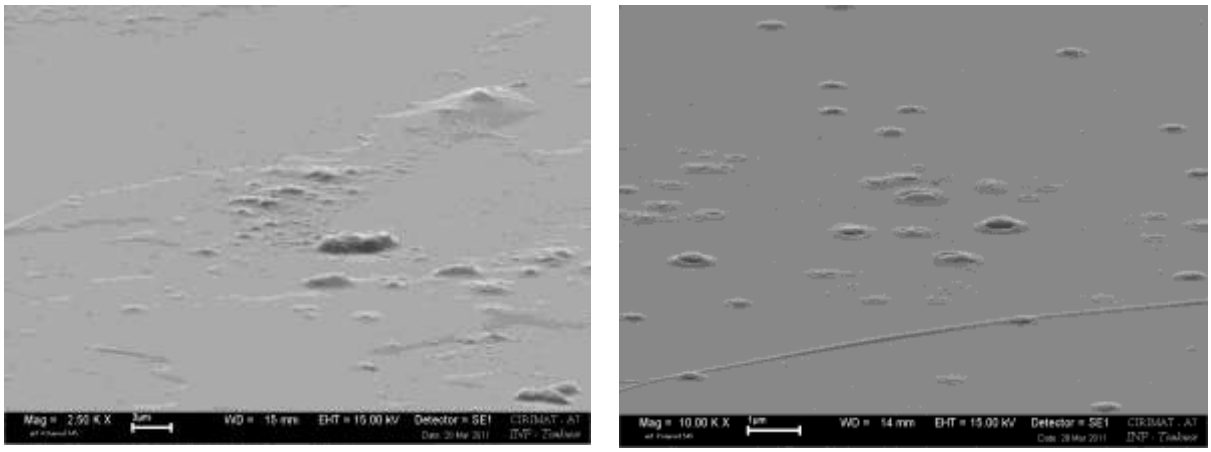

a) *b)*

Figure 2.12: SEM images over the thin film deposited on a) Si(111) and b) Si/SiO_x

The substrate influence on the main features of the films is shown for Si(111) (*Figure 2.12 a*) and for Si/SiO_x (*Figure 2.12 b*). The Si(111) deposited sample seems to reveal encapsulation of liquid and of different geometrical shape heterogeneities in the film.

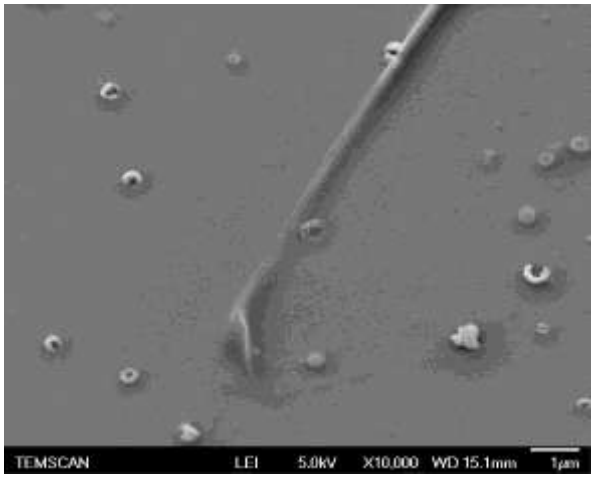

Figure 2.13: FESEM image of the deposited thin film over the Si/SiOx substrate

As shown in *Figure 2.11*, a 42 ºC temperature variation can be observed around –44 ºC. This leads to an expansion or contraction of the deposited film that is material-dependent.

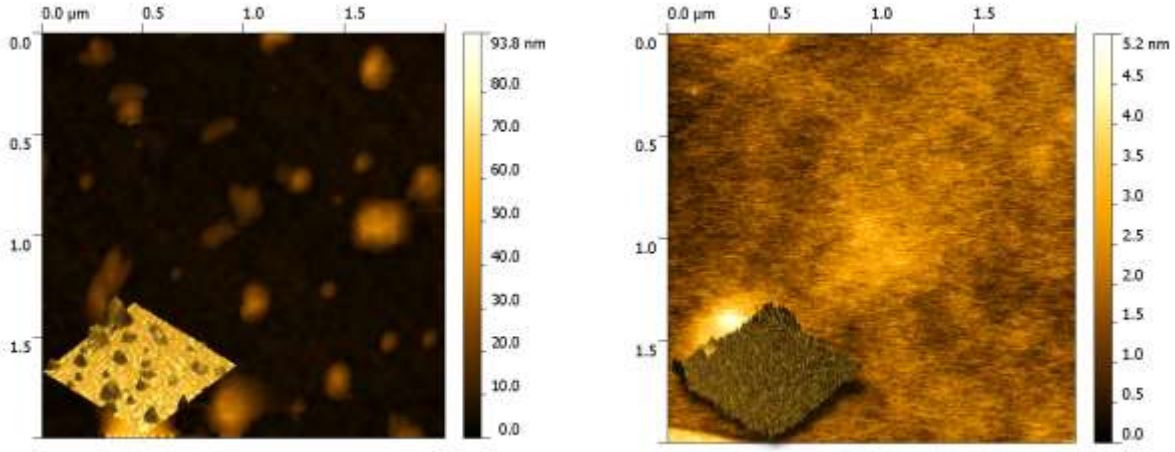

a) *b)*

Figure 2.14: AFM micrographs of the thin film deposited over a) glass and b) Si(111) In the lower left a 3D topographic representation of the same area

According to the literature, thermal expansion coefficient for MMA is $\alpha_{MMA} = 5.76*10^{-4}$ K^{-1} and for PMMA is $\alpha_{PMMA} = 3.21*10^{-4}$ K^{-1} [12]. This implies a 1.3% expansion of the PMMA volume compared to the 2.4% expansion volume of MMA, for a the temperature increase of 42 ºC. Roughly, the expansion volume is almost double for the monomer compared to the one for the polymer.

The microscopy data presented in subchapters *2.2.2. 2.2.3.* and *2.3.* indicate the MMA monomer presence in the film, monomer that is in liquid form. If we consider that the blister structures contain liquid, the expansion coefficient almost two-times higher for MMA than for PMMA leads to a polymer covering breakdown due to the monomer expansion stress. Thus a subsequent release of the monomer to the low pressure CVD environment is expected.

Such a breakdown effect can be observed in the SEM (*Figure 2.12 b*) and FESEM (*Figure 2.13*) micrographs. The images show 'crater-like' heterogeneities on the surface. In the same images the observed wrinkles can be associated to the expansion and compression of the thin film.

Considering the above values for thermal expansion and the AFM micrographs, a numeric approximation of the expansion phenomena involved in the film deposition will be made over a 2x2 μm^2 surface.

The *AFM* images were scanned in the same acoustic mode and are presented in *Figure 2.14* with the 3D profile in the inset. On glass, the film reveals species of consistent height (up to 93.8 nm) compared to the flat area determined for Si(111) substrate (up to 5.2 nm).

For samples deposited on Si(111) substrate, statistical values were determined using Gwyddion 2.25 software. All of the processed statistical quantities results are presented in *Table 2.5*. The Average (avg.) value represents the mathematical average of the height profiles. The median (med.) represents the numerical value that separates the upper part from the lower part of the height populations. Of course, the minimum (min.) and maximum (max.) values of the height are also presented in the table. The Skewness describes the asymmetry of the height profile while the Kurtosis is a coefficient that describes the flatness of the same height profile.

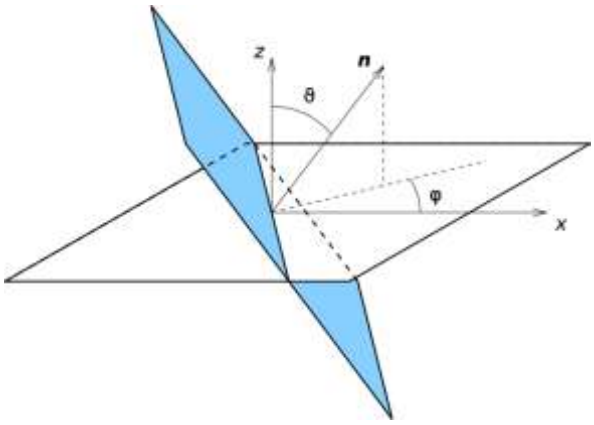

Figure 2.15: The spherical coordinates that were considered while computing the AFM statistical data

The facet and plane inclinations are displayed as the spherical angles (θ, φ) of the plane normal vector. Angle θ is the angle between the vertical direction and the normal to the plane. This means that $\theta = 0$ ° for horizontal facets and it increases with the slope. Angle φ is the counter-clockwise measured angle between axis x and the projection of the normal to the xy plane, as shown on the *Figure 2.15*.

The focus will be set mainly on the roughness parameters (R_a) and surface slope (θ angle). The glass substrate that contains relatively increased height species is also characterized by high roughness (4.30 nm). The Si(111) substrate has values 10 times lowered with that respect (0.42 nm).

Table 2.5: AFM statistical data of the film deposited over glass and Si(111)

Sample	*Avg. value (nm)*	*Min (nm)*	*Max (nm)*	*Med (nm)*	R_a *(nm)*	R_{ms} *(nm)*	*Skew (nm)*	*Kurt (nm)*	*Surface area* (μm^2)	θ (^{o})	φ (^{o})
Glass	6.92	0.00	93.79	4.53	4.30	7.49	3.82	18.00	4.07054	0.3	80.4
Si	1.83	0.00	5.15	1.79	0.42	0.57	0.99	2.74	4.00520	0.0	157.6

Considering the deposition direction perpendicular to the substrate, the statistical slope of the deposited species should theoretically be 0. This aspect is confirmed by the AFM scans, as θ angle is around 0 ^{o} for both of the samples. The 0.3 ^{o} slope for glass is an indication of a dynamic on the surface that is different to that of the vertical deposition. If we consider the thermal expansion and contraction of the film, we can expect a slight alteration from the 0 ^{o} slope. This will also lead also to a roughness increase, as observed in *Table 2.5*. As glass has species of relatively increased heights (implying higher volume also), the expansion/contraction effect should be increased compared to the one for Si(111). The image for the glass substrate was processed in order to obtain the volume of the larger species presented onto the substrate. To neglect the smallest species, everything below 10.32 nm was masked. The result is shown in *Figure 2.16*. Thus the volume of the species (generally called grains) with heights over 10.32 nm was calculated. The resulted projected area was of 86.4 % from the total of the initial AFM topography. The volume of the selected grains was of $156*10^{-2}$ μm^3.

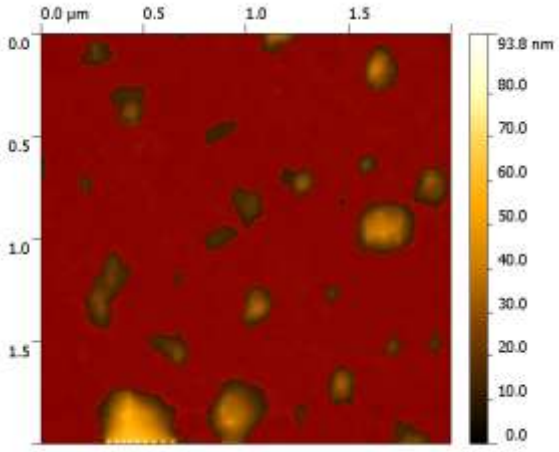

Figure 2.16: Mask applied in order to delete the contribution of the smallest species from the surface topography from Figure 2.14 a

If we consider that the grains are formed of solid (PMMA polymer), for that specific volume in the 42ºC range (-66ºC / -24ºC), the expansion accounts in $2.03*10^{-3}$ μm^3 volume increase. If we consider that grains are formed of liquid (MMA monomer) the expansion increases the volume with $3.74*10^{-3}$ μm^3. If there is a thin layer of polymer that encapsulates the monomer, the polymer is likely to break due to the stress. This stress can be attributed mainly to the $1.72*10^{-3}$ μm^3 difference in expandability for the $156*10^{-2}$ μm^3 volume of the polymer versus the monomer.

These AFM results show that there is a difference over the surface species for the glass and Si(111) substrate. Also, an indication of the extent of surface stress was estimated with the help of volumetric determination by AFM.

2.4.1.2. Spectroscopy Characterization

FTIR measurements show that the best measurements were obtained for glass (*Figure 2.17 a*).

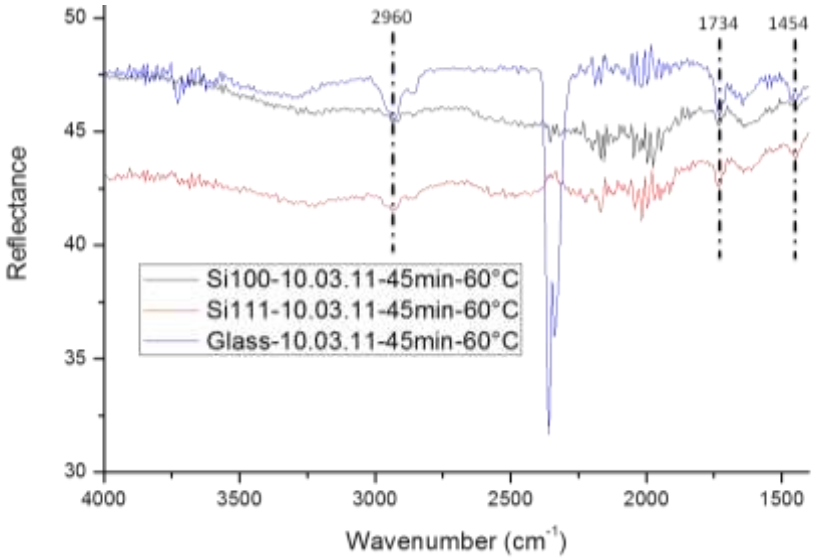

Figure 2.17: ATR-FTIR spectra with specific bands that correspond to the deposited film

The glass topography and morphology associated with the increase in IR signal intensity for the film grown over the glass substrate can indicate that blisters enhance the signal/noise ratio.

The typical film reflectance of PMMA film are observed at 2960 cm^{-1}, 1734 cm^{-1} and 1454 cm^{-1} associated to the CH_3 streching, C=O stretching and $CH+CH_3$ bending and deformation respectively [13–15] (*Figure 2.17 a*). At this low deposition temperature (-44 ± 21 ^oC) the signal/noise ratio shows improvement with respect to previous results, obtaining better differentiation of the bands.

a) *b)* *c)*

Figure 2.18: The focus area over which the Raman spectra was taken for a) the photo-initiator; b) thin film and c) the blister structure on Si(111) substrate

The *Raman* analysis will provide further data on the composition related to blister areas over the thin film. It will highlight the composition of the covered substrate and of the photo-initiator presence.

Three Raman spectra were recorded as shown in *Figure 2.18*:

- the photo-initiator, as reference (a thin layer of photo-initiator powder);
- a flat area of a thin PMMA film;
- a blister area.

The main difference in intensity can be observed in the Raman spectra from *Figure 2.19*. The flat film area has a maximum of 1457 counts in the Raman Intensity. The blister area has an implicit higher area as the focal area covers more material, with an increase to 1610 counts in Raman Intensity.

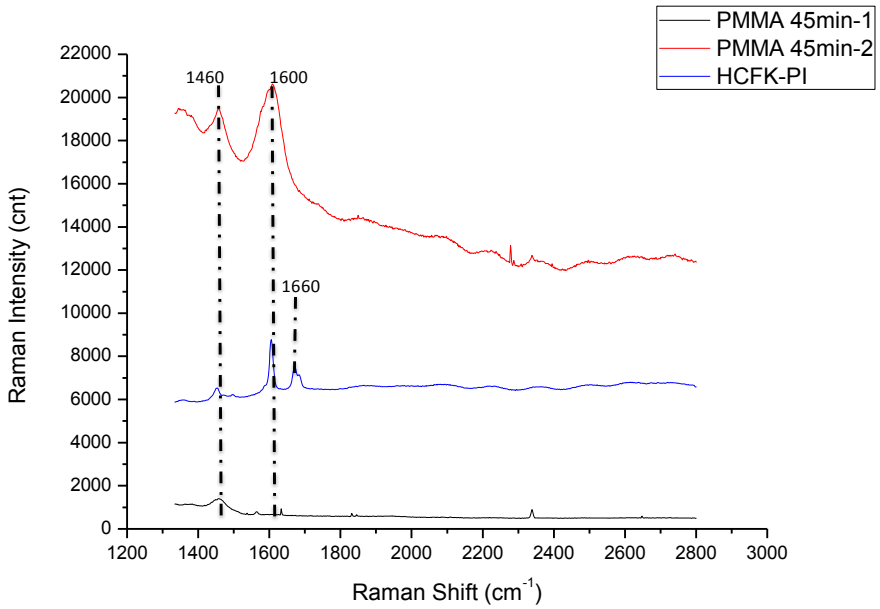

Figure 2.19: Raman spectra for different areas over the substrate; HCFK-PI shows the photo-initiator spectra; PMMA 45min-1 was focused over the thin film and PMMA 4min-2 was focused over the blister area

The flat area of the deposited film (*Figure 2.19*), only the 1460 cm^{-1} band corresponding to CH and CH_3 deformations are distinguished [16]. The blister area presents the same band with increased intensity plus a specific high band at 1600 cm^{-1} that is specific only to the photo-initiator aromatic ring, which is higher in intensity than the 1660 cm^{-1} one for the same group. The absence of the aromatic ring bands for the spectra over the flat area indicates that no photo-initiator is present, only (P)MMA.

For the next experiment, the temperature of the substrate will be further stabilized around 0ºC.

2.4.2. Substrate Temperature 0ºC ± 4ºC

The experimental procedure is identical to the one described at *2.4.1.* Also the experimental parameters are identical with the previously presented parameters, except for the temperature that for this set of experiments varies between 3.5 ºC and -4.5 ºC in an increased 90 min deposition interval (as seen also in the temperature variation during the deposition from *Figure 2.20*). The parameters are presented in *Table 2.6.*

Notably, an oil drop was also put on the surface of a sample as for the previous experiment. This will provide indications of the liquid encapsulation that will be covered in subchapter *2.5.2.*

Table 2.6: The Photo-CVD experimental parameters

Gas flow		**Pressure**		**Temperature**		**Injector**	
Q_{N2}	108 sccm	P_{N2}	2.8bar	T_{inj}	45˚C	t_{on}	1ms
		P_T	9.5Torr	T_{uv}	80˚C	f	1Hz
		-	-	$T_{substrate}$	~0±4ºC	-	-

The main feature of this 2nd experiment is the increase of the deposition temperature from a median value of -44ºC in the 1st series to a median value of 0ºC in the 2nd one. Another difference between the two series is a significant decrease of the amplitude of the temperature change from ΔT = 42ºC to 8ºC.

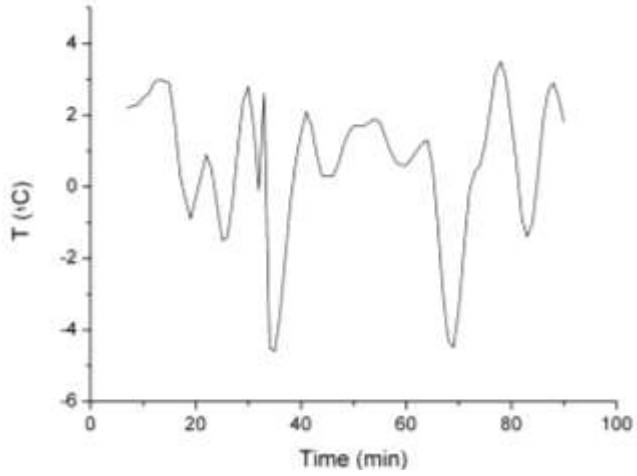

Figure 2.20: The temperature variation of the samples during the deposition experiments (average temperature = 0 ± 4 ^{o}C)

In the graphic that represents the temperature variation *(Figure 2.20*) it can be observed that there are two *main* and deep minimums, each indicating a significant compression/expansion cycle.

2.4.2.1. Microscopy Characterization

The *AFM* graphs taken in acoustic mode are shown in *Figure 2.21*, with a 3D representation in the inset. Also the obtained statistical results of the same AFM images are inserted in *Table 2.7*.

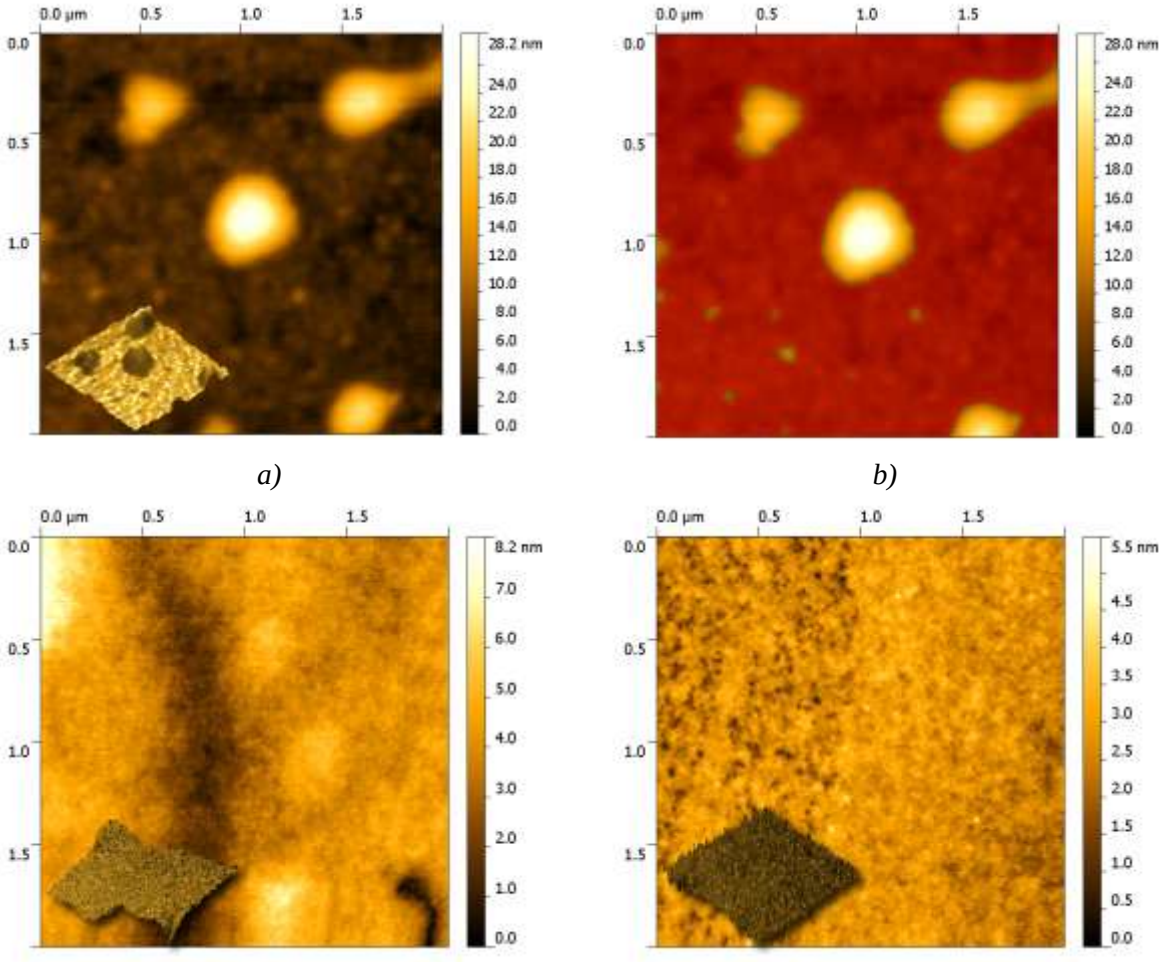

a) *b)*

c) *d)*

Figure 2.21: AFM micrographs for the deposit over glass a) without or b) with background mask, c) over Si(111) and d) over Si/SiO_x

Table 2.7: AFM statistical data of the films deposited on glass, Si/SiO_x and Si(111)

Sample	*Avg. value (nm)*	*Min (nm)*	*Max (nm)*	*Med (nm)*	*R_a (nm)*	*R_{ms} (nm)*	*Skew (nm)*	*Kurt (nm)*	*Surface area (μm^2)*	*θ (º)*	*φ (º)*
Glass	5.83	0.00	28.23	4.71	2.59	4.21	2.60	7.03	4.00870	0.1	32.2
SiO_x	2.66	0.00	5.49	2.69	0.34	0.44	-0.37	0.83	4.00362	0.0	12.2
Si	7.79	0.00	11.67	8.02	1.33	1.73	-0.72	0.80	4.00258	0.0	43.7

The total volume of the selected grains was determined to be $162*10^{-2}$ µm^3. In the 8ºC temperature range, the volume of the selected PMMA would theoretically expand with $0.76*10^{-2}$ µm^3 and the volume of the MMA with $0.42*10^{-2}$ µm^3. This small expansion is likely not to cause PMMA a significant film breakdown.

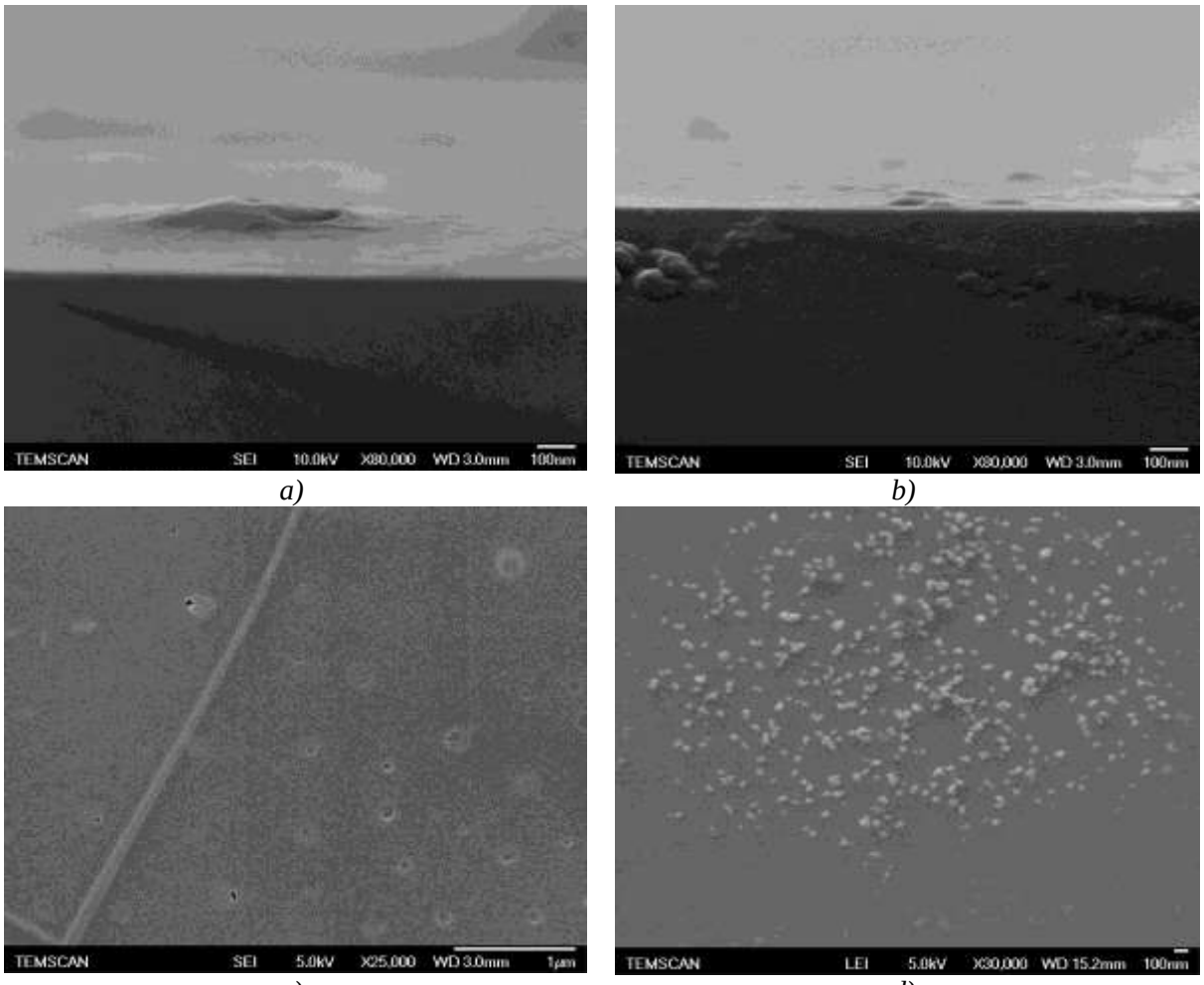

a) *b)*

c) *d)*

Figure 2.22: FESEM images of the deposit over a), b) bare Si(111) and c), d) Si/SiO_x

According to the literature, the pristine PMMA has an elastic behavior up to 0.2% elongation, followed by a small elongation before fracture until a strain-to-break point of 0.57% elongation [17]. Considering the successive stress due to the 2 compressions and 2 expansions, an additive strain of the film combined with the specific low pressure environment is likely to occur.

In the conditions of the relatively low temperature change during the deposition as for the 2nd series (0 ^{o}C; ΔT = 8 ^{o}C), it is likely that PMMA membrane of the blisters would not break and would not release suddenly the internal phase into the CVD chamber. The film can

generate release points for the accumulated strain with geometries dictated by the difference between the thermal expansion values of the monomer and of the polymer.

Strain release through punctures can be expected when the expansion/compression cycles are induced by the temperature difference sufficiently high as observed in the FESEM images presented in *Figure 2.22*. It seems that for Si/SiO_x substrate, the film presents punctures over the blister areas (*Figure 2.22 c)*, where probably liquid was released. These punctures appear for blister species that have more than 130 nm in diameter (*Figure 2.22 a*). Sites of empty blister with lower diameter seem to be covered with a thin layer of polymer, as it can be observed in *Figure 2.22 d).* A strain release at the level of the whole film can be another aspect observed by the signs of film wrinkles in *Figure 2.22 c)*. These wrinkles can also be observed in *Figure 2.23 a)* over a blister area (due to what it seems as a partial liquid draining).

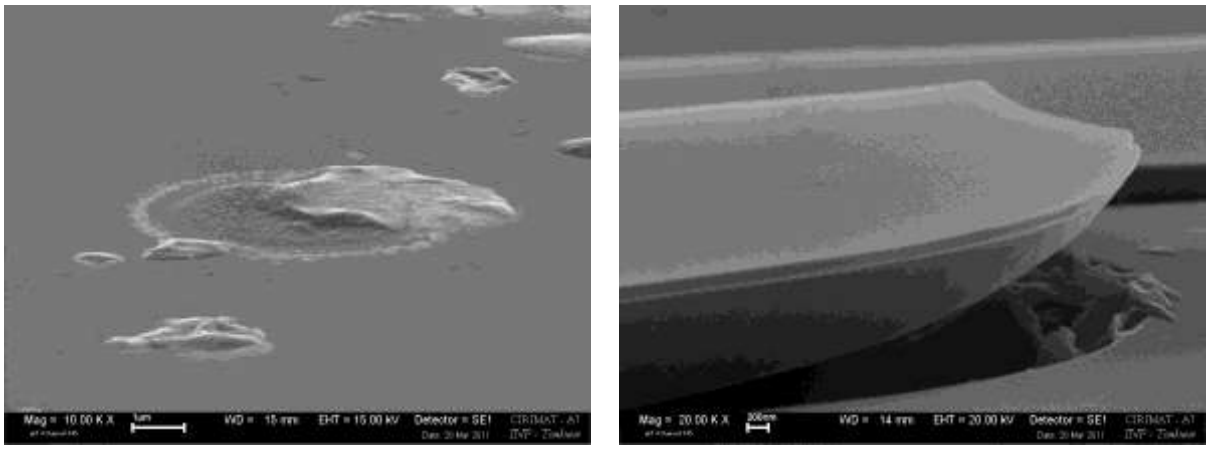

a) *b)*

Figure 2.23: SEM images of the deposit over a) Si(111) and b) Si/SiO_x

A part of the deposited Si/SiO_x substrate was cracked previously to the deposition (*Figure 2.22 a*). A piece of the SiO_x material was separated from the substrate, revealing a 150 µm height layer over the substrate, probably the SiO_x thermally grown layer. The conformal covering of the polymer cannot be observed, although indications of a polymeric deposit are observed at the base of the cracking.

2.4.2.2. Spectroscopy Characterization

The signal/noise ratio of the *FTIR* spectra indicates that the film obtained at the average temperature around 0 ºC is thinner than the one obtained around -44 ºC. This indicates that the temperature is an important factor in the film deposition, with a higher influence than the deposition time.

The bands characteristic to the (P)MMA corresponding to the CH_3 stretching and C=O stretching are observed are observed at 2960 cm^{-1} and 1734 cm^{-1} respectively (*Figure 2.24 a*). The CH and CH_3 deformation band at 1454 cm^{-1} cannot be clearly highlighted, although for Si(111) it can be speculated that it has a contribution.

Further studies will investigate the oil deposited on the surface of the substrate. This will further contribute with information regarding the encapsulation of the liquid phase in the film.

For the *Raman* spectra of the obtained samples, the regions of interest are focused again over a flat area of the film and a wrinkle area of the polymeric film as presented in *Figure 2.25* with the purpose of determining its composition. The photo-initiator spectrum is the same as the one presented in *Figure 2.19*. The Raman spectra for those points of interest in

Figure 2.26 can be regarded in conjunction with the 1st experimental series (experiment at -44 ± 21ºC).

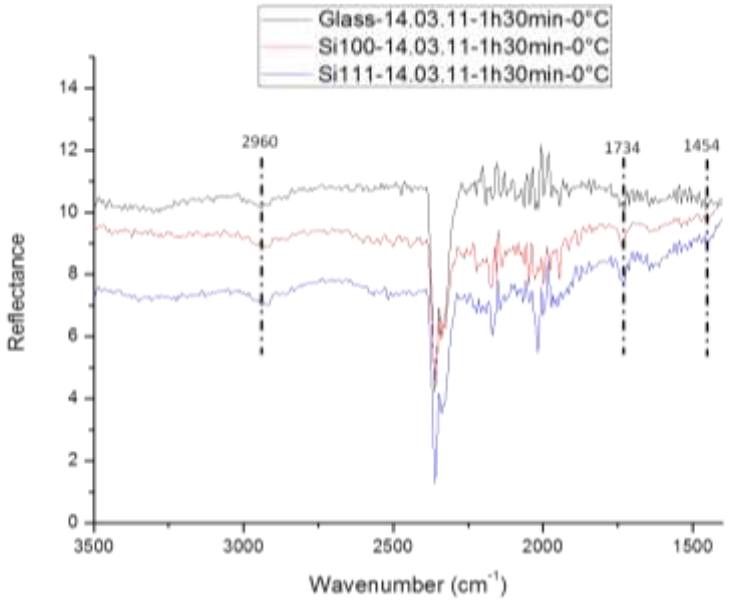

Figure 2.24: ATR-FTIR spectra with bands that correspond to the polymeric film

It can be observed that the band of the photo-initiator aromatic ring at 1600 cm^{-1} is missing from the planar thin film. As an indication of the polymeric film, the 1460 cm^{-1} bands (CH and CH_3 deformations) specific to PMMA is identified [16].

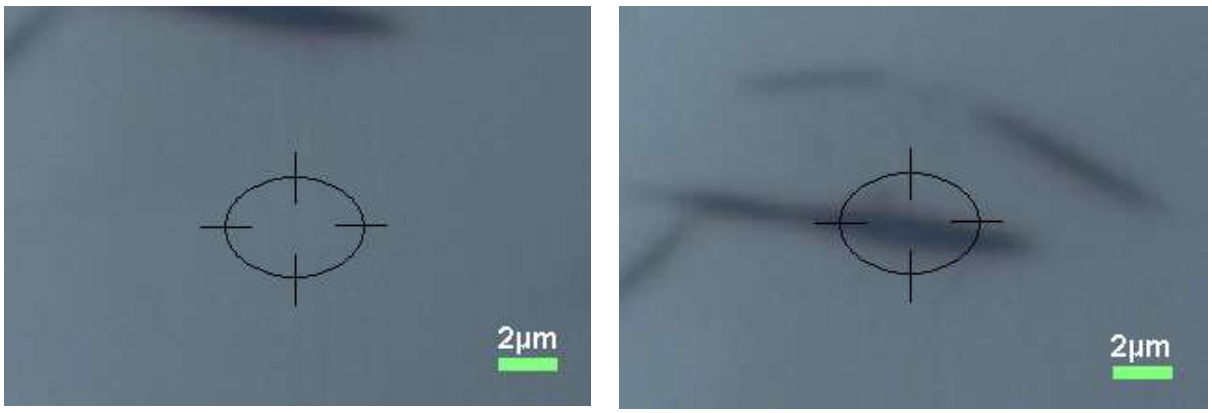

a) *b)*

Figure 2.25: The focus area over which the Raman spectra was taken for a) thin film and c) the wrinkling structure

In the wrinkled area the same 1460 cm^{-1} band is higher in intensity than the one for photo-initiator 1600 cm^{-1}, indicating an increase in (P)MMA contribution to the spectrum compared to the one of the HCFK photo-initiator. Also, at 1640 cm^{-1} a band is highlighted that indicates the presence of the monomer.

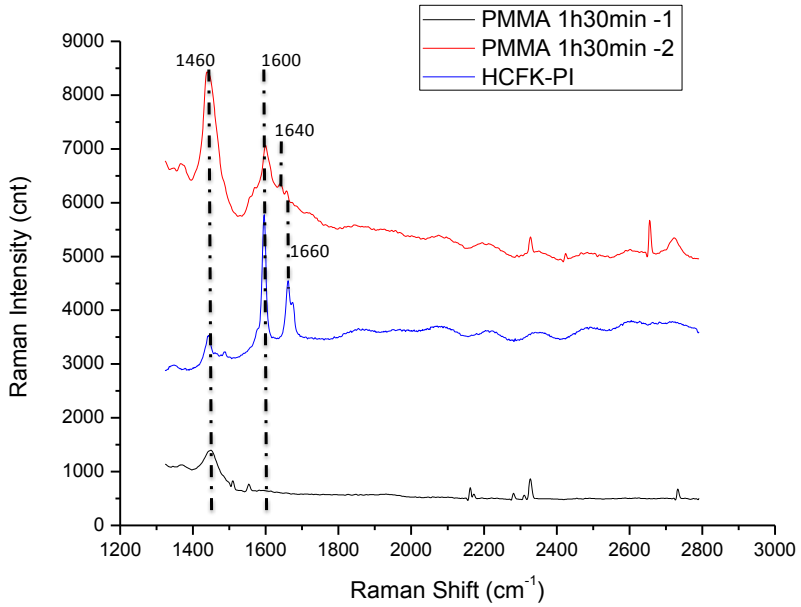

Figure 2.26: Raman spectra for different areas over the substrate; HCFK-PI shows the photo-initiator spectra; PMMA 45min-1 was focused over the thin film and PMMA 4min-2 was focused over the wrinkling area

2.4.3. Overview of the Substrate Temperature Variations

During the deposition experiments previously presented it was imposed a temperature variation of ΔT = 42 ºC with the median temperature of –44 ºC (subchapter *2.4.1.* 1st series) and ΔT = 8 ºC with the median temperature of 0 ºC (subchapter *2.4.2.* 2nd series). For both experiments the presence of wrinkles over the surface were observed (*Figure 2.12 b* and *Figure 2.22 c*).

For the experiment that involved ΔT = 42ºC, microscopy images shown crater-like structures with micrometric size, as seen also in *Figure 2.27 a)* and *b)*. These craters can be associated to an intense process during the deposition. This process is likely thermal expansion. Generally, the thermal expansion of a liquid (α_L) is higher than the one of a solid (α_S). For MMA the thermal expansion coefficient is $\alpha_L = 5.76\ 10^{-4}\ K^{-1}$ and that of PMMA $\alpha_S = 3.21\ 10^{-4}\ K^{-1}$ [12].

The AFM technique was used to estimate the thermal expansion for the blisters that were observed after the deposition. For a determined volume of $156*10^{-2}\ \mu m^3$ at ΔT = 42ºC there will be theoretically a difference of expansion factors between the monomer (α_L) and the polymer (α_S) of around $1.72*10^{-2}\ \mu m^3$.

For the experiment that involved ΔT = 42ºC, microscopy images shown crater-like

The second experiment with a temperature variation of only ΔT = 8ºC presented only small punctures (nanometric size) over the blisters. Such aspects are also observed in the micrographs from *Figure 2.27 c)* and *d)*. This indicates a more moderate release of the thermal strain. For a volume of $162*10^{-2}\ \mu m^3$ calculated from AFM data, the difference between α_L and α_S for the applied temperature difference is only of $0.34*10^{-2}\ \mu m^3$.

The thermal expansion of the material during a temperature difference induces a strain over the material. This thermal strain (ϵ_t) related to the thermal expansion of the polymer is defined as:

$$\epsilon_t = \alpha_S \Delta T \qquad (2.6)$$

where $\Delta T = T_{final} - T_{initial}$, with $T_{final} > T_{initial}$ since here the thermal expansion is considered.

The faster thermal expansion of the monomer compared to the one of the polymer leads to a thermally induced elastic strain (ϵ_τ):

$$\epsilon_\tau = (\alpha_L - \alpha_S)\,\Delta T \qquad (2.7)$$

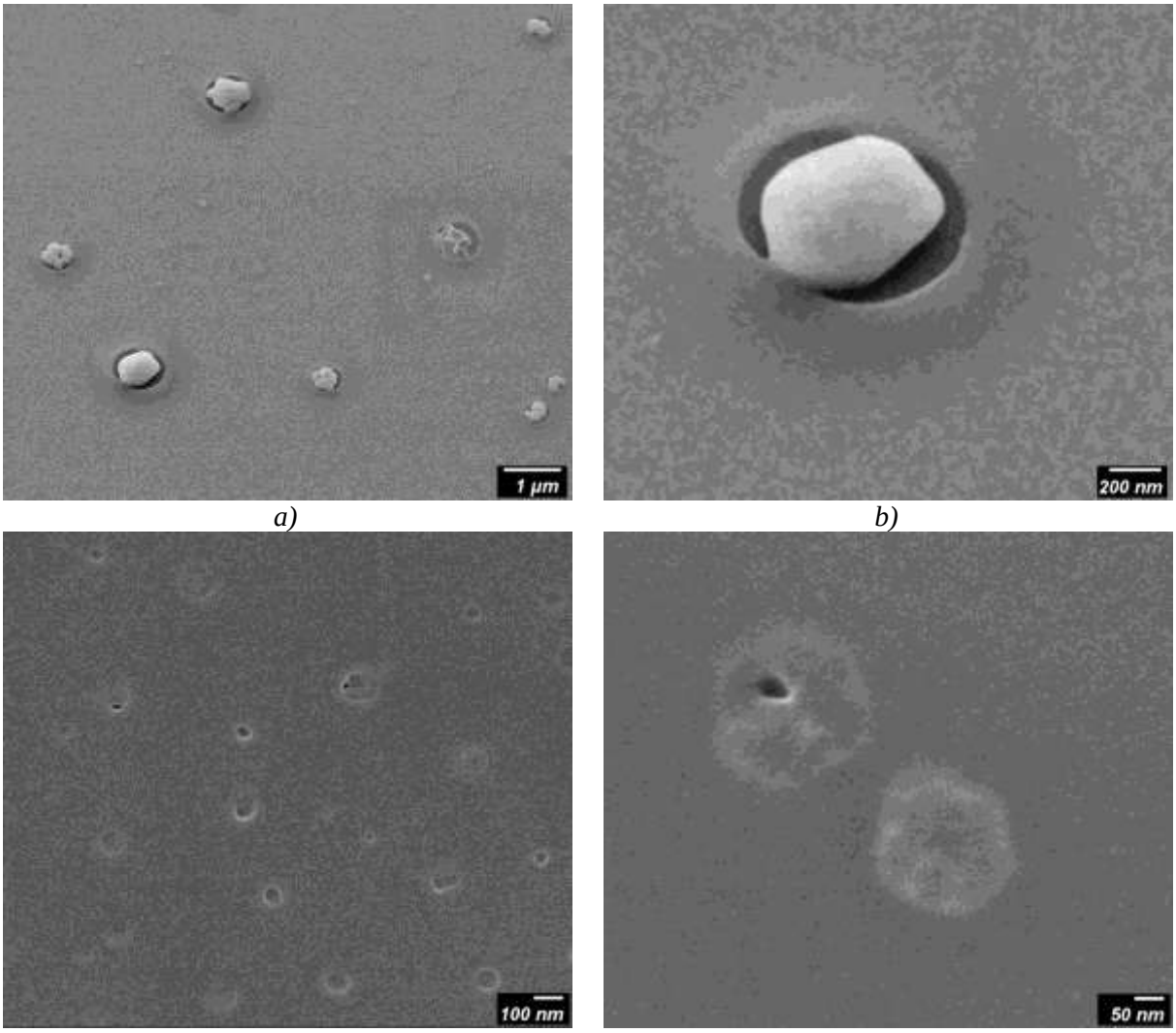

Figure 2.27: FESEM micrographs of Photo-CVD PMMA films grown under an in situ thermal strain of (a,b) ΔT = 42°C and (c,d) ΔT = 8°C. Morphologies of crater-like heterogeneities (b) and small punctures (d) are emphasized onto the surface.

Overall, the combined strain (ε_T) of the thin polymeric film that covers the liquid droplets sums the two strain components:

$$\epsilon_T = \epsilon_t + \epsilon_\tau \qquad (2.8)$$

The point at which the bulk PMMA breaks (called the strain-at-break point) was determined at ϵ_f = 0.5% [17]. According to equation *(2.8)*, the temperature changes of ΔT = 42 K will induce a thermal strain of ϵ_T = 2.4%. This value is almost five times higher than the strain-at-break point of the macroscopically determined value [17]. For the temperature variation of ΔT = 8 K, the thermally induced strain value is of ϵ_T = 0.46%. This is the same order of magnitude with the bulk value.

This process at which the faster thermal expansion of the liquid pushes over the solid encapsulate (ϵ_T) can be generally called as the Thermally Induced-Release of Internal Phase (TI-RIP) and is schematically presented in *Figure 2.28*.

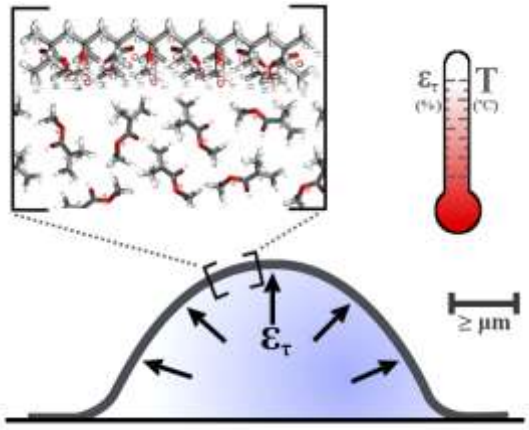

Figure 2.28: TI-RIP process schematic description; It is emphasized the proportionality of the temperature difference (T) and the thermally induced elastic strain (ϵ_τ)

The crater-like defects over the encapsulating membrane of the blisters shows a catastrophic failure for the high temperature difference of ΔT = 42 K that perturbs the smoothness of the film. If the temperature differences are lowered (ΔT = 8 K) the smaller defects appearing as punctures preserve the smoothness of the surface morphology. Under the low pressure conditions, the TI-RIP process allows the release of the containing fluidic monomer and, in the same time, acts as a self-healing mechanism for the polymeric film during the Photo-CVD run. The concept of self-healing material as means of preventing catastrophic failure is already investigated for a wide range of materials [18,19]. This gives an added versatility to the Photo-CVD process by the prospect of the internal phase controlled release through TI-RIP.

2.5. Liquid Encapsulation

Some aspects of liquid encapsulation were studied at microscopic scale. This can provide industrial solutions for microelectronics and other applied fields. The liquid release through the TI-RIP process during the growth can already be a mean to achieve a release of a liquid phase covered by a thin layer membrane at micrometric scale. The aspects involved in this process are described in subchapter *2.4.3.* The monomer phase (a fluid by itself) was already proved to be encapsulated in thin polymeric films (as presented in subchapters *2.3.3. 2.4.1.1.* or *2.4.2.1.*) at microscopic scale. Evidences of encapsulation will be presented below. Further results will highlight the liquid encapsulation both at room temperature and at lower temperatures by using another fluid compound that is subject to encapsulation, namely Balzers Betriebsmittel F9 (P275140211) turbomolecular pump oil (product code PM 006 336-T).

2.5.1. Liquid Encapsulation at Room Temperature

An experiment with oil as encapsulated liquid was made at room temperature, in order to avoid the compression/decompression effects due to the temperature difference (*Table 2.8*).

Table 2.8: The Photo-CVD experimental parameters for liquid encapsulation at room temperature

Gas flow		*Pressure*		*Temperature*		*Injector*	
Q_{N2}	*108 sccm*	P_{N2}	*2.8bar*	T_{inj}	*45˚C*	t_{on}	*1 ms*
		P_T	*9.5Torr*	T_{uv}	*80˚C*	f	*1 Hz*
		-	-	$T_{substrate}$	*~18ºC*	t_{exp}	*45 min*

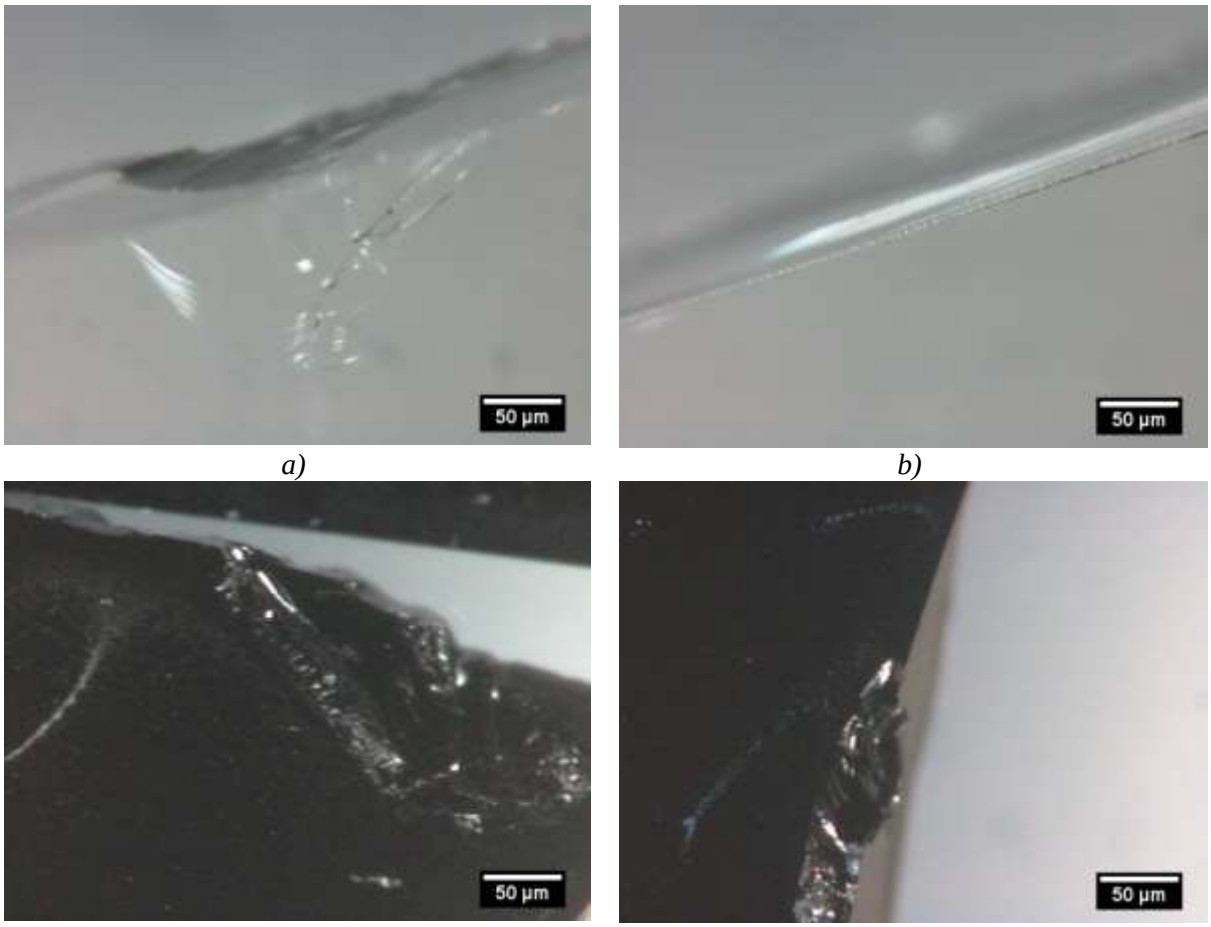

a) *b)*

c) *d)*

Figure 2.29: Optical microscope images of the deposition over a), b) glass and c), d) Si(111)

To place a drop of liquid on the flat surface of glass and Si(111) was difficult because it tends to spread and move during sample handling. This spreading was facilitated both by the low total pressure in the CVD reactor and the surface energy of the substrate. As previously observed in the microscopy images and highlighted by the difficulty to obtain FTIR signal with a high resolution, the thickness of the deposited film is very low. During the CVD run the low thickness of the film also offers low resistance to the liquid spreading over the surface. As a result, it is hard to determine the composition of the deposited film and to demonstrate that the encapsulation was successful.

Some optical microscopy studies revealed what seems to be a polymer layer covering the oil film spread on the surface of the substrate (*Figure 2.29*). The breaking point of the film can be observed at the edges, as peeling takes place and reveals a transparent thin film. Also, the small monomer bubbles seem to be observable as white conglomerates over the dark Si(111) substrate (specially in the *Figure 2.29 c* upper left conglomerate).

2.5.2. Liquid Encapsulation at Low Temperatures

In the two series of CVD experiments where the temperature was varied during the growth process a few droplets of pump oil was put on the surface of a glass substrate (subchapter *2.4.*).

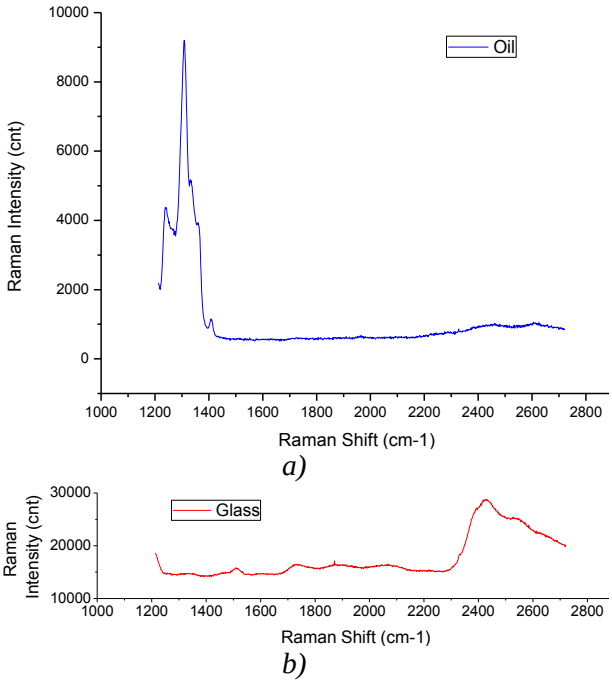

Figure 2.31: Raman spectra of a) pump oil on glass and of b) glass substrate

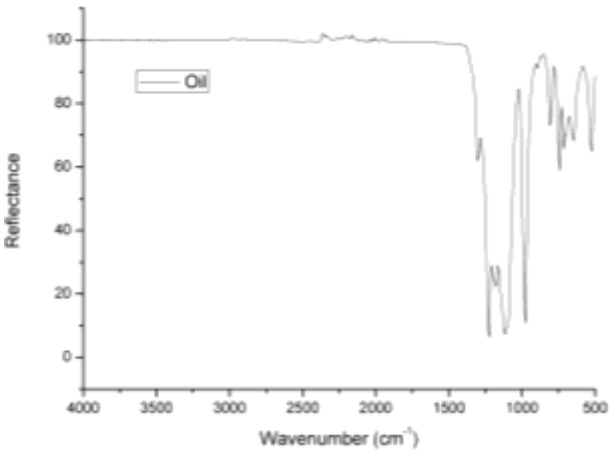

Figure 2.30: ATR-FTIR spectra of the pump oil used in deposision experiments

- Comment on the oil used for encapsulation -

The Raman (*Figure 2.31*) and FTIR (*Figure 2.30*) spectroscopies of the oil pump show that the oil bands do not overlap the polymer bands (*Figure 2.24*), offering an experimental advantage by a clear separation of the two chemical species.

The oils can be chemically grouped in four categories: *hydrogenated polyolefins*, *esters*, *silicones* and *fluorocarbons*. Examples can be seen in *Figure 2.33*.

The first two groups of oils are the polyolefins and esters. They contain exclusively C, H and O atoms as PMMA films. As a result, overlaps are expected between the IR (especially in the range 3700 cm^{-1} - 600 cm^{-1} [20]) and Raman bands of oil and PMMA. For this reason, the used oils is not of this class.

The silicon oil is easily identified by two specific sharp bands at 1000 cm^{-1} and 1590 cm^{-1} [21,22]. None of the two sharp bands are appearing in the spectrum of the oil used here (*Figure 2.30*), indicating that is not a silicon-type oil.

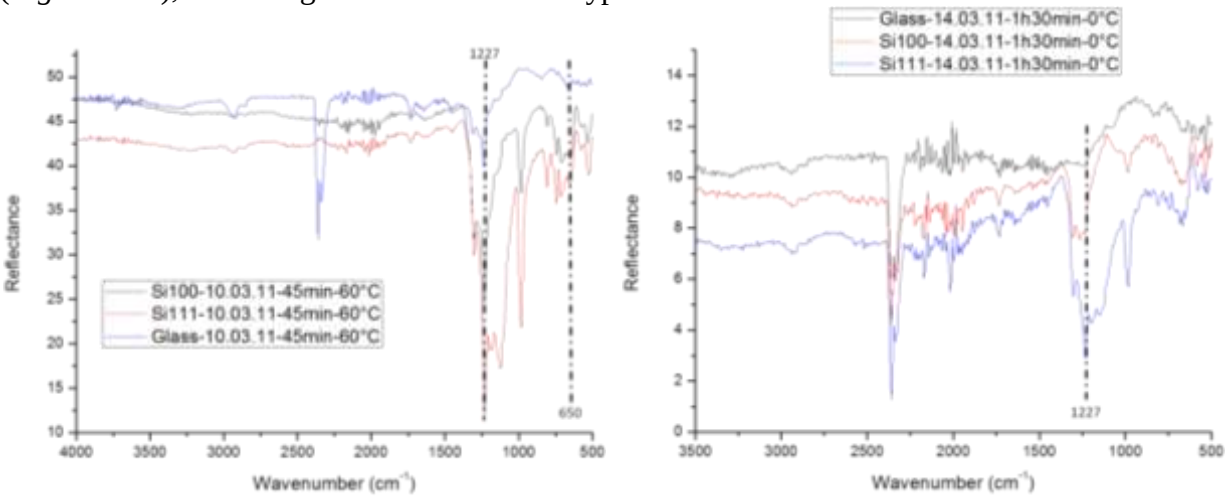

Figure 2.32: ATR-FTIR spectra with specific bands that correspond to the oil present over the thin PMMA film grown under an in situ thermal strain of a) ΔT = 42°C and c) ΔT = 8°C

Finally, our analyses demonstrated that the oil used was from the family of polychlorotrifluoroethylene compound. Indeed, according to [20], in the 1400 – 500 cm^{-1} spectral range the main chemical groups are CF (1400-1000 cm^{-1}), -NH_2 (900-700 cm^{-1}), Cl-C-H (650 cm^{-1}), R-SO_3 (1090-1010 cm^{-1}) and [SO_4] (1140-1080 cm^{-1}).

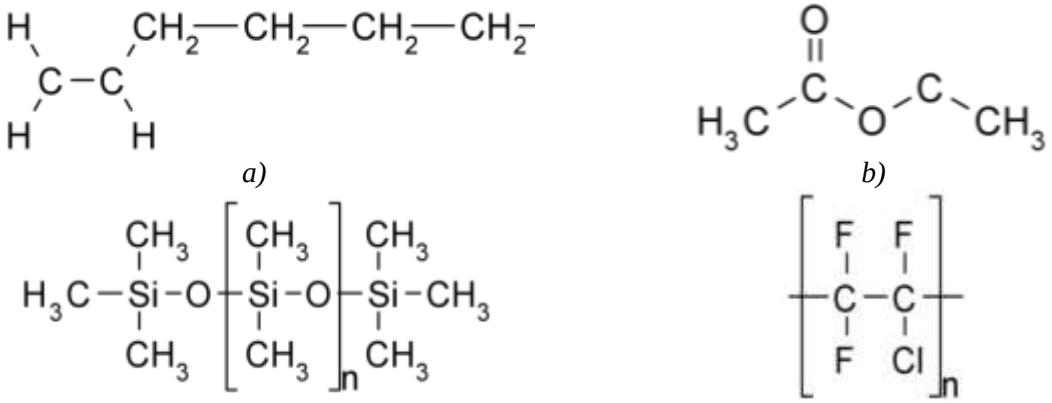

Figure 2.33: Examples of basic oil types: a) polyoefins (alpha-olefin), b) ester (ethyl acetate), c) silicone (silicone polydimethylsiloxane) and d) fluorocarbons (polychlorotrifluoroethylene)

- Characterization of the polymeric film deposited on the oil/substrate samples -

The FTIR spectra of these samples exhibits bands over 1400 cm^{-1} (*Figure 2.32 a*) giving evidence for the presence of PMMA. The 1227 cm^{-1} band characteristic of a trifluoride group (CF_3) confirms also the presence of oil [15,23,24]. The results are similar for the two series of CVD experiments.

The presence of all of the species on the surface (oil, PMMA / MMA) is spectroscopically observed. The monomer MMA and the fluorocarbon oil are not easily immiscible because of the molecular weight [25] (MMA has 100 g/mol, while the oil has around 3500 g/mol [26]). As a result, polymerization can occur on the surface of the oil to form a thin PMMA membrane that encapsulates the oil.

2.6. Chapter Overview

This chapter detailed some practical aspects with respect to the Photo-CVD process used to deposit PMMA thin films. Direct indications of the deposited thin films were difficult to be obtained. However, some experimental results highlighted indirectly its presence, but also the presence of a fluid phase.

A direct evidence for the presence of the polymeric film with blisters containing liquid is given by the fact that the samples kept for 2 months (under dark conditions, at room temperature) preserve the same blister distribution over the surface, despite the volatile character of the monomer indicating that it is tightly encapsulated.

Since the blisters are constituted by liquid monomer protected by a thin polymeric membrane they are sensitive to post-treatments. Consequently, both thermal and UV post-treatments have revealed that the liquid phase is composed by fluid monomer (MMA) and photo-initiator. The presence of a thin polymeric film covering the blisters was also indicated by SEM as a film rupture of a blister was observed when the sample undergoes sudden change of pressure (as required for sputtering process). The liquid encapsulation was also investigated by using oil droplets on the substrate.

By the variation of the temperature during deposition, a process of Thermal Induced-Release of Internal Phase (TI-RIP) was also highlighted. Numeric estimations of the implications for such a process were given by the use of the AFM topographical data.

Aspects of the surface nucleation were also observed by SEM and AFM analysis. Such a nucleation phenomenon is important as it can lead to a controlled patterning of the surface.

The polymerization occurs also by a nucleation process. However, the spectroscopic data could not offer information with the polymerization nucleation. The results presented in the next chapter will treat such aspects.

Bibliography

[1] V. Sankar, T.S. Kumar, K.P. Rao, Preparation, characterisation and fabrication of intraocular lens from photo initiated polymerised Poly (methyl metacrylate), Trends Biomater. Artif. Organs. 17 (2004) 24–30.
[2] C. Soares, Gas Turbines: A Handbook of Air, Land, and Sea Applications, Butterworth-Heinemann, 2007.
[3] V.K. Shukla, S. Kumar, Investigations of environmental induced effects on AlQ3 thin films by AFM phase imaging, Applied Surface Science. 253 (2007) 6848–6853.
[4] M.J. Hamer, J.A.D. Wattis, R.S. Graham, Analytic calculation of nucleation rates from a kinetic Monte Carlo simulation of flow induced crystallization in polymers, Journal of Non-Newtonian Fluid Mechanics. 165 (2010) 1294–1301.
[5] Z. Kožíšek, M. Hikosaka, P. Demo, A.M. Sveshnikov, Nucleation kinetics of polymer formation on nucleation agent, Journal of Crystal Growth. 275 (2005) e79–e83.
[6] Q. Jiang, Z. Wen, Thermodynamics of Materials, Springer, 2011.
[7] F. Pallikari, G. Chondrokoukis, M. Rebelakis, Y. Kotsalas, Raman spectroscopy: A technique for estimating extent of polymerization in PMMA, Mater. Res. Innovations. 4 (2001) 89–92.
[8] P. Yang, The Chemistry of Nanostructured Materials, World Scientific, 2003.
[9] C. Gardrat, R. Ruggiero, W. Hoareau, L. Damigo, A. Nourmamode, S. Grelier, et al., Photochemical study of 4-(4,9-dimethoxy-2,11-n-dipropyl-6,7-dihydro-5,8-dioxa-dibenzo[a,c]cycloocten-6-yl)-2-methoxyphenol, a lignin model of phenolic dibenzodioxocin unit, Journal of Photochemistry and Photobiology A: Chemistry. 169 (2005) 261–269.
[10] K.L. Rhudy, S. Su, H.R. Howell, M.W. Urban, Self-Stratified Films Obtained from Poly(methyl methacrylate/n-butyl acrylate) Colloidal Dispersions Containing Poly(vinyl alcohol): A Spectroscopic Study, Langmuir. 24 (2008) 1808–1813.
[11] K.P. Le, R. Lehman, A. Mann, J. Idol, Raman Characterization in Blends of Poly (L-lactide) and Poly (methyl methacrylate), Applied Spectroscopy. (2006).
[12] A. Faldi, M. Tirrell, T.P. Lodge, E. von Meerwall, Monomer Diffusion and the Kinetics of Methyl Methacrylate Radical Polymerization at Intermediate to High Conversion, Macromolecules. 27 (1994) 4184–4192.
[13] R. Ortiz, O.P. Márquez, J. Márquez, C. Gutiérrez, FTIR spectroscopy study of the electrochemical reduction of CO2 on various metal electrodes in methanol, Journal of Electroanalytical Chemistry. 390 (1995) 99–107.
[14] A. Balamurugan, S. Kannan, V. Selvaraj, S. Rajeswari, Development and Spectral Characterization of Poly (Methyl Methacrylate) / Hydroxyapatite Composite for Biomedical Applications, Trends Biomater. Artif. Organs. 18 (2004) 41–45.
[15] M. Deepa, N. Sharma, S.A. Agnihotry, FTIR investigations on ion – ion interactions in liquid and gel polymeric electrolytes: LiCF3SO3-PC-PMMA, Journal of Material Science. 37 (2002) 1759 – 1765.
[16] K.J. Thomas, M. Sheeba, V.P.N. Nampoori, C.P.G. Vallabhan, P. Radhakrishnan, Raman spectra of polymethyl methacrylate optical fibres excited by a 532 nm diode pumped solid state laser, Journal of Optics A: Pure and Applied Optics. 10 (2008) 055303.
[17] D. Blond, V. Barron, M. Ruether, K.P. Ryan, V. Nicolosi, W.J. Blau, et al., Enhancement of Modulus, Strength, and Toughness in Poly(methyl methacrylate)- Based Composites by the Incorporation of Poly(methyl methacrylate)- Functionalized Nanotubes, Advanced Functional Materials. 16 (2006) 1608–1614.
[18] J. Wang, K. Van Tittelboom, N. De Belie, W. Verstraete, Use of silica gel or polyurethane immobilized bacteria for self-healing concrete, Construction and Building Materials. 26 (2012) 532–540.
[19] G. Couégnat, G.L. Vignoles, V. Drean, C. Mulat, W. Ros, G. Perrot, et al., Virtual material approach to self-healing CMCs, in: 4th European Conference for AeroSpace Sciences (EUCASS), 2011: pp. 1–8.
[20]Tables of Physical & Chemical Constants (16th edition 1995). 3.8.5 Infrared and Raman spectrophotometry. Kaye & Laby Online. Version 1.0, (1995).
[21] J. Hird, M. Bloomfield, I. Hayward, Investigating the mechanisms of diamond polishing using Raman spectroscopy, Philosophical Magazine. 87 (2006) 267–280.

[22] N. Freebody, A. Vaughan, A. Macdonald, On optical depth profiling using confocal Raman spectroscopy, Analytical and Bioanalytical Chemistry. 396 (2010) 2813–2823.
[23] Y. Alias, I. Ling, K. Kumutha, Structural and electrochemical characteristics of 49% PMMA grafted polyisoprene-LiCF3SO3-PC based polymer electrolytes, Ionics. 11 (2005) 414–417.
[24] K. Kumutha, Y. Alias, FTIR spectra of plasticized grafted natural rubber–LiCF3SO3 electrolytes, Spectrochimica Acta Part A: Molecular and Biomolecular Spectroscopy. 64 (2006) 442–447.
[25] B.A. Wolf, Solubility of polymers, Pure Appl. Chem. 57 (1985) 323–36.
[26] R.E. Banks, B.E. Smart, J.C. Tatlow, Organofluorine Chemistry: Principles and Commercial Applications, Springer, 1994.

CHAPTER 3 - PMMA THIN FILMS OBTAINED BY DRY ROUTE - KEMSTREAM G2.8 DLI

3.1. Experimental approach

The previous CVD experiments showed the presence of liquid monomer covered by an very thin film of polymer on the substrate. The presence of the monomeric species is most likely due to a low efficiency in the polymerization process. The low polymerization efficiency at the substrate level can be due to (*i*) an insufficient flash vaporization and/or (*ii*) an inefficient photo-activation of the gas phase. In order to address the flash vaporization efficiency issues the DLI system was upgraded to a newer generation Kemstream injector system.

3.1.1. DLI setup and parameters

The upgraded Kemstream G2.8 DLI system is composed by two-stage injectors. The outlet of the DLI system has 8 apertures which allow an increased flow rate of precursor and different features of the spray injected in the flash vaporization chamber (average droplet size, size distribution …).

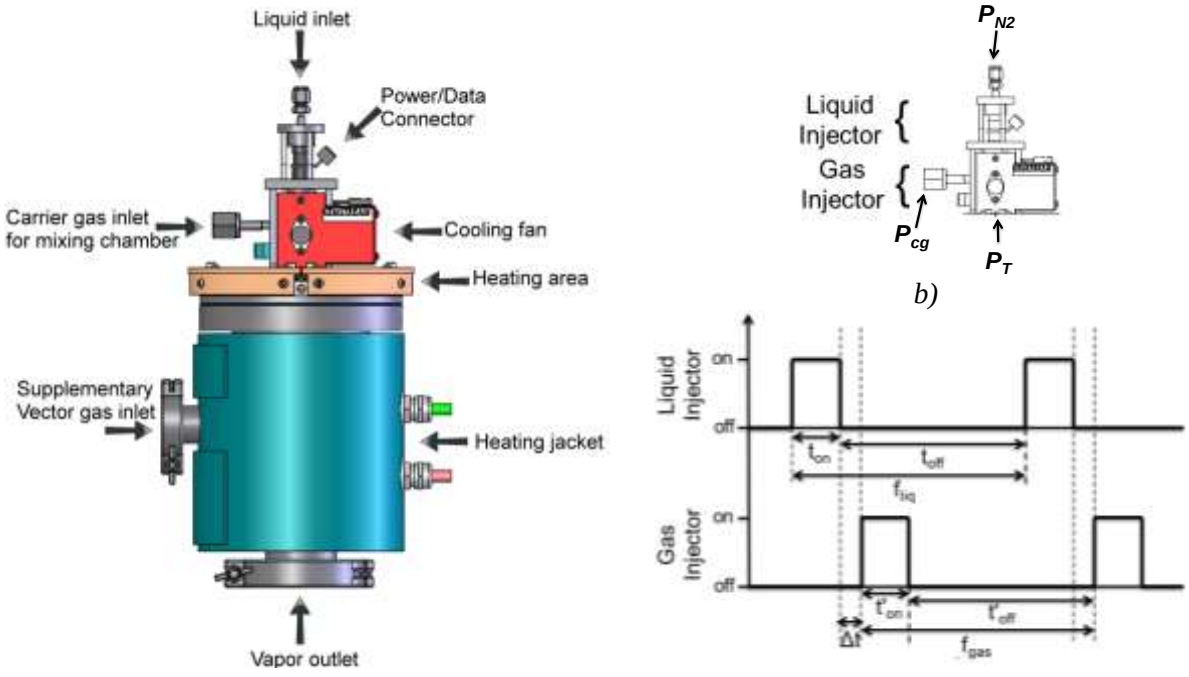

Figure 3.1: The new DLI system components a), the liquid and gas injectors b) and their operating parameters c)

The first injector, namely the liquid injector, is fed with the liquid monomer that is pushed by a first motive pressure (P_{M1}). The monomer is injected to a second injector (gas injector) that is fed with the carrier gas which acts as a second motive pressure (P_{M2}). The carrier gas which mixes the liquid in a mixing chamber (the same as the gas injector chamber) is flash vaporized in a vaporization chamber (*Figure 3.1 a*). For future reference, the injectors will be named based on their controlled inlet parameter: liquid injector and gas injector

(*Figure 3.1 b*). An Interface Control Unit (ICU) controls the DLI parameters, using the Vapsoft software user interface.

In this manner, the two injectors divide the motive pressure and the mixing chamber pressure in two categories:

- for the liquid injector the motive pressure (P_{M1}) that is the N_2 gas pressure (P_{N2}) that pushes the liquid, and the mixing chamber pressure (P_{C1}) is the carrier gas pressure (P_{cg}) of the gas injector's mixing chamber;
- for the gas injector the motive pressure (P_{M2}) is the carrier gas pressure (P_{cg}) and the chamber pressure (P_{C2}) is the total pressure of the CVD reactor (P_T).

Between the liquid injector pulse and the gas injector pulse there is a time lag (see Δt in *Figure 3.1 c*). For this Kemstream G2.8 DLI system the time lag is Δt = 2 ms. Because of this time lag, the operating regimes are separated. First, the liquid injector supplies liquid (with $P_{M1} = P_{N2}$) to the gas injector mixing chamber (with and $P_{C2} = P_{cg}$) and then, secondly, the gas injector sprays the gas/liquid mixture (with $P_{M2} = P_{cg}$) into the flash vaporization chamber connected to the CVD reactor (with $P_{C2} = P_T$).

The liquid injection of the *liquid injector* is controlled by setting an opening time of the aperture (t_{on}) and by setting a frequency (f_{liq}) of this repeating process. If we consider t_{off} as the time when the aperture is closed, then the frequency is:

$$f_{liq} = \frac{1}{t_{on} + t_{off}} \qquad (3.1)$$

The *gas injector* controls the amount of gas that is inserted in the system by setting a certain opening time of the mixing chamber. It is characterized by the same variables: opening time of the apertures (t_{on}'), the time the apertures are closed (t_{off}') and the frequency (f) that is expressed by the formula (*Figure 3.1 c*):

$$f_{gas} = \frac{1}{t_{on}' + t_{off}'} \qquad (3.2)$$

The upgraded Vapsoft software allows changing the gas injector frequency independent to the one for the liquid injector. In order to achieve the synchronization of the pulses, the gas injector frequency needs to have a value that is an even multiple of the liquid injector frequency:

$$f_{gas} = 2n\, f_{liq} \qquad (3.3)$$

To control the gas quantity inserted in the CVD reactor, the system is equipped with a Mass Flow Meter (MFM). This allows a pulsed insertion of a predetermined carrier gas quantity (through the gas/liquid mixture) by the gas injector. A proprietary algorithm makes the conversion from N_2 gas flow (Q_{N2}) to aperture opening time (t_{on}'). The conversion is achieved by a process of integration such as:

$$t_{on}' = \int_0^{Q_{N2}} t\, dQ_{N2} \qquad (3.4)$$

The above formulas describe the operating parameters of the G2.8 DLI system. For complementary information, the discussion on the simplified G1.5 DLI can be consulted.

3.2. First G2.8 Experimental Run – Preliminary Characterization of the Deposit

The objective of this experimental run is to evaluate the injector influence by changing some CVD parameters not DLI dependent. Towards this end, the experimental parameters of the subchapter *2.2.* were used. To be noted the fact that the carrier gas flow (Q_{N2}) in the injector is not continuous as for the previous experiments with the G1.5 model. It is

introduced in a pulsed regime. The pulsed regime (*Setpoint*) is monitored by a MFM calibrated in the 0 – 1500 sccm range (see previous subchapter *3.1.1.* for further details). The *Setpoint* percentage gives the numeric value for the Q_{N2} gas flow. The full experimental parameters are shown in *Table 3.1*.

Table 3.1: The Photo-CVD experimental parameters; the liquid precursor was MMA monomer with 2 % HCPK photonitiator

Gas flow		Pressure		Temperature		DLI system			
						liquid		gas	
Q_{N2}	150 sccm	P_{N2}	3.5 bar	T_{inj}	60 °C	t_{on}	1 ms	F	1 Hz
		P_{cg}	2 bar	T_{uv}	80 °C	f	1 Hz	Setpoint	10%
		P_T	9.5 Torr	$T_{substrate}$	~18 °C	t_{exp}		45 min	

Before deposition the substrates were prepared by rinsing, mechanical cleaning, sonic bath cleaning and Ar gas stream drying. The rinsing and the mechanical cleaning were repeated two times, once with acetone and once with ethanol. The mechanical cleaning involved a slow sweep by applying pressure with a cleanex tissue over the previously rinsed substrate. The sonic bath cleaning also involved two treatments of 5 min each: one in acetone and one in ethanol. After the ultrasonic cleaning, the substrates were dried under Ar gas stream in ambient conditions. Subsequently, the samples were introduced in the Photo-CVD reactor.

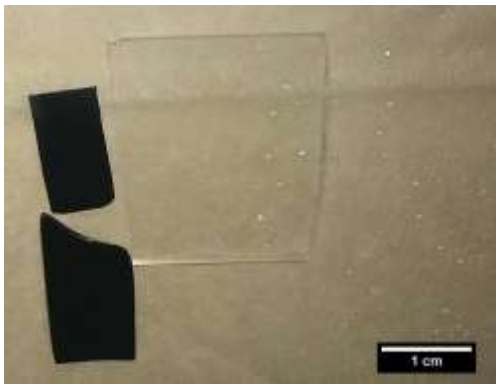

Figure 3.2: The samples obtained after the Photo-CVD deposition (experimental data in Table 3.1)

The total duration of the experiment was considered as t_{exp} and is associated to the time the liquid injector runs (the time it effectively injects the reactive monomer into the CVD).

After the deposition experiment under the above conditions, relatively large blisters with an average size of about 60 µm can be observed over the deposited substrates by optical misropscopy (*Figure 3.2*).

3.2.1. UV-VIS-NIR Characterization

The UV-VIS-NIR transmittance spectroscopy gives an overall view of the film properties. The information revealed in the spectra will be treated in the ultraviolet (UV) region (200 – 400 nm), visible region (VIS) (400 – 750 nm) and near infrared (NIR) (750 – 2500 nm).

The interaction of and radiation with the matter is described by: scattering, absorption, emission, refraction and reflection. During the spectroscopy measurements the main phenomena are the reflection, scattering (especially in the case of the liquid solutions) and absorption [1]. The reflection and scattering are described as perturbing components. An automatic background was made for the microscope-purpose glass using a substrate from the same batch as those used for the deposition. This allowed obtaining a reasonable control over

the reflection component of the spectroscopic investigation. The resulting spectrum of the film on glass substrate is presented in *Figure 3.3*.

Although the glass substrate used for the deposition has a general low transmission in the **UV** region (< 250 nm), an isolated absorbtion band assigned to the film appears at 277 nm. It is associated to the conjugated systems of the MMA monomer (it is not the case for the polymer) and/or of the aromatic system of the HCPK photo-initiator [2]. The high absorption of glass is probably responsible for the observed transmittance cut below the 245 nm wavelength.

In the **VIS** region an increased transmission of around 91 % (± 4 %) is obtained. Compared to the previous results with the G1.5 DLI injector this is the lowest measured transmittance. This likely indicates an increasing quantity of coating over the substrate with the upgraded G2.8 DLI system.

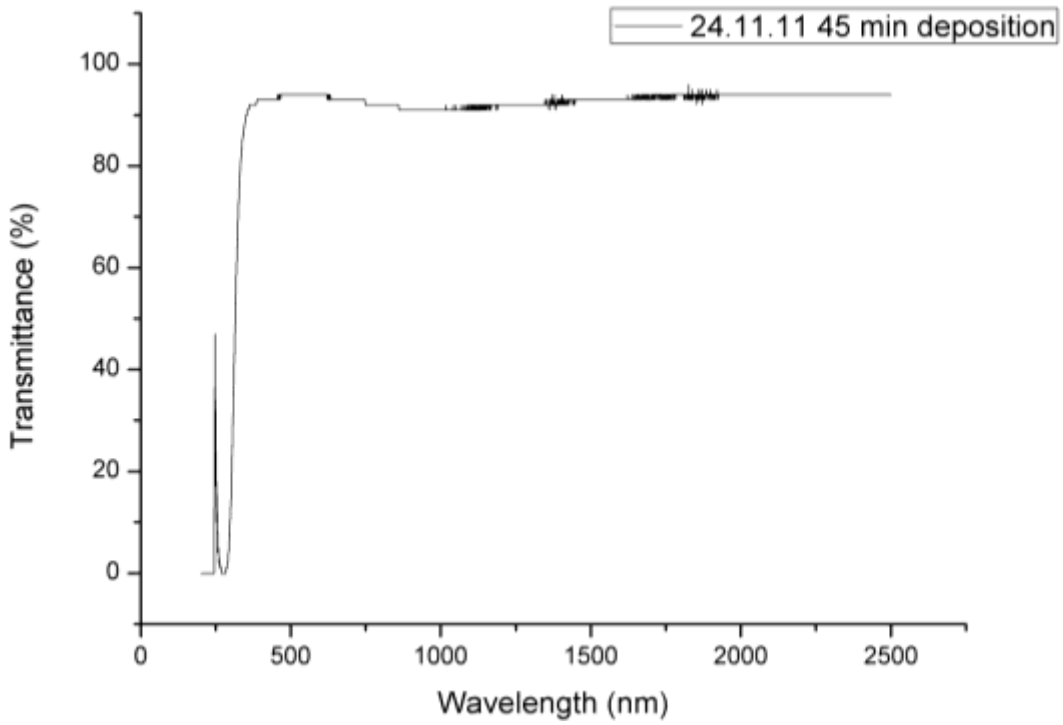

Figure 3.3: UV-VIS-NIR spectra of the deposited film on glass substrate

In the **IR** region vibration bands can be observed, however without clear bands corresponding to any of the chemical species deposited over the substrate.

As specified before, the scattering of the UV-VIS-NIR spectroscopy is a perturbing factor. However, a king of light scattering, Raman scattering, reveals complementary informations with respect to the chemical composition and will be treated in the next subchapter.

3.2.2. Raman Spectroscopy – Chemical Approach

The Raman characterization was achieved in two parallel approaches: spectroscopic and microscopic. The spectroscopic approach offers insight over the chemical structure of the film, while the microscopic approach extrapolates information with respect to the film properties. Such a dual approach is presented in *Figure 3.4*.

The Raman spectrum (*Figure 3.4 a*) shows several distinctive bands: two of high intensity (1450 and 1600 cm^{-1}), two of medium intensity (1690 and 1720 cm^{-1}) and one of low intensity (1555 cm^{-1}).

Notably, a wide band for the C=C double bond is also observed in 1620 - 1660 cm^{-1} range associated to the presence of the liquid species (the C=C band of the monomer at 1640 cm^{-1} mixed with that of the photo-initiator band at 1660 cm^{-1}).

The highest intensity bands at 1450 cm^{-1} and 1600 cm^{-1} are associated to CH_3 asymmetric deformation, present in the monomer, and to the HCPH photo-initiator ring vibration respectively [3–6]. The two medium bands observed at 1690 cm^{-1} and 1720 cm^{-1} are both associated to the C=O stretching [6,7]. The low intensity band present at 1555 cm^{-1} can be associated to the CH_2 bond [8].

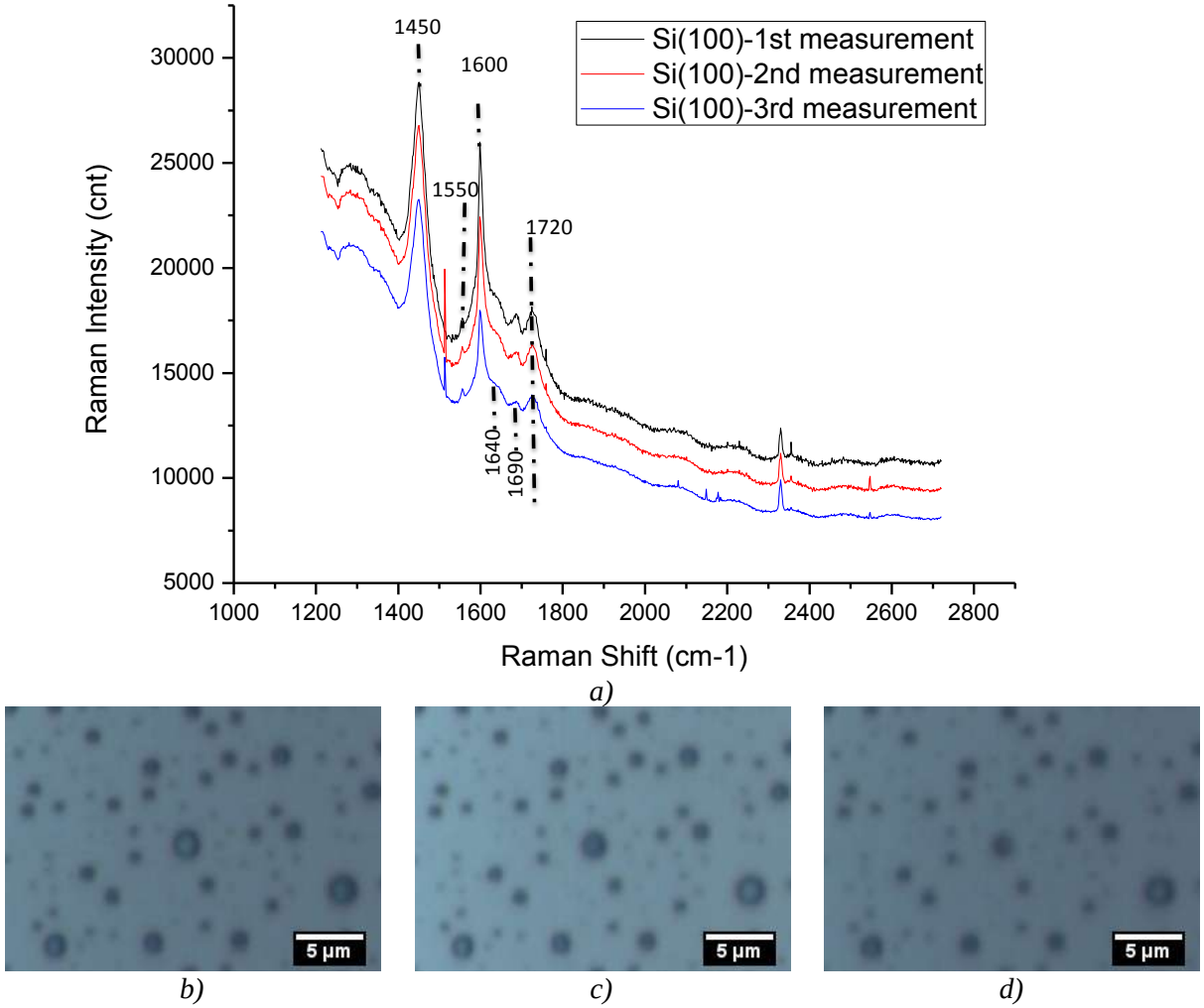

Figure 3.4: The Raman Intensity decrease during 532 nm laser exposure a) and the blister evolution in time b), c), d) over Si(100) substrate

With subsequent exposures, a uniform decrease of all Raman signals is observed. Also, in the Figure 3 b), c) and d) the decrease in size of the investigated blisters is observed. This indicates a coupled physical-chemical process of polymerization, degradation and/or vaporization. As the Raman Confocal Microscope indicates a phenomenon of decrease in blister size, the physical processes that occur are hard to be observed and extrapolated. They will be highlighted by further analyses. However, chemical evidences are found with respect to some aspects of the processes involved.

In the Raman spectra (*Figure 3.4*) it can be observed that the intensity decrease of the signal for specific chemical species is not fully proportional. The relative decrease in Raman response of the high and medium intensity vibrations are shown in *Figure 3.5*. This is the case of the CH_3 asymmetric vibration at 1450 cm^{-1}, the C=C stretching at 1600 cm^{-1} and the C=O

stretching at 1690 cm^{-1} and 1720 cm^{-1}. The wide band of the CH_3 vibration is associated to (P)MMA (both the polymeric and monomeric components).

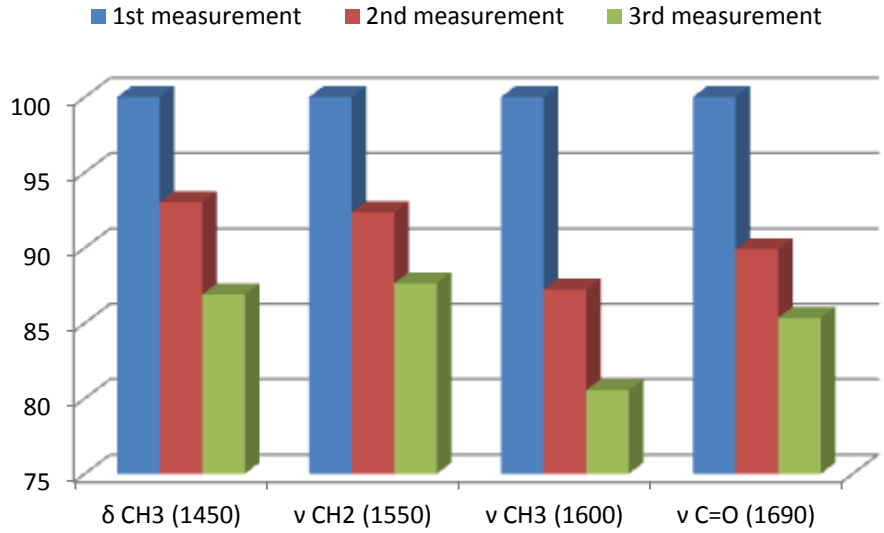

Figure 3.5: The relative Raman Intensity decrease with each successive exposure to the 532 nm Raman laser radiation over the same surface; the CH_3 asymmetric deformation of the(P)MMA, C=C stretch of the HCPK and the C=O stretch at 1690 cm^{-1} and 1720 cm^{-1} Raman shifts associated to the coupled MMA/HCPK are shown

The sharp band at 1600 cm^{-1} is associated to the ring structure of the HCPK photonitiator. The C=O vibration is a combined effect of (P)MMA and HCPK. However, the previous study (chapter 2, subchapter *2.3.2.*) showed that 1690 cm^{-1} vibration is associated mainly to the HCPK change, while the 1720 cm^{-1} vibration is not so specific with respect to the MMA/HCPK ratio. The rates of the Raman intensity changes indicates a steeper decrease of the HCPK photo-initiator (related C=C vibration at 1600 cm^{-1} and 1690 cm^{-1} vibration of C=O) compared to the (P)MMA (CH_3 band at 1450 cm^{-1}). Thus, as the volume of the analyzed blisters decreases, a preferential depletion of photo-initiator is suspected.

a) *b)* *c)*

Figure 3.6: Chemical formula of HCPK photo-initiator (a) highlighting the phenyl group; the para (b) and ortho (c) orientation of the quinone methide

The term “depletion” can be viewed as a chemical transition that alters photo-initiators bonds by the reduction of C=C bonds. Literature studies had reported that the phenyl group of the photo-initiator oxidizes by UV exposure into another compound, quinine methide (*Figure 3.6 b* and *c*) [9], thus depleting the phenyl group of the HCPK (*Figure 3.6 b* and *c*). This decreases the number of C=C double bonds from 3 (three) for a phenyl molecule to only 2 (two) for a quinine methide molecule. Such a chemical process can be suspected by a thermal oxidation during laser irradiation in air, explaining the decrease of the C=C bond associated mainly to HCPK. The decrease of the C=O band associated mainly to the HCPK contribution could also indicate changes of the photo-initiator as it passes to a radical state [10].

The AFM technique will be further used to characterize the obtained films from a structural point of view.

3.2.3. AFM characterization – Phase shift

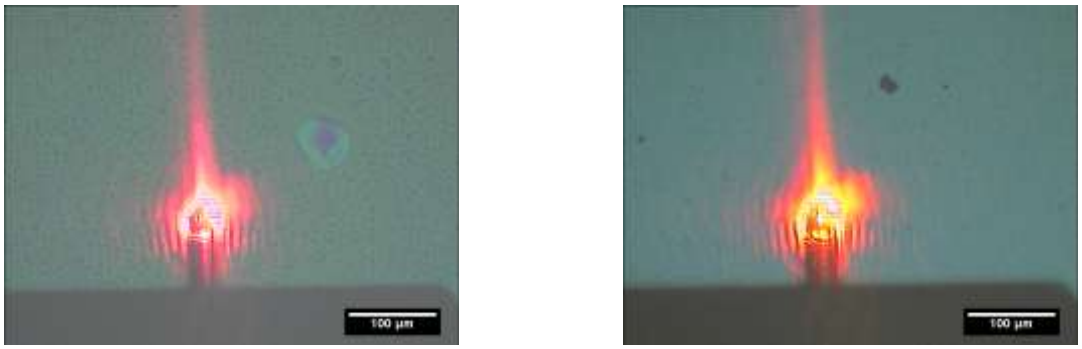

a) *b)*

Figure 3.7: In situ Microscopy image of the AFM cantilever over the probed area of the film on a) Si(100) and b) Si(111) substrate

From the Raman microscope small blisters of around 2 µm in diameter were observed. The AFM image of the tip (*Figure 3.7*) indicates that the surface distribution is relatively uniform at the microscopic scale both on Si(100) and Si(111).

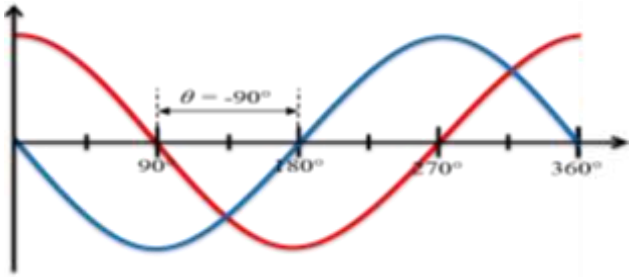

Figure 3.8: An example of phase shift; the phase shift (θ) between the blue wave and the red wave is expressed in angles (°)

To have an overview at a smaller scale the three dimension topography is shown (*Figure 3.9 a* and *c*). Notably, *Figure 3.9 a), c)* has a slope that occurred due to the experimental setup (inclination of the AFM cantilever).

The AFM data was obtained in acoustic mode (AC). The AC AFM describes the mode when the AFM cantilever oscillates at a specific resonance frequency.

In *Figure 3.8* an example of negative phase shift is shown. The blue signal is considered the 'referenced' wave signal. The 'referenced' wave is considered as the acoustic wave at which the AFM cantilever resonates. The red wave is considered as the acoustic wave of the AFM cantilever as it interacts with the sample. If the horizontal shift is positive, the shifting moves to lower angle values. If the horizontal shift is negative, the shifting moves to higher angle values. In *Figure 3.8* example, a negative phase shift is represented (-90 °).

When the AFM cantilever interacts with the sample, the oscillation frequency presents a phase shift. This phase shift is dependent to the resonant physical properties of the interacting area (such as the substrate, thin film and encapsulated blisters).

Figure 3.9 shows a 100 μm^2 area of the 3D topography and the phase, with an increased magnification at the edge of the observed blister (around 2 µm in diameter). The height of the encapsulated blister, reaches to around 120 nm. The calculated slope for the blister edge is 258 nm/µm. The blister seems to follow the substrate features, not having a perfect circular distribution of the edges (*Figure 3.9 b*). In the magnified image from *Figure 3.9 b)* the irregular shape of the blister edge is highlighted. This can be due to a polymerization on a fluid that is moving over the surface. The fluid movement is related to the surface energy, while the liquid encapsulation is related to the reaction kinetics of the polymerization. A balance between the two will lead to a liquid presence, the formation of polymer or a mixture

of the two. In chapter 2 aspects of surface energy and liquid nucleation were highlighted. In this chapter (*3.3.2.*), an increase in deposition time will allow studying non-invasive aspects of surface polymerization.

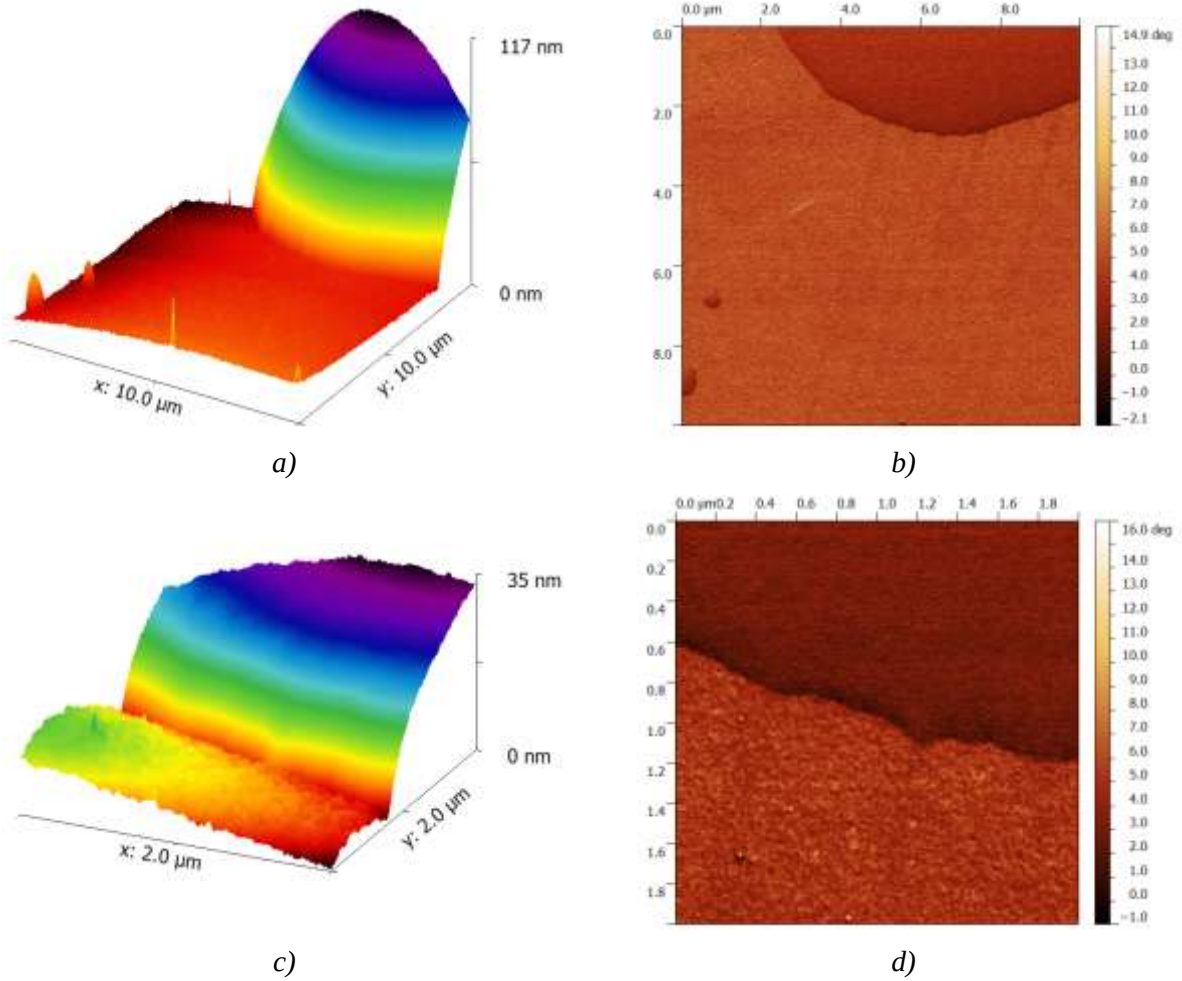

Figure 3.9: AFM topography a), c) and phase images b), d) of a film deposited on Si(100) substrate with an encapsulated blister

The phase images in *Figure 3.10* were made in acoustic mode with the same AFM cantilever over both of the substrates: Si(100) (*Figure 3.10 a, c, e*) and Si(111) (*Figure 3.10 b, d, f*).

The AFM topography indicates maximum heights from 7 nm for the flat area of the film on Si(100) (*Figure 3.10 a*) to about 200 nm for the blister-containing deposit (*Figure 3.10 b*).

The AFM phase image shows a uniform phase shift at around 0° for the film on Si(100) (*Figure 3.10 c*) and about 14° for the deposit onto Si(111) substrate (*Figure 3.10 d*). This accounts for the general change in color intensity of the two images. In order to have a clear observation of the phase shift, two linear profiles were chosen from the two phase images. For the film deposited on Si(111), a section of the phase response of a blister was selected (*Figure 3.10 f*). It can be observed that initially the signal drops to a minimum phase shift at 1° and has a constant plateau around 5° shift. For the rest of the sample, the average phase shift is observed at around 14° (*Figure 3.10 f* dotted line).

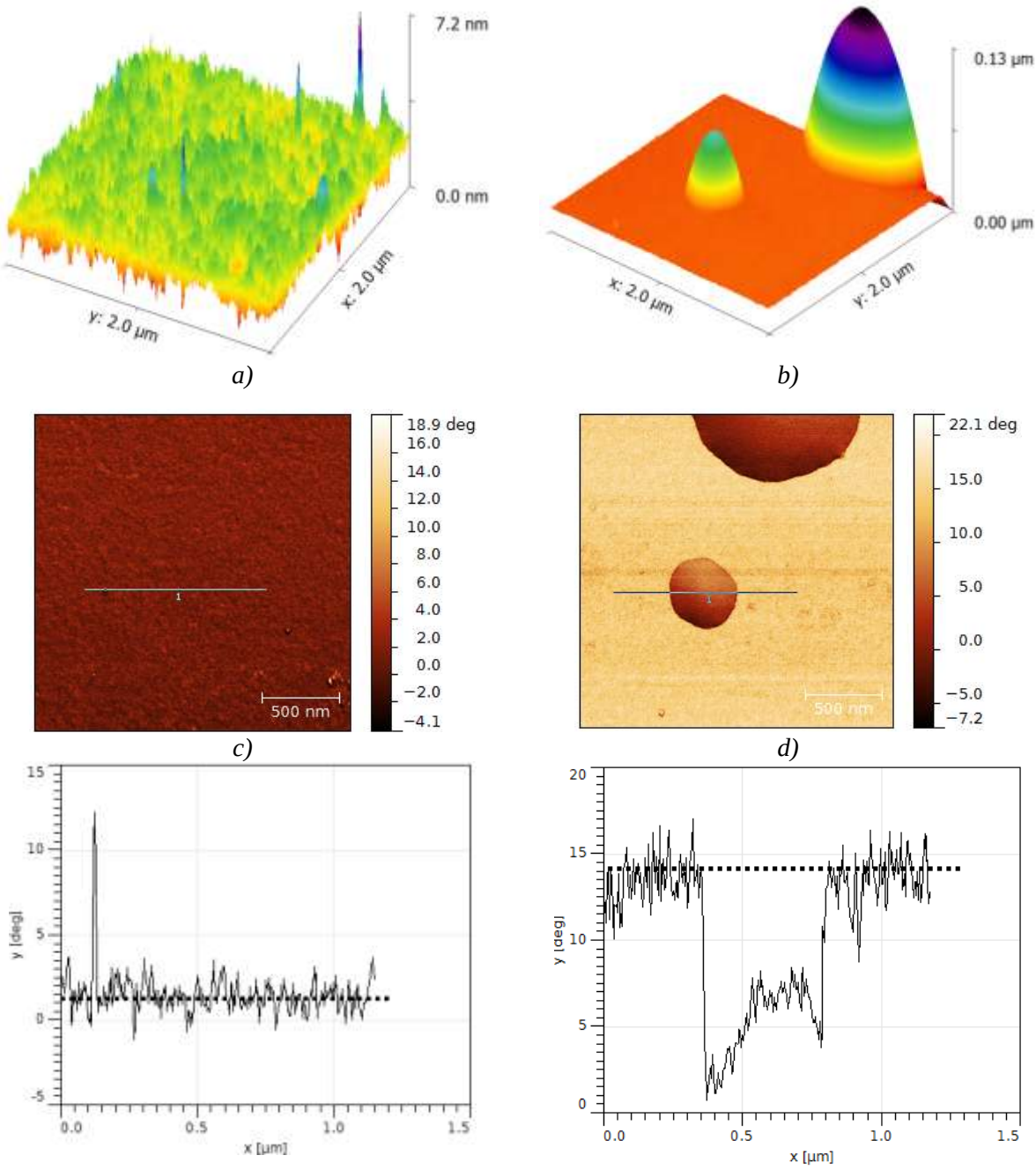

Figure 3.10: AFM 3D topography of the deposit over a) Si(100), b) Si(111), the AFM phase images for the same areas over the c) Si(100) d) Si(111) with the selected line profiles for e) Si(100) and f) Si(111)

The AFM cantilever interaction with the sample is described by the Van der Waals model. The phase shift of the AFM cantilever vibration can be an expression of relaxation in the intramolecular vibration modes of the analyzed sample. As this relaxation is more favored for liquids than for solids [11], the phase angle shift will increase from the liquid to the solid state. Thus, as observed in our experiments, the 1 to 5° phase shift can be associated to the liquid relaxation. The difference of 5° phase shift between the minimum and the maximum shift can be due to the AFM tip interaction with the blisters.

The film deposited on Si(100) shows a median phase shift at around 1° (*Figure 3.10 e*). This is an indication that the studied area presents a fluid phase below the deposited film. The heterogeneity presence increases the phase shift to around 13°. This heterogeneity is likely

covered by the same thin film, because the phase shift of 13° is close to the value of 14° determined for the thin film deposited on Si(111).

3.3. Aspects Related to the Increase in the PMMA Deposition Time

The objective of this experiment is to investigate the film grown in the same CVD conditions as before, but doubling the deposition time to 90 min of deposition. In this manner, the Photo-CVD parameters for this experiment (*Table 3.2*) are identical to the previous one (subchapter *3.2.*), except for the experiment duration t_{exp} = 90 min.

For these experiments the precursor contained 2 % HCPK photo-initiator dissolved in the monomer.

The substrate preparation protocol was identical with the one described in subchapter *3.2.* It involved a degreasing (mechanical cleaning of the substrates), ultrasonic cleaning and drying under Ar gas stream.

Table 3.2: The Photo-CVD experimental parameters;
the liquid precursor was MMA monomer with 2 % HCPK photonitiator

Gas flow8		Pressure		Temperature		DLI system			
						liquid		gas	
Q_{N2}	150 scc m	P_{N2}	3.5 bar	T_{inj}	60 °C	t_{on}	1 ms	f	1 Hz
		P_{cg}	2 bar	T_{uv}	80 °C	f	1 Hz	Setpoint	10%
		P_T	9.5 Torr	$T_{substrate}$	17 °C	t_{exp}		90 min	

The sample obtained in this run the presence of a relatively significant liquid quantity of liquid on the surface (*Figure 3.11*). The blister diameters reach up to 300 µm. A liquid accumulation near the glass sample can be due to eventual condensation of liquid, as the respective area was close to the cooling tubes.

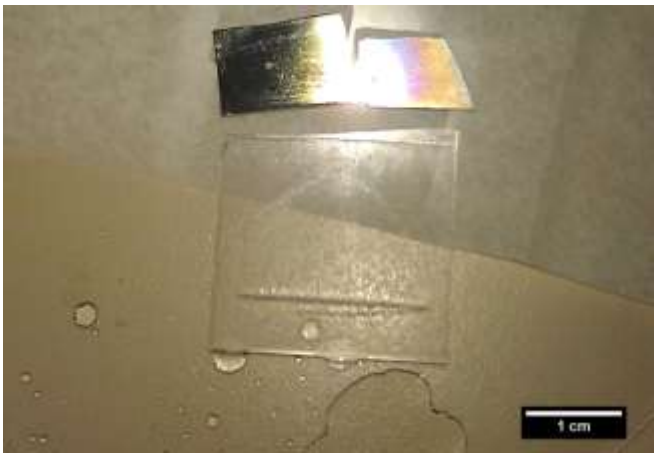

Figure 3.11: The samples obtained after the Photo-CVD deposition for 90 min

The further characterization of the films will be achieved mainly by a mix of spectroscopic and microscopic techniques that will offer complementary information over the same area of investigation.

8 Pulsed gas flow : 150 sccm / 1 Hz

3.3.1. Raman Spectroscopy – MMA Polymer Flammability

The previous Raman experiment (subchapter *3.2.2.*) indicated that during the Raman laser irradiation the photo-initiator species were preferentially depleted. The increase in the analysis time had a significant impact on the Raman characterization.

In *Figure 3.12* an obvious change in Raman spectrum of a blister was found (discussion of the bands will be made from left to right). The first significant change concerns the band at 1448 cm^{-1} that exhibits a medium intensity while it was significantly higher in the previous study (subchapter *3.2.2.*). This is mainly associated to the asymmetrical bending of the $O(CH_3)$ which is assumed to describe the *cis* orientation of the C=O and C-CH_3 bonds [12].

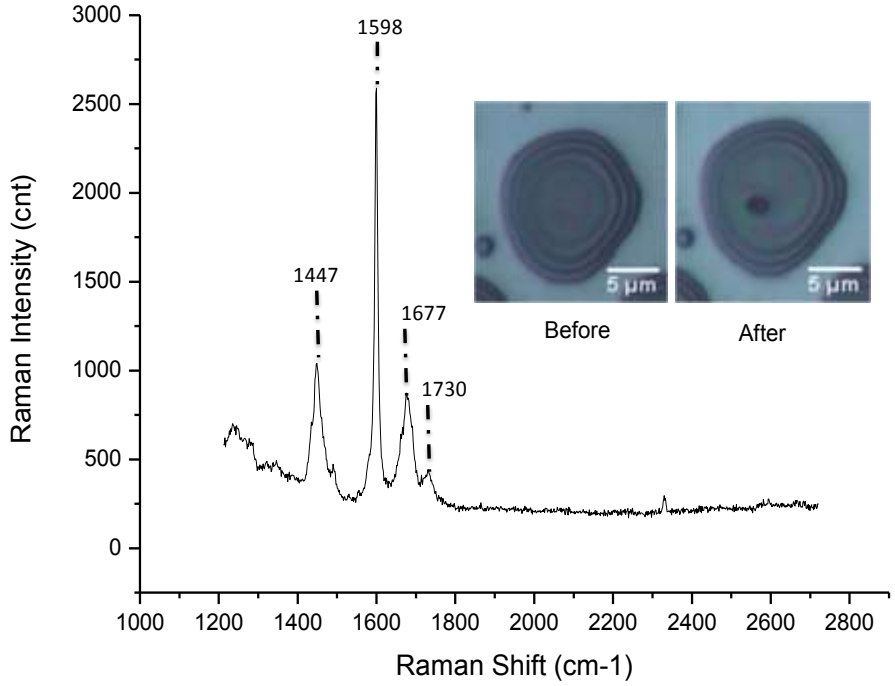

Figure 3.12: Raman spectra of the deposited sample over Si(111) substrate, with micrography of the region of interest before and after the analyze in the inset

Further, the 1600 cm^{-1} band of the C=C of the aromatic ring shifted slightly to 1598 cm^{-1} that will be discussed in the next subchapter. The Raman shift of the HCPK photo-initiator is characterized mainly by a high intensity and sharp band also around 1600 cm^{-1}. Another medium band is observed at 1677 cm^{-1}. With respect to previous studies, that band can be associated to the C=O vibration of the monomer MMA and polymer species. It had been deduced in previous characterization that the HCPK has a band at around 1690 cm^{-1} (see Chapter 2). Extrapolating the MMA association of the C=O band, we can deduce that the low intensity band observed at 1730 cm^{-1} in *Figure 3.12* can be associated to the (P)MMA species only. Although the previous post-treatment study did not highlighted a significant difference in the C=O stretching band around 1725 cm^{-1} range, this was partially supported by the analyses (see Chapter 2).

After the surface irradiation it can be observed that the sample was already altered as shown in the *Figure 3.12* inset before and after the 532 nm Raman laser exposure.

Further characterization was made by increasing the exposition time to the Raman laser radiation. The spectra are shown in *Figure 3.13 a*), with an arrow indicating the increasing exposure time. With respect to the $O(CH_3)$ group vibration, it is observed that the respective band gradually disappears after subsequent exposures to the laser radiation.

The thermal degradation of PMMA occurs over 200 °C with two main competing reactions: depolymerization or ester decomposition (see *Figure 3.14*) [13].

The diminishing Raman band confirms the decomposition process. Furthermore, the decrease in $O(CH_3)$ vibration at 1448 cm^{-1} is coupled with the increase in a broad band at around 1340 cm^{-1}, and is in agreement with the decomposition mechanism [13]. According to a reported study on the flammability of the PMMA, the 1340 cm^{-1} band represents the disordered structures left after the PMMA degradation, resulting from the alternating ring stretching vibration of the aromatic clusters [14]. Also, the fact that the 1597 cm^{-1} band losses its sharp maxima indicates a possible decomposition of the HCPK. The relative intensity of the bands at 1340 and 1597 cm^{-1} after the extended laser exposure is close to the one reported after the thermal degradation of a functionalized MMA polymer by cone calorimetry (technique used to study the fire behavior of small samples of various materials in condensed phase) [14]. This highlights not only the similarity in chemical composition but also regarding th degradation processes that lead to their formation.

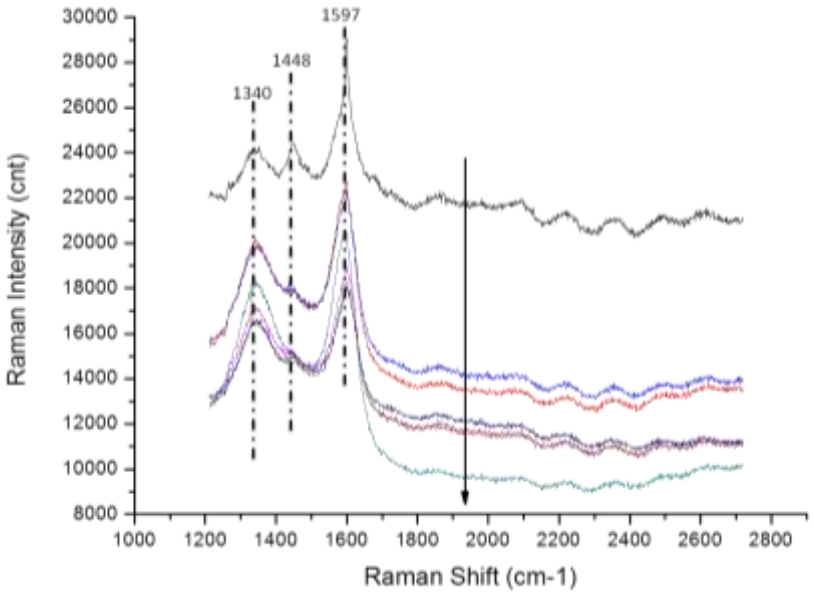

a)

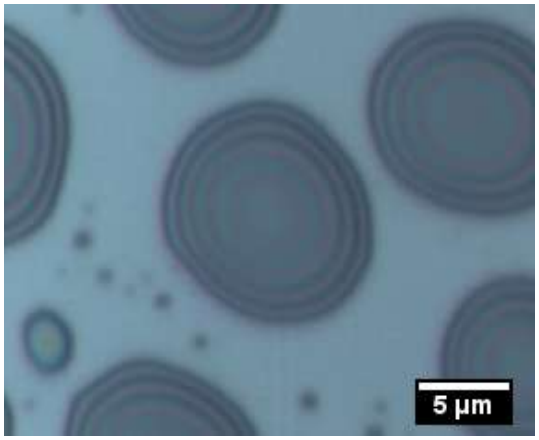

b)

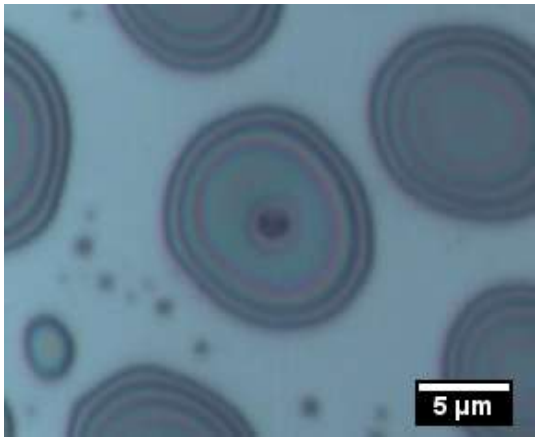

c)

Figure 3.13: Raman spectra of the deposited film over a Si(111) substrate after subsequent exposure times a) to the 532 nm Raman laser radiation and its effect over the studied blister before b) and after c) measurements

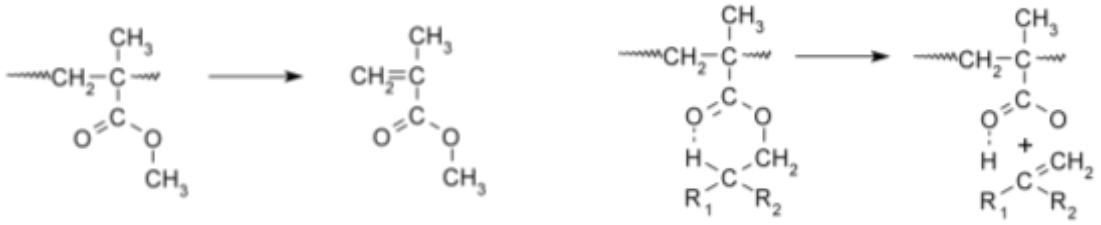

a) *b)*

Figure 3.14: Mechanism of PMMA depolymerization (a) and of the ester decomposition of PMMA (b) according to [13]

The destructive effect of the Raman laser prevents from obtaining relevant information with respect to the initial state of the deposited film. To observe the chemical composition without the invasive effect, FTIR spectroscopy will be used.

3.3.2. FTIR Spectroscopy – Noninvasive Insight

The Raman spectroscopy finds the source of information in the scattering of light by the vibrating groups or molecules. It provides insight onto the covalent character of the molecule. By comparison, the IR spectroscopy finds the source of information by the absorption of light by the vibrating molecules. In order for the vibration to be IR active, the vibration should involve a change in the dipole moment. As a consequence, the IR spectrum gives an indication of the ionic character in the molecule. Several chemical groups as C=O bonds that expresses both in Raman and FTIR spectroscopy. The FTIR technique has been used to investigate the film growth by Photo-CVD experiments with the upgraded G2.8 injector.

A FTIR comparison between the samples deposited for 45 min and the ones deposited for 90 min can be observed in the study detailed further. The 500 cm^{-1} and 1500 cm^{-1} range is also called the fingerprint region because each different compound produces specific bands. Some sharp peaks reveal the presence of the film.

The interpretation of the data of the *Figure 3.15* spectra regions will be treated in two directions: (*1*) about the conformal coverage of the PMMA film and (*2*) about the photo-initiator presence in the film.

3.3.2.1. PMMA Tacticity

Figure 3.15 b) confirms the specific vibrations of the PMMA backbone at 2990 and 2940 cm^{-1} [15] and also the in-plane symmetrical stretching of C-H at 2860 cm^{-1} [16].

To further investigate the tacticity of the PMMA thin film, a study into the fingerprint region of the spectrum will be undertaken. Tacticity (from the Greek 'taktikos': of or relating to arrangement or order) refers to the orientation of adjacent chiral centers. When it takes into consideration two adjacent structures in a polymer molecule that are identically oriented, the arrangement is called *diades* and is most commonly used terminology. The number of the considered adjacent structures can be higher, such as *triades* (three identically oriented structures) or *tetrads* (four identically oriented structures). The possible tacticities of the PMMA polymer are shown in *Figure 3.16*.

The tacticity was studied in literature by the IR spectroscopy following the specific IR peaks and their behavior with respect to the conformational cooperativity of the polymer backbone and side-chain [17]. In *Figure 3.15 a)* the fingerprint-region shows relevant vibrational peaks that will be further discussed based on the literature results [17,18].

The two key regions that offer information to the tacticity of the PMMA are between 1260 - 1275 cm and between 1150 - 1165 cm and are implicitly related to the conformational energy of the side-chain (as observed in *Figure 3.15*). The peak at 1240 cm-1 is associated mainly to the conformational energy of the backbone.

In the first key region, the 1260 cm^{-1} vibration correspond to the isotactic conformation of the polymer (i-PMMA) [17]. The 1275 cm^{-1} was due to the syndiotactic conformation (s-

PMMA) [17]. The change from the isotactic to syndiotactic conformations leads to both a wavenumber shift (from 1260 cm^{-1} to 1275 cm^{-1}) and on intensity (a 50 % decrease in absorbance from i-PMMA to s-PMMA) [17].

In the second key region, the 1153 cm^{-1} peak is observed to correspond to s-PMMA while the 1265 cm^{-1} peak responds to i-PMMA conformation. The intensity ratio of the two peaks has approximately the same value.

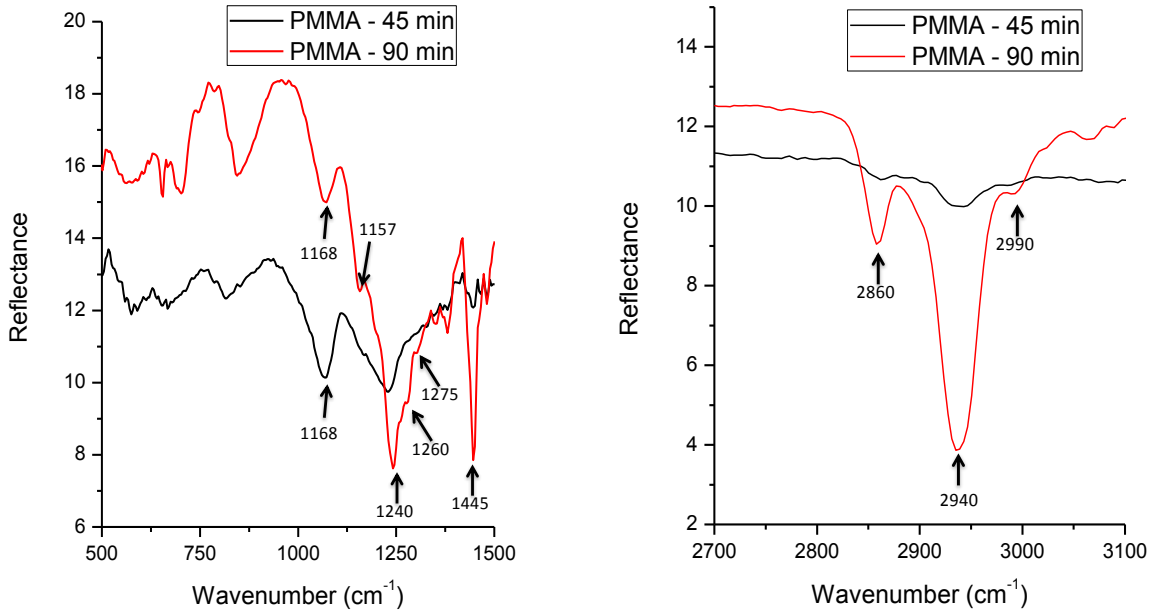

Figure 3.15: ATR-FTIR comparison of the samples deposited for 45 and 90 min a) in the fingerprint range, b) in the range of CH3/CH2 stretching range.

In the literature study [17], the IR resolution chosen was 2 cm^{-1}. For the measurements made on the film obtained by Photo-CVD, the FTIR resolution was set to 4 cm^{-1} (two times less resolute). This means that, in order to separate two neighboring peaks (say 1260 cm^{-1} and 1270 cm^{-1}) they should present a significant change in intensity, in order to have the clear separation in wavenumber (one low peak and a upper one). If the intensity is the same, the convoluted peak will present a peak at the middle of the two vibrational peaks. Since the conformational changes from i-PMMA to s-PMMA at 1260 cm^{-1} and 1275 cm^{-1} are reported to have also a significant change in intensity [17] they should be easily observed in the spectra for the Photo-CVD samples (mainly this deposited for 90 min): this is effectively the case (*Figure 3.15 a*). In literature the presence of i-PMMA and s-PMMA peaks with the same intensity is reported at 1150 cm^{-1} and 1165 cm^{-1} [17], Due to the decreased resolution, only an averaged peak centred at 1157 $cm^{-1}$is observed experimentally.

The overall conclusion in agreement with Y. Grohens *et al* observations [17] is that both of the i-PMMA and s-PMMA conformational states are present in the Photo-CVD thin films.

Stereotactic conformations (of two different tactic arrangements) were studied under the form of PMMA monolayers spread at the air-water interface [19]. Also, after a treatment that implies a thermal stretch due to an applied difference of temperature (for further information and implications, see expansion coefficient in Chapter 2) a double-stranded helical structure was obtained [20]. The two approaches are valuable in the understanding of the PMMA chain arrangement, which in these particular cases can be traced back to the orientation that occurs during the polymerization process.

The experiments reported in literature dealt with relatively isolated observations of each tactic states to study the FTIR response (one predominant tactic orientation was chosen). In

this manner a relative uniform arrangement of the side chains were achieved, which resulted in a common vibration specific to the tactic arrangement.

When we consider a mixture of two tactic arrangements, the polymer conformation with respect to the polymer backbone can be defined. However, the IR expresses the collective vibrations of the molecules. When we consider the side chain, it will lead to an IR response that will be an expression of the cumulative side chain interactions. This will not allow the tacticity separation of two conformations that are in the same film.

Based on the experimental results observed in *Figure 3.15 a)* the two tactic states seem to be clearly separated. This will imply the separate presence of two homogeneous tacticity conformations and not a mixture of the two.

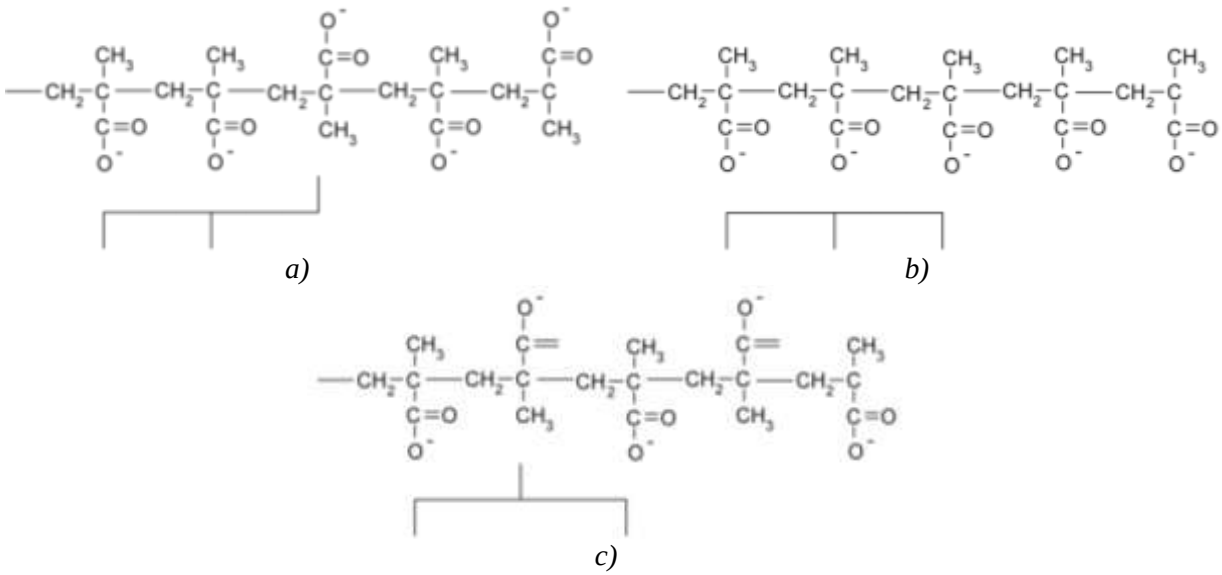

Figure 3.16: The tacticity of the MMA polymer: a) atactic, b) isotactic, c) syndiotactic

In a study on stereoregular PMMA obtained at air/water interface, W-P Shu et al. [21] reported that i-PMMA had a higher flexibility of the chain segments, while the s-PMMA formed a more condensed monolayer with lowered flexibility. Considering a dynamic fluid, the higher flexibility of i-PMMA suggests a better possibility for encapsulation of the fluidic liquid-phase MMA. **As a result the polymer membrane encapsulating the liquid droplets would have a preferred i-PMMA configuration.** On the other hand, to reach the minimum of energy during polymerization onto a solid surface, rearrangement over the surface can occur during polymerization. **The high cohesive interaction between the polymer chains of s-PMMA due to their symmetric arrangement** (see *Figure 3.16 c*) **makes this type of stereoregular conformation a good candidate for polymerization on solid surfaces**.

The different stereoregular arrangements of PMMA over the liquid and solid phases could explain the clear separation of the FTIR peaks for the two polymer tacticities. As it is possible to polymerize i-PMMA over liquid and s-PMMA over solid, the clear separation between the solid and liquid areas previously observed in the microscopy images explains the simultaneous contribution of them to the FTIR spectrum.

As the i-PMMA and s-PMMA orientations are separated by the polymerizing environment over liquid or solid that reaches to significant areas (as observed by previous AFM, Raman microscopy and SEM images), a clear separation of the isotactic and syndiotactic populations with their specific vibrations can be separately observed by FTIR.

By this approach, the possible PMMA conformations over liquid and solid are highlighted by their separation of the IR-sensitive vibrations, a separation that can occur if there is a homogeneous isolation of the isotactic and syndiotactic polymer. Such a

homogeneous isolation of the two arrangements describes aspects related to nucleation process [22] for the PMMA thin film.

The increase in ATR-FTIR signal after this set of experiments with the new G2.8 Kemstream DLI system (resulting from a higher deposition rate) allowed obtaining information into the PMMA tacticity. Also, as the deposition time increases a significant increase in FTIR signal is obtained due to the increasing thickness of the film.

3.3.2.2. HCPK Presence

In the previous chapter a Raman study was made by two post-treatments that helped to identify the contribution of the monomer and photo-initiator species focusing on a C=C bond common to the two. Although in monomer (and polymer) there are also the same C=O bond as for the HCPK photo-initiator, a separation in Raman bands allowed to extrapolate their contributions to the spectra.

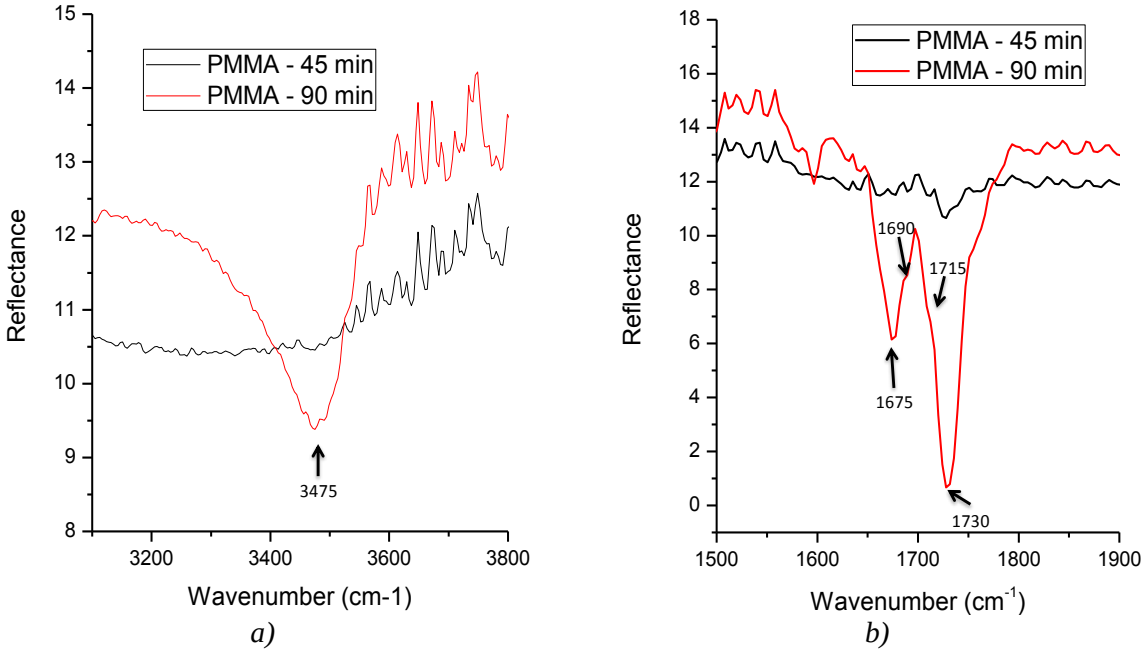

Figure 3.17: ATR-FTIR spectra of a) spectral region for the OH vibration and b) the C=O vibration range peaks

The increase of deposition time highlights a peak at 3475 cm^{-1} clearly observed only for the 90 min deposition time and not for 45 min deposition (*Figure 3.17 a*). The peak is associated to the hydroxyl groups [23–25]. The O-H bond is found in the HCPK photo-initiator and is not identified in the MMA species. As such OH bond is not thermally stable [25], its presence would not be detected in the Raman spectra.

Due to the lowered ratio of the photo-initiator dissolved in MMA (2 % HCPK) it is expected that the specific peaks of the photo-initiator absorbtion bands will be lower than those of MMA and PMMA. This is observed in *Figure 3.17 b)* by the presence of the low peaks at 1715 and 1690 cm^{-1} assigned to the C=O vibration of the photo-initiator (see subchapter *3.3.1.*). The higher intensity peaks observed at 1730 and 1675 cm^{-1} correspond to the (P)MMA species in good agreement to the previous Raman analysis (subchapter *3.3.1.*). Another indication of the photo-initiator presence is also given by the presence of the observed peak at 1445 cm^{-1} (*Figure 3.15 a*) [26].

As another noninvasive technique, the AFM spectroscopy will be further used to attest the presence of a thin polymeric film covering the blisters.

3.3.3. Atomic Force Characterization

Figure 3.18, *Figure 3.19* and *Figure 3.20* shows two sizes of AFM data that was obtained during the characterization of films on different substrates at two scales: one of 10 µm and other of 2 µm. These results are included in the microscopy category as they were obtained by scanning the scale at and below the microscopic scale. Another characterization mode of the AFM technique, namely the force spectroscopy, will be further presented.

3.3.3.1. AFM Microscopy Characterization

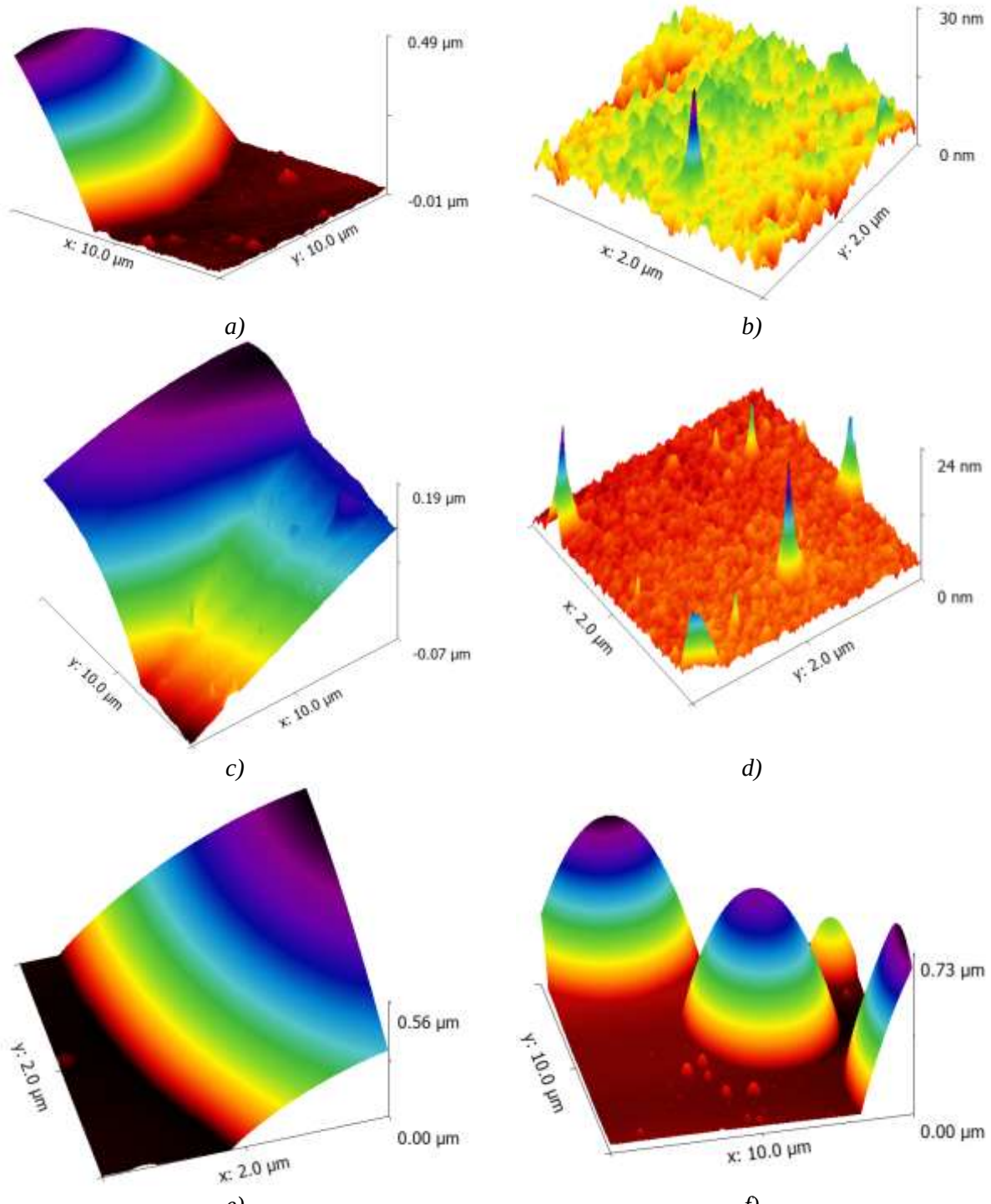

Figure 3.18: AFM 3D topography of the deposited film over a), b) glass, c), d) Si(100) and e), f) Si(111)

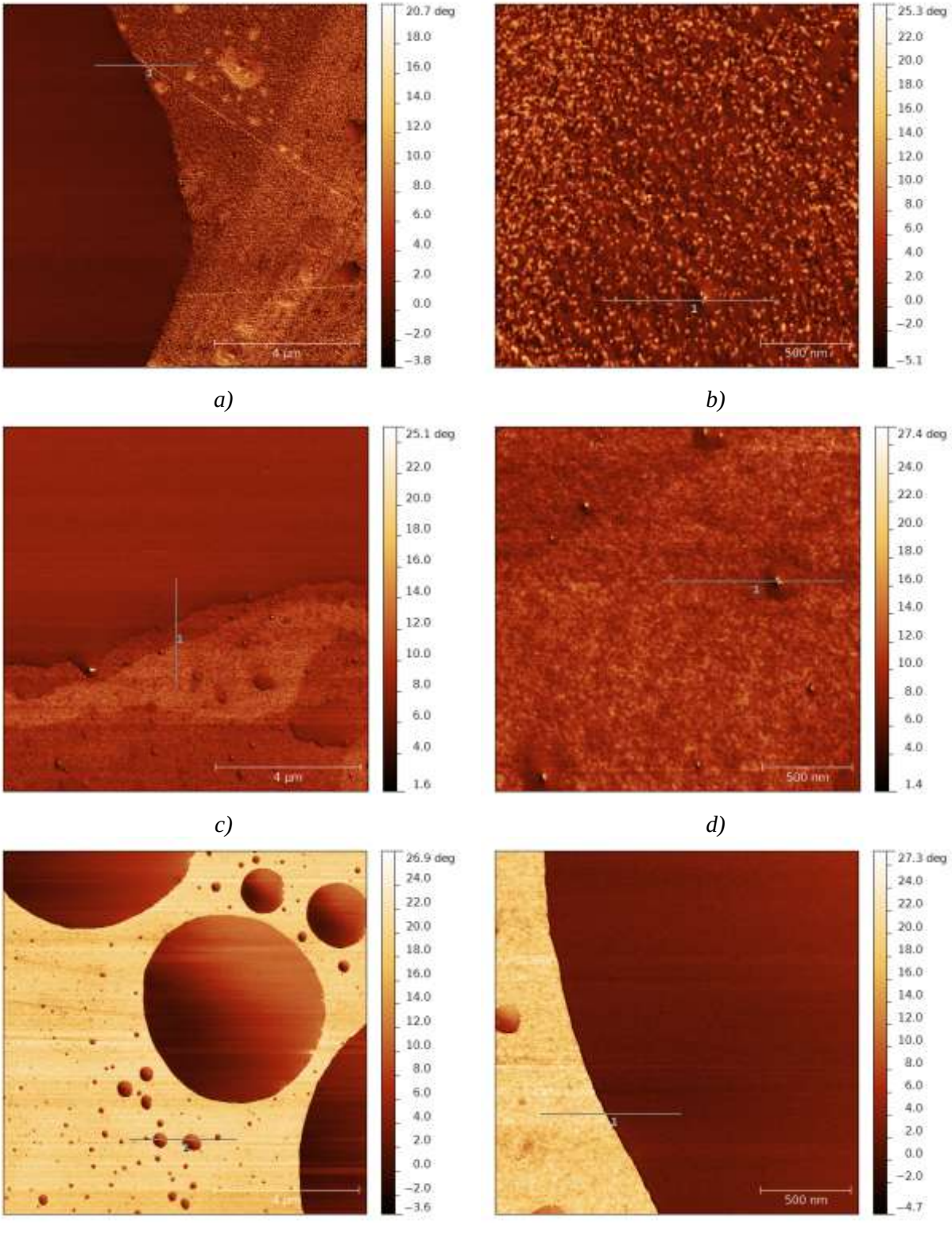

Figure 3.19: AFM 512x512 pixels phase image of the deposited film over a), b) glass, c), d) Si(100) and e), f) Si(111)

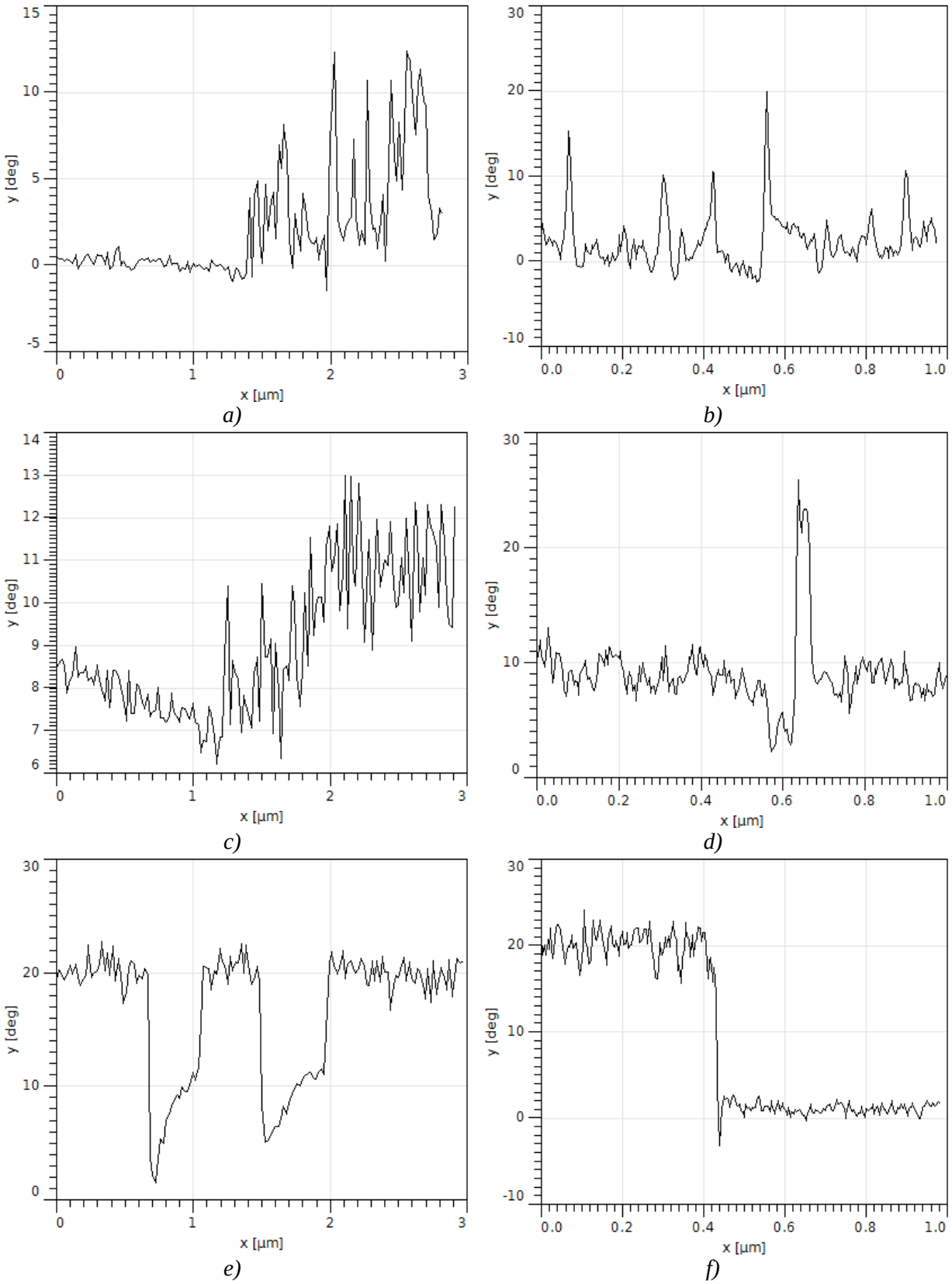

Figure 3.20: Linear profile of the AFM phase images of the deposited film over a), b) glass, c), d) Si(100) and e), f) Si(111) of the selected lines traced in Figure 3.19

Figure 3.18 shows the scanned topography of the samples deposited on different substrates. All of the images were corrected for an instrument-specific AFM slope, except for the image in *Figure 3.18 c)*. Heights that vary from tens of nanometers for flat surfaces to hundreds of nanometers for the blister structures can be observed.

The phase images that offer information from the phase shift of the vibrating AFM cantilever show roughly a behavior similar to the experiments achieved for the film deposited in 45 min. The topography images that was used to identify the drop-like structures and the flat surfaces are shown *Figure 3.18.* From the phase profiles (*Figure 3.19)*, line profiles representative for the drop-like structures (which contain liquid) and thin film (from the flat surfaces) were selected. These profiles are represented in *Figure 3.20.*

The spatial resolution (pixels/nanometers) and the scan speed are important parameters that reflect in the phase image. As the scan speed is increased (or resolution decreased), the relaxation in the AFM cantilever may not occur as it spends less time on the investigated region. This will lead to an increase in the phase shift for an area with the same relevant properties. The measurements at each order of magnitude had the same resolution and scan speed.

Under the suspected presence of the liquid (the blister site in the topography image *Figure 3.18*), the phase shift descends to around 1° (*Figure 3.19*). Although in some cases the phase shift shows negative values, these values can be associated to the first interaction of the tip with the ascending change in height of the topography. With the areas where the thin film is supposed to be deposited (flat surface area), the line profile shows roughly two phase shift maximums: 10° and 20°. Interestingly, their average value is at 15 °, the same as for the obtained deposit grown in 45 min under the same conditions (see *3.2.3.*).

Since the AFM cantilever vibration is sensitive to the intramolecular vibrational relaxation of the matter it interacts differently depending on the material: a relaxation is achieved more easy for liquid than for solid. This suggests that for the phase shift around 1° (including the observable 0° phase shift) the interaction occurs with a liquid and not with a solid polymeric thin film.

The thin film presence that encapsulates the liquid phase will be further highlighted by the AFM force spectroscopy.

3.3.3.2. AFM - Force Spectroscopy

AFM Force Spectroscopy is the technique where the interaction force of the AFM tip with the sample is measured. Theoretical bases will be further presented with respect to the AFM mode used for the Force Spectroscopy measurements and the values that were observed.

3.3.3.2.1. Fundamental Insight

The AFM Spectroscopy involves an approach-retract cycle of the AFM tip with the sample. The schematic diagram of the Force Spectroscopy cycle is presented in *Figure 3.21*.

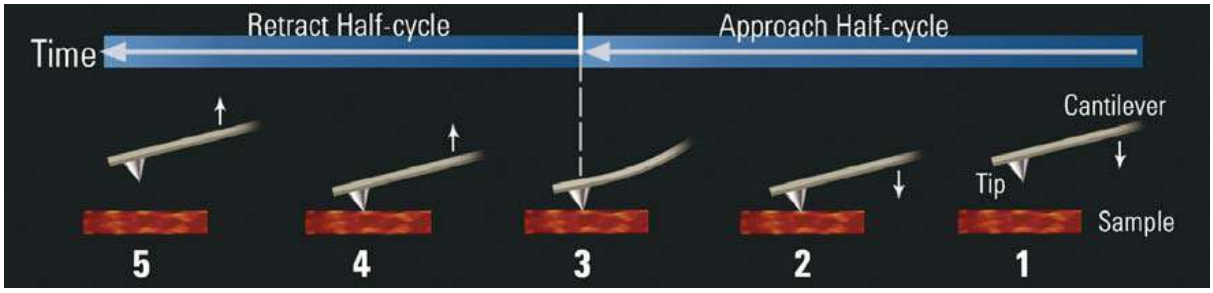

Figure 3.21: The approach and retract halph cycles of the AFM cantilever in the AFM spectrosocpy measurement

The information obtained by the AFM Force Spectroscopy comes from the Van der Waals interaction forces between the sample and the AFM cantilever. As observed in *Figure 3.21*, the AFM cantilever bends when the cantilever tip interacts with the sample. As the cantilever interacts with the sample, a displacement occurs. The distance of displacement (x) is measured by the AFM system.

If the spring constant of the AFM cantilever (κ) is known, the force of interaction can be found by using the Hooks Law:

$$F = \kappa x \qquad (3.5)$$

The displacement is determined by a position-sensitive split photodiode detector in volts (V_P) and is multiplied by a factor called deflection sensitivity (δ) that converts the diode response to distance (x in nanometers). Considering these, the displacement for the AFM cantilever is expressed as:

$$x = \delta V_P \qquad (3.6)$$

The deflection sensitivity (α_d) is determined by a curve of force as a function of distance:

$$\delta = \frac{F}{\kappa V_P} \qquad (3.7)$$

The three parameters, κ, δ and V_P and the additional value of time (t) (either continuous or discrete as frequency) are the basic quantities measured in AFM spectroscopy.

There are two types of AFM cantilevers: rectangular Non-Contact (used for these measurements) and triangular Contact Mode (*Figure 3.22*). Considering the values of the rectangular cantilever for length (l), width (w), mass density (ρ), fundamental resonance frequency (υ_0) and Young modulus of elasticity (E), the cantilever spring constant (or bending stiffness constant), is given by [27]:

$$\kappa = 2\pi^3 l^3 w \sqrt{\frac{\rho^3}{E}} \upsilon_0^3 \qquad (3.8)$$

For the triangular Contact Mode cantilever the spring-constant is estimated by the manufacturer. Agilent also offers the possibility of a 'Thermal Tune' method by considering the time-domain of the cantilever thermal noise response, computes the time-domain of the frequency spectrum for the cantilever and extracts the resonant frequency (f_o) from a fit.

a) *b)*

Figure 3.22: Schematic diagram of a) rectangular Non-Contact Mode cantilever and b) triangular Contact Mode cantilever

In the case of a rectangular cantilever, and the determined AFM quantities (V, δ and υ_0) the tip/sample force is given by:

$$F = 2\pi^3 l^3 w \sqrt{\frac{\rho^3}{E}} \upsilon_0^3 \delta V_P \qquad (3.9)$$

3.3.3.2.2. Experimental Results

The AFM force spectroscopy is a useful tool to prove the uniform covering of a thin polymeric film over both solid and liquid surfaces. The three force spectroscopy points (*Figure 3.23 a*) were chosen in regions that indicated the presence of (*1*) a solid film (observed at around 15° phase shift), (*2*) an heterogeneity (identified by an AFM comparison with the bare glass substrate) and (*3*) over a blister (observed with a phase shift around 0° in subchapter *3.3.3.1.*).

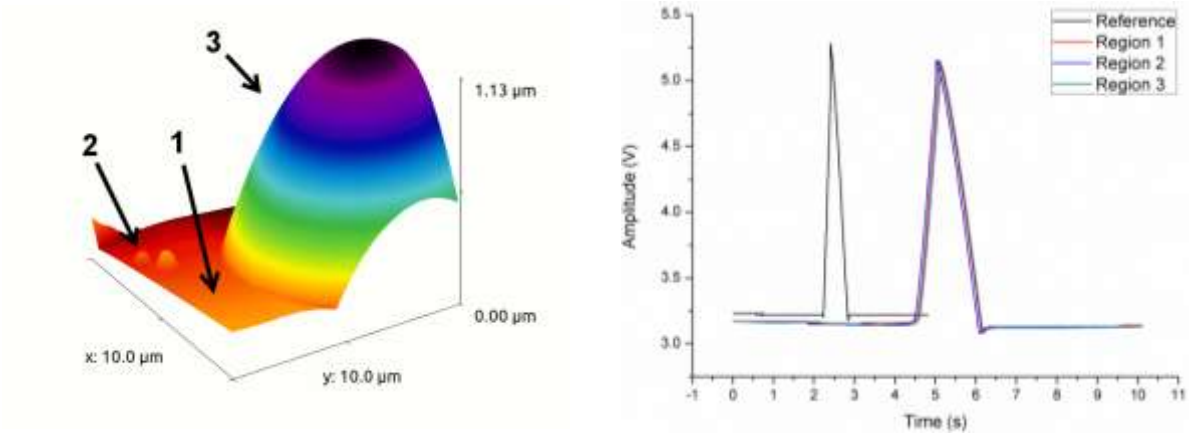

a) *b)*

Figure 3.23: The 3D topography over Si(111) substrate with a) the marked areas where b) the force spectrometry was made

For the bare substrate (namely the reference), the approach-retract cycle lasted around 0.55 s while for the entire deposited region the cycles time increased to 1.6 s. The different cycle times for the coated samples indicate a uniform covering, as the same approach-retract duration is observed. The approach-retract cycles are identical for the heterogeneity, drop-like structure and the flat surface, indicating the uniform covering with a thin film.

The encapsulation of the liquid is in this manner directly highlighted. Further, the presence of this liquid phase of the monomer after the Photo-CVD deposition will be treated from a theoretical point of view.

3.4. Theoretical Evaporation Rate

Different techniques are used to transfer a liquid phase into a vapor phase. This process can be roughly described as ‘atomization’ or ‘vaporization’. The term does not necessarily describe a direct phase change from liquid to gas, but also an intermediary step where the liquid is reduced to a fine spray of microscopic droplets, which can appear as mist, fog or clouds. This intermediary state facilitates the gas phase transformation from liquid to solid.

The human eye can detect particles of over 40 - 50 µm in diameter [28]. With respect to this limit, natural occurring mist droplets can be observed as their diameter ranges from 70 to 350 µm [29]. The burning wood however, releases particles in the smoke of around 0.2 – 3 µm in diameter that are not observable with the naked eye [29].

By artificial techniques, small liquid droplets that facilitate the phase change from liquid to gas are also obtained. In this manner the ordinary sprinkler sprays liquid particles with an average diameter between 1300 - 200 µm [30], mist-blower sprays droplets that can reaches around 150 µm [31] and by enhancing the spraying with electrostatic charging, the averaged diameter particles dimensions are decreased to around 20 – 35 µm [32]. However, a highly

efficient vaporization system is readily found in the aerosol packages such as flying insect killers and aerosol air freshener products which produce particles with less than 25 μm in diameter [33].

The atomization technique is based on the same principle: the liquid is pushed by a motive pressure (P_M) that is lower than the chamber pressure (P_C). Here the chamber pressure can be the ambient pressure, the DLI mixing chamber (see *Figure 3.1*) or the CVD sample chamber.

The higher the difference between the two pressures, the higher is the spray velocity and liquid flow which leads to lower droplet sizes [34,35]. At low P_M the Kemstream DLI G2.8 system produces particles with average diameters between 5 to 40 μm (maximum population at around 10 μm) compared to the classical injectors form other providers that produce particle diameters in 100 – 300 μm range. The question is raised with respect to the required vaporization time in order to obtain a vapor phase from the liquid droplets before they arrive at the substrate level (sample chamber).

Estimation with respect to the evaporation rate is offered by the *Langmuir evaporation method*. It essentially approximates the evaporation rate of the liquid at a planar interface (such as a hot cup of tea). The approach takes into consideration the environment temperature (T), the vapor pressure of the liquid (P_V), the pressure of the environment (such as P_C), the molecular weight of the liquid (M) and the universal constant of the gases (R). Considering the mass (m), then the mass loss rate (m / t) per unit area (A) is thus described as [36]:

$$\frac{m}{At} = (P_V - P_C)\sqrt{\frac{M}{2\pi RT}} \qquad (3.10)$$

In the case of the liquid droplet, we have to take into consideration that the evaporation does not occur on a planar interface, but on the entire interface of the droplet. In order to treat these conditions, we need to consider the relationship between mass (m), volume (V) and density (ρ):

$$m = \rho V \qquad (3.11)$$

Thus:

$$\frac{m}{At} = \frac{\rho V}{tA} \qquad (3.12)$$

If we consider the droplet is a sphere with the radius r, then the area (A) and volume (V) are defined as:

$$A = 4\pi r^2 \qquad (3.13)$$

$$V = \frac{4}{3}\pi r^3 \qquad (3.14)$$

The droplet decrease in volume is directly proportional to its surface area:

$$\frac{V}{A} = \frac{r}{3} \qquad (3.15)$$

Replacing the volume/area ratio in equation *(3.15)* to equation *(3.12)* and equalizing it with the evaporation rate in equation *(3.10)* it results that:

$$\frac{\rho r}{3t} = (P_V - P_C)\sqrt{\frac{M}{2\pi RT}} \qquad (3.16)$$

Since in case of the spherical liquid droplet the focus is on the evaporation time as a function of particle radius, *(3.16)* can be rewritten as:

$$t = \frac{\rho r}{3(P_V - P_C)}\sqrt{\frac{2\pi RT}{M}} \qquad (3.17)$$

With respect to the evaporation rate as function of pressure, two parameters are relevant: P_V and P_C. Equation *(3.17*) shows that the higher the vapor pressure of the liquid (P_V) and the lower chamber pressure (P_C) the lower the evaporation time. Considering a droplet of 50 µm (10 µm larger than the highest size reported by the supplier of the DLI G2.8 system), the theoretical influence of pressure and temperature on the evaporation rate on MMA droplets is shown in *Figure 3.24*. The vapor pressure of the MMA monomer was considered of P_V = 3906 Pa at T = 20 °C [37].

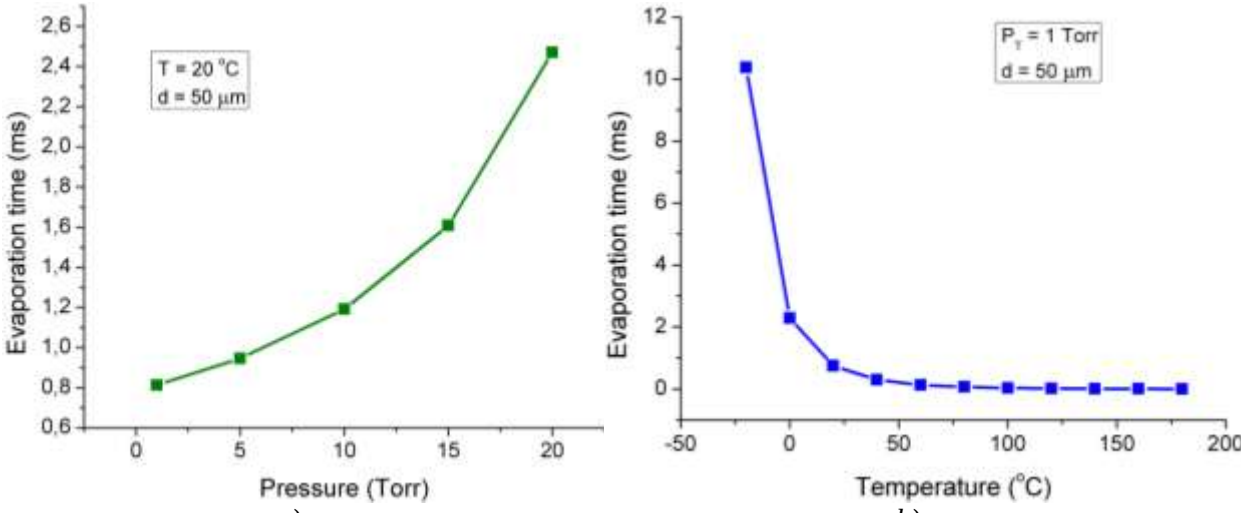

a) *b)*

Figure 3.24: Theoretical evaporation rate of a liquid droplet of MMA with diamater of d = 50 µm a) as function of pressure at constant temperature (T = 20 °C) and b) as function of temperature at constant pressure (P_T = 1 Torr)

If temperature (T) is not constant, the vapor pressure (P_V) changes. Defining ΔH_{vap} as the molar heat of vaporization for a liquid, the Claussius-Clapeyron equation can describe the relationship between P_V and T [38]:

$$\ln\left(\frac{P_2}{P_1}\right) = \frac{\Delta H_{vap}}{R}\left(\frac{1}{T_1} - \frac{1}{T_5}\right) \qquad (3.18)$$

Considering for MMA the value of heat vaporization ΔH_{vap} = 36 kJ/mol at room pressure and 100.5 °C [39], the evaporation time as a function of temperature is shown in *Figure 3.24 b)*. Notably, ΔH_{vap} also varies slightly with temperature. However, considering the above value, the calculated vapor pressure of P_V = 4205 Pa at T = 20 °C is in good agreement with the literature value experimentally determined [37].

From *Figure 3.24 b)* it can be observed that close to 0 °C the time of evaporation increases drastically. If for a 50 µm MMA droplet it takes 2.3 ms to be completely evaporated at T = 0 °C, the evaporation time can reach to over 1 min at a temperature of T = – 35.5(2) °C. At temperatures below that value, the vapor pressure (P_V) will reach a value below P_C = 1 Torr.

Furthermore, the higher the difference between the chamber pressure P_C and the motive pressure P_M, the higher is the spray velocity and liquid flow which leads to lower droplet sizes [34,35]. Since the ambient pressure P_C is considered the Photo-CVD sample chamber pressure, or P_T, then the lower that pressure is, the better the vapor phase, as is favoring the decrease in the droplet size but also the decrease in vaporization time. In the next experiment, the pressure is lowered to 1 Torr in order to decrease the evaporation time of the monomer droplets and improve the vaporization.

3.5. Optimizing Droplet Vaporization Time

As presented in the previous section, the lower the CVD pressure, the higher the evaporation rate of the liquid droplets. In the same way, the more the pressure is lowered in the CVD reactor the more the droplet diameter is decreased.

For the G1.5 injector and using the liquid MMA monomer, with the CVD parameters of P_{N2} = 2.8 bar, P_T = 5.6 Torr, continuous flux of Q_{N2} = 250 sccm and with the injector parameters of f = 1 Hz and t_{on} = 1 ms, the calculated dwelling time of the droplet in the CVD reactor is 1.2 s [40]. This is enough to evaporate droplets of significant size.

With respect to above conditions which are related to the vapor phase quality, limit values had been taken into consideration with respect to the DLI Photo-CVD parameters of liquid flow rate and total pressure.

Firstly, the P_T of the system was left at the minimum, with the butterfly valve open at 100 %. With the DLI injection in the conditions given in *Table 3.3*, the P_T reached a vacuum limit of 10^{-3} before the injection and about 1 Torr during injection. In this manner, the evaporation rate is maximized and the droplet size is minimized.

To enhance the vaporization of the liquid, the injector was set to pulse liquid once for 4 s (0.25 Hz). In order to prevent the condensation of the monomer, the pulsed gas flow was not set to a frequency lower than 1 s (1 Hz).

Table 3.3: The Photo-CVD experimental parameters;
the liquid precursor was MMA monomer with 2 % HCPK photonitiator

Gas flow[9]		Pressure		Temperature		DLI system			
						liquid		gas	
Q_{N2}	150 sccm	P_{N2}	3.5 bar	$T_{below\ inj}$	60 °C	t_{on}	1 ms	f	1 Hz
		P_{cg}	2 bar	T_{UV+hj}	80 °C	f	0.25 Hz	Setpoint	10%
		P_T	1 Torr	$T_{substrate}$	17 °C	t_{exp}		570 min	

To inject a total quantity of monomer comparable with the previous experiments, the deposition time was extended to t_{exp} = 570 min.

After the CVD experiment under the above conditions selected to improve te vaporzation of the liquid monomer, liquid droplets were still observed on the samples. As a result, one conclusion that can be drawn is that the liquid condenses at the substrate level. Also, according to the above calculation it can be considered that the droplets do not drop directly from the injector without being vaporized. Furthermore, condensation is possible because the difference in temperature between the UV activation zone and the substrates was $T_{UV+hj} - T_{substrate}$ = 63 °C.

The further characterization of the film will offer insight into the film properties and will treat some aspects relating to the film composition.

3.5.1. AFM Characterization

As a base of reference, in *Figure 3.25 a)* and *b)* the bare glass substrate is shown. Heterogeneities with heights of up to 13 µm are observed. The covering over the same substrate can be observed as the topography changes (height increases to around 45 µm).

Also the phase image does not highlight the same granulation for the deposited film compared to the bare substrate (*Figure 3.25 b* and *d*). Selecting two line profiles for the bare and deposited glass (shown in *Figure 3.26 a* and *b*) it can be observed that the phase shift values are relatively close. The bare glass substrate has a median phase shift of -4°, while the deposited one shows a phase shift around -1°. Also, the bare glass shows that the

[9] *Pulsed gas flow : 150 sccm / 1 Hz*

heterogeneities respond in phase with a positive angle: 5° for the heterogeneity selected from *Figure 3.25 d)* and shown in *Figure 3.26 a*).

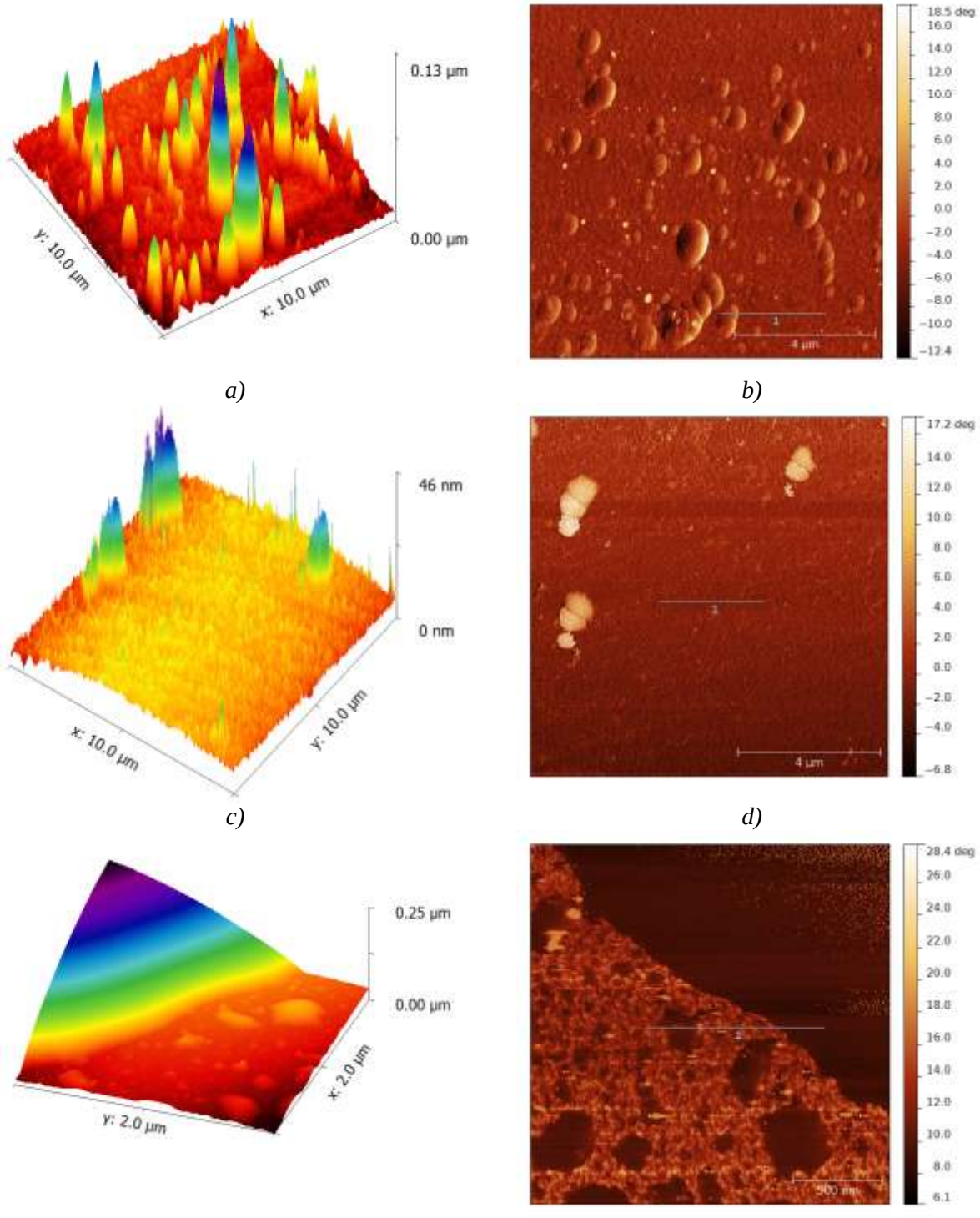

Figure 3.25: AFM 3D topography of a) bare glass, film deposited on c) glass and e) Si(100) with the corresponding phase images for a) bare glass, film deposited on c) glass and e) Si(100); the line profiles marked with 1 are in Figure 3.26

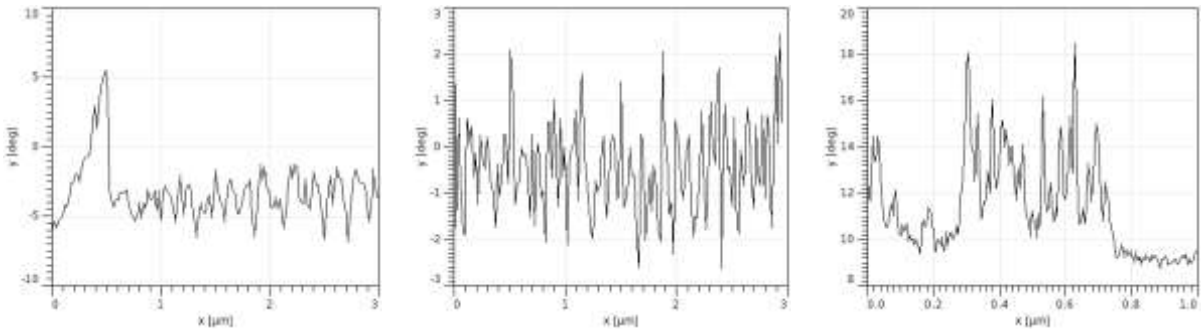

a) *b)* *c)*

Figure 3.26: Line profiles from the images in Figure 3.25 for a) bare glass, b) deposited glass and c) deposited Si(100) substrate

For the Si(100) substrate drop-like structures that start from 1 µm in diameter can be observed (*Figure 3.25 e, f*). Also, the previously reported phase shift medians of 10 and 15 ° for the PMMA deposited Si(100) substrates (subchapter *3.3.3.1.*) can also be found in the line profile of the phase shift for the film deposited in this experimental run for 570 min (*Figure 3.26 c*).

3.5.2. Raman Characterization – Physical Approach

This subchapter brings forth a discussion with respect to the physical parameters involved during the laser irradiation experiments. This discussion will be based on Raman results and will be continued with respect to the physical processes that are involved.

3.5.2.1. Raman Characterization

In the Raman spectra of *Figure 3.27* two high intensity bands are observed at 1091 and 1000 cm^{-1}. They are associated to the Si-O stretching mode of the glass substrate [41,42]. The glass signal is also responsible for the broad plateau that is observed starting from 2300 cm^{-1} (see chapter 2 for the detailed spectra of the glass).

The previous Raman studies (subchapters *3.2.2.* and *3.3.1.*) highlighted a set of bands that are fingerprints of the MMA monomer and HCPK photo-initiator: at 1450 cm^{-1} for CH_3 asymmetric deformation of MMA monomer, and around 1600 cm^{-1} for the aromatic ring of the photo-initiator [3–6]. Also, the laser effect over the (P)MMA deposit was reported in literature at 1340 cm^{-1} that was associated to the carbon residues left after a flammability study on PMMA by a cone calorimeter experiment [14]. A chemical reaction of PMMA degradation (subchapter *3.3.1.*) explains the decrease in the band at 1450 cm^{-1} for CH_3 asymmetric deformation and the increase of the 1340 cm^{-1} band of the aromatic clusters left after chemical degradation of MMA.

In *Figure 3.27 b), c)* and *Figure 3.28 b)* are presented the optical microscopy images of the *in-situ* Raman analysis where the spectra were recorded. In the spectra of *Figure 3.27 c)*, a destructive effect is observed by a crater-like geometry for maximum magnification (x100). *Figure 3.28 b)* shows a lowered magnification(x10) used to focus the laser onto the sample. Although in the optical microscopy image the film degradation is slightly present (an heterogeneity has been formed), but not obvious, the Raman spectra (*Figure 3.28 a*) shows the presence of the 1340 cm^{-1} band that confirms the destructive effect over the deposited (P)MMA. Interestingly, although in optical microscopy images of the investigated area of *Figure 3.27 b), c)* before and after the irradiation, the 1340 cm^{-1} band is very weak, whereas the MMA 1450 cm^{-1} bans is significant.

To explain the observed aspects, a discussion will be made with respect to the physical properties of MMA and the phenomena of laser interaction with the matter.

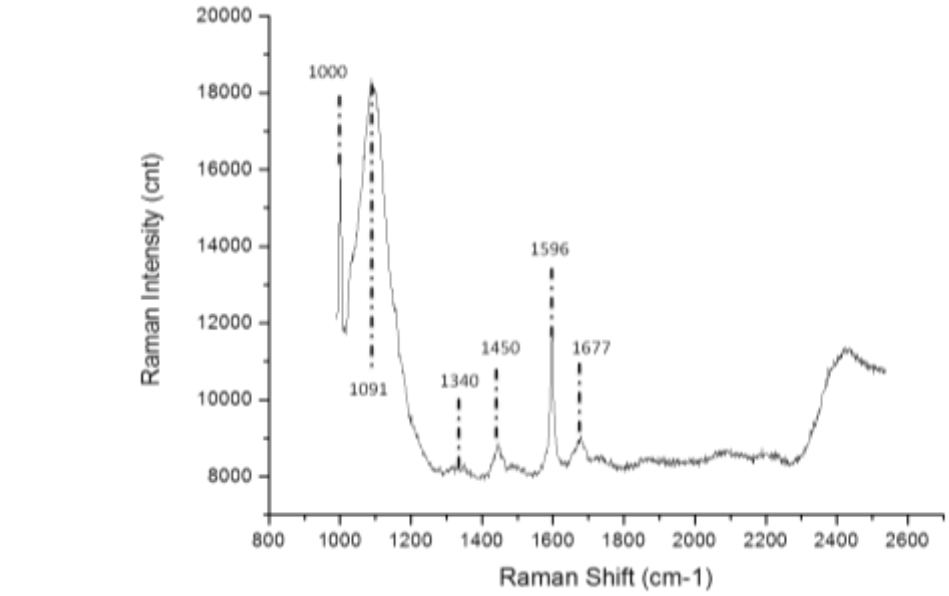

a)

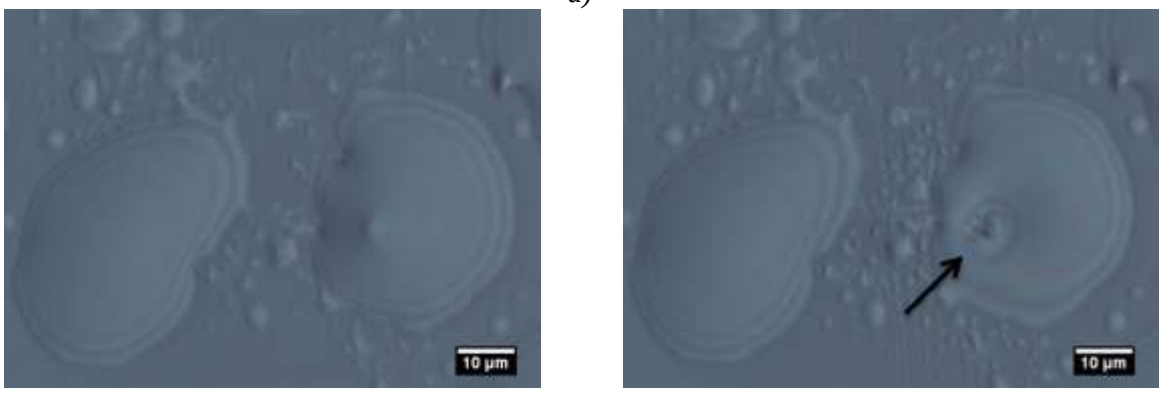

b) *c)*

Figure 3.27: The evolution of a) the Raman spectra of the deposition over the glass substrate with the in-situ region of interest b) before and c) after the measurement (the arrow points to the crater-like morphology with an heterogeneity at the center)

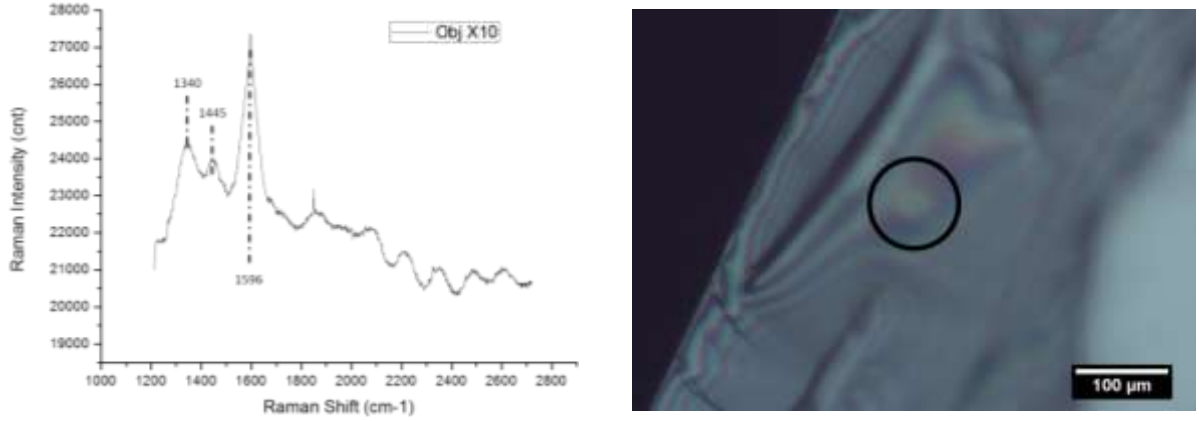

a) *b)*

Figure 3.28: The a) Raman spectra acquired over Si(100) substrate withb) the x10 objective microscopy image after acquisition (the circled area indicate the spectra acquisition region)

3.5.2.2. Physical Approach

The MMA monomer has a boiling point at 100 °C. If the MMA monomer is constrained into a solid network of PMMA, a temperature of 115 °C will lead to further polymerization [43]. At the temperature of 230 °C the polymer depolymerizes into MMA [44]. At higher

temperatures the PMMA undergoes a degradation process [45]. The degraded MMA at spontaneously ignites at 435 °C (auto-ignition), while in the polymeric form, PMMA auto-ignites at 580 °C. These aspects can be seen in *Figure 3.29*.

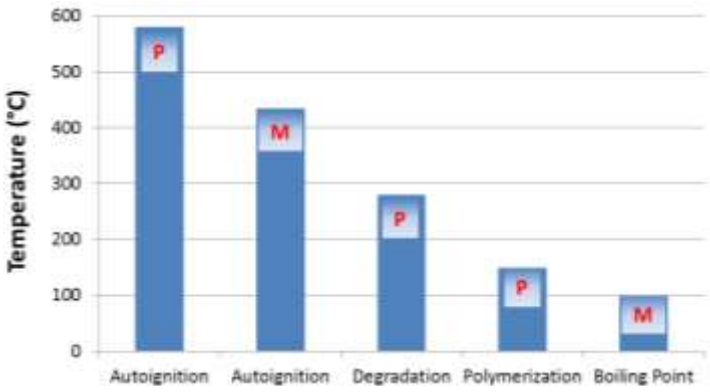

Figure 3.29: transformation phenomena of the methyl metacrylate monomer (M) and polymer (P) at different temperatures in atmospheric pressure conditions in air

The laser interaction with the matter is described by three steps [46]: (*i*) laser energy absorption at the thin film interface with the substrate leading to a sudden and local temperature increase; (*ii*) thermal strain and possibly melting (such as depolymerization of PMMA [44] in liquid monomer) (*iii*) disintegration by auto-ignition.

Studies on the thermal effects of Raman laser were studied on carbon nanotubes and on magnetite oxidation [47,48]. Also, with respect to PMMA, laser welding was also reported [49].

The laser heating has a Gaussian profile with a maximum of the temperature to the center and a minimum at the extremities [46]. The maximum temperature can be approximated based on literature data.

N. Shebanova et al [47] used variable power Raman laser in range of 7–60 mW on an area of around 7 μm in diameter. The Raman laser used for these experiments has a nominal power of 5 mW and emits at the wavelength of λ = 532 nm. The spot size can be experimentally calculated if the objectives numeric opening (*NO*) is known after the formula:

$$d = \frac{1.22\lambda}{NO} \qquad (3.19)$$

For the x100 objective d = 430 nm (used for *Figure 3.27* spectra). We can estimate that for our conditions, the power/surface area is 10 times higher, with a rough equivalent of 50 mW for the laser power. For that equivalent laser power N. Shebanova et al reported a laser temperature of 380 °C using thermodynamic Gruneisen parameter method and 480 °C by quasi-harmonic approximation using the high-pressure phonon shift. The 480 °C estimated value is in the auto-ignition range of the monomer and confirms the result that suggests flammability of the film (subchapter *3.3.1.*).

In subchapter *3.3.1.* , for the optical microscope images in *Figure 3.12* and *Figure 3.13 c)*, the crater-like region after the exposure presents a darker color (almost black) and has diameters slightly over 1.5 μm. The dark color can be associated to aromatic clusters remained after the (P)MMA degradation.

For the 570 min experiment, when focusing the Raman laser on a spot size of 0.43 μm (x100 objective) on the liquid blister with an encapsulated heterogeneity, a surface with the diameter over 5 μm is exposed. After the surface exposure, the heterogeneity is also observed. The 5 μm in diameter of the crater-like geometry that suffered the catastrophic damage is roughly 10 times higher than the spot size. Using an x10 objective with the spot diameter of 2.5 μm the film suffered degradation (1340 cm^{-1} band in *Figure 3.28 a* spectra) leaving a fingerprint on the exposed area of about 25 μm in diameter (*Figure 3.28 b*). This preserves the 10 fold size of the fingerprint of the 2.5 μm laser spot for the x10 objective.

The liquid monomer is sealed inside an ultra-thin polymeric film and no contamination with the monomer can be observed in the area surrounding the laser irradiated area. At a certain distance from the focal center of maximum temperature, an optimum temperature is achieved that will offer conditions for MMA polymerization. This results in a self-healing of the region that suffered a catastrophic failure due to the same laser radiation.

A particular property of PMMA is to depolymerize into the monomer state. This can be achieved at a specific temperature and/or at a specific pressure. P.A. Small studied the monomer and the polymer state transitions of MMA and observed that in the temperature range of 100 and 160 °C a linear behavior for the equilibrium of the monomer/polymer which respects the 12.56-(4260/T) [50]. This property could prevent an efficient polymerization during the Photo-CVD experiments outside the reported range, especially at the total pressure of P_T = 1 Torr used for the 570 min experiment.

3.6. Chapter Overview

For this chapter the Photo-CVD injection was upgraded to a newer technology. The aspects of the DLI technological changes were discussed while defining in parallel the operating parameters.

The formation of the gas phase from the liquid phase of the monomer is treated theoretically and indicates that the vapor phase is efficiently obtained by the DLI system. The liquid presence at the substrate level is thus likely obtained by a process of nucleation, as observed in Chapter 2, not by a bulk monomer droplet adhesion over the substrate.

As a consequence of the nucleation during the polymerization, FTIR studies highlighted the PMMA orientation (tacticity) over the liquid and solid. The AFM spectroscopy offered supplementary evidences of the liquid encapsulation with PMMA under the form of blisters but also of the polymerization at the substrate level.

During the Raman characterization disruptive effects over the blisters were highlighted. They were associated mainly to the laser energy used to obtain the Raman spectra. These disruptive effects over the blisters were found to be destructive and constructive. The constructive effect is a self-healing behavior of the PMMA thin films (likely dictated by polymerization parameters such as temperature or UV exposure).

Chemical and physical insights of the Raman laser interaction with the deposited film were also studied. During laser irradiation, chemical changes in the film and over the blisters were investigated. For instance phase transitions of the liquid MMA and solid PMMA film were treated with respect to the laser irradiation. As discussed, PMMA can undergo depolymerization under certain thermodynamic conditions.

The next chapter will involve the study of a polymer that does not possess this property, namely polypyrrole (PPy).

Bibliography

[1] B.J. Clark, T. Frost, UV Spectroscopy: Techniques, Instrumentation, Data Handling, Springer, 1993.
[2] L.D. Field, S. Sternhell, J.R. Kalman, Organic Structures from Spectra, John Wiley & Sons, 2008.
[3] C. Esen, T. Kaiser, G. Schweiger, Raman Investigation of Photopolymerization Reactions of Single Optically Levitated Microparticles, Appl. Spectrosc. 50 (1996) 823–828.
[4] L.A. Leites, Y.P. Egorov, G.S. Kolesnikov, S.L. Davydova, Study of the vibration spectra of methacrylic acid derivatives containing group IV elements, Russian Chemical Bulletin. 10 (1961) 1844–1849.
[5] M. Masashi, H. Jun, I. Hirohiko, F. Seiichi, O. Hideo, K. Hideki, et al., Application of Laser Raman Micro-spectroscopy for the Analysis of Resin-dentin Interdiffusion Zone., Adhesive Dentistry. 18 (2000) 43–50.
[6] K.P. Le, R. Lehman, A. Mann, J. Idol, Raman Characterization in Blends of Poly (L-lactide) and Poly (methyl methacrylate), Applied Spectroscopy. (2006).
[7] K.L. Rhudy, S. Su, H.R. Howell, M.W. Urban, Self-Stratified Films Obtained from Poly(methyl methacrylate/n-butyl acrylate) Colloidal Dispersions Containing Poly(vinyl alcohol): A Spectroscopic Study, Langmuir. 24 (2008) 1808–1813.
[8] J.W. Martin, T. Nguyen, E. Byrd, B. Dickens, N. Embree, Laboratory apparatus and cumulative damage model for linking field and laboratory exposure results, in: ACS SYMPOSIUM SERIES, 2001: pp. 119–143.
[9] C. Gardrat, R. Ruggiero, W. Hoareau, L. Damigo, A. Nourmamode, S. Grelier, et al., Photochemical study of 4-(4,9-dimethoxy-2,11-n-dipropyl-6,7-dihydro-5,8-dioxa-dibenzo[a,c]cycloocten-6-yl)-2-methoxyphenol, a lignin model of phenolic dibenzodioxocin unit, Journal of Photochemistry and Photobiology A: Chemistry. 169 (2005) 261–269.
[10] H.R. Allcock, Introduction to Materials Chemistry, John Wiley & Sons, 2011.
[11] D. Chandler, J.D. Weeks, H.C. Andersen, Van Der Waals Picture of Liquids, Solids, and Phase Transformations, Science. 220 (1983) 787–794.
[12] Q. Gu, R. Song, D. Shen, Stereocomplex formation in atactic poly(methyl methacrylate) I. Effect of solvents, Polymer Bulletin. 44 (2000) 533–538.
[13] N. Grassie, Photodegradation of methacrylate/acrylate copolymers, Pure Appl Chem. 34 (1973) 247–57.
[14] A. Gentilhomme, M. Cochez, M. Ferriol, N. Oget, J.L. Mieloszynski, Thermal degradation of methyl methacrylate polymers functionalized by phosphorus-containing molecules. III: Cone calorimeter experiments and investigation of residues, Polymer Degradation and Stability. 88 (2005) 92–97.
[15] K. Dayananda, R. Dhamodharan, ATRP of methyl methacrylate using a novel binol ester-based bifunctional initiator, Journal of Polymer Science Part A: Polymer Chemistry. 42 (2004) 902–915.
[16] X. Cheng, M. Caironi, Y.-Y. Noh, J. Wang, C. Newman, H. Yan, et al., Air Stable Cross-Linked Cytop Ultrathin Gate Dielectric for High Yield Low-Voltage Top-Gate Organic Field-Effect Transistors, Chem. Mater. 22 (2010) 1559–1566.
[17] Y. Grohens, R.E. Prud'homme, J. Schultz, Cooperativity in Backbone to Side-Chain Conformational Rearrangements in Stereoregular PMMA, Macromolecules. 31 (1998) 2545–2548.
[18] O.N. Tretinnikov, K. Ohta, Conformation-Sensitive Infrared Bands and Conformational Characteristics of Stereoregular Poly(methyl methacrylate)s by Variable-Temperature FTIR Spectroscopy, Macromolecules. 35 (2002) 7343–7353.
[19] J.A. Henderson, R.W. Richards, J. Penfold, C. Shackleton, R.K. Thomas, Neutron reflectometry from stereotactic isomers of poly(methyl methacrylate) monolayers spread at the air-water interface, Polymer. 32 (1991) 3284–3294.
[20] F. Bosscher, G. Ten Brinke, G. Challa, Association of stereoregular poly(methyl methacrylates). 6. Double-stranded helical structure of the stereocomplex of isotactic and syndiotactic poly(methyl methacrylate), Macromolecules. 15 (1982) 1442–1444.
[21] W.-P. Hsu, Y.-L. Lee, S.-H. Liou, Monolayer characteristics of stereoregular PMMA at the air/water interface, Applied Surface Science. 252 (2006) 4312–4320.
[22] K. Kelton, A.L. Greer, Nucleation in Condensed Matter: Applications in Materials and Biology, Elsevier, 2010.

[23] C.L.E. Nijst, J.P. Bruggeman, J.M. Karp, L. Ferreira, A. Zumbuehl, C.J. Bettinger, et al., Synthesis and characterization of photocurable elastomers from poly (glycerol-co-sebacate), Biomacromolecules. 8 (2007) 3067–3073.
[24] M. Fırlak, M.V. Kahraman, E.K. Yetimoğlu, Preparation and characterization of photocured thiol-ene hydrogel: adsorption of Au(III) ions from aqueous solutions, Journal of Applied Polymer Science. (2012) n/a–n/a.
[25] H. Zweifel, R.D. Maier, M. Schiller, Plastics Additives Handbook, Hanser Verlag, 2009.
[26] V. Gomez-Serrano, J. Pastor-Villegas, A. Perez-Florindo, C. Duran-Valle, C. Valenzuela-Calahorro, FT-IR study of rockrose and of char and activated carbon, Journal of Analytical and Applied Pyrolysis. 36 (1996) 71–80.
[27] J.P. Cleveland, S. Manne, D. Bocek, P.K. Hansma, A nondestructive method for determining the spring constant of cantilevers for scanning force microscopy, Review of Scientific Instruments. 64 (1993) 403 –405.
[28] M.J. Akers, D.S. Larrimore, D.M. Guazzo, Parenteral Quality Control: Sterility, Pyrogen, Particulate, and Package Integrity Testing, CRC Press, 2003.
[29] J. Fraden, Handbook of Modern Sensors: Physics, Designs, and Applications, Springer, 2010.
[30] J.R. Lawson, W.D. Walton, D.D. Evans, Measurement of Droplet Size in Sprinkler Sprays, U.S. Commerce Departmen, 1988.
[31] H.E. Snyder, D.W. Senser, A.H. Lefebvre, R.S. Coutinho, Drop size measurements in electrostatic paint sprays, IEEE transactions on industry applications. 25 (n.d.) 720–727.
[32]Mist blower-sprayer - 120 -180 µm MMD (average diameter particle by mass), (n.d.).
[33] J.C. John, Particle Size Control in Aerosol Packages, Spray Technology & Marketing. (2004).
[34] S. Sarkar, Three-dimensional Multiphase Flow Modeling of Spray Cooling Using Parallel Computing, ProQuest, 2008.
[35]Thermal Spray 2004: Advances in Technology and Application : Proceedings of the International Thermal Spray Conference, 10-12 May, 2004, Osaka, Japan, ASM International, 2004.
[36] M.W. Zemansky, R. Dittman, Heat and thermodynamics: an intermediate textbook, McGraw-Hill, 1997.
[37]Methyl Methacrylate | US EPA, (n.d.).
[38] K.W. Whitten, R.E. Davis, M.L. Peck, G.G. Stanley, Chemistry, Cengage Learning, 2009.
[39] C.A.S.. No, Physical Constants of Inorganic Chemitry, (n.d.).
[40] V. Santucci, Élaboration et caractérisation de couches minces polymères par CVD et photo-CVD pour des applications optiques originales, Thèse de doctorat, INP Toulouse, 2009.
[41] P. Colomban, M.-P. Etcheverry, M. Asquier, M. Bounichou, A. Tournié, Raman identification of ancient stained glasses and their degree of deterioration, Journal of Raman Spectroscopy. 37 (2006) 614–626.
[42] A. Tournié, L.C. Prinsloo, P. Colomban, Raman spectra database of the glass beads excavated on mapungubwe hill and k2, two archaeological sites in South Africa, arXiv:1012.1465. (2010).
[43] F. Pallikari, G. Chondrokoukis, M. Rebelakis, Y. Kotsalas, Raman spectroscopy: A technique for estimating extent of polymerization in PMMA, Mater. Res. Innovations. 4 (2001) 89–92.
[44] G. Lopez, M. Artetxe, M. Amutio, G. Elordi, R. Aguado, M. Olazar, et al., Recycling poly-(methyl methacrylate) by pyrolysis in a conical spouted bed reactor, Chemical Engineering and Processing: Process Intensification. 49 (2010) 1089–1094.
[45] B.B. Troitskii, G.A. Domrachev, L.V. Khokhlova, L.I. Anikina, Features of the Thermooxidative Destruction of PMMA, Doklady Physical Chemistry. 375 (2000) 268–270.
[46] J. Bovatsek, A. Tamhankar, R. Patel, N.M. Bulgakova, J. Bonse, Effects of pulse duration on the ns-laser pulse induced removal of thin film materials used in photovoltaics, Proceedings of SPIE. 7201 (2009) 720116–720116–13.
[47] O.N. Shebanova, P. Lazor, Raman study of magnetite (Fe3O4): laser-induced thermal effects and oxidation, J. Raman Spectros. 34 (2003) 845–852.
[48] Y. Zhang, H. Son, J. Zhang, J. Kong, Z. Liu, Laser-heating effect on Raman spectra of individual suspended single-walled carbon nanotubes, The Journal of Physical Chemistry C. 111 (2007) 1988–1992.
[49] I. Jones, J. Rudlin, Process monitoring methods in laser welding of plastics, in: Proceedings of the 2nd International Conference on Joining Plastics. National Physical Laboratory, 2006: pp. 25–26.

[50] P.A. Small, The equilibrium between methyl methacrylate and its polymer, Trans. Faraday Soc. 49 (1953) 441–447.

CHAPTER 4 - PPy AND HYBRID PPy THIN FILMS OBTAINED BY DRY ROUTE (CVD)

During the previous experiments the encapsulation of the liquid monomeric phase was observed as a result of the PhotoCVD deposition. The encapsulation of liquid MMA monomer was achieved by the conformal coverage of a polymeric PMMA thin film, forming a protective membrane. This polymeric film was identified not only over the blisters, but also the other part of the substrate.

The evaporation of liquid droplets rate was investigated theoretically using the Langmuir evaporation model. The evaporation rate was calculated in the range of hundreds of µs range for pressures up to 20 Torr. This result indicated that the dwelling time of the species in the Photo-CVD reactor is largely enough to evaporate the 40 µm droplets produced by the Kemstream G2.8 DLI system. With respect to the temperature, the evaporation rate decreases logarithmically with the increase in temperature.

During the deposition a process of Thermally Induced-Release of the liquid Internal Phase (TI-RIP) was used to break the thin polymeric membrane and to release of the liquid internal phase. The release of the liquid encapsulated into the membrane was achieved due to the difference of thermal expansion of the monomer and polymer at temperatures around and below 0 °C. According to the Langmuir evaporation calculus, the decreased temperature slows the evaporation of the monomer, until a point where this evaporation stops.

A low efficiency of the polymerization process was experimentally observed during the PhotoCVD of PMMA. Indeed, this polymer has the ability to depolymerize in certain conditions of pressure and temperature. The low pressures used in the CVD reactor could lead to thermodynamic conditions that do not facilitate polymerization on a substrate.

Figure 4.1: Chemical formula of Polypyrrole

By contrast with PMMA, it was interesting to carry out PhotoCVD of polymers that does not possess the ability to depolymerize. Pyrrole (Py) is a monomer that was evaluated for deposition of Polypyrrole (PPy) thin films (see *Figure 4.1*) PhotoCVD. The experiments were made using Kemstream DLI G2.8 injection system.

Polypyrroles (PPy - the polymeric form of Py) exists naturally and is present as copolymer in some melanins [1]. DE Weiss *et al* reported in a series of papers on the synthesis of PPy with high conductivity after doping the oxidized PPy with iodine [2–4]. Its conductive properties after doping recommends it for a wide area of application such as vapor sensors [5], drug release systems [6], tissue engineering [7] and optoelectronics [8]. To enhance the properties, it can be synthesized as copolymer for “artificial muscles” [9], used as catalyst dispersion in the carbon supported layers [10] or as a possible enhancement of the oxygen reduction by the coordination to metal catalysts [11].

The present chapter will be focused on the growth of PPy or PPy hybrid films (with Ag nanoparticles) and its characterization. The growth will be made by CVD. The characterization will highlight particular properties that can be exploited for various applications. These applications will be commented in the last chapter as perspectives of this work.

4.1. First Py polymerization with HCPK photo-initiator

4.1.1. Experimental

The PhotoCVD conditions were identical to the previous PMMA runs (see subchapter 3.2.). The Py monomer was mixed with the same amount of 2% 1-hydroxycyclohexil phenil ketone photo-initiator.

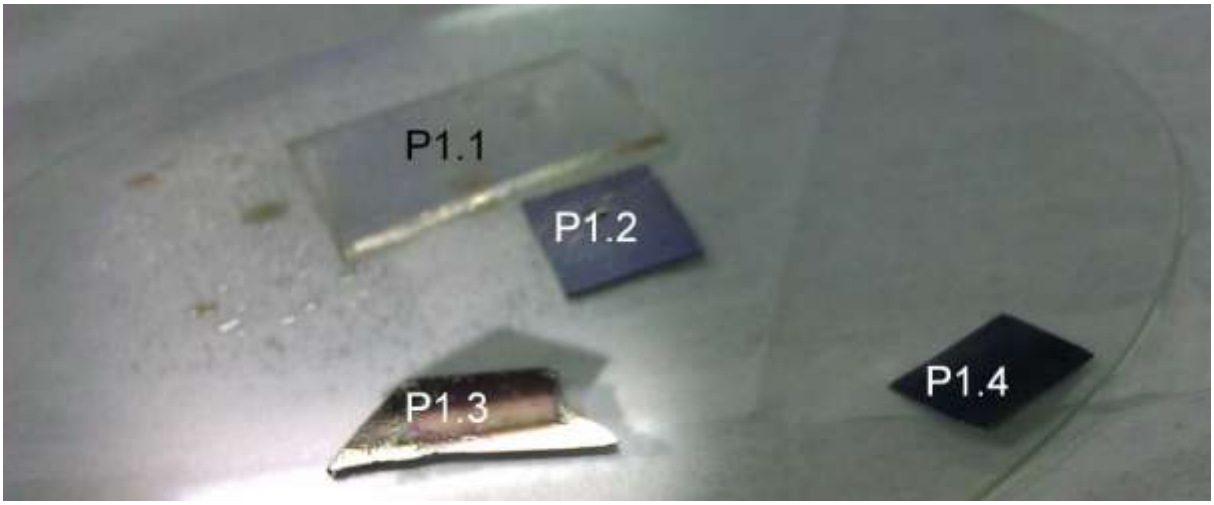

a)

b)

Figure 4.2: The substrates after the deposition a) noted as P1.1 glass, P1.2 Si(111), P1.3 SiOx/Si(100), P1.4 Si(111) and b) the substrates glass holder with the deposited droplets one week later

The substrates were degreased first with acetone and then with ethanol (mechanical cleaning with a cleanex tissue). Subsequently they were introduced in the ultrasound bath for 5 min in acetone and for 5 min in ethanol. The drying of the substrates was made under inert Ar gas stream at room conditions. The PhotoCVD experimental conditions are summed in *Table 4.1*. The N_2 carrier gas (the value for the gas flow in *Table 4.1*) is a pulsed flow, given by the value of the Setpoint of the gas injector. For further details with respect to the DLI system see chapter 3.

The substrates were named for easier identification with respect to the placement onto the substrate holder and the substrate type (*Figure 4.2 a*). The substrates used for this

experiment were: one glass substrate – named P1.1, one Si/SiO_x substrate – named P1.3 and two Si(100) substrates – named P1.2 and P1.4 (see *Figure 4.2 a*).

Table 4.1: The PhotoCVD experimental parameters;
the liquid precursor was Py monomer with 2 % HCPK photonitiator

Gas flow		Pressure		Temperature		DLI system			
						liquid		Gas	
Q_{N2}	150 scc m	P_{N2}	3.5 bar	T_{inj}	60 °C	t_{on}	1 ms	f	1 Hz
		P_{MFM}	2 bar	T_{uv}	80 °C	f	1 Hz	Setpoint	10%
		P_T	9.5 Torr	$T_{substrate}$	17 °C	t_{exp}		45 min	

After the deposition, the presences of droplets on the substrate indicates a low polymerization efficiency (*Figure 4.2 b*). The light brown color suggests that the polymer is not conductive. Notably, the conductive PPy has a black color [12], while the monomer is transparent. Spectroscopic characterization investigates the chemical aspects of the deposit.

4.1.2. Chemical Characterization

4.1.2.1. UV-VIS Spectroscopy

Both absorbance and transmittance spectra of the film in the UV-VIS-NIR range is shown in *Figure 4.3*.

Usually for liquids, where high dilutions are involved, the UV-VIS-NIR data are presented as absorption spectra. The formula that describes the relationship between the absorption *(A)* and transmission *(T)* is:

$$A = 2 - \log_{10} T\% \qquad (4.1)$$

The conversion of the UV-NIS-NIR spectra was made in order to highlight the chemical composition (absorbance) and possible applications (as transparent films - transmittance).

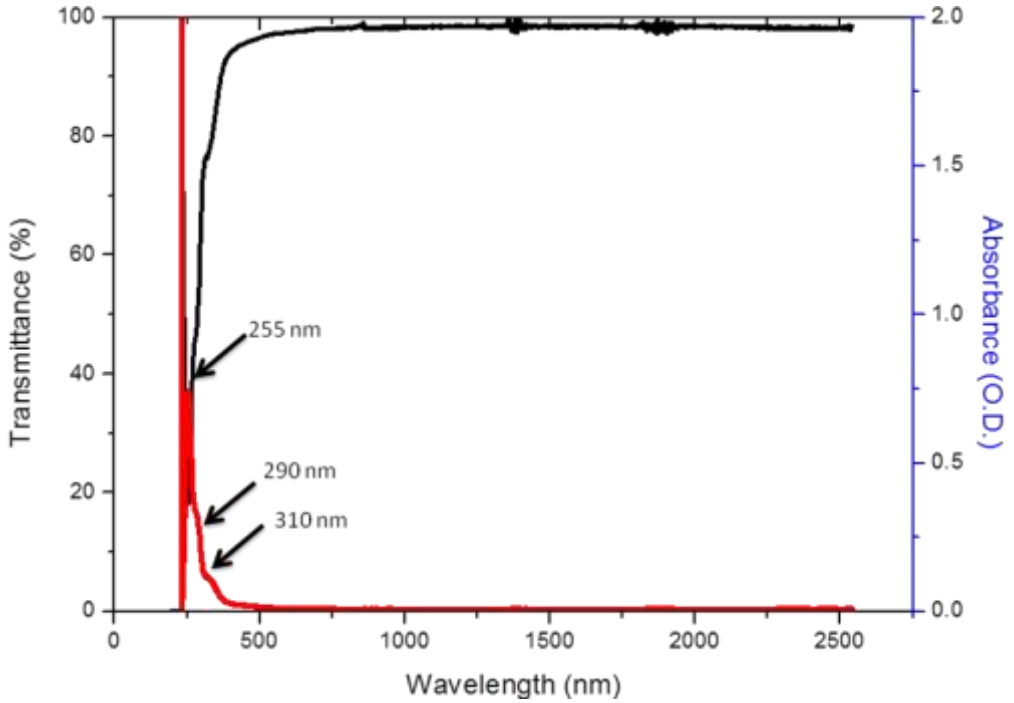

Figure 4.3: Transmittance (black curve) and absorption (red curve) UV-VIS-NIR spectra of the deposited sample

The transmittance around 98 % above 500 nm indicates the probable presence of a thin film. However the issue of the droplets found on the surface of the sample needs to be addressed as it can be related to a poor efficiency of the polymerization. The HCPK photo-initiator absorbs at around 250 nm according to Sigma Aldrich[10]. Also, according to National Institute of Standards and Technology[11], the pyrrole absorbs at 290 and 310 nm. The peaks of HCPK and Py observable in the spectrum. However, peaks specific to the polymer cannot be clearly identified. The UV-VIS absorption of the PPy polymer will be treated after further deposition experiments.

Further structural characterization will be achieved by Raman spectroscopy.

4.1.2.2. Raman Spectroscopy

The Raman spectrum of the deposited PPy is shown in *Figure 4.4*. On the spectra bands specific to PPy can be observed.

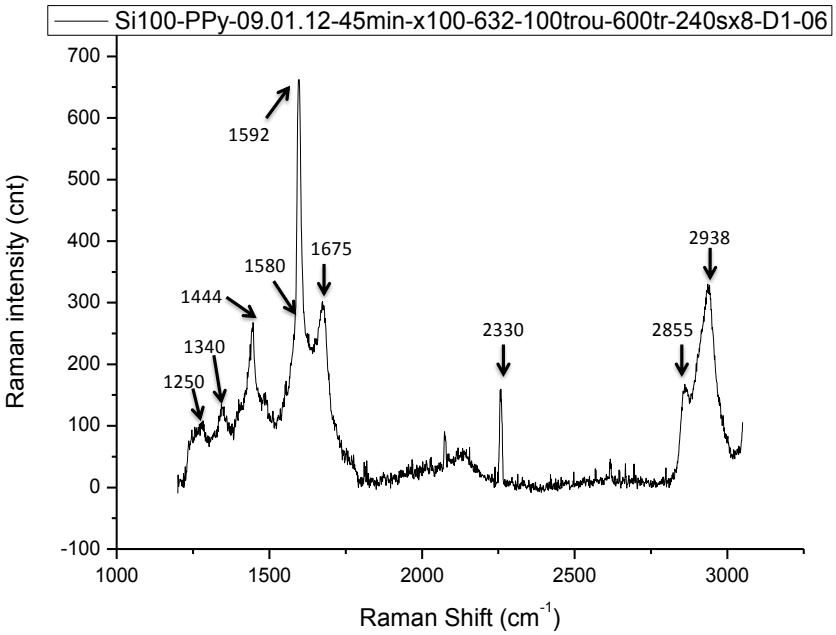

Figure 4.4: Raman spectra of the film deposited over a Si(100) substrate with 632 nm laser

The C-H bending mode can be identified at 1250 cm^{-1} [13]. The bands at about 2855 cm^{-1} and 2938 cm^{-1} can be associated also to the C-H vibrations of the Py ring [14,15]. The band at 1340 cm^{-1} is associated to the ring stretching of PPy [16–18]. With respect to the PPy ring, individual bands for the C-N stretching and the C=C bond can be found at 1444 cm^{-1} and 1592 cm^{-1} respectively.

The peak observed at 2330 cm^{-1} is due to the Raman mode of N_2 gas present in the air that surrounds the sample [19]. Coherently the O_2 vibrational mode around 1580 cm^{-1} [20] appears as a shoulder of the most intense peak.

To investigate the laser effect over the droplets, a separate study was made on which a blister was subjected to successive increase of laser exposure. The *in-situ* area after the exposures can be seen in the optical microscopy images in *Figure 4.5*. Also, the Raman spectra evolution is shown in *Figure 4.5* insets.

In *Figure 4.5* it can be observed the Raman laser had almost the same effect as in the case of PMMA (subhapters *3.5.2* and *3.3.1*). The damage of the blister seems to have the same ability to self-heal. It can be observed that the diameter increases from around 1.1 µm,

[10] *Sigma Aldrich* UV-VIS Spectra of Photoinitiators

[11] *NIST* WebBook

to 1.4 μm and 1.6 μm as the exposure time to the 532 nm laser radiation increases from 3 to 30 s.

In the Raman spectra (*Figure 4.5* left insets) a decrease in Raman intensity with increasing laser exposure is observed. This decrease in signal intensity can probably be associated to the chemical changes of the species found in the focal area responsible for the Raman signal. Processes of monomer evaporation, polymerization and polymer damage are expected.

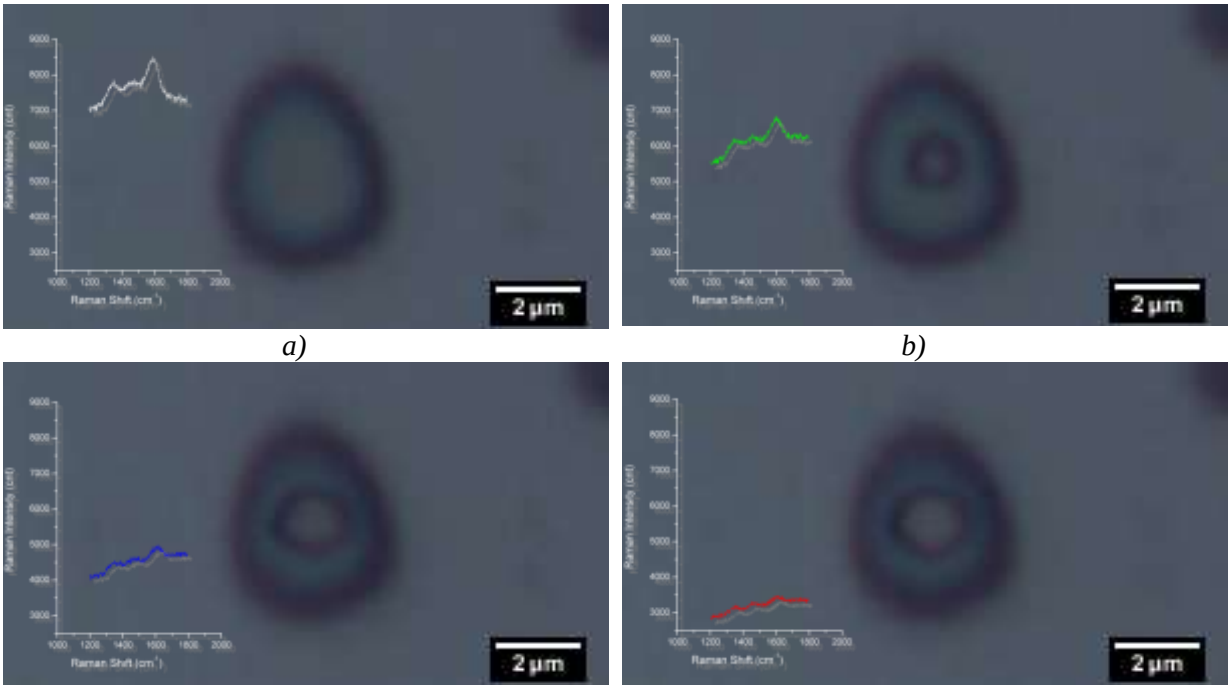

a) *b)*

c) *d)*

Figure 4.5: Optical Microscopy of the blister (a) as-deposited and damaged by the 532 nm laser for different times: (b) 12 sec, (c) 21 s and (d) 30 s. The Raman spectra are shown on the left inset

4.1.3. Surface Energy and Liquid Encapsulation

4.1.3.1. FESEM analysis and evidences for the growth of a polymeric film

To study the surface, FESEM technique was used due to the fact that it uses low energy electron beam. The fact that PPy is known as an intrinsically conductive polymer allowed making the analyses without metallization pre-treatment by sputtering.

The droplets are probably grown at the film interface due to the oversaturation of monomer vapor at the substrate level. The condensation is more likely to occur on the surface of the substrate as result of heterogeneous nucleation (as observed in subchapter *2.2.4*). If we consider the encapsulated droplets as a functional system, we can address them as droplets.

The total pressure in the FESEM sample chamber during the films analysis reached at 5 Pa ($40*10^{-3}$ Torr). This is much below the vapor pressure of the Py monomer of 1127 Pa at 25 ^{o}C [21], which will indicate a fast evaporation (see Chapter 3 for details). This emphasizes the fact that the liquid monomer is encapsulated by a polymeric film which does not allow monomer evaporation.

During the growth at low pressure, possibly metastable processes are expected at the substrate interface as liquid monomer nucleation, evaporation and polymerization.

The heterogeneous nucleation centers for the liquid monomer were highlighted with the aid of the Acoustic mode AFM in the case of PMMA (subchapter *2.2.3*). The formation of the nucleation centers can lead to a patterned growth onto the surface. The wettability of the

surface can induce aggregation of the liquid over the surface. However, the evaporation process can be responsible for the re-vaporization of some droplets. This can be considered the case for the droplets that did not achieve a "critical size" to compensate the lost mass over the surface during the low-pressure quasi static regime, when the carrier gas is not *pulsed*.

In this manner, the liquid aggregation due to the surface wettability can lead to relatively large droplets. Due to the evaporation processes, a circular area around each large droplet is expected to be observed, as local nucleation zone where is not enough mass to compensate the evaporation. Such aspects can be at the basis of the formation of 14 µm droplets radius surrounded by a 28 µm radius of blister free area as shown in *Figure 4.6 b).*

If we consider that the droplets merge due to the wettability, indications with respect to the surface energy of the substrate interfacial atoms should be found. In *Figure 4.6 b)* the almost ordered patterned network of the large droplets was approximated by drawing the grid of the network. It can be observed that a roughly 55 µm length of a square structure can be drawn. However, the droplets are not arranged in a square matrix. They form a 60^o tilted parallelogram (*Figure 4.6 b*).

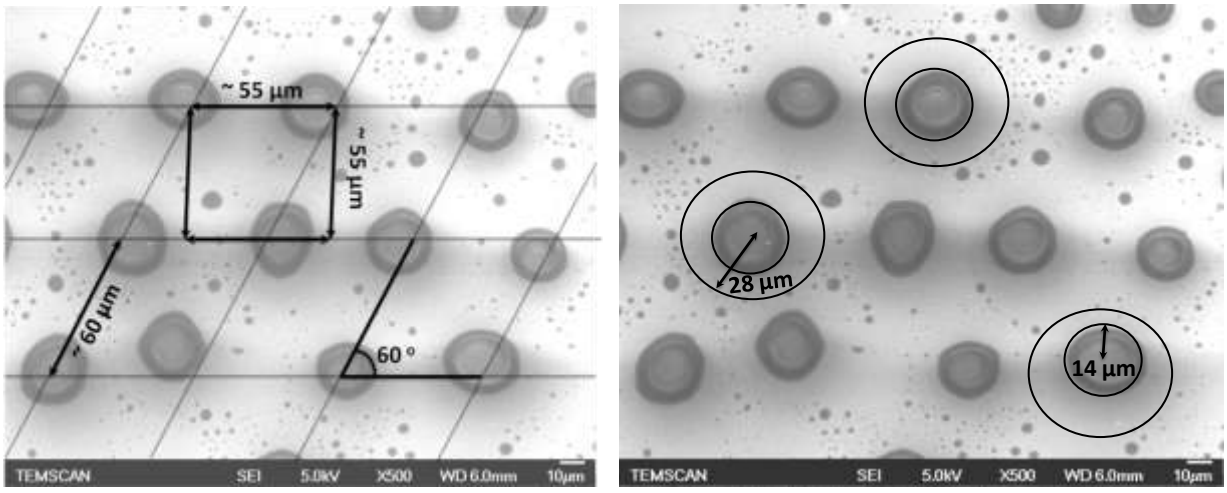

a) *b)*

Figure 4.6: FESEM microcopies of the deposited film over a Si(100) substrate with a) the marking repetitive patterns and the observed blister and b) the radius of blisters and of the blister free area around it.

If we consider the Si(100) crystal arrangement, the cubic 55 µm square length could be an indication of the square interfacial arrangement of the (100) planes. However, the orientation is not ideal because a 60^o tilt is observed. With respect to the atomic arrangement of Si(100) atoms at the interface, in the literature a perfect 60^o dislocation is reported for a step composed of two atomic planes [22]. This 60^o dislocation in the lattice is also reported for other heteroepitaxial systems and is described as corresponding to Burger vector (that describes the lattice distortion magnitude) corresponding to a line direction [23].

The Si(100) atomic planes gave an indication of the liquid presence onto the surface and sustains a possible nucleation process during the PhotoCVD growth. However, as for the previously investigated PMMA, the presence of the polymeric thin film is not so obvious. The AFM technique will further be used to demonstrate its presence.

4.1.3.2. AFM Spectroscopy as evidence for the liquid encapsulation

The AFM spectroscopy had shown its contribution in the PMMA ultra-thin film study. The AFM spectroscopy involves one approach and one retract cycle of the AFM cantilever onto the thin film. The approach and retract time (and profiles) vary for different materials. In *Figure 4.7 a)* two different points were chosen for measurement: one over a blister and one

over a flat surface. If the liquid is not covered with a polymeric film, the approach/retract cycles would shown different behavior compared to the cycle for the solid substrate. This is not the case for this deposit, **as the approach/retract are identical for the two points (*Figure 4.7 b*), indicating a conformal coverage of a thin polymeric film both on the liquid and solid surfaces.**

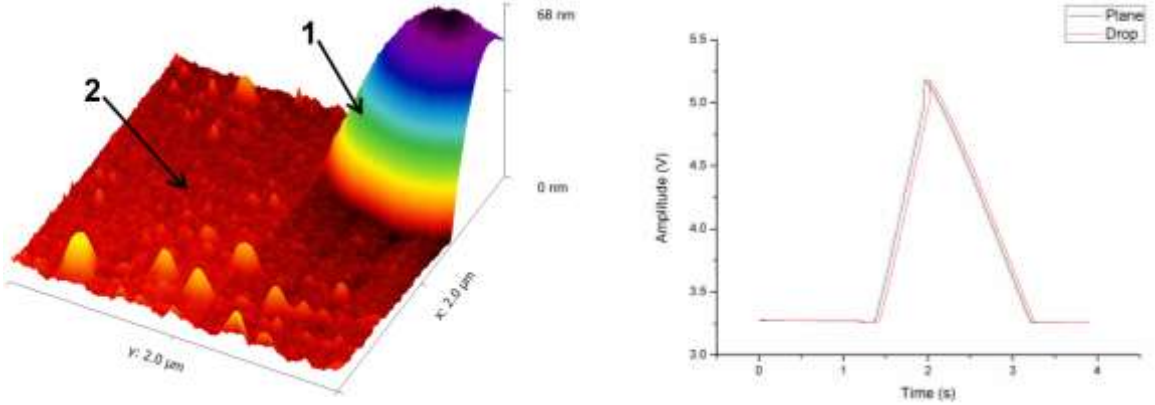

a) *b)*

Figure 4.7: AFM 3D topography of the film deposited over Si(100) substrate with marked refion for a) and the force spectroscopy b); The point marked with 1 corresponds to the drop and the point marked 2 corresponds with plane on the spectreosopy image

In this manner **the liquid encapsulation of Py monomer with an ultra-thin film of PPy in the form of blisters is confirmed**. The next study will focus on the evaluation of the Py polymerization efficiency that leads to such an ultra-thin film of PPy during the PhotoCVD experiments.

4.2. PPy polymerization test in the condensed phase

As observed in the previous subchapter, the phenomena involved during the polymerization by CVD are: wettability (that also influences nucleation), evaporation and polymerization.

To study the implications of such factors a test in ambient air was made in order. In this test a drop of a Py monomer mixed with 2% photo-initiator was exposed to 254 nm UV radiation for various times (the lamps of the CVD activation zone). During irradiation the sample was at about 60 ^{o}C. Preliminary results for different times are shown in *Figure 4.8*. After 60 min of UV exposure the brown color of the obtained PPy likely indicates a possible lack of conduction of the polymer. A black color of the PPy would indicate a conductive coating [12].

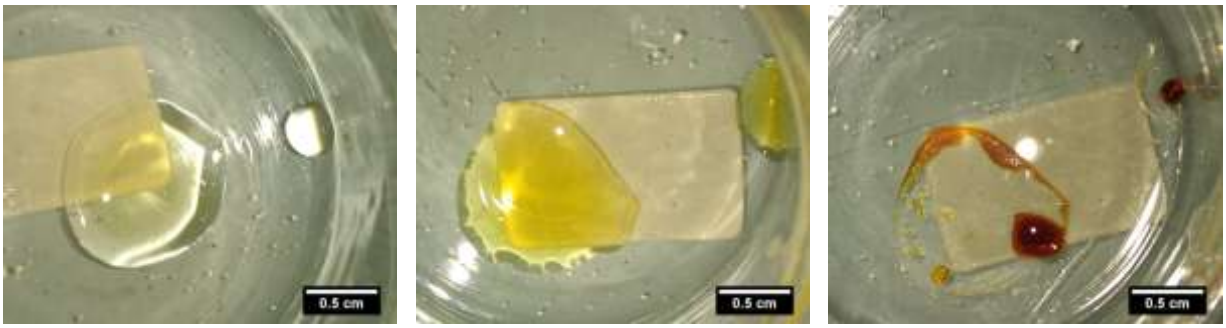

a) *b)* *c)*

Figure 4.8: The behavior of a Py + 2% HCPK blister under 254 nm UV irradiation at 60 °C for a) 0 min; b) 15 min; c) 60 min

If the polymerization was efficient, a crust should be formed at the interface between the liquid and the atmosphere. This is expected because the surface of the liquid receives the greatest photon flux and it will first initiate the polymerization at the blister interface.

If the polymerization efficiency is low, the wettability and the evaporation are the competitive phenomenon with polymerization that influences the surface area. When the evaporation is predominant, the blister surface area will decrease. If the wettability is the main phenomena, the surface area will increase. The competition of the two will lead to a predominant effect that can be identified by analizing the area of a 200 µl Py blister (*Figure 4.9*).

During the test, at 60 °C (Py boiling point is at 130 °C) and under 245 nm UV exposure, a predominant wettability effect and evaporation were observed in the first 12 min. The polymerization effects is visually observed by the change in blister color, but it is not significant until *ca.* 12 min. As a result the liquid on the substrate is not protected by a membrane during these 12 min and the changes of its surface area reveal different dominant behaviors as evaporation in the early stage then wettability (*Figure 4.9*).

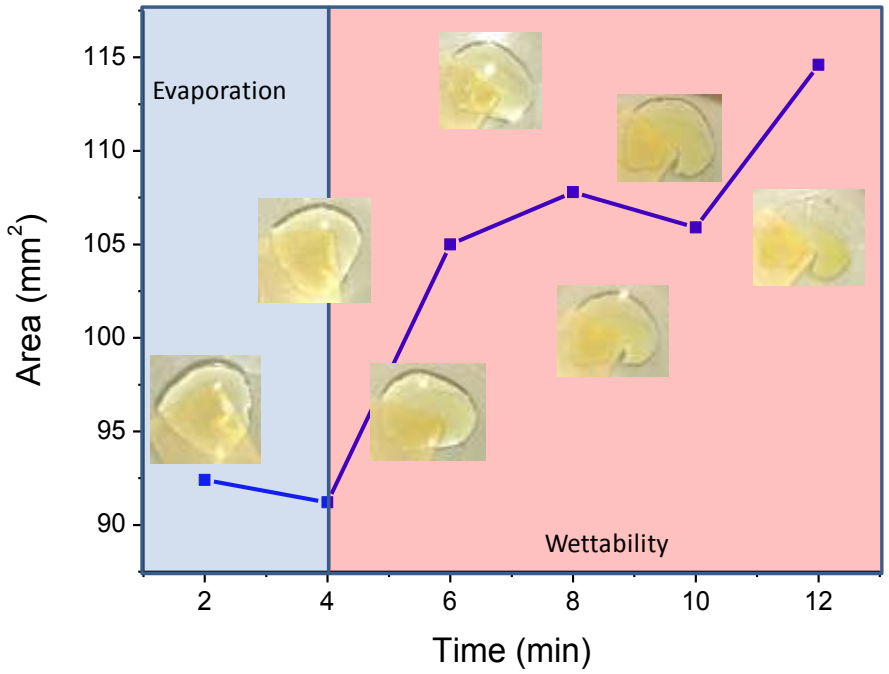

Figure 4.9: Evolution of the evaporation area during the UV exposure at 60 °C of a Py blister; the probable effects of predominant evaporation and wettability are separated

4.3. Chemical enhancement of PPy with Ag nanoparticles

The purpose of the next experiment will be to enhance the polymerization of the Py monomer. A chemical approach is taken to achieve this goal that involves the change of the photonitiator mixture.

4.3.1. Experimental

The increase in the polymerization efficiency can be achieved in two ways: by physical or chemical optimization. The physical optimization can be made adjusting the physical parameters such as the activation energy (by increasing the UV intensity or changing the temperature) or by adjusting the geometrical parameters of the CVD process. The chemical optimization can be achieved by using chemical compounds that help the photo-initiation. The HCPK compound mixed previously with the Py monomer seemed to provide insufficient

contribution. Murphy *et al* investigated the contribution of such photo-initiator compounds on the polymerization [12]. They also compared the UV curing (UV energy) with a temperature curing (thermal energy). For the following experiment the focus will be on the optimum chemical composition of the monomer solution. The mixture Py:$AgNO_3$ with a molar ratio of 50:1 with 3 % HCPK was found a good candidate and it will be the precursor solution used in PhotoCVD experiments. The parameters are summed in *Table 4.2*.

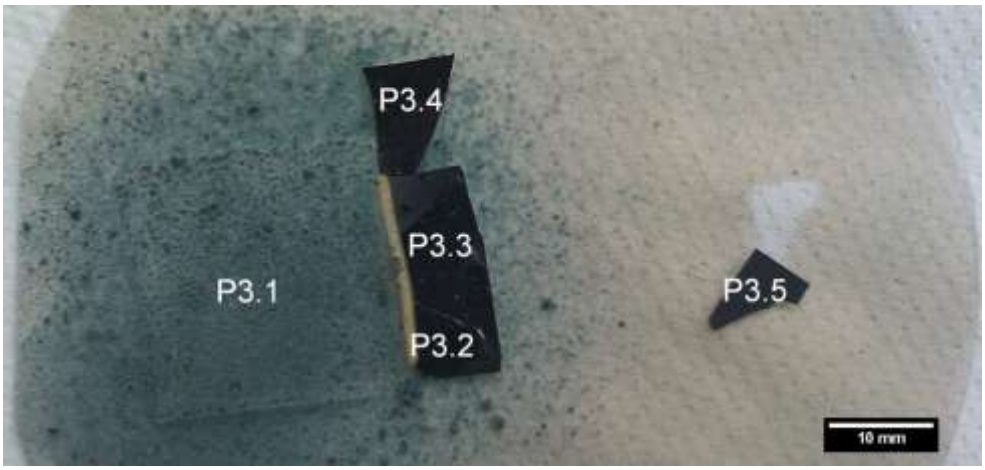

a)

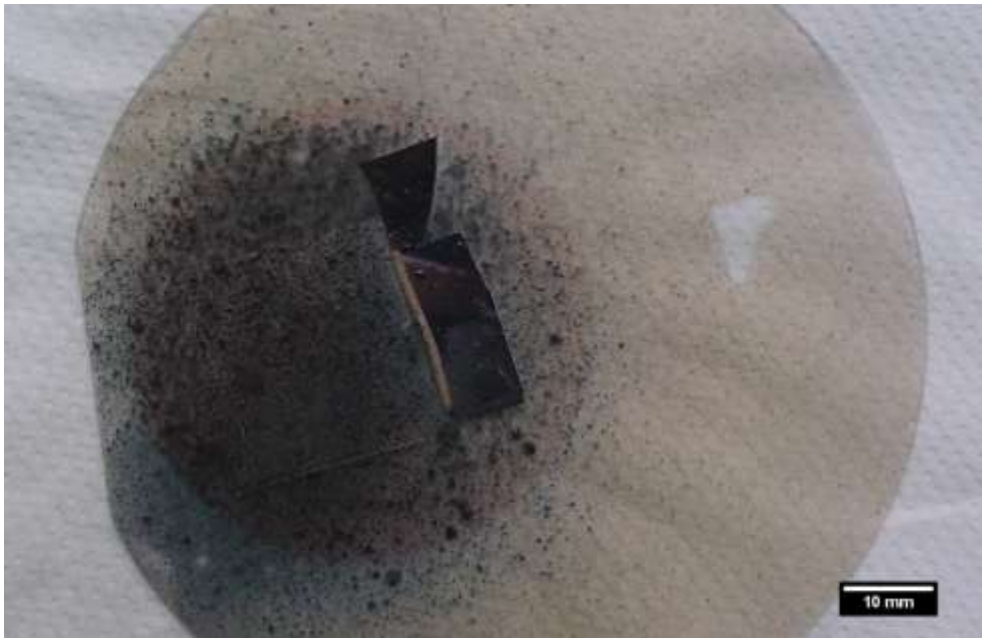

b)

Figure 4.10: The substrates as removed from the sample chamber a) and after 75 min after deposition b)

Table 4.2: The PhotoCVD experimental parameters; the liquid precursor was a mixture of Py:$AgNO_3$ with a molar ration of 50:1 and 3 % HCPK photonitiator

Gas flow		Pressure		Temperature		DLI system			
						liquid		gas	
Q_{N2}	150 sccm	P_{N2}	3.5 bar	T_{inj}	60 °C	t_{on}	1 ms	f	1 Hz
		P_{MFM}	2 bar	T_{uv}	80 °C	f	1 Hz	Setpoint	10%
		P_T	9.5 Torr	$T_{substrate}$	17 °C	t_{exp}		45 min	

The substrates were coded for easy reference in the text as following: glass as P3.1, Si(100) as P3.2, P3.3 and P3.5, Si/SiO_x as P3.4 (*Figure 4.10 a*).

Immediately after PhotoCVD a dark-blue coating can be seen over the substrates (*Figure 4.10 a*). After storage in air for 75 min a circular area with ca. 130 mm diameter turned black-brown. The circular distribution of the dark area where the color was changed could be an indication of scattered UV photons towards the sample chamber.

In order to obtain an insight of the chemical composition and morphology spectroscopic and microscopic characterizations were further treated.

4.3.2. Chemical Composition of the Film

UV-VIS-NIR and Raman techniques will be used to evaluate the composition of the deposit obtained with the PhotoCVD parameters in *Table 4.2*.

4.3.2.1. UV-VIS-IR characterization

The deposit indicates a higher degree of polymerization after the $AgNO_3$ addition. The previously presented photographs (*Figure 4.10*) indicate the presence of different visible absorptions that were revealed by the UV-VIS-NIR spectra (*Figure 4.11*).

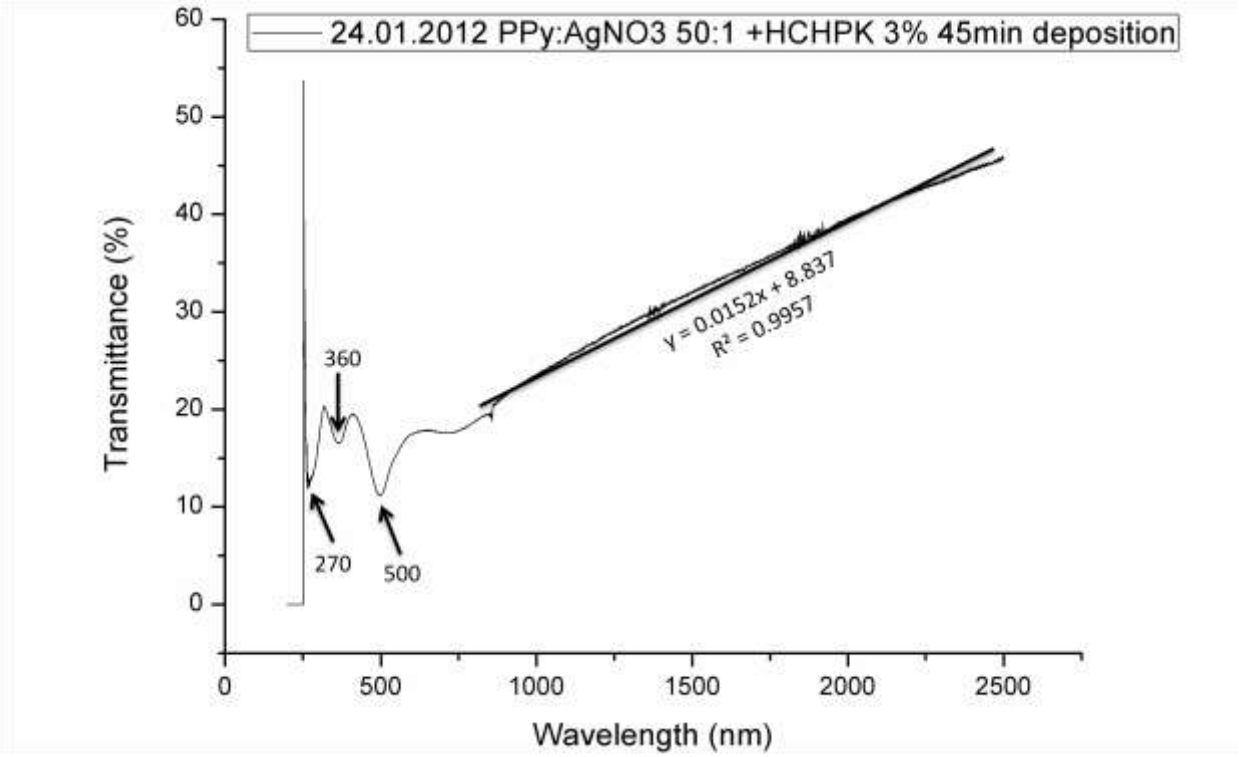

Figure 4.11: UV-VIS-NIR spectra of the deposited sample

The absorption observed in UV at 270 nm can be associated to the HCPK photointiator. The wavelength can be probably affected by the high absorption of the glass substrate in that range. At 360 nm absorption is associated to the π - π* transitions of the PPy [16] confirming the formation of the polymer.

In the visible range, an absorbtion band is observed 500 nm. It is associated to the high energy polaron transition of the PPy [16,24]. Li and Qian reported that the 500 nm absorption is due to the proton-acid doping structure of PPy with NO_3^- [25]. The same counter ion was used during the PhotoCVD experiment, and is an indication of the NO_3^- doping. Street et al suggested that the bands around 400 nm and 500 nm and above 800 nm are due to the π - π* transitions [26]. Absorbtion bands above 652 nm towards NIR are associated to the PPy oligomers in doped state [27]. An increasing band from 750 nm is observed in the measured

VIS-NIR spectrum. A fit was made from 850 nm (where a slight jump in intensity is observed probably due to the lamp change to NIR). In this NIR region the transmittance increase (absorbance decrease) was fitted by a slope of *ca.* 0.015 %/nm. This slope can probably give a spectroscopic indication of the doping degree of the thin film.

To have a clear insight over the doping of the PPy thin film, Raman spectroscopy will be used.

4.3.2.2. PPy Doping analyzed by Raman

In the Raman spectra, the main peak present in PPy thin film is around 1600 cm^{-1} and it is associated to the backbone stretching of the C=C bond. Its shift can give an indication of the redox state of the PPy [16,17,28,29]. This band can be deconvoluted in two specific bands: at 1560 cm^{-1} that is associated to the neutral species, and at 1615 cm^{-1} that is associated to the oxidized species [18,28,29]. In *Figure 4.12* it can be observed that the area over which the Raman spectra was taken contains only neutral species of PPy.

Two ring stretching modes of PPy are identified at 1380 cm^{-1} and 1320 cm^{-1}. Also C-H in plane deformation of the pyrrole ring was identified at 1080 cm^{-1} and 1050 cm^{-1}. The bands at 1080 and 1380 cm^{-1} are associated to the oxidized PPy. The 1320 cm^{-1} and 1050 cm^{-1} can be associated to unconductive (undoped) species, being confirmed also by the spectra in *Figure 4.12* where the neutral species are observed

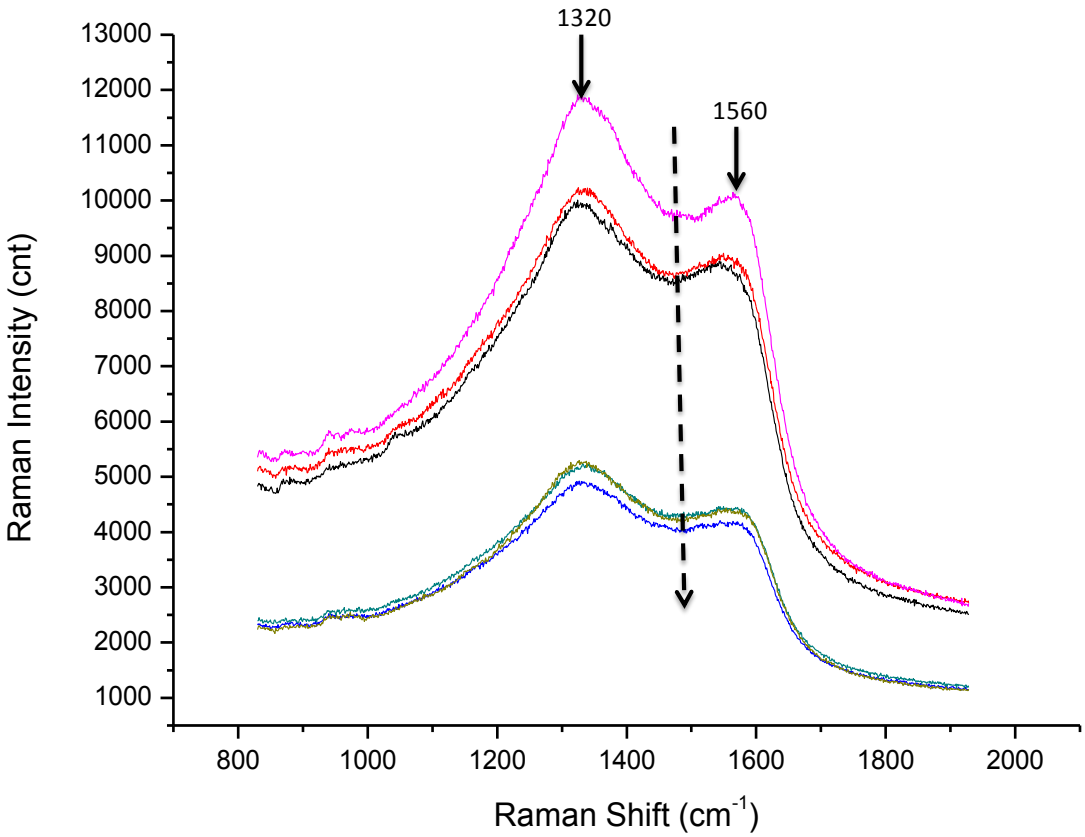

Figure 4.12: Raman spectra evolution as the acquisition time progresses (sample P3.3) with 532 nm laser; the dashed arrow indicates the increasing exposure time

Chen *et al* made a Raman study that treat the thickness dependence of the doping level of a PPy film grown [18] and observed that the thinner the film, the lower the doping. However, in the study the aspect of the PPy thermal dedoping were not discussed. For example chloride-doped PPy can dedope at temperatures < 80 ^{o}C [30,31]. This temperature can vary with respect to the used dopant. A thinner film can promote a more in-dept dedoping of the thin film during the exposure to the Raman laser radiation, while for a thicker one the

dedoping can occur harder (see subchapter *3.3.1.* for the an estimation of the Raman laser temperature).

The temperature of the Raman laser is responsible for the decrease of the signal observed in *Figure 4.12* and experimentally it was also observed that the laser has also an influence over the structure of some areas.

When a gold or silver substrate is roughened, the Raman signal is enhanced due to a phenomenon called Localized Surface Plasmon Resonance (LSPR) (see Chapter 1). To obtain such a roughened gold or silver surface, oxidation-reductions cycles are made [32]. The Raman spectra obtained in these enhanced conditions is called Surface Enhanced Raman Spectroscopy (SERS). The same effect can be obtained if gold or silver nanoparticles (NPs) are used. However, in these cases, NPs with diameters in the range of 20 – 100 nm are required to obtain LSPR that can induce the SERS [33,34].

Since the $AgNO_3$ was used, it is expected that after the UV activation the NO_3^- ion will contribute to the PPy doping (as observed in UV-VIS-NIR spectra of subchapter *4.3.2.1.*), leaving free Ag^+ ions. The Ag^+ ions then form Ag NPs. To achieve this transformation, the Ag^+ needs to be reduced by recovering an electron from electron donor specie [35]:

$$Ag^+ + e^- \rightarrow Ag$$

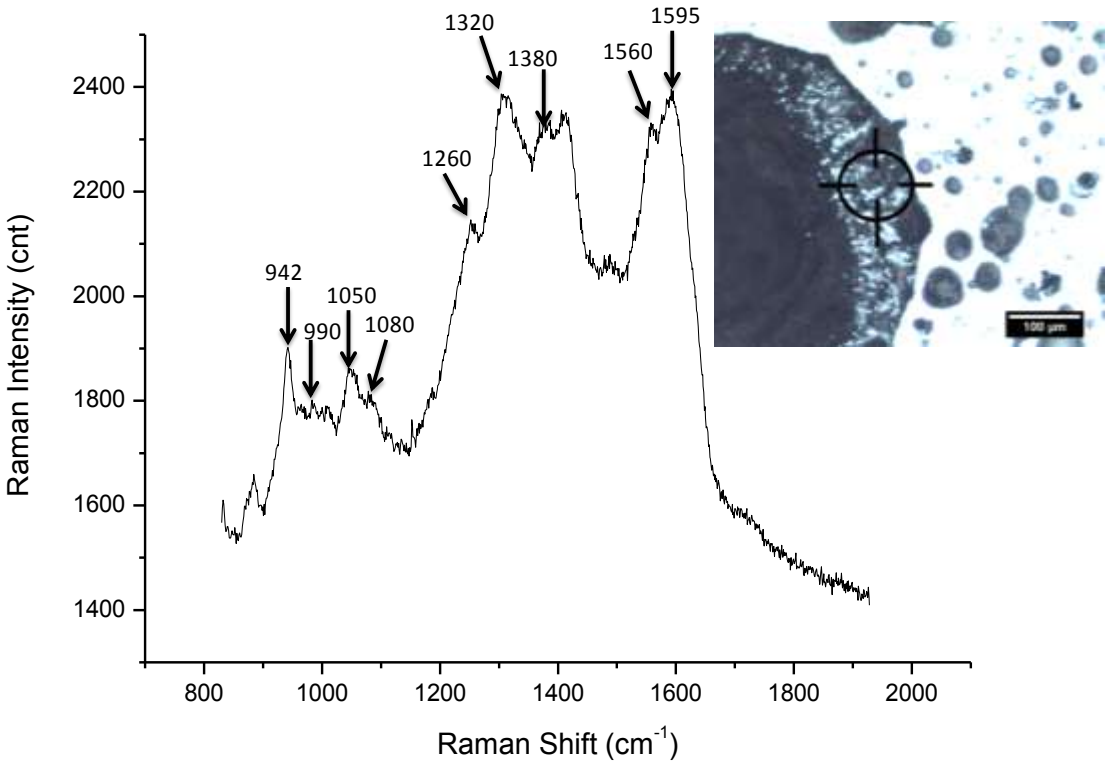

Figure 4.13: The Raman 532 nm spectra; In the inset is presented the in-situ area of the spectra acquisition (sample P3.3)

In this manner, after the UV radicalization of $AgNO^{3-}$, Ag NPs are expected to be obtained. Indeed, the Raman spectrum in *Figure 4.13* shows typical SERS bands that indicate the presence of Ag NPs. In the SERS spectra the C=C stretching associated to the conductive PPy is observed at 1595 cm^{-1}, but also the neutral species are present at 1560 cm^{-1}. The 1595 cm^{-1} shift is associated to the superposition of two oxidation states [36] and can also be associated as belonging to the cations [37]. Another indication of the oxidized state is given by the presence of the 940 cm^{-1} band [16,28]. The presence of the neutral species in the same spectral area is given by the presence of the 990 cm^{-1} band [37], and confirmed by the

presence of the 1320 cm^{-1} and 1050 cm^{-1} bands. The band observed at 1260 cm^{-1} is assigned to NH/CH in-plane deformation.

The above discussion highlighted evidences of the Ag NPs presence was given by the enhanced Raman spectra. To investigate the Ag NPs size, SEM characterization will be further presented.

4.3.3. Ag Nanoparticle sizes by FESEM

The knowledge of the NPs size is very important to control the properties. As the size decreases, the particles lose their metallic character, and become nonmetallic or semiconductive [38].

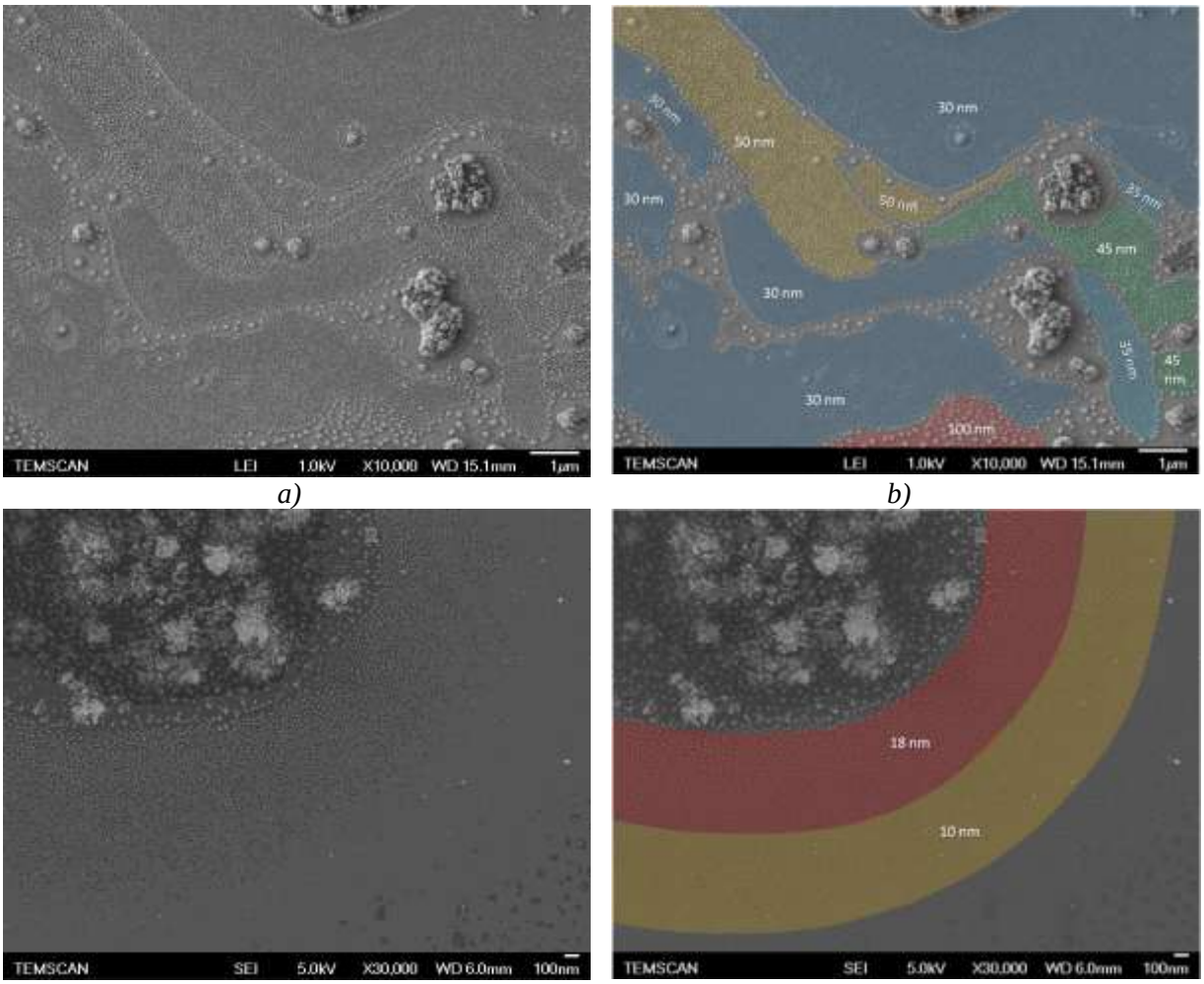

a) *b)*

c) *d)*

Figure 4.14: FESEM micrographies of a film on the Si(100) substrate deposition (P3.2 sample) with raw images (a, c) and the images highlighted with regions where nanoparticles of specific diameter reside (b, d); the numbers in the images represent the nanoparticle size

This is mainly because the interfacial atoms are coordinatively highly unsaturated, interacting only with the atoms inside the particle and having free valences outside. For example a three shell cluster has 92 interfacial atoms of Au (62.6 %) and 147 total atoms. With respect to the size, a 5 nm cluster has 23 % surface atoms, 2 nm atom clusters has 58 % surface atoms[39], while a 1 nm particle has all of the atoms at the interface except one.

For the obtained PPy/Ag NPs film, the distribution of the Ag NPs size is highlighted in *Figure 4.14 b)* and *d)*. In *Figure 4.14 a)* a fluid flow behavior is suggested. This can be indeed the case as the SEM image was taken in the vicinity of a 500 μm polymerized blister (such as the one presented in the *Figure 4.13* inset). This aggregation around the observed

"polymerized blister" can originate from the same conditions as the ones discussed with respect to the surface energy (subchapter *4.1.3.1.*). In those conditions a high concentration of Ag^+ ions can be suspected, leading to islands of Ag NPs ranging between 30 and 100 nm, as observed in *Figure 4.14 b)*.

In an area more isolated, close to what seems to be a 4 µm polymerized blister, two particle sizes are observed: 18 nm close to the blister and 10 nm further from the blister, as observed in *Figure 4.14 d)*. This is a first indication that the size of the Ag NPs is dependent to the quantity of the material available for the reaction (namely close to a bulk area of a polymerized blister).

Indirectly, the same size is obviously related to the concentration of Ag^+ ions. The limited concentration of Ag^+ ions in certain areas leads to the formation of a closed packed 30 nm (*Figure 4.13 b*) or 10 nm particles (*Figure 4.13 d*). When the NPs size increases (such as the case of NPs of 100 nm sizes in *Figure 4.13 b* and 18 nm in *Figure 4.13 d*) the NPs interdistance increases also. This is an indication for a NPs growth process limited by the Ag^+ ions concentration.

4.4. Addressing the UV gas phase activation

The presence of "polymerized blisters", *i.e.* structures without encapsulated liquid, is indicative of UV activation of the liquid droplets on the substrate (*Figure 4.14 a* and *b*). The UV exposure of the samples due to the scattered radiation is suspected. This can be seen by optical microscopy analysis, especially 75 min after the deposition experiment, when a change of color was observed (*Figure 4.10 b*). The experiment presented further is devised to address this issue.

4.4.1. Experimental

The experimental setup of the substrate was designed to minimize the scattered UV radiation on certain substrates and to allow a segment of the deposition to be based strictly on the monomer gas infiltration.

Table 4.3: The PhotoCVD experimental parameters; the liquid precursor was a mixture of Py:AgNO3 with a molar ration of 50:1 and 3 % HCPK photonitiator

Gas flow		Pressure		Temperature		DLI system			
						liquid		gas	
Q_{N2}	150 sccm	P_{N2}	3.5 bar	T_{inj}	60 °C	t_{on}	1 ms	f	1 Hz
		P_{MFM}	2 bar	T_{uv}	80 °C	f	1 Hz	Setpoint	10%
		P_T	9.5 Torr	$T_{substrate}$	17 °C	t_{exp}		150 min	

This was achieved by overlapping two optical microscope glass substrates separated by an inset with a height of about 5 mm, as seen in *Figure 4.15*. Also, a smaller 1x1 cm^2 Si(100) substrate (*Figure 4.15 a*) was covered by another 2x2 cm^2 Si(100) substrate (*Figure 4.15 b*) with a 3 mm inset to enhance the UV screening. In this manner, a variation in covering the substrate area was achieved (6.25 cm^2 glass vs 1 cm^2 Si(100)) and also a variance in height separation (the inset ranging from 5 cm to 3 cm).

The substrates were previously prepared by the degreasing, ultrasonication and Ar gas stream drying.

The gas infiltration is expected to imply a lowered flow rate of gaseous monomer to the covered substrate, thus the experimental time was prolonged to 150 min. The rest of the PhotoCVD parameters are given in *Table 4.3*.

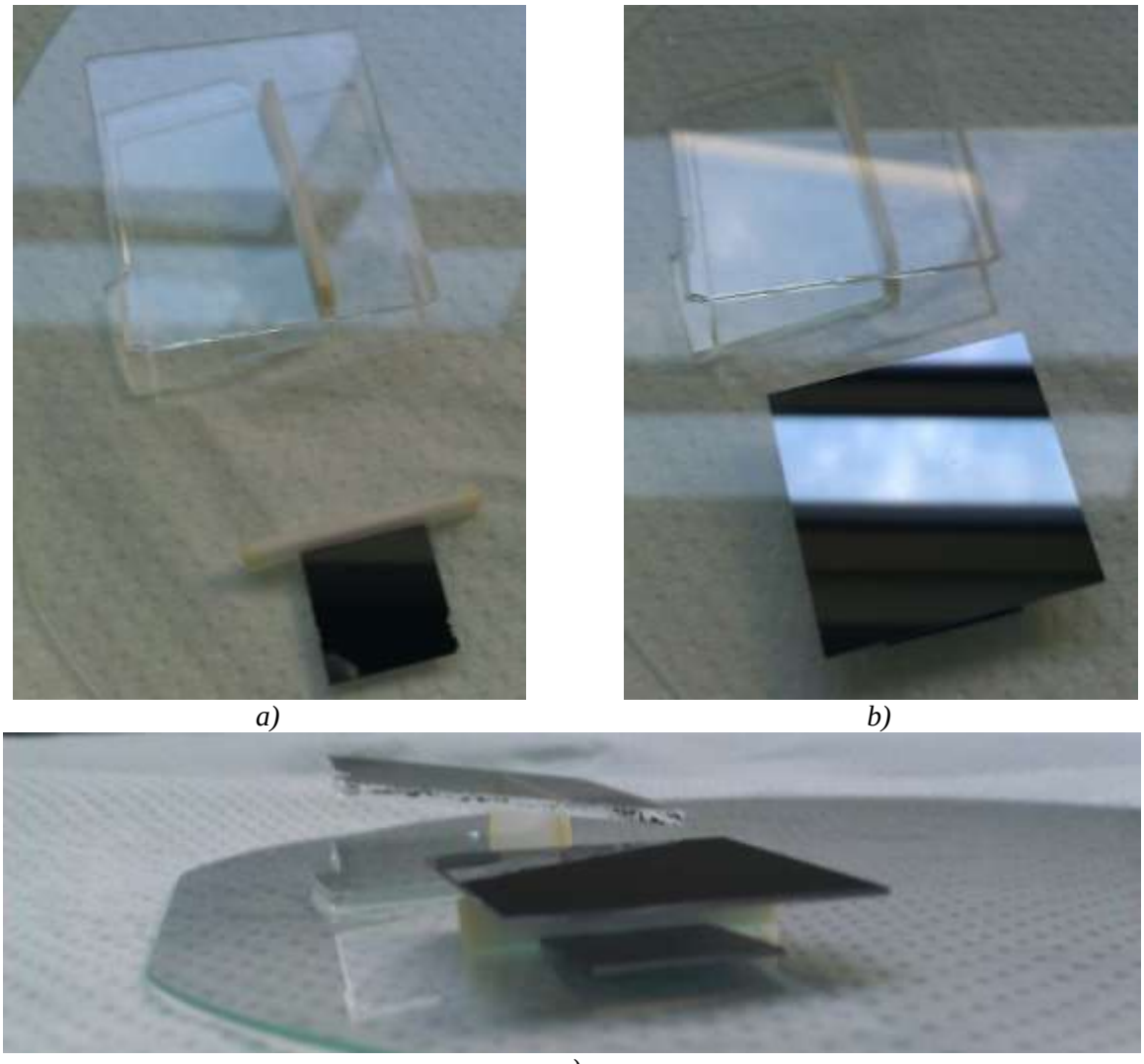

a) *b)*

c)

Figure 4.15: The superimposed substrate setup

All the substrates on the sample holder were not aligned with the vertical axis of the UV chamber. In *Figure 4.16 a)* this deviation is highlighted. After the samples removal from the CVD reactor, a thick black PPy deposition was observed over a circular area of D_1 = 3 cm in diameter. The 3 cm diameter area is observed only for the glass substrate (separated by an inset 2 mm higher than the Si(100) substrate). The Si(100) does not show significant increase in thickness in that range. Condensation and drops falling from the UV region are suspected.

A wider zone over the entire glass sample holder is highlighted that describes a circular area with a diameter D_2 = 6 cm. The samples were coded for subsequent identification during the characterization. The coding is shown in *Figure 4.16 a)* and *b).*

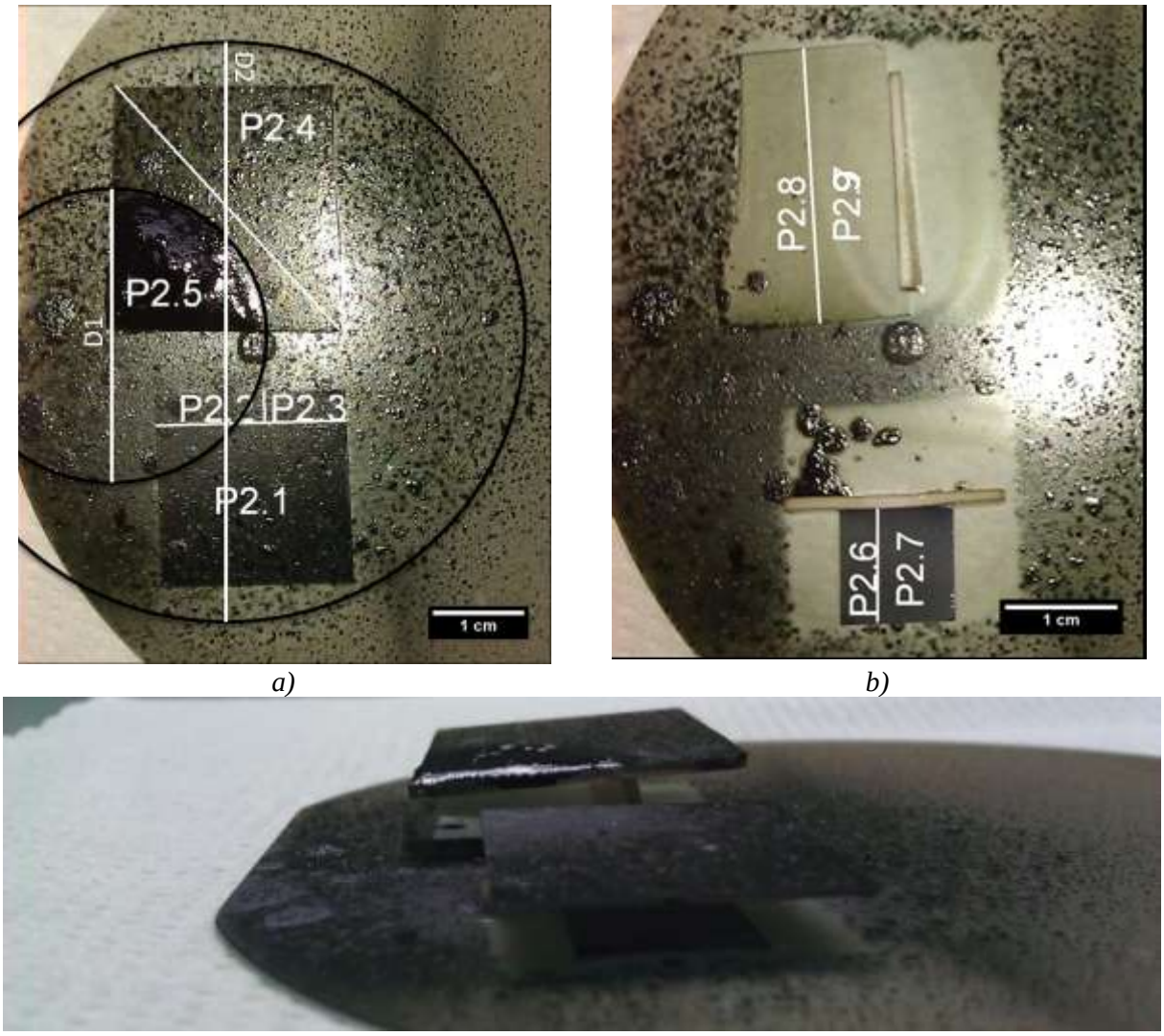

a) *b)*

c)

Figure 4.16: The covering of the superimposed substrates c) with the top a) and bottom b) substrates

4.4.2. Chemical Characterization of the PPy Thin Films

The characterization will be focused on the polymer doping, Ag NPs presence and the properties of the films deposited both in the vertical axis direction of the setup (line of sight), namely the "top substrates", and on the "bottom substrates" where the growth occurred by gas infiltration and without direct UV activation of the substrate.

4.4.2.1. UV-VIS-NIR investigation

As discussed previously, the film thickness over the glass substrates is very different depending on its position. The transmittance varies with the film thickness. A transmittance of about 85 % in visible range was reported for PPy films of thicknesses between 35 and 45 nm thick [24]. It decreases to *ca.* 60 % for films of around 70 nm thick [24].

In our case, it can be observed from the transmission spectra that a relatively high transmittance of 60 % was obtained for P2.9 and P2.8 bottom samples (*Figure 4.17 a*). However, as observed in the photographs obtained after the PhotoCVD run (*Figure 4.16*), the film is not homogenous over the entire substrate. Thus the transmittance is an averaged response for the analyzed area, and it only offers a rough estimation of the film thickness.

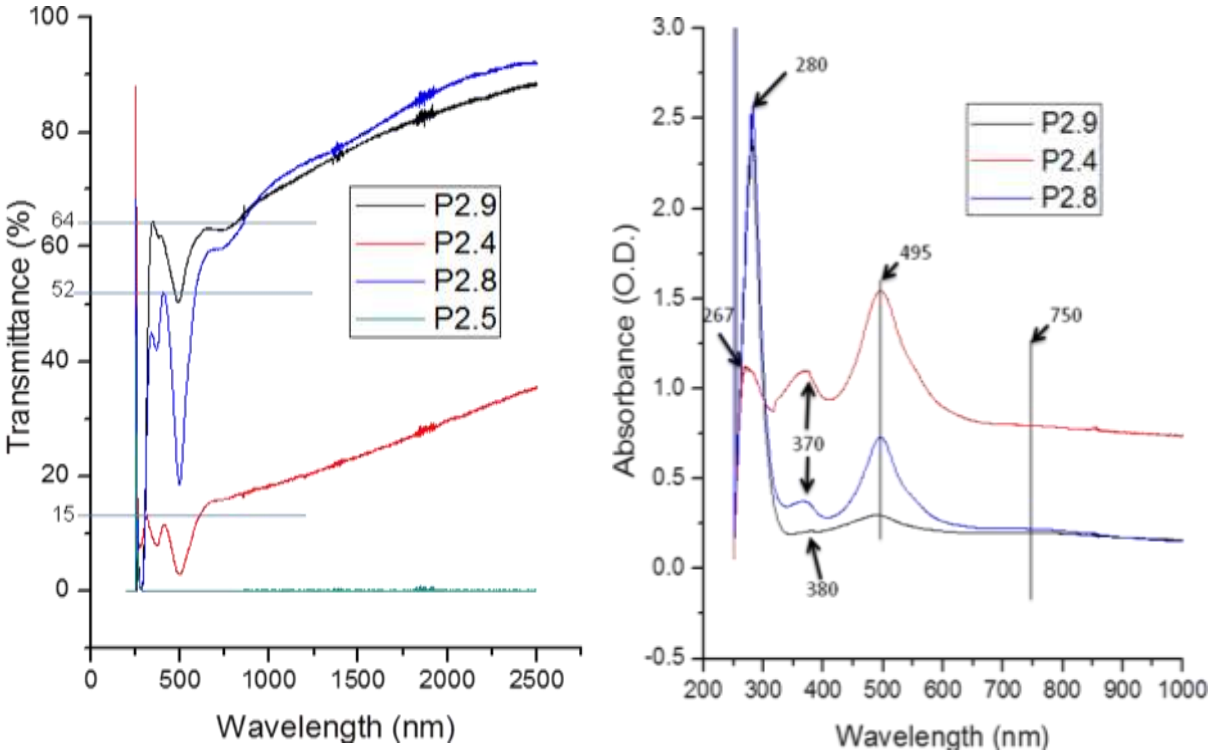

a) *b)*

Figure 4.17: UV-VIS transmission (a) and absorption (b) spectra for different substrates both above and below the direct vapor flux (See Figure 4.16 for sample names)

One aspect that needs to be mentioned is the fact that the thick inset used to separate the two glass substrates contaminated the glass area marked as P2.9 as observed in *Figure 4.16 b*. FTIR measurements showed that the contamination did not extend to P2.8 area. This explains the slight difference in transmission for the two samples.

In the UV region of the absorption spectra, two distinct peaks can be observed at 267 and 280 nm (*Figure 4.17 b*). This can be due to the photo-initiator remained in the film. The wavelength shift can be an effect of the glass cutoff in UV region.

An absorption peak at 370 nm is reported in literature to be associated to the neutral form of PPy [40], and is increasing as the free carrier peak observed at 800 nm is decreasing. At 750 nm a peak is observed that can be associated to the conductive state of PPy, as it is close to the reported peak at 800 nm and confirms the literature report that indicates the contribution of the doped Py oligomers as a peak which starts at 652 nm and extends into NIR [41]. The low absorption at 750 nm can be an indication of a low doping of PPy film grown on the glass substrate. The peak observed at 495 nm can be associated to the PPy π - π^* transitions and the Ag NPs contribution [27,42].

The results indicate the presence of PPy polymer, both over the "top" and "bottom" substrates. Also a low doping of the polymer is indicated for the films on the glass substrate.

4.4.2.2. Doping investigation

As previously presented, the Raman spectra can provide a further insight into the doping of PPy thin films *(4.3.2.2.*). The area that is most indicative with respect to the doping is the one for the C=C backbone stretching around 1600 cm^{-1}. The monomer can be in polaron (cation) or bipolaron (dication) state. The bipolaron state indicates higher conductivity for the PPy films. The bands associated to the dipolaron state were extrapolated in literature as expressed in 1613 – 1620 cm^{-1} range [37]. A small band of the dipolaron state is observed in the Raman spectra in *Figure 4.18* for the coated Si(100) substrate (P2.4). Raman bands in the range of 1605 and 1585 cm^{-1} are associated to the cations (polarons) [16,18,37]. The peak

observed in *Figure 4.18* for P2.4 indicates the cation presence, and it extends down until 1590 cm^{-1} [37]. Peaks in the range of 1557 and 1560 are indicative to the neutral species [37]. The neutral species can be observed on both substrates, however with a dominant contribution for the glass substrate. The neutral species of PPy on the glass substrate confirm the previous UV-VIS results. The Raman spectrum for glass in *Figure 4.18* indicates that the Ag NPs is not present (no SERS enhancement) but also it indicates that no doping is involved. The doping may be occurring on glass; however no evidence of this was found by the limited number of Raman analysis.

To further confirm the doping observed on Si(100) substrate, a high dication peak is observed at 940 cm^{-1}[37]. The presence of neutral species is probably indicated by a small shoulder at 927 cm^{-1} [37].

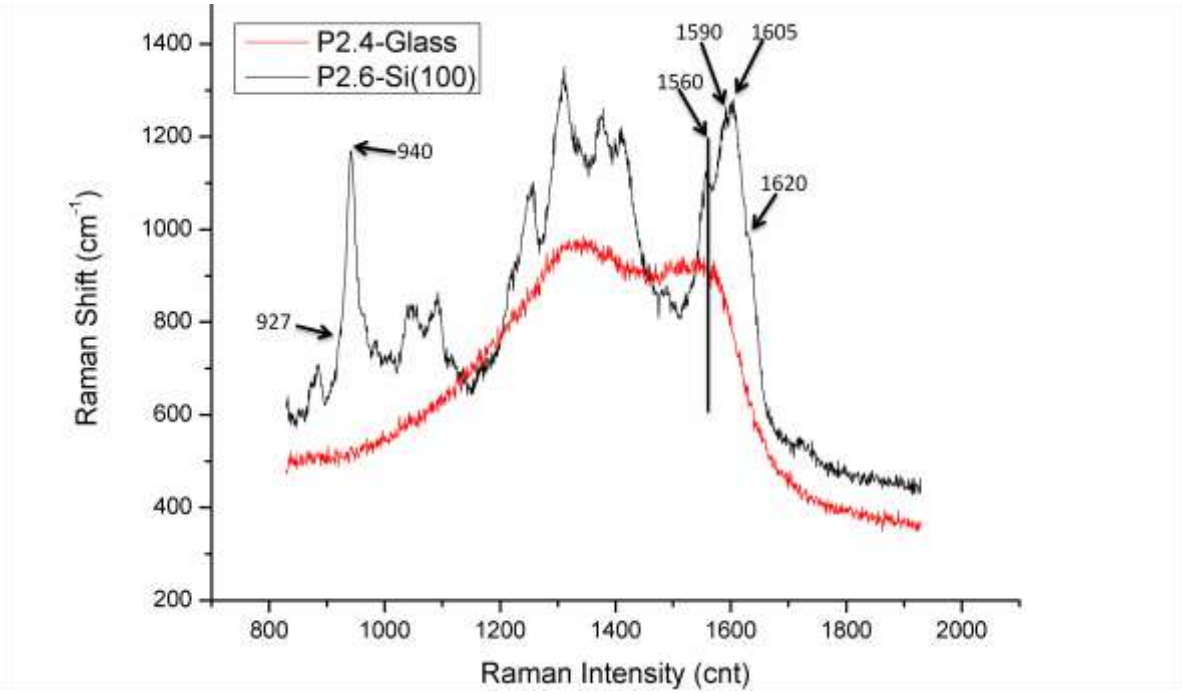

Figure 4.18: Raman spectra of different substrates: glass (P2.4) and Si(100) (P2.6)

As observed by SERS, the deposition by gas phase infiltration without direct UV irradiation (bottom sample) leads to a PPy thin film with high doping. As the experimental setup was designed to minimize the UV scattering over the studied substrate, it can be concluded that deposition occurred mainly by the polymerization from a UV activated gas-phase.

4.4.3. Surface self-ordering

In order to investigate the thin films obtained over the exposed (top) and the covered (bottom) substrates, the low energy FESEM technique was used.

The surface for the thin film deposited in the line of sight with the vertical axis of the setup indicates a rough surface (*Figure 4.19 a*). This is confirmed by AFM measurement that shows a roughness of R_a = 149 nm. In *Figure 4.19 a)* structures of crystalline aspect are highlighted with white rectangles. A zoom over three of such structures is presented in *Figure 4.19 b), c)* and *d)*. They present geometrical shapes that can be described as facets. The edges of the facets are decorated with Ag NPs with diameters around ~ 40 nm. On all of the crystalline structures, the Ag NPs on the facets are ordered on a line of 3 µm in length. In *Figure 4.19 b)* an equilateral triangle of Ag NPs is observed. An angle of 60° between two Ag

NPs self-ordered lines is also observed in *Figure 4.19 d)*, but the Ag NPs are not ordered to finalize the third side of the equilateral triangle.

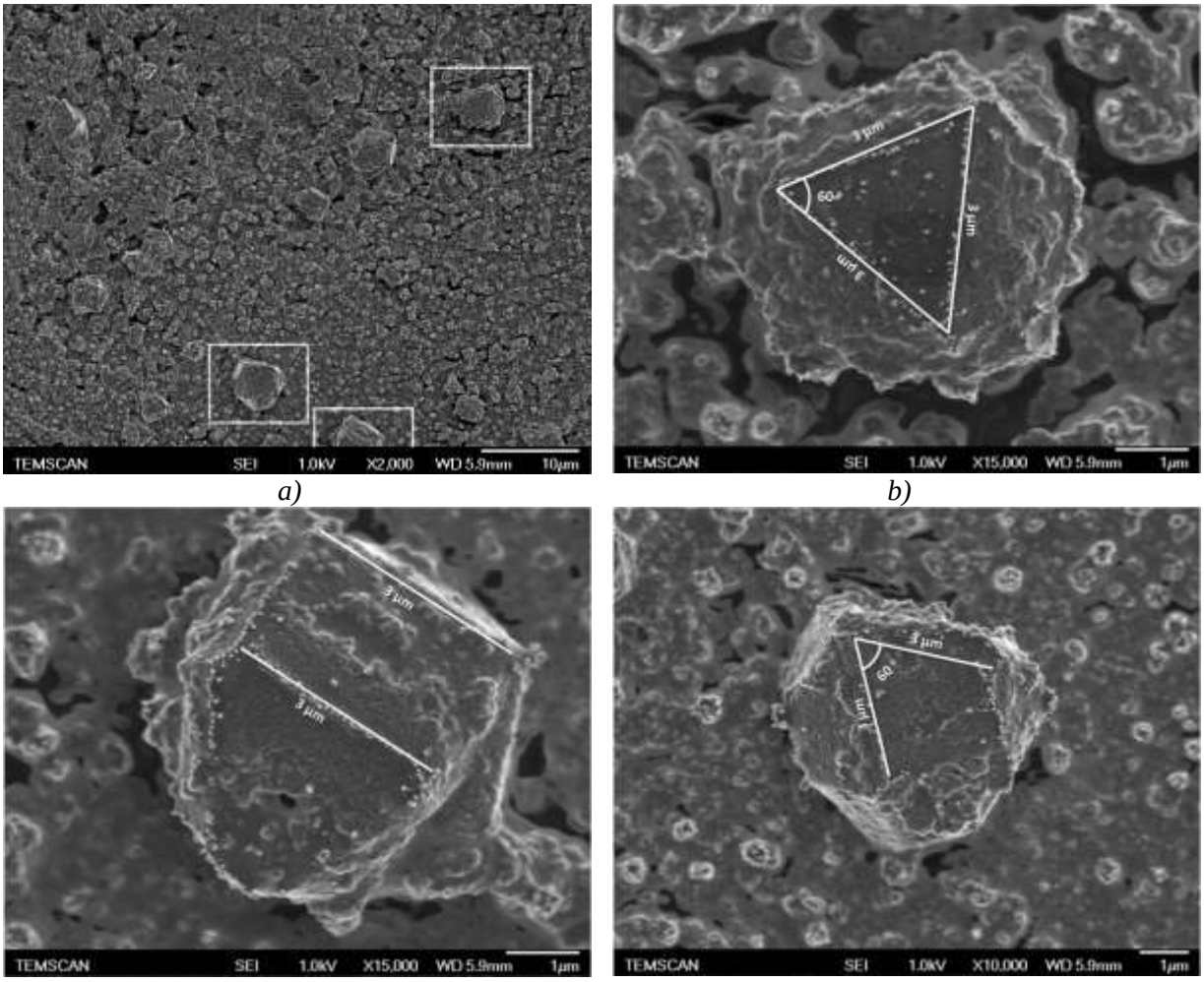

a) *b)*

c) *d)*

Figure 4.19: FESEM micrographs of the film deposited on Si(100)
(P2.2 – "top" sample in the line of sight to the carrier gas)

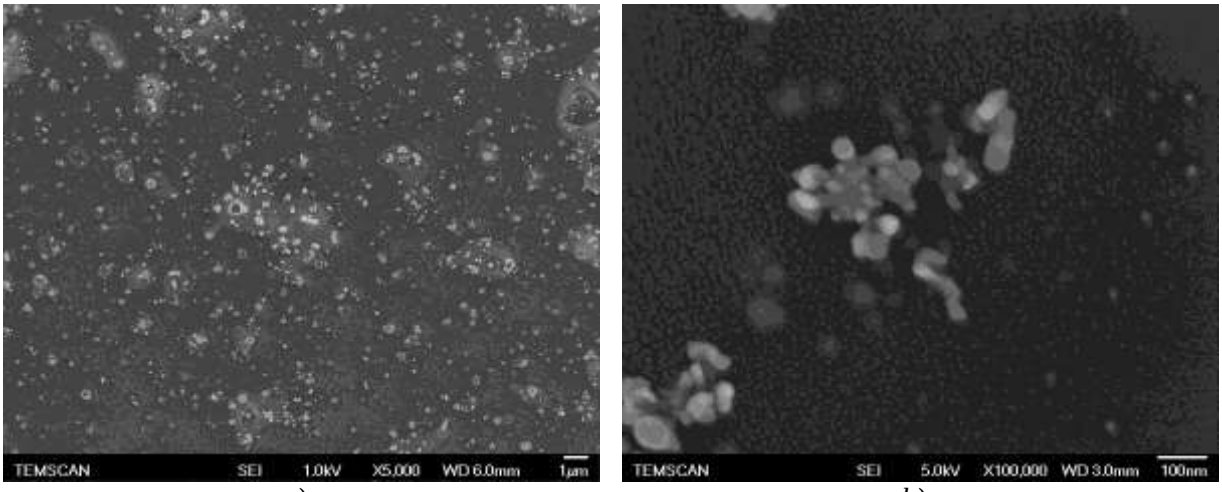

a) *b)*

Figure 4.20: FESEM micrographs of the film deposited on Si(100)
(P2.4 – "bottom" sample posted under a Si(100) substrate)

The reproducibility of the length and angle for the crystalline morphology suggest processes that are related to the surface energy. The surface energy involved can be probably the one of Si(100) substrate at the first stages (as observed previously in subchapter *4.1.3.1.*), and subsequently controlled by Ag NPs interfacial energy, as the Ag interfacial atoms are coordinatively highly unsaturated (see subchapter *4.3.3.*).

The film obtained on the "bottom" samples by gas phase infiltration is shown in *Figure 4.20*. The surface has a relatively smooth morphology (R_a = 68 nm). Ag NPs with diameters around 7 nm are observed without self-order

4.5. Chemical Mechanism Overview of the PPy Deposition by CVD

The Photo-CVD experiment was made by vaporizing the liquid Py monomer into a reactive gas phase transported to the substrate. In order to enhance the photo-initiation in the gas phase, an electron donor (1-hydroxycyclohexyl-phenyl ketone - HCPK) was mixed with the monomer. The HCPK photo-initiator generates a radical state after the UV activation [43]:

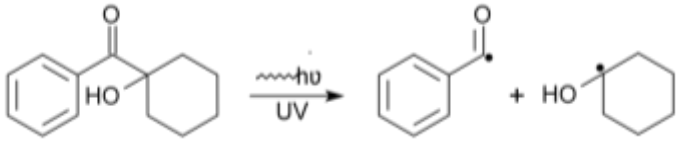

With the aid of the HCPK as photo-initiator, Py can polymerize according to the relation [44–46]:

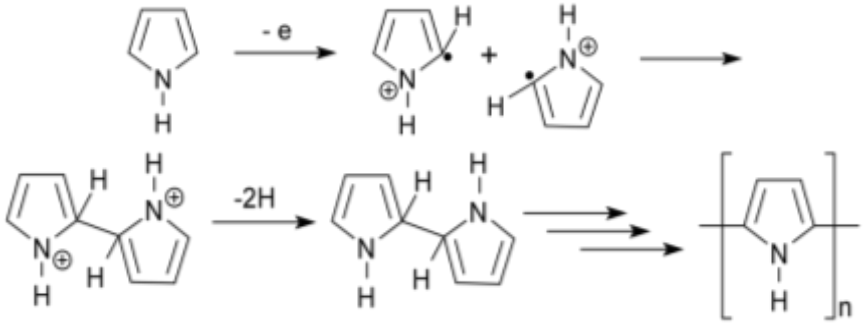

The PPy obtained by this manner is undoped and its main feature is a low conductivity around 10^{-12} S/cm [44]. Also the efficiency of the polymerization is very low. In order to enhance the polymerization, $AgNO_3$ was added with a Py:$AgNO_3$ molar ratio of 50:1 with 2% HCPK. The $AgNO_3$ is a source NO_3^- anion (A^-) for the PPy reaction [47]:

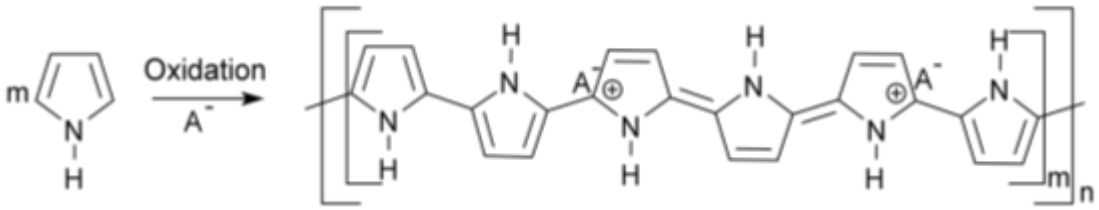

where *m* describes the degree of doping and *n* is the length of the polymer chain that determines the molecular weight. The presence of the conductive (doped) or neutral (undoped) species in PPy film was investigated by Raman. Also, the PPy doping level was determined by XPS (NO_3^-/N-H ratio) to be at around 16 % for P2.3 sample (see *Figure 4.16* in subchapter *4.4.1.* for sample setup and naming). It is a relatively good value, as in the literature the doping of the film grown electrochemically was reported to have a doping level of around 22 - 26 % [25]. Lower values are also found for different doping elements, such as Cl^- (9 – 19 %) [48] or benzensulfonic acid (7 – 20 %) [49].

By a parallel process, Ag^+ anion aggregates to form nanoparticles:

$$Ag^+ + e^- \rightarrow Ag$$

The PPy samples obtained with $AgNO_3^-$ did not indicate a good homogenous surface (*Figure 4.16* and *Figure 4.10*). To obtain a better homogeneity of the film, a wet synthesis route will be treated, namely the electrochemical deposition of PPy.

Bibliography

[1] E.H. Yu, K. Sundmacher, Enzyme Electrodes for Glucose Oxidation Prepared by Electropolymerization of Pyrrole, Process Safety and Environmental Protection. 85 (2007) 489–493.
[2] R. McNeill, R. Siudak, J.H. Wardlaw, D.E. Weiss, Electronic conduction in polymers. I. The chemical structure of polypyrrole, Australian Journal of Chemistry. 16 (1963) 1056–1075.
[3] B.A. Bolto, D.E. Weiss, Electronic Conduction in Polymers. II. The Electrochemical Reduction of Polypyrrole at Controlled Potential, Australian Journal of Chemistry. 16 (1963) 1076–1089.
[4] B.A. Bolto, R. McNeill, D.E. Weiss, Electronic conduction in polymers. III. Electronic properties of polypyrrole, Australian Journal of Chemistry. 16 (1963) 1090–1103.
[5] M.F. Mabrook, C. Pearson, M.C. Petty, Inkjet-printed polypyrrole thin films for vapour sensing, Sensors and Actuators B: Chemical. 115 (2006) 547–551.
[6] D. Svirskis, J. Travas-Sejdic, A. Rodgers, S. Garg, Electrochemically controlled drug delivery based on intrinsically conducting polymers, Journal of Controlled Release. 146 (2010) 6–15.
[7] J.H. Collier, J.P. Camp, T.W. Hudson, C.E. Schmidt, Synthesis and characterization of polypyrrole–hyaluronic acid composite biomaterials for tissue engineering applications, Journal of Biomedical Materials Research. 50 (2000) 574–584.
[8] I.D. Sharma, V.K. Sharma, S.K. Dhawan, P.K. Saini, Modification and designing of electrodeposited polypyrrole film for optoelectronic applications, NISCAIR-CSIR. 50 (2012) 184 – 187.
[9] E. Smela, Conjugated Polymer Actuators for Biomedical Applications, Advanced Materials. 15 (2003) 481–494.
[10] S.M. Unni, V.M. Dhavale, V.K. Pillai, S. Kurungot, High Pt Utilization Electrodes for Polymer Electrolyte Membrane Fuel Cells by Dispersing Pt Particles Formed by a Preprecipitation Method on Carbon "Polished" with Polypyrrole, J. Phys. Chem. C. 114 (2010) 14654–14661.
[11] T.S. Olson, S. Pylypenko, P. Atanassov, K. Asazawa, K. Yamada, H. Tanaka, Anion-Exchange Membrane Fuel Cells: Dual-Site Mechanism of Oxygen Reduction Reaction in Alkaline Media on Cobalt−Polypyrrole Electrocatalysts, J. Phys. Chem. C. 114 (2010) 5049–5059.
[12] O.J. Murphy, G.D. Hitchens, D. Hodko, E.T. Clarke, D.L. Miller, D.L. Parker, Method of forming electronically conducting polymers on conducting and ..., U.S. Patent 6210537, 2001.
[13] S. Ghosh, G.A. Bowmaker, R.P. Cooney, J.M. Seakins, Infrared and Raman spectroscopic studies of the electrochemical oxidative degradation of polypyrrole, Synthetic Metals. 95 (1998) 63–67.
[14] Z.Y. Li, X.J. Zhu, L. Li, Y.N. Zhang, Synthesis of glucoside bonded metal porphyrins, Chinese Chemical Letters. 12 (2001) 425–428.
[15] W. Lian, Y. Sun, B. Wang, N. Shan, T. Shi, Synthesis and properties of 5,10,15,20-tetra[4-(3,5-dioctoxybenzamidephenyl] porphyrin and its metal complexes, Journal of the Serbian Chemical Society. 77 (2012) 335–348.
[16] J. Arjomandi, A.-H.A. Shah, S. Bilal, H. Van Hoang, R. Holze, In situ Raman and UV–vis spectroscopic studies of polypyrrole and poly(pyrrole-2,6-dimethyl-β-cyclodextrin), Spectrochimica Acta Part A: Molecular and Biomolecular Spectroscopy. 78 (2011) 1–6.
[17] Y.-C. Liu, Characteristics of vibration modes of polypyrrole on surface-enhanced Raman scattering spectra, Journal of Electroanalytical Chemistry. 571 (2004) 255–264.
[18] F. Chen, G. Shi, M. Fu, L. Qu, X. Hong, Raman spectroscopic evidence of thickness dependence of the doping level of electrochemically deposited polypyrrole film, Synthetic Metals. 132 (2003) 125–132.
[19] M.A. Pimenta, G. Dresselhaus, M.S. Dresselhaus, L.G. Canado, A. Jorio, R. Saito, Studying disorder in graphite-based systems by Raman spectroscopy, Physical Chemistry Chemical Physics. 9 (2007) 1276.
[20] K. Sugimoto, H. Fujiwara, S. Koda, Raman spectroscopic study on the local structure around O2 in supercritical water, The Journal of Supercritical Fluids. 32 (2004) 293–302.
[21] A. Das, M. Frenkel, N.A.M. Gadalla, S. Kudchadker, K.N. Marsh, A.S. Rodgers, et al., Thermodynamic and Thermophysical Properties of Organic Nitrogen Compounds. Part II. 1- and 2- Butanamine, 2- Methyl- 1- Propanamine, 2- Methyl- 2- Propanamine, Pyrrole, 1- ,2- , and 3- Methylpyrrole, Pyridine, 2- ,3- , and 4- Methylpyridine, Pyrrolidine, Piperidine, Indole, Quinoline, Isoquinoline, Acridine, Carbazole, Phenanthridine, 1- and 2- Naphthalenamine, and 9- Methylcarbazole, Journal of Physical and Chemical Reference Data. 22 (1993) 659–782.

[22] J. Godet, L. Pizzagalli, S. Brochard, P. Beauchamp, Surface step effects on Si (100) under uniaxial tensile stress, by atomistic calculations, arXiv:0709.1583. (2007).
[23] W.K. Liu, M.B. Santos, Thin Films: Heteroepitaxial Systems, World Scientific, 1999.
[24] J. Kim, D. Sohn, Y. Sung, E.-R. Kim, Fabrication and characterization of conductive polypyrrole thin film prepared by in situ vapor-phase polymerization, Synthetic Metals. 132 (2003) 309–313.
[25] Y. Li, R. Qian, Electrochemical overoxidation of conducting polypyrrole nitrate film in aqueous solutions, Electrochimica Acta. 45 (2000) 1727–1731.
[26] G.B. Street, T.C. Clarke, M. Krounbi, K. Kanazawa, V. Lee, P. Pfluger, et al., Preparation and characterization of neutral and oxidized polypyrrole films, Molecular Crystals and Liquid Crystals. 83 (1982) 253–264.
[27] M.D. Bedre, S. Basavaraja, R. Deshpande, D.S. Balaji, A. Venkataraman, Preparation and Characterization of Polypyrrole Silver Nanocomposites via Interfacial Polymerization, International Journal of Polymeric Materials. 59 (2010) 531–543.
[28] H. Nguyen Thi Le, M.. Bernard, B. Garcia-Renaud, C. Deslouis, Raman spectroscopy analysis of polypyrrole films as protective coatings on iron, Synthetic Metals. 140 (2004) 287–293.
[29] J.L. Bredas, G.B. Street, Polarons, bipolarons, and solitons in conducting polymers, Acc. Chem. Res. 18 (1985) 309–315.
[30] H.H. Kuhn, W.C. Kimbrell, Jr, Electrically conductive textile materials and method for making same, U.S. Patent 4803096, 1989.
[31] R.V. Gregory, W.C. Kimbrell, H.H. Kuhn, Conductive textiles, Synthetic Metals. 28 (1989) 823–835.
[32] Y.-C. Liu, B.-J. Hwang, W.-J. Jian, Effect of preparation conditions for roughening gold substrate by oxidation–reduction cycle on the surface-enhanced Raman spectroscopy of polypyrrole, Materials Chemistry and Physics. 73 (2002) 129–134.
[33] H.-J. Kim, M.-S. Lee, D.-G. Lee, M.-K. Son, K.-J. Lee, Optimal ablation of fluorine-doped tin oxide (FTO) thin film layers adopting a simple pulsed Nd:YAG laser with TEM00 mode, Optics and Lasers in Engineering. 47 (2009) 558–562.
[34] S.E.J. Bell, M.R. McCourt, SERS enhancement by aggregated Au colloids: effect of particle size, Physical Chemistry Chemical Physics. 11 (2009) 7455.
[35] K.-S. Chou, Y.-C. Lu, H.-H. Lee, Effect of alkaline ion on the mechanism and kinetics of chemical reduction of silver, Materials Chemistry and Physics. 94 (2005) 429–433.
[36] J. Duchet, R. Legras, S. Demoustier-Champagne, Chemical synthesis of polypyrrole: structure–properties relationship, Synthetic Metals. 98 (1998) 113–122.
[37] M.J.L. Santos, A.G. Brolo, E.M. Girotto, Study of polaron and bipolaron states in polypyrrole by in situ Raman spectroelectrochemistry, Electrochimica Acta. 52 (2007) 6141–6145.
[38] D. Astruc, Nanoparticles and Catalysis, John Wiley & Sons, 2008.
[39] K. Rurack, R. Martínez-Máñez, The Supramolecular Chemistry of Organic-Inorganic Hybrid Materials, John Wiley & Sons, 2010.
[40] J.Y. Wong, R. Langer, D.E. Ingber, Electrically conducting polymers can noninvasively control the shape and growth of mammalian cells., Proc Natl Acad Sci U S A. 91 (1994) 3201–3204.
[41] S. Gu, B. Li, C. Zhao, Y. Xu, X. Qian, G. Chen, Preparation and characterization of visible light-driven AgCl/PPy photocatalyst, Journal of Alloys and Compounds. 509 (2011) 5677–5682.
[42] C. Martins, Y. de Almeida, G. do Nascimento, W. de Azevedo, Metal nanoparticles incorporation during the photopolymerization of polypyrrole, Journal of Materials Science. 41 (2006) 7413–7418.
[43] N.S. Allen, Radiation curing in polymer science and technology vol, II: Photoinitiating systems, edited by J. P. Fouassier and J. F. Rabak. Elesvier Aplied Science Publishers, London (distributed by Chapman and Hall, Andover, Hamsphire), 1993. pp. viii + 717, price £95.00. ISBN 1-85166-933-7, Polymer International. 35 (1994) 106–106.
[44] H.R. Allcock, Introduction to Materials Chemistry, John Wiley & Sons, 2011.
[45] D. Braun, H. Cherdron, M. Rehahn, H. Ritter, B. Voit, Polymer Synthesis: Theory and Practice: Fundamentals, Methods, Experiments, Springer, 2004.
[46] T.A. Skotheim, J. Reynolds, Conjugated Polymers: Theory, Synthesis, Properties, and Characterization, Taylor & Francis, 2006.
[47] G.G. Wallace, S. Moulton, R.M.I. Kapsa, M. Higgins, Organic Bionics, John Wiley & Sons, 2012.

[48] Gautier J.L., Marco J.F., Gracia M., Gancedo J.R., de la Garza Guadarrama V., Nguyen-Cong H., et al., Ni0.3Co2.7O4 spinel particles/polypyrrole composite electrode: - Study by X-ray photoelectron spectroscopy, Electrochimica Acta. 48 (2002) 119–125.
[49] M. Aldissi, Intrinsically Conducting Polymers: An Emerging Technology, Springer, 1993.

CHAPTER 5 - PPy THIN FILMS OBTAINED BY WET ROUTE (ELECTROCHEMICAL)

The wet route of the PPy thin film growth involves a chemistry that is done in liquid phase. In this particular case, it implicates the electrochemical growth of the PPy in an aqueous solution. The advantage of the growth by this route is mainly that it is facile to polymerize the Py monomer in a basic electrochemical cell under a low difference of potential, namely around -0.8 V.

The synthesis will be treated at low (in the order of nano mole nM) and relatively normal (in the order of micro mole µM) concentrations of Py monomer. The growth will be achieved on different substrates (named as working electrode with respect to the electrochemical cell configuration).

The growth at low concentrations will be investigated by the technique called Surface Plasmon Resonance (SPR). The technique is classically based on the refractive index changes at the interface of a gold electrode (substrate). To understand the approach that treats the SPR mechanism, a theoretical insight over the mathematical and the physical significance of the variables will be further treated.

5.1. The Harmonic Motion and its Physical Implications

The processes that are involved in some of the investigation techniques can be understood theoretically by analyzing the harmonic motion. The term harmonic gives an indication that the motion is synchronized as a wave or in a circular manner. For example such a synchronized motion can be considered for ions or electrons under certain perturbation conditions.

5.1.1. General Aspects

In *Figure 5.1 a)* it can be observed that the *y* axis has multiple values. If we define the period Π as the time it takes for an object to complete one oscillation and return to the starting position, we can define the angular speed (measured in *rad/s*) as:

$$\omega = \frac{2\pi}{\Pi} \qquad (5.1)$$

Furthermore, the frequency can be defined as the inverse of the period (measured in *Hz*= 1/*s*):

$$\upsilon = \frac{1}{\Pi} = \frac{\omega}{2\pi} \qquad (5.2)$$

If we consider a certain time *t*, then the *z(t)* is at a point of a circle with radius *A* at an instant angle ωt to the *x* axis is:

$$z(t) = A\cos\omega t + iA\sin\omega t \qquad (5.3)$$

When a certain type of energy is applied over a system in a periodic manner described by a harmonic oscillation, that energy can be absorbed or it can be stored. The transmitted energy does not imply any change to the state of the receiving system, thus it will not be considered at this point. The absorbed energy is described by the real part of the harmonic function ($A\sin\omega t$).The stored energy is described by the imaginary of the harmonic function

($iA\sin\omega t$). The stored energy is released after a period of time, generally called the relaxation time.

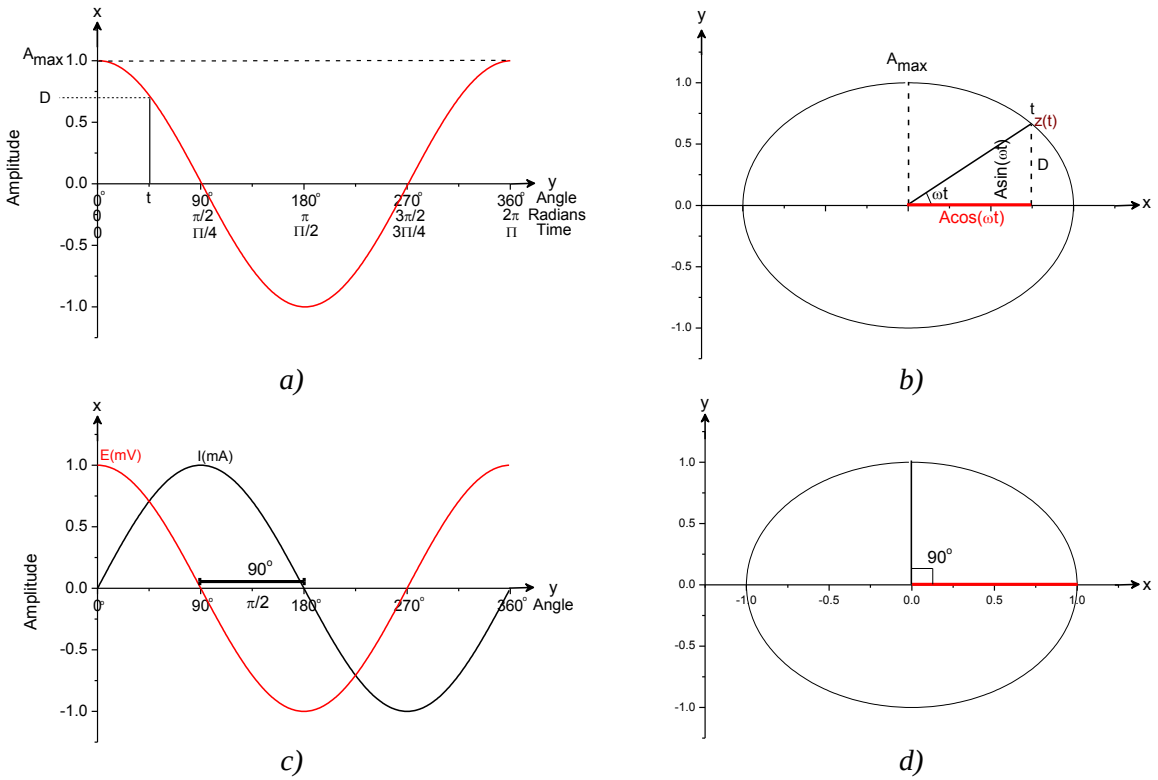

Figure 5.1: Simple harmonic motion (a, b) and the shift between two harmonics (c,d); the harmonic motion is represented in real (a, c) and in real/complex planes (b, d)

Further examples of physical implication of this mathematical model in the investigation techniques will be further treated.

5.1.2. AFM Phase Images

The previous studies on the phase images of the deposited films were used to indicate the liquid presence over the substrate (subchapters *3.2.3.* and *4.1.3.2.*). The phase images were obtained by a simple process that can be described by the harmonic motion of the AFM cantilever. The AFM cantilever in "Acoustic Mode" is set to oscillate at a frequency of around $150*10^3$ Hz. When it interacts with the sample, the cantilever's oscillation presents a phase shift (measured in angles). This was associated mainly to the Van der Waals interactions that induce a phase shift. The phase shift occurs due to the relaxation process of the intramolecular vibrational modes [1]. In an AFM study reported in literature, the prediction of the repulsive Van der Waals forces over a specific material system was possible by considering the dielectric response function [2]. The dielectric response is another example of the harmonic motion.

5.1.3. Dielectric Relaxation Spectra

The dielectric permittivity is the measure of a materials resistance to an electric field. If we consider an applied polarizable difference of potential over a sample (AC) around the equilibrium state, the system response will be described by the relative permittivity as [3]:

$$\varepsilon_r(\omega) = \varepsilon_r'(\omega) + i\varepsilon_r''(\omega) \qquad (5.4)$$

The term relative refers to the fact that the measured permittivity is defined as the ratio of the absolute permittivity (ε) and the vacuum permittivity (ε_0):

$$\varepsilon_r(\omega) = \frac{\varepsilon(\omega)}{\varepsilon_0} \qquad (5.5)$$

The real term of the permittivity ($\varepsilon_r^{'}$) is considered as describing the energy storage of the system and the imaginary part ($\varepsilon_r^{''}$) is considered as representing the dielectric loss. The period it takes for a system to reach the equilibrium after a perturbing energy was applied is called the relaxation time and can also be described by the phase shift (such as the one observed in *Figure 5.1 c* and *d*) through the angular speed ω. The perturbing energy can be due to an applied difference of potential (such as the one in an electrochemical cell) in a polarized manner. If the perturbing energy is an electromagnetic energy of a photon, the frequency is equal with the ratio between the speed of light (c) and the wavelength (λ):

$$\upsilon = \frac{c}{\lambda} \qquad (5.6)$$

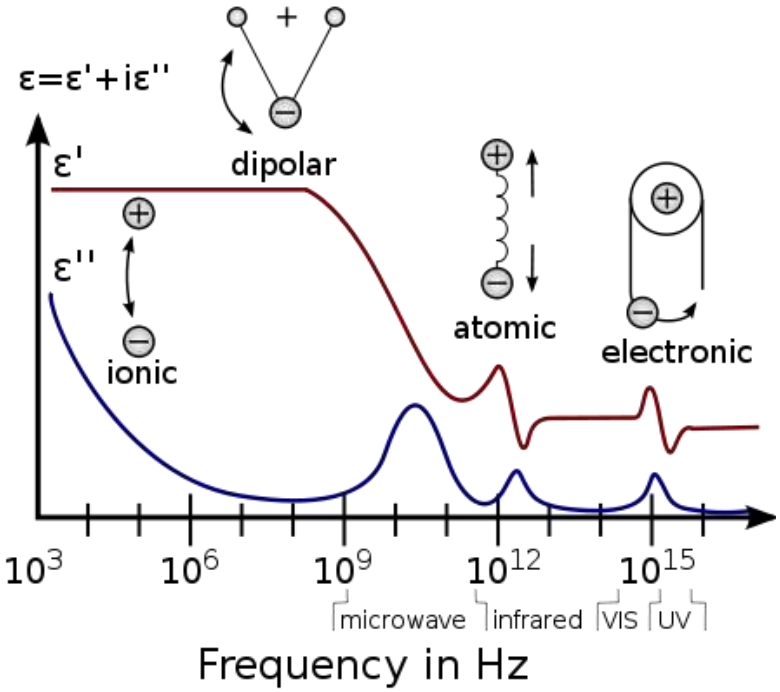

Figure 5.2: A dielectric permittivity spectrum over a wide range of frequencies[12].

While applying a perturbing energy with various frequencies over a dielectric medium, relaxation occurs and it varies differently with frequency. The dielectric permittivity spectrum over a wide range of frequencies is shown in *Figure 5.2*. The ionic and dipolar relaxation is observed at relatively low frequencies (in the kHz and GHz range) and the atomic and electronic relaxation is observed at high frequencies in the UV-VIS-IR range (from THz to PHz). Relaxation models had been considered to describe the frequency behavior [4].

A generalization of the Debye model that treats the frequency spectrum is given by the Harviliak-Negami formula:

$$\varepsilon_r^{'}(\omega) = \varepsilon_\infty + \frac{\varepsilon_s - \varepsilon_\infty}{\left[1 + \left(i\frac{\upsilon}{\upsilon_{rel}}\right)^{(1-\beta)}\right]^{\alpha}} \qquad (5.7)$$

The term ε_s describe the "static frequency" (υ_0) of the dielectric constant that is the lowest frequency which does not induce a change of the orientation in the studied particles

[12] © Prof. Dr. Kenneth A. Mauritz (see original source page)

(the molecules, ions or electrons). The ε_∞ term describes the "infinite frequency" (υ_∞) for which the orientation (of the molecules, ions or electrons) does not have time to contribute to the polarization. The relaxation frequency, υ_{rel}, is the frequency at which the permittivity is (ε_s + ε_∞)/2. The β parameter describes the spread in relaxation frequency and the α parameter describes the asymmetric distribution of the relaxation times. Thus, α and β are used to describe different spectral shapes.

When β = 0 and α = 0 then the equation reduces to the Debye model for pure polar materials.

When $\alpha = 0$ and $0 \leq \beta \leq 1$, then the symmetric relaxation time is described by the Cole–Cole model.

For an asymmetric relaxation time and with no spread in frequency, thus for $\beta = 0$ and $0 < \alpha < 1$, the model is called the Cole-Davidson model.

For certain materials, conductivity loss due to ion motions (under DC conditions at $\upsilon = 0$) is taken into consideration by introducing σ_0 as the static electrical conductivity:

$$\varepsilon_r(\omega) = \left\{ \varepsilon_\infty + \frac{\varepsilon_s - \varepsilon_\infty}{\left[1 + \left(i \frac{\upsilon}{\upsilon_{rel}} \right)^{(1-\beta)} \right]^\alpha} \right\} - i \frac{\sigma_0}{\omega \varepsilon_0} \qquad (5.8)$$

As observed in *Figure 5.2* the frequency of the perturbation energy can reach into the visible range. When the discussion is focused in that spectral range, the term refractive index is usually used to discuss about the electromagnetic interaction of the light with different environments. The refractive index, *n*, can be viewed as the real part of the photons harmonic motion (oscillation) responsible for the transmitted energy when it passes in a solid medium. The absorbed energy of the same photon through the same medium can be described as the imaginary part of the harmonic motion, and is called the extinction coefficient, ξ. In wet chemistry ξ is considered as the absorbed light intensity in the UV-VIS range multiplied with the molecular mass of the investigated compound in the solution). The dielectric permittivity is the square root of the optical constants for solids (*n* and ξ) for the real and imaginary components [5]:

$$\varepsilon = \varepsilon' + i\varepsilon'' = (n + i\xi)^2 \qquad (5.9)$$

The real and imaginary parts of the dielectric permittivity with respect to the optical properties for solid yield:

$$\varepsilon' = n^2 - \xi^2 \qquad (5.10)$$

$$\varepsilon'' = 2n\xi \qquad (5.11)$$

The above formulas unite the range of the photons wavelengths with the dielectric permittivity frequency ranges, describing the common effect of a perturbing energy.

As observed in *Figure 5.2*, perturbation energy in the range of the kHz reveals aspects of the ionic relaxation. Under the wet electro-chemistry conditions a technique that investigates these aspects is the Electrochemical Impedance Spectroscopy (EIS).

In the visible range of frequencies for the perturbing energy (at THz scale) the relaxation of electrons can be addressed. The photon energy loss due to the electron interaction (collision excitation) at the interface of a dielectric (water) and metal (gold) is also investigated by the Surface Plasmon Resonance (SPR) technique.

The physical principles of the EIS and SPR technique based on the harmonic motion of ions and electrons respectively will be addressed as following.

5.1.4. Electrochemical Impedance Spectroscopy (EIS)

The EIS principle is based essentially by the delay in the current response as a result of an applied potential difference. The applied potential difference describes a sine wave with certain amplitude above and below an equilibrium state. The equilibrium state in a solution is generally called as Open Circuit Potential (OCP) or Open Circuit Voltage (OCV). The measured OCP is the potential of the working electrode relative to the reference electrode. In a classical three electrode electrochemical cell, the current is measured between the working electrode and a counter electrode.

The current response for EIS can occur with a delay with respect to the applied potential, and is described by a phase difference, θ. The impedance as defined by the phase difference, θ, can be written in polar form as:

$$Z = \cos\theta + j\sin\theta \qquad (5.12)$$

To avoid the confusion between the physical notation for electric current as i, and the mathematical notation of the imaginary number with the same notation, for EIS imaginary part is described by j.

In *Figure 5.1* the representation of the real part (Re = cos θ) and imaginary part (Im = sin θ) of the current response, also named Nyquist plots, can be seen. The real part is associated with a resistive behavior and the imaginary part is associated to a capacitive behavior. For calculus it is convenient to use radians, however for physical meaning the discussion will be taken in terms of degrees as it is closer to the previous discussions with respect to the AFM spectroscopy.

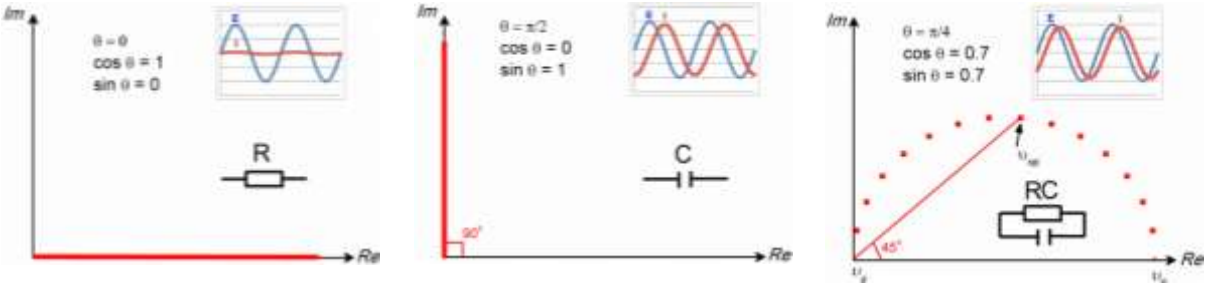

a) *b)* *c)*

Figure 5.3: The EIS representation of the imaginary (Im) and the real (Re) of different phase shift angles (θ) between the potential (E) and the current (I)

Figure 5.1 a) shows that a phase angle of 0 ^{o} reduces the imaginary (sin θ = 0) part and only the real part is observed. This indicates a pure resistive behavior. The current in *Figure 5.1 a)* was not reduced effectively to 0 (it was kept at 0.2 % intensity) in order to observe the wave profile of the response, but theoretically it should be represented as a straight line.

Figure 5.1 b) shows the case when the phase angle is at 90 ^{o} the imaginary part reaches the unit (sin θ = 1) and the real part gets reduced (cos θ = 0). This is indicative for a fully capacitive behavior. However in most of the experimental cases, such as the case of polymers, a combined resistive/capacitive behavior is observed. This behavior can be different for various frequencies. For such a behavior the Cole-Cole mathematical model previously described is used (subchapter *5.1.3.*).

The semicircle presented in *Figure 5.1 c)* has different phase shifts at various frequencies and it describes a shape associated to a combined parallel circuit of a resistance and a capacitance. The semicircle is analyzed at a relaxation frequency (υ_{rel} = (υ_s + υ_∞)/2) characterized by a phase shift of 45 ^{o} in *Figure 5.1 c).* The semicircle can be experimentally

obtained flattened or elongated. This semicircle shape is described by the β element in the Cole-Cole formula (*(5.8)*. More semicircles observed, more circuits connected in series are usually used.

As discussed, a decrease in amplitude indicates a resistive behavior. The loss of energy due to the resistivity converts it in thermal energy, as the resistor is heated. However, in the case of the photons, the loss of energy occurs not in amplitude, but in frequency and, conversely, in wavenumber (see equation *(5.6)*).

5.1.5. Surface Plasmon Resonance (SPR)

In 1887 H. Hertz observed that if electrodes are irradiated by UV light, then sparks of electrons can be obtained more easily [6]. This phenomenon was named as the Hertz effect. Max Planck published a law on the black body radiation which presents the assumption that Hertzian frequency can occur at energy (E) that is directly proportional to the frequency [7]:

$$E = h\upsilon \qquad (5.13)$$

where h is the Planck's constant. This indicates that when energy is lost by the photon, a change in photon frequency will occur.

Let's consider that light is composed of discrete energy particles (described by a wave function as the harmonic motion previously presented), called photons. When such a photon interacts with an electron, it transfers its energy to the electron by generating a *photoelectron*.

Einstein described this photoelectron effect by an equation that was later proved to agree with experimental results [8,9]:

$$\frac{1}{2} m_{pe} v_{pe}^2 = h\upsilon - p \qquad (5.14)$$

where m_{pe} and v_{pe} are the mass and the speed of the photoelectron and p is the work necessary to get the electron out of a metal. The above formula highlights the fact that in order to obtain a photoelectron (an emitted electron) the photon frequency will *decrease* (and conversely the wavelength will increase according to equation *(5.6)*) as the photon energy is ceased. With respect to an observable increase of a light intensity, this is given by the increase in photons flux (increased number of photons that flow per unit area), not by an increase in amplitude or frequency.

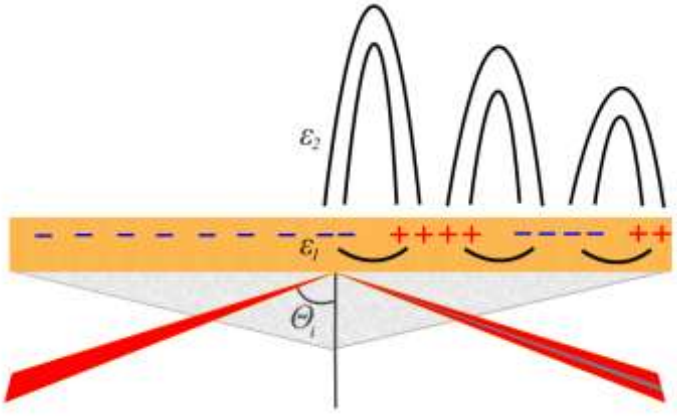

Figure 5.4: Surface Plasmon Resonance principle; Θ_i is the critical angle and ε_1 and ε_2 represent the dielectric permittivityes of the gold and the dielectric respectively

These aspects are at the basis of the Surface Plasmon Resonance investigation technique. When a VIS radiation (in the case of the apparatus that is used, 670 nm for Au) is reflected below a critical angle Θ_i at a metal interface (usually Au or Ag), a minimum of intensity occurs on the reflected side. This minimum is observed due to the photon energy that is ceased to the free electrons in the metal network. The free electrons are also generally

called plasmons. By this process, the electrons are moved from the metal network to the outer environment, and back, under the form of a collective oscillation. The collective oscillation can be also named as a resonant movement of plasmons (hence plasmon resonance). If the plasmon resonance occurs at a planar surface, it is called Surface Plasmon Resonance (SPR), and if the plasmon resonance occurs at a nanoparticle interface it is called Localized Surface Plasmon Resonance (LSPR).

In order for the SPR to occur, real part of the dielectric must change sign over the surface. The gold offers the negative dielectric function (ε_1 = - 12.57 + i 1.21) required for measurements [10], while water can provide the positive one.

The information offered by the SPR resides in the fact that the electron wavefront is sensitive to the dielectric permittivity (essentially defined as the resistance to an electric field) of the investigated dielectric medium (such as water). This implies also the change of the refractive index (as indicated in subchapter *5.1.3.*) and is dependent to the frequency imposed by the photon energy (see *Figure 5.2* for the dielectric permittivity spectrum of the frequencies).

5.1.6. Outline

The mathematical model for harmonic oscillations has significant physical implications in the fundamental understanding of energy interaction between different systems. The implications include the use of such a model in Dielectric Spectroscopy (particularly in the Electrochemical Impedance Spectroscopy) and in Surface Plasmon Resonance technique. Their use reveals relevant information with respect to the material properties and their behavior. The practical implications in wet electro-chemistry will be further presented.

5.2. Electrochemical Approach

The PPy thin films were previously obtained by the dry route of the Photo-CVD technique. By the wet route, the growth will be followed both by classical electrochemistry but also coupled with the SPR technique in a novel approach. Insight into the chemistry of the deposition will help to understand the SPR response with respect to the electrochemical conditions. The physical implications of the harmonic motions will be highlighted as the experimental steps are progressing towards the overall characterization. This characterization will highlight the key properties that recommend them for versatile applicability.

The electrochemical techniques used to study the reactions at the working electrode that are treated in this thesis are:

- Electrochemical Impedance Spectroscopy (EIS) that involves a sinusoidal variation of potential differences;
- Cyclic Voltammetry (CV) that involves a linear scan between a minimum and a maximum difference of potential in a cyclic manner;
- Chronoamperometry is the technique where the current is measured when a certain potential difference is constantly applied between two electrodes; when the growth of a chemical compound occurs, this can also be called anodizing;

Two electrochemical setups are used:

- The electrochemical setup that involves the high potential difference anodizing (60 V for TiO_2 nanotubes presented in subchapter *5.4.1.*) uses Ti as working electrode and graphite as second electrode; the potential difference was applied by a high-voltage MATRIX MPS-7163 power source and the current was measured by a digital multimeter connected to a PC with supporting acquisition software;
- For the rest of the electrochemical measurements, the current is read between the working electrode (Ti, Ti/TiO_2 or Au) and a counter electrode (Pt); the potential difference is read and applied between the working electrode and a Ag/AgCl

reference electrode; two potentiostat-galvanostat sources were used to apply and measure the electrochemical parameters, namely Autolab PGStat 302N and PGStat 100.

Coupled with the electrochemical system is the SPR Springle device from Autolab. The gold surface where the SPR occurs is in the same time the working electrode for the electrochemical cell allowing a simultaneous measurement. The SPR and electrochemical signals were configured to be simultaneously acquired by Autolab NOVA software.

Considering the measured current (I) between two electrodes, the charge (Q_C) transferred between an initial time (t_i) and a final time (t_f) is obtained by calculating:

$$Q_C = \int_{t_i}^{t_f} I dt \qquad (5.15)$$

To estimate the deposited mass (Δm), a modified version of Faraday's law was used [11,12]:

$$\Delta m = \eta \frac{Q_C M_{eq}}{n F_{ct}} \qquad (5.16)$$

where Q_C is the charge passed through the cell, F_{ct} is the Faraday constant (96 485.3 C mol^{-1}), n is the number of electrons transferred per mole of product, M_{eq} is the equivalent weight while η represents the efficiency of the chemical reactions that can be decreased by different physico-chemical processes that occur at the electrode interface.

5.3. PPy Grown on Gold Substrate

The PPy films were grown on a gold substrate in order to allow a coupled Electrochemical/SPR (ESPR) investigation and to highlight the chemical reactions that occur over the same working electrode.

5.3.1. Electrochemical Surface Plasmon Resonance (ESPR) – Baseline

In this subchapter the SPR response with respect to the classical electrochemical processes is treated. To obtain a better understanding of the phenomenon, a "baseline" over the SPR behavior in Millipore ultrapure water (18.2 MΩ cm) and supporting electrolyte solutions is studied.

In *Figure 5.5* the response in current and SPR are seen as the potential difference between the gold electrode and the Ag/AgCl reference electrode is cyclically varied (x 10 cycles) between 0 and 1 V with step of 0.1 V/s by cyclic voltammetry. The curves were sine fitted in order to isolate the repetitive response parameters. The fitting is obtained using the equation:

$$y = y_0 + A\sin\left(\frac{\pi}{T}(x - x_0)\right) \qquad (5.17)$$

where y_0 is the offset between the fitted signal and the beginning of the sinusoidal behavior on the y axis while x_0 is the designated "phase shift" between the fitted value and the sinusoidal behavior on the x axis, A is the amplitude of the signal, and T is the sine period. The y_0 and A values are form the y axis, the unit of measure is either amperes (A) for current or milidegree (10^{-3} degrees - m^o) for SPR angle. The T and x_0 values are from the x axis and are both described by the time in seconds (or they can be converted to frequency as 1 s = 1 Hz^{-1} according to equation *(5.2)*. The fitting results are shown in *Table 5.1*. The experimentally imposed value of 10 s for a cycle is confirmed by the period value of the fitted results.

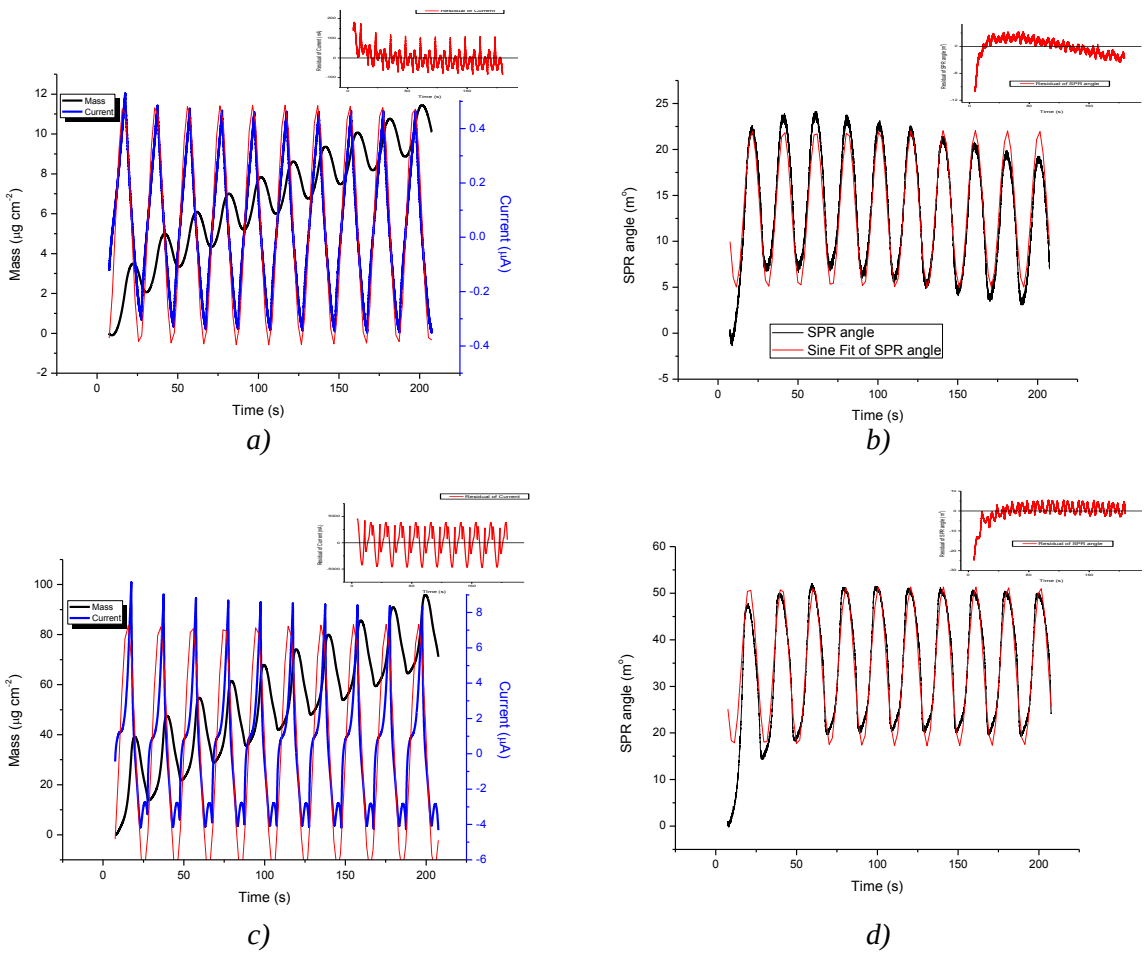

Figure 5.5: The current response (a, c) and SPR angle response (b, d) for 10 cycles ranging between 0 and 1 V (vs Ag/AgCl) in Millipore deionized water (a, b) and in Na_2SO_4 50 mM solution in deionized water (c,d); a sine fitting was made (red lines) and the residuals resulted after the fitting are shown in the insets

For Millipore deionized water, the rate of change during the potential sweep for the current and the SPR angle is determined by the ratio of the current/SPR angle amplitudes at the relatively low ratio of 51,64 nA/m°.

Table 5.1: Sine fitting of the current and SPR resonse of gold to a cyclic voltammetry sweeping linearly between 0 and 1 V vs. Ag/AgCl

Substance / Type	Deionized Water				Deionized Water + Na_2SO_4 50mM			
	Current		SPR		Current		SPR	
	Value	*Sd.Err.*	*Value*	*Sd.Err.*	*Value*	*Sd.Err*	*Value*	*Sd.Err.*
R-square error	0.84102		0.91466		0.37698		0.89281	
Phase Shift (x_0)	11.38	0.02	-3.88	0.02	10.13	0.03	15.71	0.02
Period (T)	10.01	0.00	9.99	0.00	10.00	0.00	10.00	0.00
Offset (y_o)	$4.5*10^{-8}$	$1.0*10^{-9}$	13.05	0.03	$3.2*10^{-7}$	$2.8*10^{-8}$	34.3	0.06
Amplitude (A)	$4.4*10^{-7}$	0	8.54	0.02	$7.0*10^{-6}$	0.00	17.06	0.04

However, after the fitting some residual peaks are still observed that present a deviation from the sinusoidal behavior (seen in *Figure 5.5* insets). With respect to the current response during the cyclic voltammetry, the peaks that indicate the deviation from the sine fitting are due to the chemical reactions that occur at the electrode interface. For the SPR the same residuals are observed that indicate a correlation with the chemical reaction.

The chemical reactions that occur in the 0.6 and 1.05 V vs Ag/AgCl range is called the pre-oxidation range [13] and corresponds to the range between 6 and 10 s of measurements for each cycle where broad peaks are observed as residuals both in SPR angle and current

response (*Figure 5.5*). These peaks are due to the oxide formation as submonolayers over the gold surface in water and can be described by the reaction [14]:

$$Au + H_2O \rightarrow Au(OH) + H^+ + e^-$$

The current passed between the gold and the counter electrode in water (*Figure 5.5 a*) allowed to determine a deposited mass of around 11 μg cm^{-2} using the Faraday law (equation *(5.16)*). The constant decrease in the SPR signal during the cycling observed in the residual (as a deviation from the sine fit in *Figure 5.5 b*) can be a response due to the OH bonds forming at the gold interface. This study was made in ultrapure water in order to limit the ions influence over the gold interface (aspects treated also in Chapter 1).

To increase the number of ions in the solution, 50 mM of Na_2SO_4 salt was added into the deionized water to act as a supporting electrolyte. The dissolution of the salt into ions occurs after the reaction:

$$Na_2SO_4 \rightarrow 2Na^+ + SO_4^{2-}$$

After the addition of the salt, a prominent peak at around 0.2 – 0.6 V (between 2 – 6 s in each cycle) is observed in the residuals for the sulfate cation and is attributed to the double layer charging (*Figure 5.5 c*) [15]. The double layer involves (*i*) an adsorbed layer of ions at the Au interface that compensate the Au charge and (*ii*) a diffusive layer that is composed by ions attracted to the surface charge via the coulomb force.

The mass deposited on the Au electrode has a significant increase of around 96 μg cm^{-2} as determined theoretically (*Figure 5.5 c*). This is mainly because of the SO_4^{2-} anions strongly adsorb on the Au interface [15], an adsorption that is reported to have an irreversible behavior in the pre-oxidation region [16]. The anion adsorption is probably responsible for keeping the SPR residual after the sine fitting relatively linear during the 10 voltammetric cycles (*Figure 5.5 d* inset). During the cycling, the current/SPR angle was found to vary with 411.3 nA/m^o (see *Table 5.1* for the full range of parameters). This variation can be associated to the increased ion adsorption over the Au surface.

The SPR angle behavior presented in *Figure 5.5 b*) and *d*) corresponds to a shift of the reflection minima (also called SPR 'dip' that is due to the photon absorption that induces the plasmon resonance) from the reflected light of the laser, a movement that is related to the dielectric permittivity (ε) at the Au/electrolyte interface. This shift occurs by the change of reflectance minimum angle with respect to an initial position measured in m^o. The movement of the angle during the cyclic voltammetry sweep in deionized water and Na_2SO_4 electrolyte is shown in *Figure 5.7 a)*.

To further investigate the phenomena at the electrolyte interface and its interaction with the SPR wavefront, oxalic acid ($H_2C_2O_4$) is used as supporting electrolyte. The oxalic acid is a polyprotic acid that contains more than one ionizable hydrogen. For such an acid, the ionization occurs in two steps, each with a specific equilibrium constants (K_a). It initially forms dioxalates at $K_{a1} = 5.9*10^{-2}$ [17]:

$$H_2C_2O_4 \rightarrow H^+ + HC_2O_4^-$$

Finally, it reaches in oxalate state when the equilibrium constant $K_{a2} = 5.2*10^{-5}$ [17]:

$$HC_2O_4^- \rightarrow H^+ + C_2O_4^{2-}$$

The chemical compositions of the oxalates and bioxalates are shown in Figure 5.6.

At the conditions +0.8 V of applied potential difference *vs.* Ag/AgCl a potential-induced change of the bioxalate species to oxalates of the anions adsorbed to the Au electrode is reported [18]. An FTIR literature study made by FTIR suggest that at +0.8V the deprotonation of bioxalate occurs (loss of H^+) that leads to the formation of an oxalate [18].

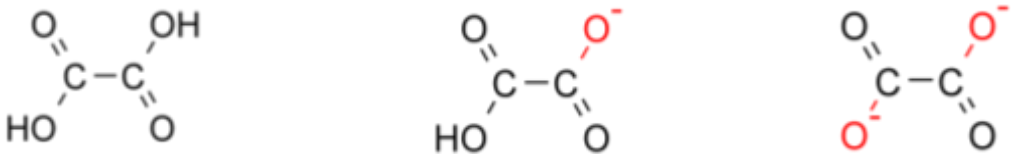

a) *b)* *c)*

Figure 5.6: Chemical formula of a) oxalic acid, b) bioxalate and c) oxalate

In *Figure 5.7 b* for the oxalic acid electrolyte at the same applied difference of +0.8 V *vs.* Ag/AgCl indicates a change in reflectivity. The minimum of reflectance is conversely viewed as a maximum of absorption. The change in refractive index seems to be reversible as the absorption maximum drops fast in the first 95 min and then increases to a stabilized value (the absorption minima behavior is shown in the inset of *Figure 5.7 b*). The change can be explained considering the chemical interactions that occur at the gold interface.

A first step involves the dissolution of the oxalic acid in bioxalates as mentioned above. A second step involves the adsorption of the bioxalates (HC_2O_4) on the Au surface. Under an applied difference of potential, deprotonation of the bioxalate occurs with the release of an H^+ and the formation of $C_2O_4^{2-}$ at the electrode interface.

In the presence of an electron, the released H^+ can be recombined according to the reaction:

$$H^+ + e^- \rightarrow H(1s)$$

This proton combination with an electron is described as Plasmon-Assisted Ion Neutralization [19]. This is mainly possible because the atom radiative lifetime (10^{-8} s in vacuum and even greater in the vicinity of a surface) is much longer than the collision time (~ 10^{-15} s), so that the radiative de-excitation does not occur [20].

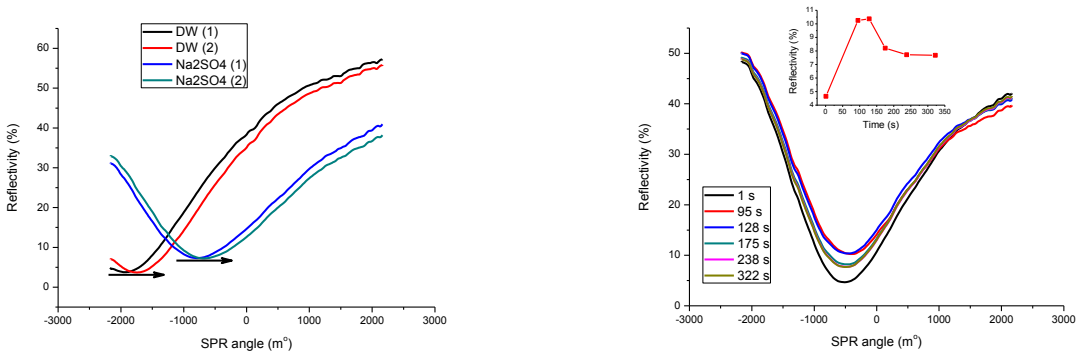

a) *b)*

Figure 5.7: SPR dip response for deionized water (DW) and DW with Na_2SO_4 50 mM during a cycling between 0 and 1 V (vs AgAgCl) (a) and the SPR dip resonse in DW with oxalic acid 50 mM during 322 s of 0.8 V (vs Ag/AgCl) applied potentials with the reflectivity minimum the inset (b)

During the SPR phenomenon, electrons oscillate into the solution due to the photon energy (see subchapter *5.1.5.* for supplementary information). As the bioxalate gets deprotonated, the released proton combines with an electron released from the Ag network. The electron combination with the proton from the solution leads to a decrease in the electron population responsible for SPR. When the electron population decreases, the absorption of the photon energy by the electrons has a decreased efficiency. This explains the steep increase in reflectivity (decrease in absorption) after the first 95 s from 4 % to 10 % and can be roughly approximated with a decrease of 6 % of electron population in the 2 mm^2 interface of the Au electrode responsible for the SPR signal.

When the bioxalate situated to the gold interface is fully converted into oxalate, the SPR reflectivity of the depleted electron population remains constant as no more electrons are consumed.

A decrease in reflectivity from 10 % to around 8 % is subsequently observed. This can be associated to a refill of electron population responsible for SPR with 2 %. The refill can occur during the metastable state (when no significant deprotonation is occurring) where electrons from the whole surface of the SPR's Au disk (25 mm^2) migrate toward the depleted regions of the electrochemical cell area (2 mm^2).

The above experiments showed that for the SPR dip response (or the reflectivity minimum) a shift in reflectance angle is indicative to the changes of dielectric permittivity (ε) at the Au/electrolyte interface. Under the experimental conditions of the working electrode polarization, periodic changed in the SPR angle were observed. The periodic changes were fitted by a sine behavior, and revealed an increase of electrochemical/SPR response from 51,6 nA/m^o in deionized water to 411,3 nA/m^o in the presence of SO_4^{2-} anions. This is indicative of the changes of the dielectric permittivity at the electrode interface through the (OH) bonds formed at the Au interface and the ion adsorption respectively.

The absorption observed in the reflectivity of the SPR has a theoretical correlation with the ceased energy of the photons to the electrons. It was previously observed that by ionic recombination that the electrons from Au can be consumed. This corresponds with a decrease in absorption, and implicitly an increase in reflectivity for the SPR minima.

A further study of electrochemical polymerization of Py will be made by the use of the SPR technique. The specific reactions responsible for the polymer electro-deposition will be investigated.

5.3.2. PPy Electrochemical Growth – ESPR Study

For the electrochemical growth of PPy a solution of 50 mM oxalic acid was used. Previous experiments were made at concentrations in the range of mM for the Py monomer; however the SPR signal suffered changes that did not allow correct measurement during deposition. The "ultra-low" concentration of 200 µM allowed obtaining a reliable SPR signal during and after the deposition.

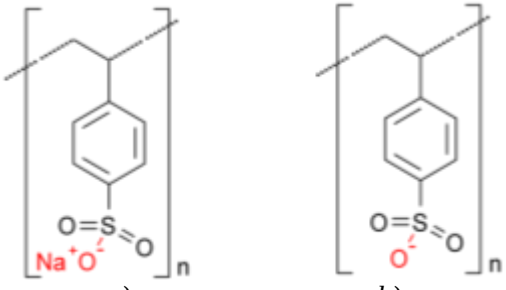

a) *b)*

Figure 5.8: Chemical formula of a) Sodium Polystirene Sulfonate (NaPSS) and b) Polystirene Sulfonate (PSS^-)

During the growth, the oxalate ($C_2O_4^{2-}$) anion is expected to act as doping agent for PPy. To investigate the doping influence, a high molecular weight (M_w = 70000) Sodium Polystyrene Sulfonate (NaPSS) was used both as anion dopant and as surfactant. The NaPSS dissolution into Polystirene Sulfonate (PSS) (see *Figure 5.8* for chemical formulas of NaPSS and PSS) can be described as:

$$NaPSS \rightarrow Na^+ + PSS^-$$

PPy was amperometrically deposited at 0.8 V *vs.* Ag/AgCl for 100 s. The polymerization of Py can be described as:

$$nPy \xrightarrow{1-2ne^-} nPy^{\bullet} \xrightarrow{1-2nH^+} PPy$$

where *n* gives an indication of PPy molecular mass. The PPy obtained by electrochemical route is reported to have an average molecular weight of about M_w = 6000 [21,22]. It can be observed that during the polymerization an electron and a proton are released.

During the oxidation (growth) reaction of Py, the insertion of anions can be described as [23]:

$$PPy + mA^- \rightarrow \left(PPy^{m+}A^{m-}\right) + me^-$$

where *m* is indicative to the doping level of the PPy polymer. It can be observed that during this reaction the release of an electron due to the doping is obtained. This will contribute with supplementary electrons to the SPR if required.

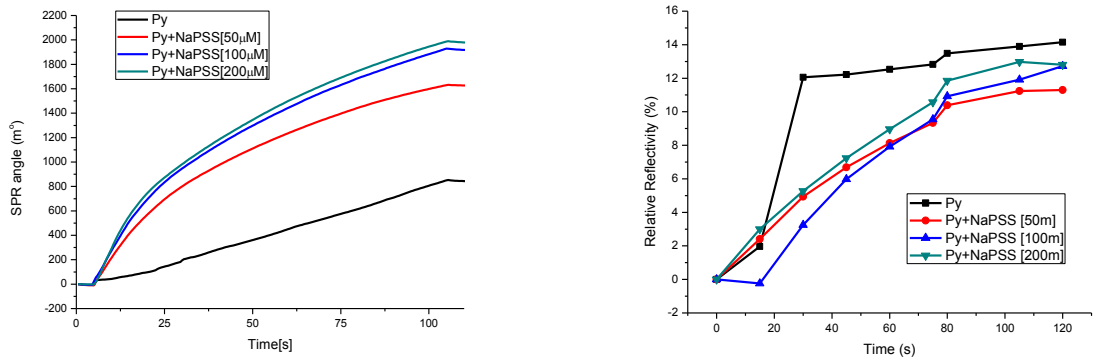

a) *b)*

Figure 5.9: SPR angle (a) and SPR reflectivity (b) response during polymerization of Py and Py with NaPSS as dopant at different concentrations (50, 100 and 200 µM) under 0.8 V (vs Ag/AgCl) potentiostatic conditions in 50 mM oxalic acid solution

The release of a hydrogen ion as a result of bioxalate ($HC_2O_4^-$) deprotonation into oxalate ($C_2O_4^{2-}$) is also expected to deplete the electrons responsible for SPR (see subchapter *5.3.1.*). The question that arises is: is that doping occur in the same time as the bioxalate deprotonation? This would allow the recombination of the electron resulted from the doping with the proton resulted from the bioxalate. These aspects can be elucidated observing the SPR reflectivity behavior during the insertion of PSS.

Firstly, as the concentration of NaPSS in the solution increases from 50 to 200 µM, the increase in SPR angle (*Figure 5.9 a*) indicates the increasing presence of PSS^- as dopant and as large-molecular mass surfactant.

The increase of the SPR reflectivity (relative to the first measured point) observed in *Figure 5.9 b)* confirms the Py polymerization by electron "depletion" in the Au responsible for the SPR signal. In the first 80 seconds however, the reflectivity increase is steeper for the PPy doped only with (bi)oxalate, compared to the one with PSS^- as dopant. Notably, during the polymerization in the presence of PSS^- cation at different concentration the reflectivity has relatively the same behavior. This is an indication that probably bioxalate is firstly doped in PPy, and subsequently suffers the electrochemical induced deprotonation.

The slow reflectance increase in the presence of the PSS^- cation that competes with the (bi)oxalates can lead to a lowered oxalate doping, resulting in less electron depletion.

The doping for the PPy film obtained at these "ultra-low" concentrations will be further investigated by EIS and SPR.

5.3.3. PPy – EIS vs. SPR

The PPy film grown in this set of experiments was obtained in the same conditions as the ones described in the previous subchapter (*5.3.2.*), with both oxalate ($C_2O_4^{2-}$) and polystyrene sulfonate (PSS^-) as dopants. The PSS^- dopant selected for this subchapter was obtained from a solution containing 50 µM of NaPSS.

The doping/dedoping kinetics for pure PPy films during the EIS characterization was not clearly observable by SPR. In order to adjust the ion release areas, phenol (chemical formula in *Figure 5.10*) was deposited as polyphenol over the surface. The deposition was achieved in cyclic voltammetry conditions that involved 10 cycles of an applied potential

difference between 0 → 1.05 → 0 V *vs.* Ag/AgCl. Phenol oxidation that occurs around 0.7 V *vs.* Ag/AgCl can be described by the reaction [24]:

$$C_6H_5OH \rightarrow C_6H_5O^{\bullet} + H^+ + e^-$$

The phenyl radical ($C_6H_5O^{\bullet}$) then undergoes polymerization over the PPy film. Notably, due to the coupled release of an electron and a proton, the reaction is expected not to have an effect over the SPR absorption. The growth of polyphenol onto the surface leads to a fouling effect [25] that essentially blocks any electrochemical activity over the electrode. In order to prevent the full electrochemical blocking of the PPy film, phenol was added at the "ultra-low" concentrations of 50 μM. This lead to a "filament like" morphology in the case of PPy doped with oxalate, while in the case PPy doped with PSS^- the "granular–like" morphology that is observed in *Figure 5.11*. This prevented the complete covering over the surface and implicitly the electrochemical fouling. Furthermore, the ions mobility was constrained in isolated areas where polyphenol was deposited. This allows the current flow inside the cell through the areas uncovered by polyphenol. It also allows the structural reorientation of the phenol-covered PPy film by polarizing the oxalate anion and the large PSS^- surfactant.

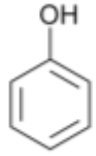

Figure 5.10: Chemical formula of Phenol

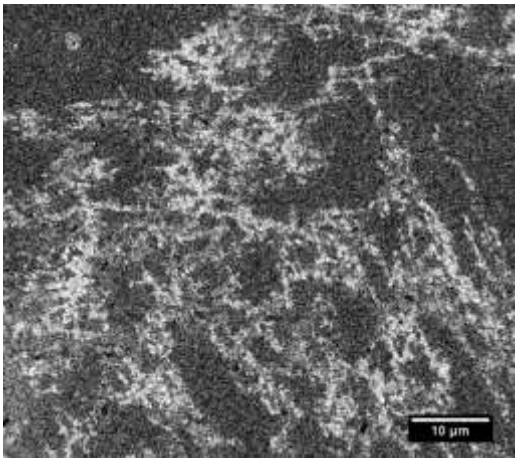

a) *b)*

Figure 5.11: SEM images of PPy (a) and PPy/PSS surfaces (b) after 10 CV scans in phenol solution

The schematic representation of the system and of the phenomenon involved in the characterization can be seen in *Figure 5.12*. They show the Au/PPy films and also the polyphenol covering only on some areas over the sample. A sinusoidal polarization with respect to OCP is applied over the working electrode in the range of ±10 mV vs. Ag/AgCl. The frequency of the polarization is in the range of 100 MHz - 100 mHz. In *Figure 5.12* is represented the mHz range, as this is the range over which the discussion in this section will be made. The mHz range is generally considered responsible for ion movement and/or reorientation into the electrode.

The SPR is responsible for the electron movement from the gold electrode inside the deposited film. This occurs as a perturbation with the frequency in THz range, as represented in *Figure 5.12*.

During the EIS polarization, the SPR response shows a periodic sinusoidal behavior, but with different frequencies, as observed in *Figure 5.13*. Their frequency was calculated from the time axes, according to the first equality in equation *(5.2)*. In *Table 5.2* the results from measured frequencies of the PPy film oxalate doped (PPy SPR response) and PSS^- doped (PPy/PSS SPR response) are shown. In the same table the applied alternative current (AC)

frequencies are given. It can be observed that some AC frequencies present an increased period or have no correspondent in the SPR response.

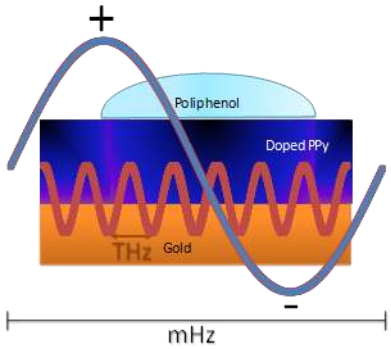

Figure 5.12: Scheme of the experimental system; in mHz range is depicted the potential variation frequency during EIS and in the THz range is depicted the electron perturbation frequency in SPR

This indicates the frequency-specific behavior of the hybrid film deposited on the Au surface. The PSS^- surfactant is a large molecule that is expected to induce a reorientation in the PPy/PSS film structure under polarization. This aspect is confirmed as a constant decrease in the SPR angle is observed in *Figure 5.13* for the PPy/PSS film compared with the one doped only with oxalate.

Table 5.2: Applied AC frequency during EIS characterization and its corresponding response measured by SPR for PPy and PPy/PSS films

AC Frequency (mHz)	10	13	19	26	37	31	71	100
PPy SPR response (mHz)	11	14	16	26	36	48	71	100
PPy/PSS SPR response (mHz)	11	-	16	29	-	47	77	-

This is explained by the fact that the dielectric constant of the PPy/PSS film is changed as the PSS^- anion is rearranged under the electric field influence. Such a reorientation of charged species is expected also for oxalate. Indeed, in *Figure 5.13* a slight decrease in the median behavior of the SPR signal is seen, indicating the same trend but in a more subtle manner.

As the EIS sinusoidal variance of the potential difference is applied, some ions at the PPy/electrolyte interface are expected to diffuse in and out of the film. Also, over areas shielded by the polyphenol presence, a polarization of the film is expected under the applied electric field that can be an indication of orientation changes inside the film.

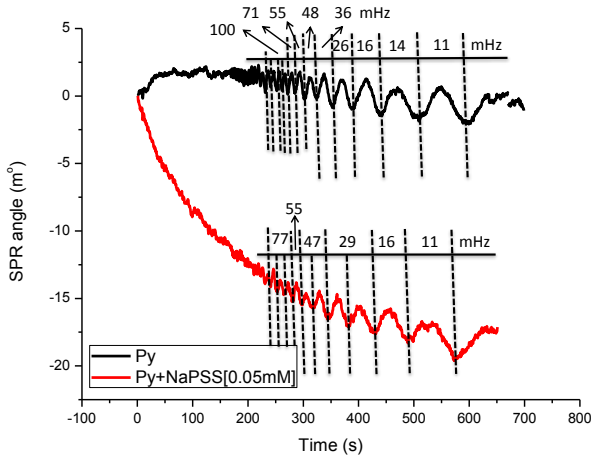

Figure 5.13: SPR angle response during the EIS experiments; in mHz range the SPR starts to respond visibly to the applied perturbation during EIS

This presumed diffusion of the ions into and outside the film will be further investigated for a PPy film deposited at concentrations of Py 3 times of magnitude higher. The supporting

working electrode will be an Au electrode connected to an Inficon RQCM Quartz Crystal Microbalance (QCM) allowing simultaneous QCM/electrochemical measurements.

5.3.4. PPy – Dedoping

The diffusion of the ions inside and outside the PPy film can be referred to an action of doping (ion insertion) and undoping (ion ejection). The aspects of the doping/undoping behavior will be studied as the PPy film will be left in deionized water after different periods of time.

5.3.4.1. PPy Growth

The PPy film was grown in 0.5 M oxalic acid electrolyte. The Py monomer concentration was of 200 mM. The working electrode was an Au electrode of a QCM quartz microbalance with an area of 137 mm^2, allowing a simultaneous measurement of the deposited mass. The mass was calculated from the frequency change of the quartz as the mass increase on the surface, according to the Sauerbery equation [26]:

$$\Delta m = \frac{-\Delta \upsilon}{K / A_p} \qquad (5.18)$$

where Δm is the mass difference as a function of frequency difference $\Delta \upsilon$, while K is the sensitivity factor and the A_p is the piezoelectrically active area; for the 5 MHz crystal used in the experiments, K/A_p value is 0.056 Hz/ng/cm^2 at 20 ^oC.

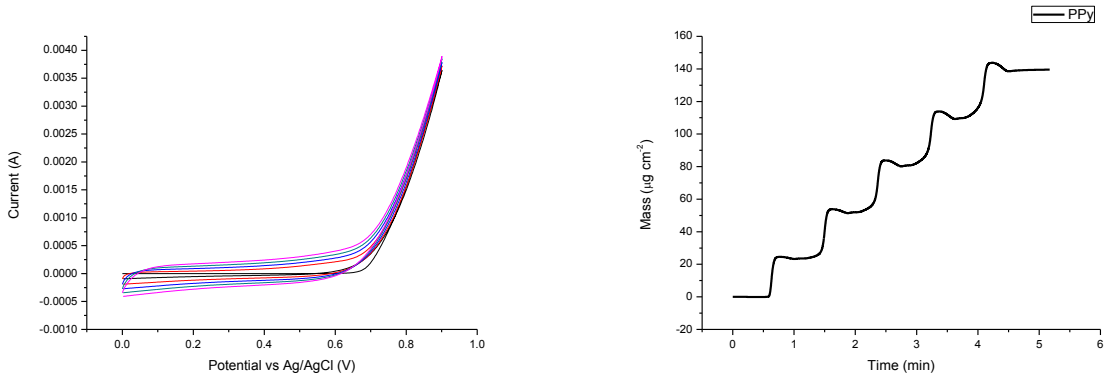

a) *b)*

Figure 5.14: Py polymerization under cyclic voltammetry conditions; current response (a) and mass increase (b) during polymerization are shown

In *Figure 5.14 a)* the cyclic voltammetry during the behavior is shown, while in *Figure 5.14 b)* the calculated mass obtained by QCM indicates a deposition of around 143 µg cm^{-2}. The doping level was electrochemically determined at 22.6 %, a slight increase compared with the PPy films obtained by Photo-CVD dry route (subchapter *2.2.*).

After the time the samples were obtained, they were left in deionized water in order to follow their electrochemical and topographical properties at different time periods.

5.3.4.2. Doping-Dedoping Characterization

A cyclic voltammetry will evaluate the ions insertion and ejection from the PPy film. The evaluation was made after different immersion times in water up to 5 days. The supporting electrolyte was a buffer solution that contains NaCl 8.74 g/l, $NaHCO_3$ 0.35 g/l, Na_2HPO_4*$12H_2O$ 0.06 g/l and NaH_2PO_4 0.06 g/l at a pH of 6.7. The potential difference was applied in the range of – 0.5 V and 0.5 V *vs.* Ag/AgCl, in order to evaluate cation and the anion behavior respectively. The electrochemical behavior is divided in four current areas (I, II, III and IV) as seen *Figure 5.15*.

During the negative potential scan (area III in *Figure 5.15*) the cation undoping is observed. This cation undoping behavior increases with the increase of immersion time in water. The cation doping is observed in the positive potential scanned in II area from *Figure 5.15*. After 2 days immersion in water, an interesting cation doping behavior is observed, as the current increases in the negative potential sweep in area I of *Figure 5.15*.

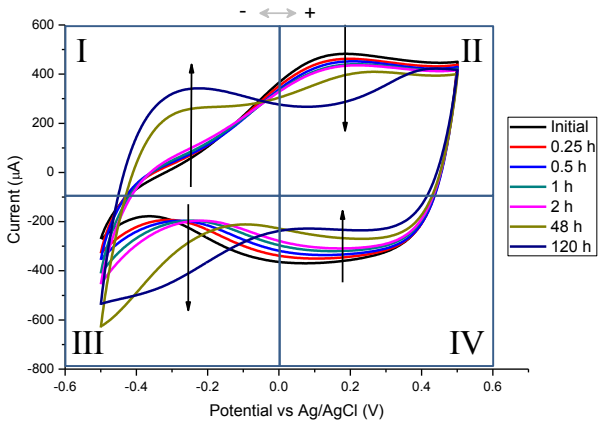

Figure 5.15: PPy film doping and dedoping under cyclic voltametry conditions for the PPy film as obtained and the evolution toward the one left in water for 5 days (120 h)

The PPy film doping level of 22.6 % indicates that for 10 Py molecules, approximately 2 of them are doped by a cation. If the ions are released in water, a change in the volume of the PPy film due to the mass transport should be observed. The aspects of volume changes will be further investigated.

5.3.4.3. Volume Change

If the ions are released into the deionized water, then a mass transport is expected. This will imply also a topographical reorientation of the PPy film due to the ion release. To follow the PPy film reorientation at the surface as the ions are diffusing into the deionized water, AFM is a powerful technique to analyze nanometric changes in topography.

In *Figure 5.16 a) c)* and *e)* the topography for different immersion times over the same area is observed. It can be seen that a change in color responsible for changes in height occurs. In order to have a better overview of the topography changes, a line profile was chosen over identical areas and are represented in *Figure 5.16 b) d)* and *f)* the. The change in surface profile can be observed. The two middle peaks selected after 30 min of immersion have almost the same height of about ~ 815 nm. After another 90 min of immersion, the height for the two middle peaks increased and differentiated to about 840 and 890 nm. The change in surface profile is thus followed by height changes that indicate reorientations in the PPy film during immersion. This confirms the assumptions that PPy suffered reorientations observed by SPR technique during the EIS experimental conditions (as discussed in subchapter *5.3.3.*). However, the correlation with the mass transport of ions is still not clearly elucidated.

To highlight any possible mass transport after the first 2 hours of immersion in deionized water, for the topography images in *Figure 5.16 a) c)* and *e)* a total volume was determined. The total volume calculated for the determined topography was of 54 μm^3, 48 μm^3, and 45 μm^3 for 30, 60 and 120 min of immersion respectively.

This accounts for a 16 % decrease in the determined volume after 90 min of immersion. Notably, this is a change of volume at the plane where the AFM image was taken (versus the minimum point determined), and can be a direct indication of ion release only at the PPy interface with the solution, not also inside the film.

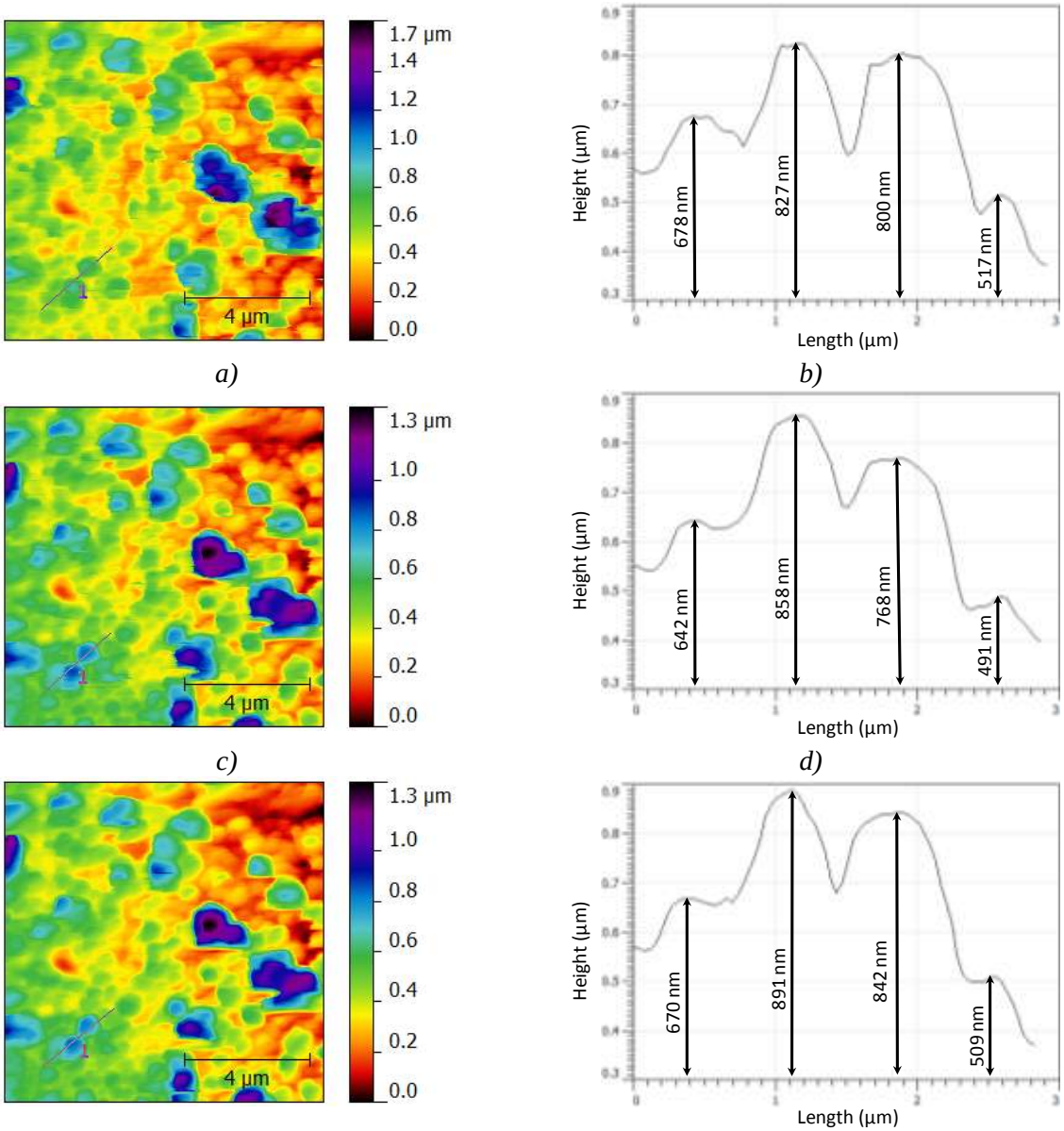

Figure 5.16: AFM topography (a, c, e) and selected linear profiles of the same region of interest (b, d, e) after 30 min (a, b), 60 min (c, d) and 120 min (e, f) in deionized water

This volume contraction and expansion could find applications for the PPy film as actuator devices. A semiconducting membrane attached to a PPy film can offer versatility in orientation by a control of volume changes for such an actuating material. Such a semiconducting membrane can be considered by the fabrication of TiO_2 nanotube self-ordered matrix. Its growth over Ti substrates and the premises of TiO_2 nanotube removal as free-standing membranes will be further studied.

5.4. PPy on Ti/TiO_2 Substrate

This subchapter will treat aspects related to the bottom-up growth of TiO_2 self-ordered nanotubes over a Ti substrate. The top-down characterization through a highly energetic post-treatment will provide an insight over the TiO_2 nanotubes composition and will also provide the bases for a process that allows the removal of the TiO_2 nanotubes from the Ti substrate as free-standing membrane. The final experiment will describe a facile and controlled growth of a PPy thin film over the Ti/TiO_2 nanotube.

5.4.1. TiO_2 nanotubes - Bottom-Up Growth

The TiO_2 nanotubes were grown by Ti anodizing in a glycerol solution containing 4 % H_2O and NH_4F 0.36 M under an applied difference of potential of 60 V. The chronoamperometry of the growth process is shown in *Figure 5.17*. The buttom-up growth over the Ti used as working electrode is also highlighted in *Figure 5.17* in three regions (*I*, *II* and *III*).

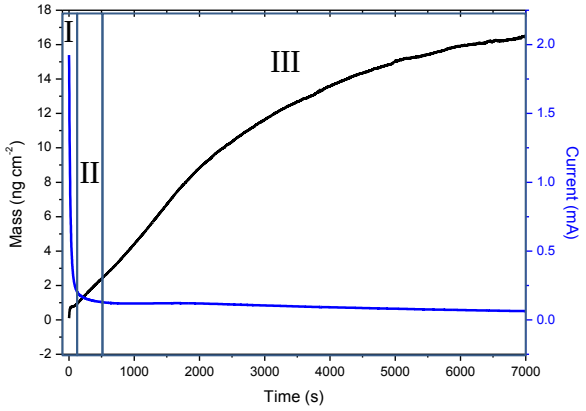

Figure 5.17: Amperometric curve (blue line) and the calculated mass of TiO_2 nanotubes (black curve) grown under 60 V potential difference

The first region, namely region *I*, involves the rapid growth of a passive layer of TiO_2 and can be described by the reaction [27]:

$$Ti + 2H_2O \rightarrow TiO_2 + 4H^+ + 4e^-$$

In region *II*, pits are formed. A pitting process etches the barrier at the bottom of the pits and drives an increase in the electric field that leads to unanodized areas [28]. In this manner field-assisted growth and fluoride dissolution is enhanced.

The fluoride dissolution is involved in the *III* region that drives the nanotubular growth of the TiO_2 nanostructures and can occur according to the reaction [29]:

$$Ti + 6HF \rightarrow [TiF_6]^{2-} + 2H_2O + 2H^+$$

According to the above reaction describing the oxide formation in region *I*, in order to obtain a mole of TiO_2, 4 electrons are used. This was considered as the deposited mass calculated by equation *(5.6)*. Side reaction such as O_2 evolution [30] can occur that decreases the growth efficiency of TiO_2. A literature study determined that in similar conditions as the ones used here for TiO_2 nanotubes growth the efficiency is determined to be at a minimum value of 90 % [31]. Considering the previously mentioned aspects, the total mass deposited was calculated at a value of 16.5 ng cm^{-2}, as observed in *Figure 5.17*.

A subsequent ultrasonication post-treatment will bring significant contribution to the characterization of the obtained TiO_2 nanotubes.

5.4.2. TiO_2 nanotubes - Top-Down Characterization

The top-down characterization involves the ultrasonication phenomenon that leads to a relatively "layered" removal of the TiO_2 nanotubes. After different ultrasonication times, an insight over the TiO_2 nanotubes composition and behavior is revealed.

5.4.2.1. Ultrasonication Phenomenon

The ultrasonication is promoted by the acoustic waves that propagate in liquid environments with frequencies in the range of 20 kHz to 50 MHz. At certain threshold energies, vapor bubbles are formed [32]. The vapor bubble collapses into itself in a very short time frame (in the range of microseconds [33]). During this collapse, local jets with speeds of 100 m/s [34] and pressure gradients around 1000 atm are released, generating hot spot

temperatures of about 5000 ^{o}C and cooling rates above 10^{10} K/s [35]. In this manner, the ultrasonication acts over the surface by a cavitation process. This offers the means of high-energy post-treatment in cold liquids.

5.4.2.2. Experimental Results

Valota et al [36] showed that for the TiO_2 nanotubes a uniformity of the connecting ridges was obtained. This was achieved in glycerol at around the optimum water content used for these experiments. The water concentration used for these experiments helped to increase the mechanical resistance in a planar direction perpendicular to the nanotubes due to the growth of such connecting ridges, as represented in *Figure 5.18*.

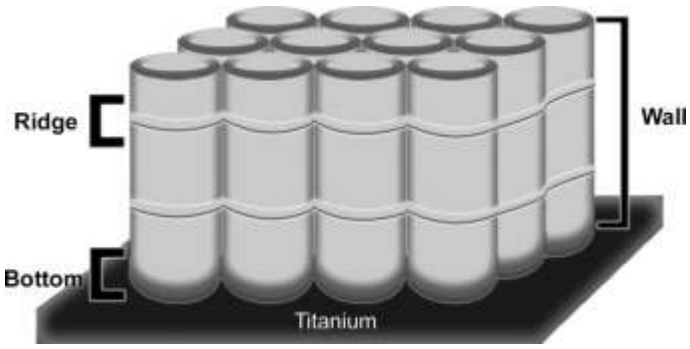

Figure 5.18: Schematic representation of the TiO_2 nanotube architecture: the connecting planar ridges that connect the individual nanotubes are indicated

After the completion of the anodizing steps, a precipitate resulting from the dissolution was found on the surface of the TiO_2 nanotubes [37] also named as nanograss [38]. A brief ultrasonication is sufficient to remove de unwanted deposit. The presence of the disordered "nanograss" over the TiO_2 nanotubes can be observed in *Figure 5.20 a)*.

Table 5.3: The EIS fitting results of the grown TiO_2 nanotubes after different ultrasonication (US) times

TiO_2 Sample	**R_s (Ω)**	**R_{nt} (MΩ)**	**Q_{nt} (μF)**	**n_{nt}**	**R_{ct} (kΩ)**	**Q_{ct} (μF)**	**n_{ct}**	**Chi square**
0 min US	129	15.00	163.0	0.850	30.0	80.0	0.615	0.32
15 min US	107	1.6	49.7	0.700	25.2	52.1	0.840	0.26
20 min US	141	0.9	35.0	0.670	24.0	60.0	1.000	0.40
25 min US	138	0.8	19.6	0.860	20.0	70.4	0.730	0.41

However, in order to investigate the effects of the energetic post treatment by ultrasound in water, extended times of ultrasonication were applied over the grown nanotubes. The treatment was made with a Raypa UCI-150 ultrasonic cleaner that operates at a frequency of 35 kHz.

EIS tests were made to evaluate the effects of the ultrasound post-treatment. The fitting of the results was achieved with a circuit that describes the resistive/capacitive behavior of the charge transfer at the Ti/TiO_2 nanotube interface (R_{ct}) and of the TiO_2 nanotubes themselves (R_{nt}). The results are presented in *Table 5.3*.

As the ultrasonication post-treatment progresses, the fitted results show the decrease in the TiO_2 nanotube resistance (R_{nt} in *Table 5.3*). This can be associated to the damage of the upper part of the TiO_2 nanotubes. Also, the charge transfer resistance associated to the

Ti/TiO_2 interface also decreases, aspect that indicates a channeling of the released energy of ultrasonication towards the nanotube basis.

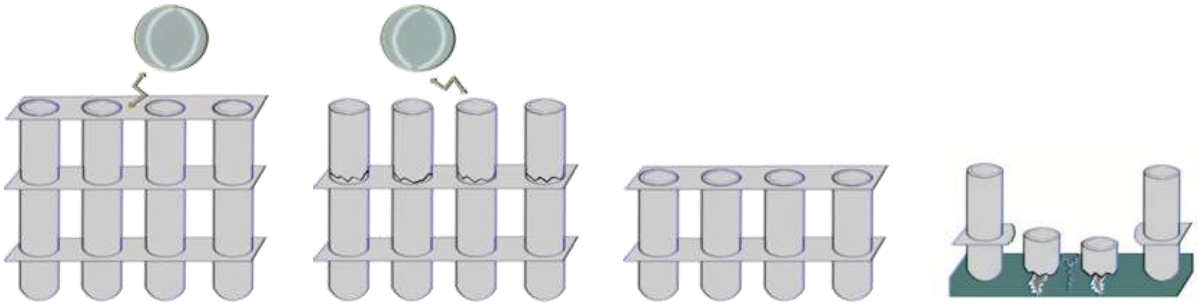

a) *b)* *c)* *d)*

Figure 5.19: Schematic overview of the ultrasonication action. The ultrasonication bubble damages the planar ridges (a) and the nanotubes (b) resulting in the layered removal of the nanostructure (c) and eventually in damaging the TiO_2 nanotubes bottom (d)

A possible mechanism of the ultrasound phenomenon over the TiO_2 nanotubes is shown in *Figure 5.17*. The presence of the connecting ridges gives a nanopore aspect of the TiO_2 nanoarchitecture, and also the increase mechanical resistance. As the ultrasound energy released at the surface acts over the nanotubes connecting ridges by a cavitation phenomenon [39], a nanotube morphology over the surface is obtained as observed in *Figure 5.20* (also represented in *Figure 5.17 a, b*). Increasing the ultrasonication times can revert the surface morphology to a nanopore aspect [40] . A contribution to a layered removal of the ridges can occur from a films stress during the TiO_2 nanotubes growth [36] that is expected to be preserved after the end of the growth process.

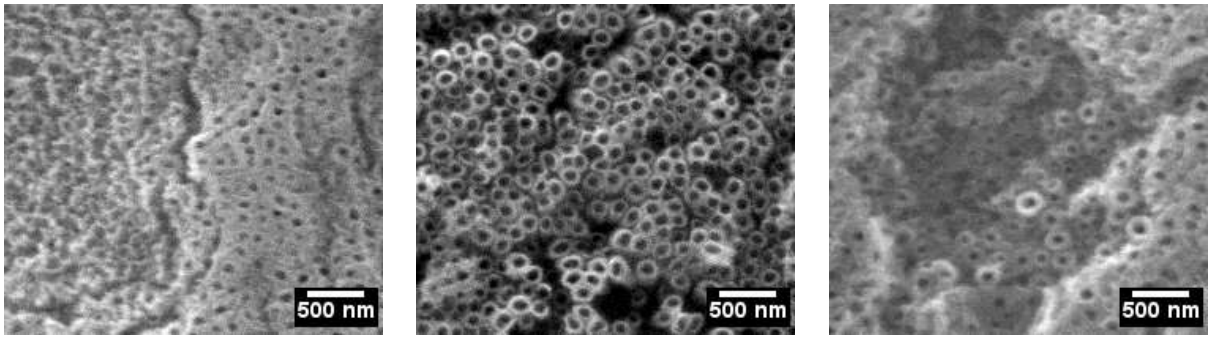

a) *b)* *c)*

Figure 5.20: TiO_2 nanotubes morphology as obtained (a) and after 25 min (b) and 35 min (c) of ultrasonication

A part of the energy is probably channeled towards the Ti substrate and damages the TiO_2 nanotubes at the bottom (*Figure 5.17 d*) [29]. This effect can be further exploited to remove the TiO_2 nanotubes from the Ti substrate as free-standing TiO_2 membranes [41].

The TiO_2 nanostructures grown in similar electrochemical conditions are reported to present a thickening of the TiO_2 nanotubes walls towards the bottom [42]. The layered action of the ultrasonication is confirmed by the experimentally observed increase in thickness of the TiO_2 nanostructures walls. In the SEM images in *Figure 5.20 b)* and *c)* the increase of wall thickness with the increase of ultrasonication time is seen. It varies from 32 nm (± 3 nm) to 60 nm (± 10 nm) at an ultrasound treatment of 25 min and 35 min respectively.

Also, EDS analysis in *Figure 5.21* of the F atomic ratio show that for the untreated TiO_2 is around 9 %. This can be due to the fluoride-rich precipitate presented on the TiO_2 nanostructures, as observed also in *Figure 5.18 a)*. After the first 15 min of ultrasound post-

treatment, the ratio decreases to around 7.5 %, probably as the fluoride precipitate is removed. Subsequently, the F atomic ratio increases with the increase in ultrasonication time. This can be an indication of the TiO_2 nanotubes walls size increase that still present traces of fluoride from the growth process [43]. The possible effect of the fluorine presence with respect to a layered removal of TiO_2 nanostructures due to ultrasonication is schematically presented in *Figure 5.22*.

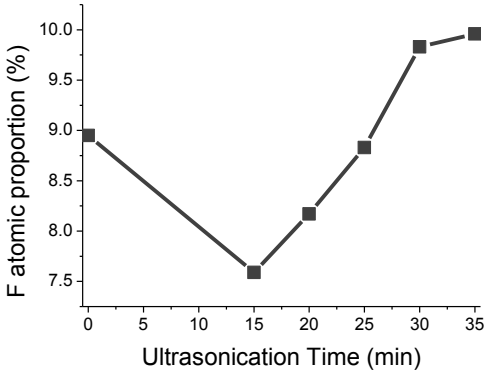

Figure 5.21: EDS atomic proportion of fluorine in the TiO_2 nanotubes after different ultrasonication times

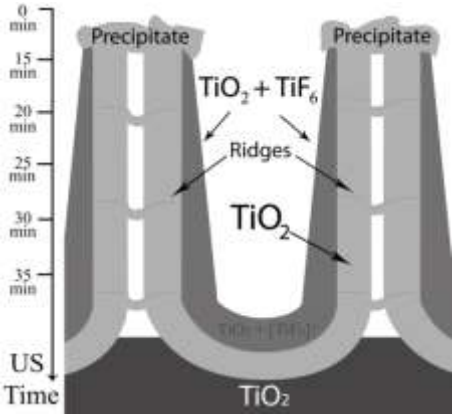

Figure 5.22: Schematic overview of ultrasonication action over the TiO_2 nanotubes

The aspects previously presented highlighted the fact that a brief ultrasound treatment can remove the disordered precipitate that resulted from the TiO_2 nanotubes growth. Subsequent increase in ultrasonication time indicated a damage of the TiO_2 nanotube bottom that offers the premises of the TiO_2 removal as free-standing membrane from the Ti substrate where the growth occurred.

Further experiments will be focused on the control of Py polymerization over the selforedered TiO_2 nanostructures.

5.4.3. PPy Growth on Selfordered Ti/TiO_2 Substrate

In order to grow the PPy film over the selfordered TiO_2 nanotubes, some constraints are applied to optimize the hybrid film growth.

To obtain the TiO_2 nanotubes, the electrolyte will be chosen as to permit a reduction in power requirements while preserving an efficient anodizing process. To respond to such a demand, an aqueous solution is chosen that allows a 10 V anodizing [44]. Notably, high viscous electrolytes are reported to require higher anodizing potentials [44,45]. Subsequently, an electrochemical characterization of the as-obtained TiO_2 nanotube will be treated in order to define the parameters required for the PPy film growth.

5.4.3.1. TiO_2 Nanotubes Growth

To grow TiO_2 nanotubes by anodization at 10 V an aqueous electrolyte that contains 0.5 % HF was used over a 4 mm^2 Ti working electrode. The chronoamperometric current and the calculated charge are shown in *Figure 5.13*.

During the anodizing, low efficiency of TiO_2 nanotube growth is expected. Only 2% of the dissolved Ti is reported to be converted into nanotubes [46], probably due to the high electrochemical diffusion in low viscosity medium (subchapter *5.4.1.*). The charge passed between the Ti electrode and the graphite counter electrode has a linear behavior of 200 µA/s. Considering a 100% growth efficiency and correlating the charge with the deposited mass (Faraday law in equation *(5.16)*), a mass addition of 8.14 pg/cm^*s is calculated. This nearly linear behavior was not observed for the high-viscous electrolyte (subchapter *5.4.1.*).

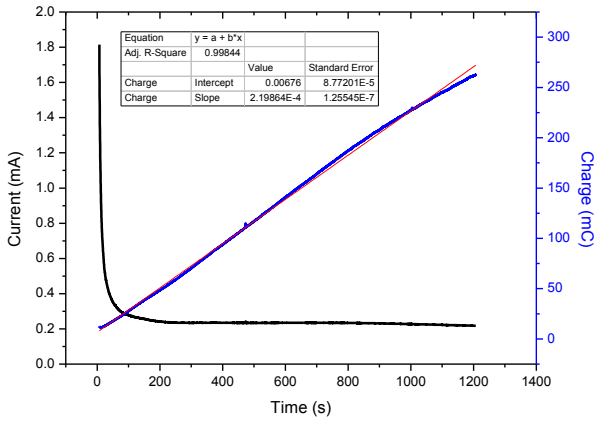

Figure 5.23: Chronoamperometric growth of TiO_2 nanotubes and the calculated charge

In order to proceed to the electrochemical polymerization of Py, the electrochemical properties of the TiO_2 nanostructures need to be evaluated. Also the morphological evaluation selfordering of the TiO_2 nanostructures will be treated.

5.4.3.2. TiO_2 Nanotubes Characterization – Polymerization Prerequisite

In *Figure 5.24 b)* it can be observed that TiO_2 nanotubes with diameters of 35 nm (±10 nm) were successfully obtained. Also the presence of precipitates that covers the TiO_2 nanostructures is observed (*Figure 5.24 a*). As previously discussed, the precipitate is expected to contain a significant quantity of fluoride. A short ultrasonication treatment can remove the precipitate; however for a facile TiO_2/PPy growth protocol, such an alternative post-treatment was not pursued.

After the TiO_2 nanotubes growth, their characterization is achieved in the same electrochemical cell, without any sample removal or post-treatment.

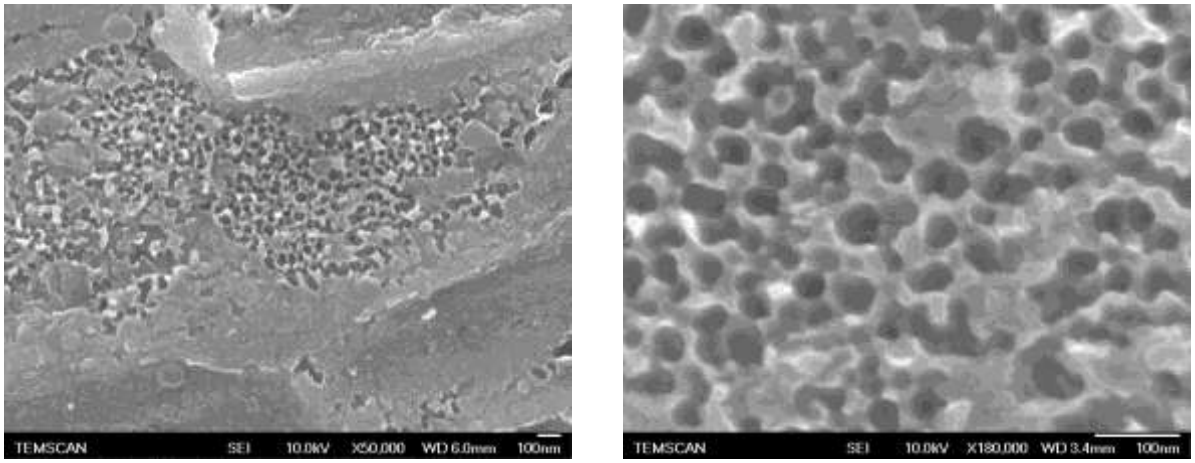

a) *b)*

Figure 5.24: FEG-SEM morphology of the TiO_2 nanotubes (b) and also of the precipitate that covers them (a)

Experiments made by cyclic voltammetry showed that Ti passivates by forming a TiO_2 layer at around 0.2 V *vs.* Ag/AgCl, and afterwards at 0.6 V *vs.* Ag/AgCl the PPy starts the oxidation [47]. This is a first indication of oxidation processes into TiO_2 and PPy at the Ti electrode interface. The presence of a TiO_2 layer onto the surface implies different electrochemical behavior during applied potential difference and can have an impact over further PPy film growth.

A first step is to determine the electrochemical aspects related to the PPy growth on a Pt electrode that does not involve the oxidation processes in low ranges of potential difference. The results of a cyclic voltammetry sweeps of the polymerization solution (0.5 % HF and 0.2 mM Py) are shown in *Figure 5.25*. The key aspects to be noted is the start of Py polymerization by oxidation at around 0.6 V *vs.* Ag/AgCl and the overoxidation peak of PPy at around 1.1 V *vs.* Ag/AgCl. The process of PPy overoxidation is detrimental to the film properties as the film loses its conductive properties by the electrochemical formation of a C=O bond [48]. Consequently, the range between 0.6 V and 1.1 V is an appropriate potential range for PPy growth.

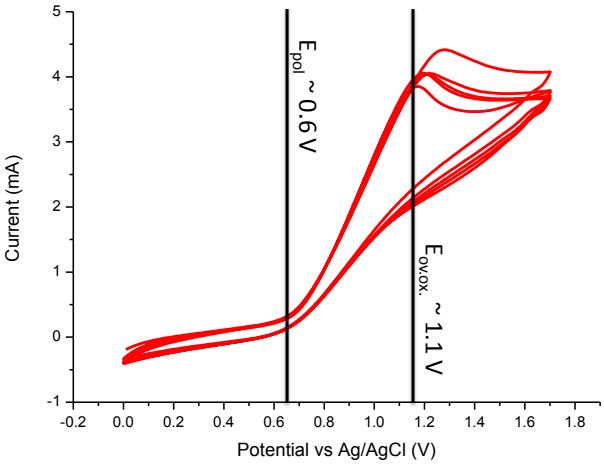

Figure 5.25: Cyclic voltammetry polymerization of Py on Pt electrode

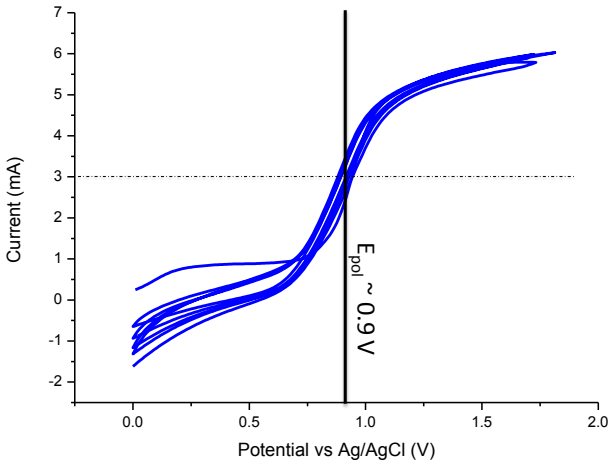

Figure 5.26: Characterization of the TiO_2 nanotubes in the same HF electrolyte used to grow the nanotubes and the PPy film

However, as TiO_2 nanostructures are present over the substrate, the change in surface chemistry can have an important contribution on the Py oxidation (growth). To evaluate the surface properties with the contribution of the TiO_2 nanostructure contributions, the cyclic voltammetry technique will be used.

Cyclic voltammetry is a technique where mainly the charge transfer is analyzed. The oxidation reactions and also the mass transport of ions have distinct fingerprints in the voltammetric cycling. The one observed in *Figure 5.25* is indicative for diffusion in what can be considered as the "semi infinite" diffusion layer [49]. In this case the fluoride diffusion through the TiO_2 nanotubes can be deduced. As anion diffusion through the TiO_2 nanotubes is an important aspect in PPy doping with the F^- anion, the middle value of 0.9 V is chosen for polymerization.

5.4.3.3. PPy Growth

In the electrolyte used to grow the TiO_2 nanotubes, the Py monomer was added to reach at a concentration of 200 mM. The electrochemical growth of the PPy film is achieved by applying a potential difference of 0.9 V vs. Ag/AgCl as previously determined. The current and the calculates mass during the polymerization are shown in *Figure 5.27*.

The mass calculated by equation *(5.16)* indicates a growth rate of 4.6 ng/cm^2. After a deposition for 60 s, a total PPy mass of 270 ng/cm^2 was determined. The calculus for these values did not account for any decrease in oxidation efficiency.

In *Figure 5.28 a)* the PPy film covered the whole region, so that TiO_2 nanostructures are not observable. However, in the area shown in *Figure 5.28 b)*, the TiO_2 nanotubes are still observed. During the PPy growth, the film is doped with F^- anions. Since the disordered precipitate is expected to contain fluoride complexes (subchapter *5.4.2.2.*), a preferential growth over such areas is expected.

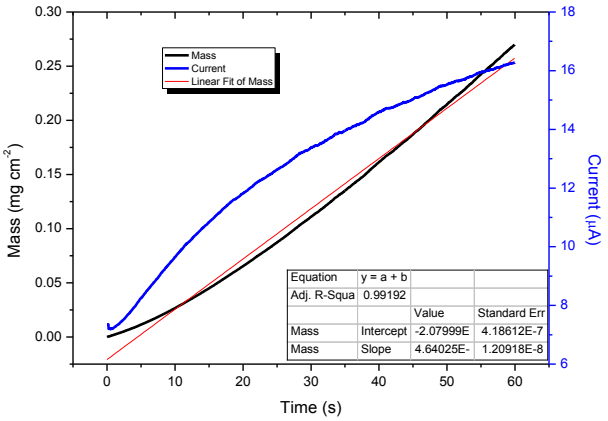

Figure 5.27: Chronoamperometric growth of PPy and the calculated deposited mass; the results of the mass linear fit are shown in the inset

Also, the fluoride was suspected to be inside the TiO_2 nanotubes walls (*Figure 5.22*). If PPy grows preferentially in fluoride rich areas, the nanotube walls will provide a favorable environment.

As observed in *Figure 5.29*, PPy polymerizes over the TiO_2 nanotube walls showing a fibrillar growth. In some areas where the fibrillar PPy merge, some nucleation centers appear, as highlighted in *Figure 5.29 b)* and *c)*.

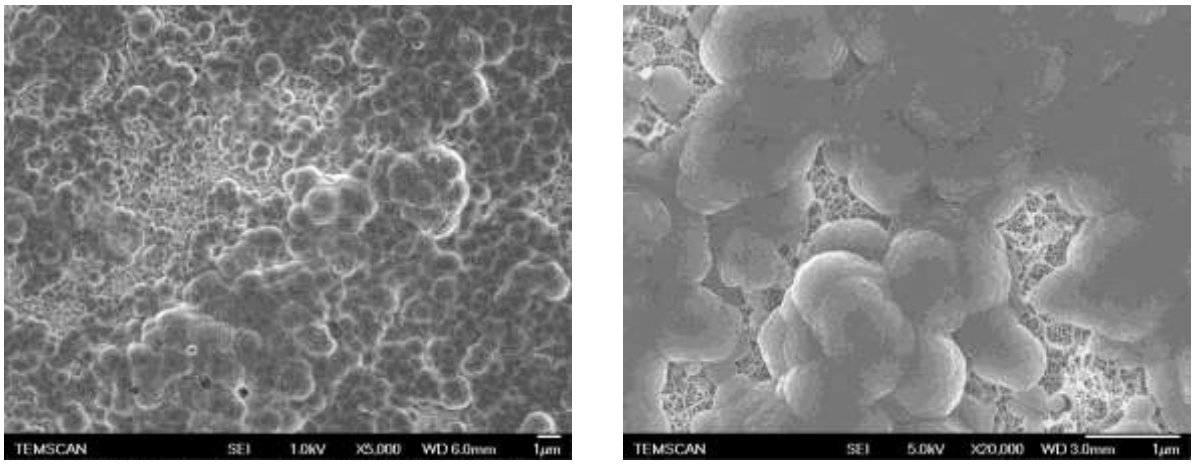

a) *b)*

Figure 5.28: FEG-SEM morphology of the PPy film deposited on the Ti/TiO_2 nanotubes substrate; uncovered TiO_2 nanotubes can be observed (b)

By the protocol described herein, a controlled electrochemical growth of PPy thin films was achieved over selfordered TiO_2 nanotubes.

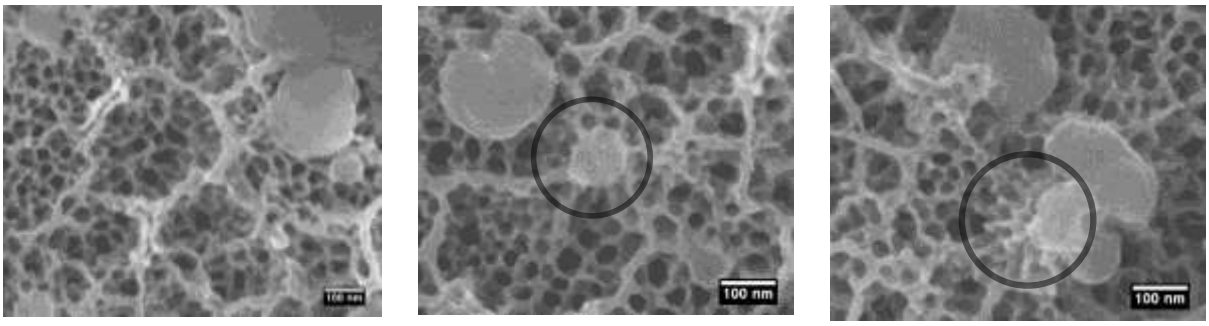

a) *b)* *c)*

Figure 5.29: FEG-SEM images that indicate the fibrillar growth of PPy over the TiO_2 nanotubes edges; two nucleation centers are highlighted (c,d)

The composed PPy/TiO_2 nanotubes film is recommended for applicability as actuator devices. The key properties investigated for this composite film, but also for the previously obtained films by dry route, will be concluded in the next chapter with respect to the applications they are recommended for.

5.5. Chapter Overview

The energy interaction with the material was treated with respect to the model of the harmonic motion as basis for the investigation techniques principles. It focuses particularly on the energy interaction with the matter described by the property of dielectric permittivity. The dielectric permittivity is a physical property explored in two spectral ranges in this thesis: the EIS and SPR.

As an important aspect of originality, the ion behavior in an electrochemical system coupled with the SPR technique is studied at the electrode interface. The implications during the polymerization of a conductive film of PPy were also investigated by these coupled techniques.

During the growth, anion doping of the PPy thin film is achieved. Under specific conditions, the dopant ions can be removed from the PPy film by a process of dedoping. The mass transports involved in the dedoping were also treated both electrochemically and by atomic force microscopy.

The implications of the TiO_2 nanostructures growth were studied bottom-up by anodization from a Ti substrate toward selfordered TiO_2 nanotubes. A subsequent top-down characterization was also performed by an ultrasonication post-treatment. The ultrasonication post-treatment has revealed aspects of the possible TiO_2 removal as free-standing membranes.

The conjunction of the organic PPy and the inorganic TiO_2 nanostructures lead to a two-step electrochemical procedure designed to grow a conductive PPy thin film over a TiO_2 nanostructured film. The growth conditions were specifically chosen to optimize the energy consumption. In this procedure, the diffusion of the dopant anion was controlled to ensure an efficient PPy doping.

Aspects related to the applicability of the composed PPy/TiO_2 thin films are further concluded in the next chapter.

Bibliography

[1] D. Chandler, J.D. Weeks, H.C. Andersen, Van Der Waals Picture of Liquids, Solids, and Phase Transformations, Science. 220 (1983) 787–794.
[2] S. Lee, W.M. Sigmund, AFM study of repulsive van der Waals forces between Teflon AF (TM) thin film and silica or alumina, Colloids and Surfaces A: Physicochemical and Engineering Aspects. 204 (2002) 43–50.
[3] L. Chen, Microwave Electronics: Measurement and Materials Characterization, John Wiley, 2004.
[4] A. Cataldo, E.D. Benedetto, G. Cannazza, Broadband Reflectometry for Enhanced Diagnostics and Monitoring Applications, Springer, 2011.
[5] M.S. Dresselhaus, Solid State Physics Part II Optical Properties of Solids, American Scientific Publishers, 1980.
[6] H. Hertz, Ueber einen Einfluss des ultravioletten Lichtes auf die electrische Entladung (About the Influence of Ultraviolet Light on the Electric Discharge), Annalen Der Physik. 267 (1887) 983–1000.
[7] M. Planck, Ueber das Gesetz der Energieverteilung im Normalspectrum (On the Law of Distribution of Energy in the Normal Spectrum), Annalen Der Physik. 309 (1901) 553–563.
[8] A. Einstein, Über einen die Erzeugung und Verwandlung des Lichtes betreffenden heuristischen Gesichtspunkt (On a Heuristic Viewpoint Concerning the Production and Transformation of Light), Annalen Der Physik. 322 (1905) 132–148.
[9] R.A. Millikan, A Direct Determination of "h.," Phys. Rev. 4 (1914) 73–75.
[10] A. Abbas, M.J. Linman, Q. Cheng, New trends in instrumental design for surface plasmon resonance-based biosensors., Biosensors & Bioelectronics. 26 (2011) 1815–24.
[11] C.G. Zoski, Handbook of Electrochemistry, Elsevier, 2007.
[12] C.K. Baker, J.R. Reynolds, A quartz microbalance study of the electrosynthesis of polypyrrole, Journal of Electroanalytical Chemistry and Interfacial Electrochemistry. 251 (1988) 307–322.
[13] S.J. Xia, V.I. Birss, A multi-technique study of compact and hydrous Au oxide growth in 0.1 M sulfuric acid solutions, Journal of electroanalytical chemistry. 500 (n.d.) 562–573.
[14] J.S. Gordon, D.C. Johnson, Application of an electrochemical quartz crystal microbalance to a study of water adsorption at gold surfaces in acidic media, Journal of Electroanalytical Chemistry. 365 (1994) 267–274.
[15] A. Hamelin, Cyclic voltammetry at gold single-crystal surfaces. Part 1. Behaviour at low-index faces, Journal of Electroanalytical Chemistry. 407 (1996) 1–11.
[16] W. Stöckel, R. Schumacher, Electrochemical in-situ investigations on polycrystalline gold electrodes with oscillating quartz crystals: The electrosorption valency and heterogeneity constant of halide and sulphate adlayers, Berichte Der Bunsengesellschaft Für Physikalische Chemie. 93 (1989) 600–605.
[17] W.L. Masterton, C.N. Hurley, Chemistry: Principles And Reactions : A Core Text, Cengage Learning, 2005.
[18] A. Berná, J.M. Delgado, J.M. Orts, A. Rodes, J.M. Feliu, In-Situ Infrared Study of the Adsorption and Oxidation of Oxalic Acid at Single-Crystal and Thin-Film Gold Electrodes: A Combined External Reflection Infrared and ATR−SEIRAS Approach, Langmuir. 22 (2006) 7192–7202.
[19] A.A. Almulhem, Bulk plasmon-assisted ion neutralization at metal surfaces, Brazilian Journal of Physics. 32 (2002) 916–920.
[20] A.A. Almulhem, M.D. Girardeau, Theory of ion neutralization at metal surfaces by surface plasmon excitation, Surface Science. 210 (1989) 138–162.
[21] K.F. Babu, R. Senthilkumar, M. Noel, M.A. Kulandainathan, Polypyrrole microstructure deposited by chemical and electrochemical methods on cotton fabrics, Synthetic Metals. 159 (2009) 1353–1358.
[22] A. Nazzal, G.B. Street, Molecular weight determination of pyrrole-based polymers, J. Chem. Soc., Chem. Commun. (1984) 83–84.
[23] C. Pirvu, C.C. Manole, A.B. Stoian, I. Demetrescu, Understanding of electrochemical and structural changes of polypyrrole/polyethylene glycol composite films in aqueous solution, Electrochimica Acta. 56 (2011) 9893–9903.
[24] A.-M. H, C. B.e, Auto-inhibition effects in anodic oxidation of phenols for electrochemical waste-water purification, Journal of the Serbian Chemical Society. 66 (n.d.) 765–784.

[25] M.A. Heras, S. Lupu, L. Pigani, C. Pirvu, R. Seeber, F. Terzi, et al., A poly(3,4-ethylenedioxythiophene)-poly(styrene sulphonate) composite electrode coating in the electrooxidation of phenol, Electrochimica Acta. 50 (2005) 1685–1691.
[26] G. Sauerbrey, Use of vibrating quartz for thin film weighing and microweighing, Z. Phys. 155 (1959) 206–222.
[27] M.P. Neupane, I.S. Park, S.J. Lee, K.A. Kim, M.H. Lee, T. Sung, Study of Anodic Oxide Films of Titanium Fabricated by Voltammetric Technique in Phosphate Buffer Media, Int. J. Electrochem. Sci. 4 (2009) 197–207.
[28] S. Rani, S.C. Roy, M. Paulose, O.K. Varghese, G.K. Mor, S. Kim, et al., Synthesis and applications of electrochemically self-assembled titania nanotube arrays, Physical Chemistry Chemical Physics. 12 (2010) 2780.
[29] C.C. Manole, C. Pirvu, Surface and electrochemical analysis for the understanding of TiO2 nanopores/nanotubes changes in post- elaboration treatment, Surface and Interface Analysis. 43 (2011) 1022–1029.
[30] J.-L. Delplancke, R. Winand, Galvanostatic anodization of titanium—II. Reactions efficiencies and electrochemical behaviour model, Electrochimica Acta. 33 (1988) 1551–1559.
[31] S.P. Albu, N. Taccardi, I. Paramasivam, K.R. Hebert, P. Schmuki, Oxide Growth Efficiencies and Self-Organization of TiO2 Nanotubes, J. Electrochem. Soc. 159 (2012) H697–H703.
[32] V.A. Akulichev, M.G. Sirotyuk, L.D. Rozenberg, others, High intensity ultrasonic fields, Ed LD Rozenberg, Plenum, New York. (1971) 239–259.
[33] C.E. Brennen, Cavitation and bubble dynamics, Oxford University Press, USA, 1995.
[34] M.S. Plesset, R.B. Chapman, Collapse of an initially spherical vapour cavity in the neighbourhood of a solid boundary, Journal of Fluid Mechanics. 47 (1971) 283–290.
[35] K.S. Suslick, L.A. Crum, Sonochemistry and Sonoluminescence, in: lcolm J.C. Editor-in-Chief (Ed.), Encyclopedia of Acoustics, John Wiley & Sons, Inc., 2007: pp. 271–281.
[36] A. Valota, D.J. LeClere, P. Skeldon, M. Curioni, T. Hashimoto, S. Berger, et al., Influence of water content on nanotubular anodic titania formed in fluoride/glycerol electrolytes, Electrochimica Acta. 54 (2009) 4321–4327.
[37] L. Huang, F. Peng, H. Yu, H. Wang, J. Yang, Z. Li, The influence of ultrasound on the formation of TiO2 nanotube arrays, Materials Research Bulletin. 45 (2010) 200–204.
[38] D. Kim, A. Ghicov, P. Schmuki, TiO2 Nanotube arrays: Elimination of disordered top layers ("nanograss") for improved photoconversion efficiency in dye-sensitized solar cells, Electrochemistry Communications. 10 (2008) 1835–1838.
[39] K.S. Suslick, G.J. Price, Applications of ultrasound to materials chemistry, Annual Review of Materials Science. 29 (1999) 295–326.
[40] C.C. Manole, A.B. Stoian, C. Pirvu, Surface Perspective of a TiO2 Nanoarchitecture, U.P.B. Sci. Bull. 72 (2010) 91–98.
[41] G. Liu, K. Wang, N. Hoivik, H. Jakobsen, Progress on free-standing and flow-through TiO2 nanotube membranes, Solar Energy Materials and Solar Cells. 98 (2012) 24–38.
[42] Q.A.S. Nguyen, Y.V. Bhargava, V.R. Radmilovic, T.M. Devine, Structural study of electrochemically synthesized TiO2 nanotubes via cross-sectional and high-resolution TEM, Electrochimica Acta. 54 (2009) 4340–4344.
[43] J.M. Macak, H. Tsuchiya, A. Ghicov, K. Yasuda, R. Hahn, S. Bauer, et al., TiO2 nanotubes: Self-organized electrochemical formation, properties and applications, Current Opinion in Solid State and Materials Science. 11 (2007) 3–18.
[44] G.K. Mor, O.K. Varghese, M. Paulose, K. Shankar, C.A. Grimes, A review on highly ordered, vertically oriented TiO2 nanotube arrays: Fabrication, material properties, and solar energy applications, Solar Energy Materials and Solar Cells. 90 (2006) 2011–2075.
[45] J.M. Macak, P. Schmuki, Anodic growth of self-organized anodic TiO2 nanotubes in viscous electrolytes, Electrochimica Acta. 52 (2006) 1258–1264.
[46] W.-J. Lee, M. Alhoshan, W.H. Smyrl, Titanium Dioxide Nanotube Arrays Fabricated by Anodizing Processes Electrochemical Properties, J. Electrochem. Soc. 153 (2006) B499–B505.
[47] S. Popescu, C. Pirvu, M. Mindroiu, C. Manole, I. Demetrescu, Electrochemical Synthesis and Characterization of Ti Modified Electrodes with Polypyrrole – Polyethylene Glycol Hybrid Coating, Revista De Chimie. 61 (2010) 245–248.

[48] A.S. Liu, M.C. Bezerra, L.Y. Cho, Electrodeposition of polypyrrole films on aluminum surfaces from a p-toluene sulfonic acid medium, Materials Research. 12 (2009) 503–507.
[49] M. Noel, K.I. Vasu, Cyclic voltammetry and the frontiers of electrochemistry, Aspect, 1990.

CHAPTER 6 - CONCLUSIONS

The introductive State of The Art chapter described both the main techniques used to obtain the thin films and the modern requirements for the applications. Subsequent chapters consisted of original scientific contribution on a practical level, but with a theoretical approach meant to highlight the important properties of the obtained films. However, the properties were not entirely emphasized with respect to the applications. In this conclusive chapter, a synthesis of those properties will be made and put into perspective with respect to the applications for which they are recommended.

6.1. General Conclusions

The thesis deals with two types of polymeric thin films: PMMA and PPy. The thin films were grown by a dry and a wet route.

The dry route involved the growth of the polymeric films by an original process of Chemical Vapor Deposition, namely Photo-CVD. The growth involves the UV activation of the monomer species in the gas phase. Both PMMA and PPy were obtained for the first time by this Photo-CVD. The characterization highlighted properties with possible applications in microelectronics, micro-optics and heat generating devices.

The wet route involved the growth of thin films by an electrochemical approach. Organic PPy and inorganic TiO_2 nanostructures were obtained and characterized by various electrochemical techniques. The growth aspects of PPy were supplementary highlighted by SPR. This characterization of these materials defined their properties.

6.1.1. Concluding Properties for Future Applications

The thin films properties covered in this thesis can be the focus of possible future applications. Thus a concluding overview of the properties will be made with respect to such applications. At this stage, these properties had not been optimized for the applications and they are rather presented as a screening for future works.

6.1.1.1. Sensor for Interfacial Reduction / Ionization Reactions

A process of electrochemically produced deprotonation was previously studied by SPR (subchapter *5.1.5.*). In chemistry the removal of a proton to form a conjugates base is called deprotonation. The removed proton is generally considered a hydrogen ion. The deprotonation process is reported to act as a colorimetric sensor by the use of amines responsible for color changes, both for fluoride [4] and for Cu (II) [5]. The deprotonation has also an important role in the processes involved in the living world [6,7] but also offers perspectives for applicability on nano-circuits [8,9]. The deprotonation processes can also be investigated by SPR considering the protonated hydrogen as an ion.

The SPR is described essentially by the collective movement of electrons from the metal network interface towards outer environment (subchapter *5.1.5.*). The energy required for this process is given by the perturbing energy of photons. The collective movement of electrons has a periodicity of 10^{-15} s (670 THz or 670 nm for the studied effects). An anion (such as the positive-charged proton) can combine with an electron form the SPR wavefront. This can occur if the anion has a lifetime higher than the electron movement periodicity ($> 10^{-15}$ s). Also, if some physical-chemical reactions are involved that uses irreversibly electrons, the SPR wavefront can be affected. These aspects offer the prospect of interrogating the reactions that occur at the interface.

- Sensing the Interfacial Ionization Reactions –

The ionization reactions can be sensed if the produced ions species are positively charged. These positively charged species can attract the negatively charged electrons. This will lead to the fulfillment of the valence band with the required electron.

The ionization reactions can be deduced by SPR starting from a meta-stable equilibrium, where the anionic species are not generated. As studied in subchapter *5.3.1.* , under the conditions of an applied electric charge, bioxalates release a positively charged ion as a proton:

$$HC_2O_4^- \rightarrow H^+ + C_2O_4^{2-}$$

If this reaction occurs in the range of the electron wave front produced by the SPR, a produced proton combines with a electron forming a hydrogen in ground state:

$$H^+ + e^- \rightarrow H(1s)$$

As this reaction occurs, an indication is observed in the recorded SPR signal by the increase in the reflectivity minima (measured in %). This behavior, described as Ion Neutralization decreases exponentially with the distance from the surface [10], making it a highly interface-sensitive process.

To highlight the quantitative aspects resulted from the measurements, the electrochemical conditions with respect to the reduction reaction will be further treated.

- Sensing the Interfacial Reduction Reactions -

A possible quantification can come from a "fundamental" calibration of the processes that occur at the SPR metal interface. For this purpose, let's consider a general reduction reaction at a metal/electrolyte interface:

$$X^+ + e^- \rightarrow X$$

The reduction process can be electrochemically monitored. From the measured current, the charge can be calculated as [11]:

$$Q_C = \int_{t_i}^{t_f} I dt \qquad (6.1)$$

During the process, the moles of electrons consumed during the reduction reaction (noted as *red*.) can be determined according to the reaction [12]:

$$mol_{e^-}^{red.} = \frac{Q_C}{F} \qquad (6.2)$$

where F is the Faraday constant (F = 96 485 C/mol), defined as the charge amount of one electron (e) multiplied by the number of electrons in a mole (Avogadro constant - N_A) [13]:

$$F = eN_A \qquad (6.3)$$

As previously observed, the electron consumption during the reaction will lead to the increase in SPR reflectivity. To experimentally correlate the reflectivity change with the moles of depleted electrons, we need initially to consider the total moles of conduction electrons in the mass of the metal (noted as *SPR*) [14]:

$$mol_{e^-}^{Au} = n_{val} \frac{\rho V}{M_W} \qquad (6.4)$$

where n_{val} is the number of valence electrons of the metal that produces the SPR, while q, V and M_W are the density, volume and respectively the molecular weight of the SPR producing metal. The interfacial electrons responsible for SPR ($mol_{e^-}^{SPR}$) are expected to respect a proportionally relation with the moles of electrons found in Au.

The ratio of the moles of electrons depleted from the metal involved in the SPR response with the moles of electrons consumed during the reaction can be evaluated with respect to the changes in reflectivity intensity (ΔR) of the SPR response:

$$\Delta R^{-1} \approx \frac{mol_{e^-}^{red.}}{mol_{e^-}^{Au}} \qquad (6.5)$$

The discussion can be addressed also in terms of the total number of electrons by multiplying equations *(6.2)* and *(6.4)* with the Avogadro constant (N_A).

In perspective, further studies will be made to highlight these aspects from an experimental perspective. Some other phenomena at the electrode interface can be eventually emphasized by the correlation between the theoretical and the practical aspects. Such aspects can involve an experimental limitation of the electron population from the SPR producing metal that participates to the Plasmon Resonance or practical implications with respect to the ion recombination in the solution.

With respect to the ions, the mass transport in polypyrrole (PPy) observed experimentally will be further emphasized with respect to its application as actuating material.

6.1.1.2. PPy Actuators

An actuator can be defined as a mechanical, electrical or electrochemical system that produces linear or rotary motion to drive mechanical events [15]. The previously studied PPy thin film indicated an important change in volume by the simple immersion in water (subchapter *5.3.4.3.*). These changes of volume observed by AFM were confirmed by the electrochemical doping and dedoping with ions from the electrolyte. This means that the ion diffusion responsible for a volume change at the PPy thin film interface of 16 % for 90 min immersion time in water can be significantly increased in the whole film by applying a potential difference to guide the ions outside and inside the PPy thin film.

However, in order to allow a significant volumetric change as the one observed experimentally, the PPy thin film requires possessing increased mechanical properties.

- Mechanical properties required for actuators -

Strain is defined as the geometrical quantity that measures the deformation of a body [16] when an external force is applied. The PMMA film has a point of breaking that occurs at a strain ε_f of 0.5 % [17]. This means essentially that when the PMMA suffers a volumetric deformation above 0.5 % the material will begin to break (subhapter *2.3.3.*). Consequently, the PPy film requires possessing a strain-at-break point above that value of the volume change. Indeed the literature reports values that start from ~ 2.5 % to the very large value of ~ 50 % [18–20]. These values can be compared to those of the artificial muscles of around 30 % [20]. This allows the efficient volume change without the PPy film breaking.

Also their high Young Modulus (0.05 to 100 GPa) and high tensile strength (1 MPa to 1 GPa) [21] indicate that considerable forces can be exerted in order to perform various mechanical tasks.

- The actuating system -

During the electrochemical growth of PPy thickness, the conduction of the film decreases. A solution for preventing this issue is the use of a gold film over which the PPy is polymerized [22]. However, the use of Au has a shortcoming with respect to the operating lifetime, as delamination of the polymer from the metal can occur [23]. A study involving the adhesion of PPy describes the TiO_2 oxide as better adhering compared with Au [24]. For this reason, the TiO_2 nanotubes as freestanding membrane are proposed for PPy growth, as schematically represented in *Figure 6-1 a)*. An ultrasound post-treatment is one of the means

by which the TiO_2 nanotubes can be removed from the Ti substrate [25]. The aspects of the TiO_2 removal by ultrasonication were highlighted in Chapter 5.1.4.2. Furthermore, the effective surface available for the mass transport of ions is increased through to the nanostructured membrane.

When a potential difference is applied to a PPy film, there is reversibility in ions movements: an ion of one charge type comes out and one of other charge type comes in. The exchange process is essentially governed by their sizes and concentration in the electrolyte [26]. For the system to operate efficiently, a large doping anion (negative ion) needs to be irreversibly bound to the PPy membrane, so that only the cation (positive ion) passes in and out the film. The use of dodecyl benzene sulfonate (DBS^-) is extensively studied [26–29]. Such a requirement can also be addressed by the use of a previously studied poly (styrene sulfonate) (PSS^-) anion (Chapter 5.3), as PSS^- is not stripped from the film [30] and has the expected results by the use in the actuating devices [31]. The dielectric changes likely associated to the PSS^- reorientations in the PPy film under the potential polarization were also observed by SPR/EIS (Chapter 5.3.3).

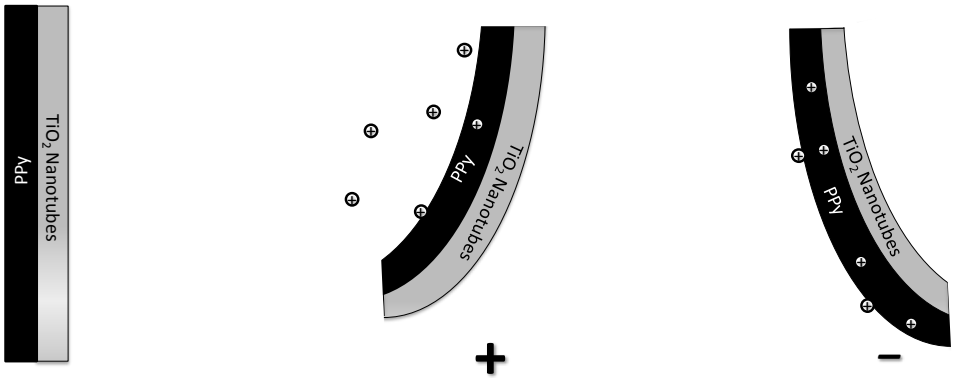

a) *b)* *c)*

Figure 6-1: PPy/TiO_2 nanotube bilayers (a) with the PPy film volume compression under oxidative conditions (b) and the PPy film volume expansion under reduction conditions (c)

The above aspects shape the overall aspects required for the efficient use of PPy as actuator. Considering the irreversibly incorporated anion into the PPy film, under a positive potential difference (oxidative conditions), the cations are removed from the PPy film. This leads to a significant decrease in volume for the PPy film. The decrease in volume acts as a muscle, contracting the TiO_2 nanotube membrane as shown in *Figure 6-1 b)*. Conversely, under negative potential difference (reduction conditions), the cations are attracted into the PPy film. This promotes a volume increase that bends again the TiO_2 nanotubes in a direction opposite to the contraction, as showed in *Figure 6-1 c)*.

The facile electrochemical control of the TiO_2/PPy film growth detailed in Chapter 5.4.3 offers the prospect of building an actuating system with dynamically adjusted parameters. Also, the conditions were optimized in order to obtain the films under low energy consumption.

6.1.1.3. Heat Generating Films (Resistors)

In Chapter 4.1.3.2.1, PPy thin films were obtained with a transmittance up to 64 % by Photo-CVD. Through the control of the PPy film thickness, the transparency and the conductivity is also controlled. A transmittance of around 85 % is reported to be obtained for films around 35 and 45 nm [32]. This indicates that PPy thin films are candidates for use as Transparent Conducting Material (TCM). However, when the thickness decreases, the resistance also increases [32].

- Heat generation -

While treating the harmonic motion and its physical implications with respect to a sinusoidal polarization of a potential difference (Chapter 5.1), the heat generation due to the resistivity was attributed to an energy loss. This heat that occurs due to the passage of an electric current is described by the Joule's law as [33]:

$$Q_J = I^2 Rt \qquad (6.6)$$

where Q_J is the Joule heat, I is the current, R is the material resistance and t is time of the current flow. This highlights the fact that the Joule heat produced by an electric current is directly proportional with the electrical resistance of the conductor. In this manner, with the thinning of the PPy film, the resistance increases, offering the prospect of generating more heat.

The high transparences low thickness and high resistivity are properties that recommend the use of PPy thin films for heat generation transparent devices. With this respect, in literature the defrosting of the inclined surface of a car windshield was theoretically modeled to account for the required properties of heat-producing material [34]. As observed in equation *(6.6)*), the resistivity is the most important one. The increase in PPy resistivity can be increased by changing the doping degree of the film or, as experimentally observed in Chapter 5.3.4.2, by immersing the film in deionized water to allow ions diffusion outside the film. The water immersion can be accompanied by applying a potential difference which enhances the dedoping by anion release.

- Functional coatings on fabrics -

One of the advantages of the Photo-CVD process is that the thin film can be deposited without a constraint related to a substrate type and with a conformal coverage of different substrate geometries. The deposition was also proved to be achieved by gas infiltration onto the surface of substrates that are not in line-of-sight from the reactor entrance, as shown in Chapter 4.1.3. This also offers the possibility of coating different fabrics with heat-generating PPy, such as the ones reported in literature for PET [35] and woven fabric [36]. The simultaneous deposition of Ag nanpoarticles with the PPy film adds versatility to the coated fabric, as Ag nanoparticles are known to have bactericidal properties [37,38].

The PPy films obtained under Photo-CVD conditions showed also the ability to encapsulate liquid in a patterned arrangement at microscopic scale. These aspects will be further treated with respect to their applicability.

6.1.1.4. Focal Micro-Lenses Array

Three key aspects need to be fulfilled in order to obtain a focal micro-lenses array: (*I*) lenses of sizes in the micrometers range or below, (*II*) means of patterning the micro-lenses into an array and (*III*) a focalizing method for the whole array. These aspects will be touched while summing some of the experimental results about the thin films grown by Photo-CVD route.

- Liquid Encapsulation -

The blister shape of the lenses was achieved by encapsulating in a thin membrane of polymer a liquid phase of its monomer. The encapsulation evidences were obtained by spectroscopic and microscopic means using both G1.5 and G2.8 Direct Liquid Injection Systems (DLI) from Kemstream.

a) Kemstream DLI G1.5 system

After Photo-CVD deposition, in Chapter 1.4.1 the peeling of a PMMA thin film that encapsulates an oil pellicle was observed through an optical microscopy investigation. Chapter 1.2.2.1 also highlighted in a SEM micrograph a possible breakdown of a PMMA thin film that enveloped a fluid phase (Figure X).

Further chemical evidences of a fluorocarbon oil encapsulation with PMMA were also obtained in Chapter 1.4.2. Other spectroscopic tests were made over samples which were stored for 2 months at around 17 ^{o}C under dark. Notably, the MMA monomer has a volatile behavior. In a long the storing period, the MMA monomer would have been evaporated. Furthermore the droplets (blisters) preserved the same shape and distribution over the surface, indicating the presence of a tight protective membrane.

The subsequent post-treatments detailed in Chapter 1.4.2. highlighted the presence of the fluid phase of the monomer and the presence of the photoinitiator as a component of the liquid solution used in the Photo-CVD deposition. The liquid MMA and the sample integrity after two months indicate the presence of a PMMA membrane in the form of a thin film that covers a fluid phase.

b) Kemstream DLI G2.8 system

The changes of the injection technology to DLI G2.8 system lead to obtain the same blister topology over the surface. Optical microscopy evaluation showed a more ordered patterning of PMMA blisters on Si substrates. These aspects are captured in *Figure 3.4* (*b, c, d*), *Figure 3.12* (*b, c*) during the film characterization by Raman Confocal Microscopy.

A different approach to study the liquid encapsulation by a membrane was taken in Chapter 1.3.3.2 and Chapter 4.1.1.3.2 by using AFM spectroscopy to confirm the uniform converging with PMMA of both the solid substrate and the fluid monomer. Also, the approach of FTIR investigation in Chapter 1.3.2 highlighted the chemical tacticity specific to the PMMA polymer. This tacticity offers the prospect of separating the PMMA orientation over a solid surface from the one on liquid.

Furthermore, a self-healing of the membrane that covers the blisters was studied by laser irradiation in Chapter 1.5.2. The concept of self-healing material as means of preventing catastrophic failure is already investigated for a wide range of materials in order to provide products with increased performances and higher operating lifetimes [39,40].

The extensive characterization, both from the microscopy and spectroscopy data, highlighted the presence of the thin membrane that encapsulates a fluid phase of monomer under the form of blisters. These curved surfaces of the microscopic blisters characterized by a high overall transparence (Chapters 2.2.3.1, 3.2.1) can define them as aspheric micro-lenses. Such aspheric micro-lenses can reduce or minimize the spherical aberration encountered in classical spherical lenses [41].

In order to achieve a symmetric array, an ordering of the blisters over the surface is required.

- Ordered patterning -

The patterning of micro lenses can be achieved by manipulating the surface energy of the substrate. The heterogeneous nucleation is an approach used in synthesizing nanoparticles by generating surface defects to act as nucleation centers [42]. It involves the deliberate creation of surface defects that changes locally the surface energy. This allows the preferential growth at the defect sites.

The presence of heterogeneities onto the surface can also act as a preferential nucleation site for the blister formation. These aspects were theoretically highlighted in Chapter 2.2.2.2. Also AFM images emphasized the liquid presence at the basis of such heterogeneities for PMMA in Chapter 2.2.2.2 and Chapter 3.3.3.1.

Atomic defects on Si(100) substrate are deduced to experimentally allow the blister growth in a self-ordered manner. These aspects, as treated in Chapter 4.1.1.3, were observed for liquid encapsulation in the case of a PPy polymer. The distinct mechanical properties of PPy with respect to PMMA offer the premises of increased resistance with respect to the focal change.

- Focal change -

The focal change can be achieved by manipulating the liquid that is encapsulated in a thin membrane. The higher resistance of the enveloping membrane, the higher focal changes can be obtained. As previously presented, PPy thin films can withstand volume expansions up to 50%. The volume changes can be followed by the AFM technique.

This liquid manipulation to obtain a focal change can be achieved by pneumatic means [43], electrokinetical means [44] or by using different refractive index liquids [45]. The material property of a liquid to change its volume under a temperature change offers an alternative route of the lens focal change. This property, called thermal expansion, can be used to induce the volume change until the mechanical breaking point of the enveloping polymeric film. A schematic representation of the process is shown in *Figure 6-2*. The volume changes due to the temperature variation can be studied *in-situ* by AFM. Such experimental examples are treated theoretically for PMMA in Chapter 2.3.1.1 or investigated practically in the case of volume changes in the doped PPy film from Chapter 5.1.3.4.3.

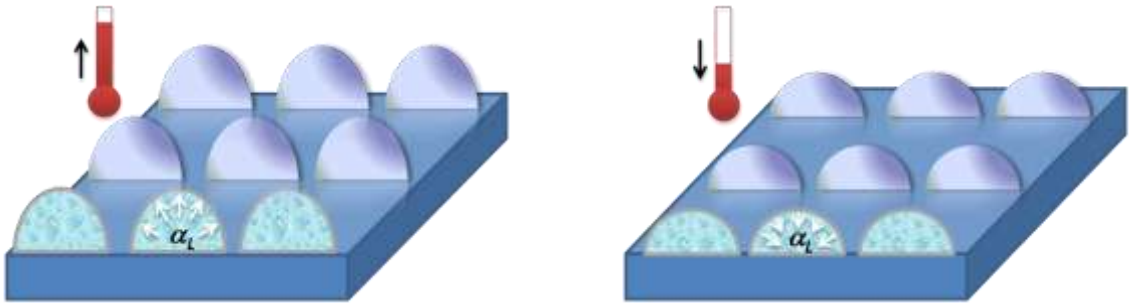

a) *b)*

Figure 6-2:The thermal expansion (α_L) of the liquid which causes the focal change a) when the temperature increases and b) when the temperature decreases

The liquid lenses are a promising candidate in the context of miniaturization in the image optics. They can provide solutions for applications ranging from mobile phone industry to the lab-on-chip systems. The above aspects contribute to a novel approach to the micro-optics that starts from the micro-lenses fabrication, follows their properties and subsequently defines its operating conditions as a system. Although the thermal expansion is presented as the main control parameter of the micro-lenses array, other alternative routes can be explored. However, the presented aspects of the thermal expansion set the basis for further applicability in microelectronics.

6.1.1.5. Micro-Lithography

Micro-lithography is a technique used to transfer a pattern or image from one medium to another, with image features in the micrometer range or smaller [46]. The pattern can be the ordered pattern obtained by Photo-CVD and characterized from a morphological point of view in Chapter 4.1.1.3.1.

In particular cases, the phenomenon of Thermal Induced-Release of Internal Phase (TI-RIP) detailed in Chapter 2.3.3 can be an alternative to Electron Beam Lithography (EBL).

For EBL two components are required: (*i*) a substrate that is a conductor or a semiconductor and (*ii*) a resist layer. If an insulator substrate is used, a thin film of gold is

usually deposited. After the exposure to a Gaussian electron flux, the backscattered electrons lead to the development of areas into the resist layer where the substrate is exposed. Subsequent steps that involve electrochemical deposition or etching on the substrate to create localized deposition or dissolution to create patterned shapes. However, with the use of classical resists (such as PMMA) it can require from 100 hours to pattern the surface of a 64 mm disk to 1000 hours depending on the pattern size, beam current and resist [47]. Consequently, misalignment can occur, requiring the machine to stop periodically (every 5 to 10 min is typical) [48]. The TI-RIP process comes as a viable alternative to this issue.

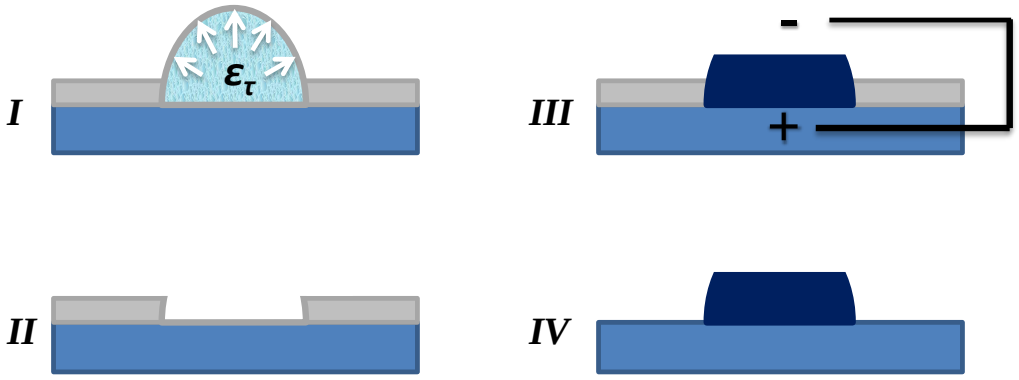

Figure 6-3: Thermal Induced-Release of Internal Phase patterning (I and II) with subsequent electrochemical growth (III) and thin film dissolution (IV)

Compared to EBL, the TI-RIP process can occur on any kind of substrates, not even having a necessary requirement of different substrate for the film, as long as liquid (or gas) encapsulation is obtained as the interface between the encapsulating film and gaseous (or even liquid) outer environment.

The patterning example by TI-RIP is schematically shown in *Figure 6-3*. The TI-RIP process, as treated in Chapter 2.3.3, describes the release of a liquid internal phase under the influence of temperature due to a thermally-induced elastic strain (ε_τ) (step *I* in *Figure 6-3*). When the liquid is released, the substrate is exposed by the rupture of the encapsulating membrane (as shown in step *II* of *Figure 6-3*). Different rupture geometries were experimentally observed during the Photo-CVD growth (Figure 2.27). This is probably related to the rate of temperature variation (namely the slope of temperature increase as a function of time). Thus, the membrane breaking can be adjusted by the control of temperature. Also, the liquid release can occur homogenously over the surface of the sample if there is no temperature gradient, allowing for a nearly instantaneous process to obtain the surface patterning. The temperature variation can be considered as starting from the room temperature towards the boiling point of the encapsulating liquid to simultaneously allow efficient evaporation. These aspects can be achieved also at low temperatures under low pressures. Additional information with respect to the temperature and pressure influence on the evaporation is treated in Chapter 3.4.

If the enveloping membrane is an resistor (insulator) such as the case of PMMA and the substrate is conductor, a controlled electrochemical growth over the exposed areas of the substrate can be achieved on the exposed conducting area (step *III* in *Figure 6-3*). After the subsequent removal of the PMMA membrane by dissolving it chemically (for example in an acetone bath [49]), a free-standing ordered microstructure can be obtained (step *IV* in *Figure 6-3*).

The microlithography aspects that can be addressed by the TI-RIP process offer a fast and facile method that can be used in microelectronics industry. The versatility of the TI-RIP highlights the fact that this process can occur on any type of surface, not limiting the

patterned growth over the surface to an electrochemical process. Furthermore, it is a fast process that can be an alternative to the time-consuming EBL.

6.2. Original contributions

The original contributions that define a significant part of this thesis objectives can be divided in three major sections: *i*) growth processes, *ii*) characterization and *iii*) properties.

6.2.1. Growth processes

A first aspect of originality is given by the means of polymerizing by a dry route. This is based on the UV activation of the monomer in the gas phase by the Photo-CVD process (Chapter 1.1). Compared with literature data, this approach does not involve the direct UV exposure of the substrate and the growing film. It allows the polymerization at room temperature and on fragile substrate (sensitive to photons).

After the Photo-CVD deposition the encapsulation of a liquid phase of monomer into an ultra-thin membrane of polymer was obtained. Also the transition from the gaseous phase into a liquid and/or a solid state was successfully influenced. This change of the phase transition route was achieved through a chemical approach by changing the photo-initiators (Chapter 4.5).

Another aspect of originality with respect to the deposition is the process concerns the elaboration of composite thin films of TiO_2 and PPy. This wet route process of growth is designed to offer a two-step electrochemical control: (*i*) a self-ordered growth of the TiO_2 nanostructures and (*ii*) a subsequent polymerization of a PPy thin film over the TiO_2 nanotubes (Chapter 5.4). Also, in the use of the experimental parameters, the efficiency of energy consumption was also pursued.

The thin films elaboration required a detailed characterization in order to investigate the aspects related to their nature and properties.

6.2.2. Characterization

An originality aspect is given by the approach of the characterization process from a unitary perspective of a mathematical model. The harmonic motion model sets into a common perspective various physical characterization means (Chapter 5.1). Thus methods of investigation used to characterize the thin films, such as AFM, EIS and the SPR, find common denominators with respect to the mathematical approach.

The use of the DLI in CVD to obtain the vapor phase required for the polymerization is a novelty in the literature. The DLI principle (not coupled to CVD) is used on the large scale in automotive industry. Its parameters however are not defined for liquids with various properties and in these particular cases of DLI operating conditions. Consequently a practical study was made to characterize the liquid injection parameters (Chapter 2.1.1.2) and a theoretical study related to the vapor phase obtainment in the low pressure conditions (Chapter 3.4). Also an experimental setup was designed in order to study and characterize the polymerization of a thin film that occurs due to gas phase infiltration of the monomer (Chapter 4.4).

The Photo-CVD process lead to the encapsulation of a fluid phase of the monomer in a solid membrane constituted of its polymer. The atomic force spectroscopy highlighted the surface covering with a thin membrane of polymer (Chapter 3.3.3.2 and Chapter 4.1.3.2) and the Raman technique highlighted the presence of the fluid monomer (Chapter 2.3.3). In the characterization process the presence of the nucleation centers for the liquid monomer were investigated (Chapter 2.2.4), but also aspects that indicate a polymerization with different orientations of the polymeric chains over solid and over liquid (Chapter 3.3.2.1). By a fundamental interpretation of various and recent scientific studies these aspects emphasize in

an original manner the obtainment of a liquid phase of the monomer that is covered with a thin membrane of its polymer.

With respect to the wet route by which the characterization of some thin films was achieved, an original study was achieved that implicates the coupling between the EIS and SPR techniques. By the use of polyphenol it was succeed to monitor in parallel the SPR response with the one of the EIS, emphasizing aspects related to the polymer network arrangement in the conditions of applying a periodic perturbing potential difference.

Another original manner of characterization was highlighted in the case of the TiO_2 nanotubes electrochemically grown. This kind of top-down characterization was achieved by applying an ultrasound treatment that leads to a layered removal of the nanotubes (Chapter 5.4.2.). Aspects of originality related to this characterization were detailed also in a series of articles published in international scientific journals [1–3].

Following the characterization, a series of properties with an important character of originality were defined for the obtained thin films.

6.2.3. Properties

A series of depositions by the Photo-CVD dry route were achieved by varying the substrate temperature. The surface characterization emphasized the possibility to release the liquid monomer from inside the blisters by breaking of the enveloping polymer membrane. This was achieved by *in-situ* changes in volume during the growth by the thermal expansion coefficient, described as the Thermal Induced-Release of the Internal Phase (TI-RIP) process (Chapter 2.4.3.).

Another thermal effect was observed also in the case of the irradiation with the VIS laser of the Raman Confocal Microscopy setup. A study was presented that investigates the laser influence that highlighted the phase transition of the MMA monomer as a function of temperature (Chapter 3.2.2. and Chapter 3.3.1.) but also the estimated temperature generated by the laser in the focal area (Chapter 3.5.2.). This effect proved to present original properties of self-healing of the blisters obtained by the dry route (Chapter 3.5.2.2.).

The original aspects presented above were obtained by studying (both theoretically and experimentally) the material properties behavior with respect to the temperature. Originality aspects were also highlighted by studies on the material properties that describe the resistance that is encountered when forming an electric field, also named permittivity (Chapter 5.1.3). The permittivity was studied both by EIS and SPR. Furthermore, aspects of novelty were emphasized by the electrochemical investigation of the Plasmon-Assisted Ion Neutralization. Thus, the SPR response was investigated in two plains that describe two different phenomena: *i*) the classical approach of monitoring the mass changes at the interface that are due to the changes in permittivity and *ii*) a new approach related to the electrochemical neutralization of the plasmons producing the SPR signal (Chapter 5.3.1.).

These properties presented above, but also other aspects emphasized in the previous chapters, set the bases for the applications for the prepared materials. These properties will be further presented from an insight into their applicability, setting the perspectives for future developments after optimization of certain parameters.

6.3. Perspectives for ulterior development

The thin film growth, characterization and the investigation of the properties emphasized their applicability. The thesis treated the original scientific contributions both from an experimental perspective and a theoretical one. The material properties define the fundament for their applicability.

In this manner the obtained thin films (either by the dry route of the Photo-CVD or by the electrochemical wet route) had been characterized in order to highlight their key properties with respect to the applications. These properties describe a wide range of possible

applications. As further perspective, an optimization of the properties can be followed having as objective the increase of the efficiency for a specific application.

Bibliography

[1] C.C. Manole, C. Pirvu, I. Demetrescu, Evaluation of TiO2 Nanotubes Changes after Ultrasonication Treatment, Molecular Crystals and Liquid Crystals. 521 (2010) 84–92.
[2] C.C. Manole, C. Pirvu, Surface and electrochemical analysis for the understanding of TiO2 nanopores/nanotubes changes in post- elaboration treatment, Surface and Interface Analysis. 43 (2011) 1022–1029.
[3] C.C. Manole, A.B. Stoian, C. Pirvu, Surface Perspective of a TiO2 Nanoarchitecture, U.P.B. Sci. Bull. 72 (2010) 91–98.
[4] A.M. Costero, S. Peransi, Colorimetric sensing of anions by a neutral biphenyl based amide receptor, Arkivoc. 4 (2007) 92–101.
[5] S.-P. Wu, K.-J. Du, Y.-M. Sung, Colorimetric sensing of Cu(ii): Cu(ii) induced deprotonation of an amide responsible for color changes, Dalton Transactions. 39 (2010) 4363.
[6] D.L. Bostick, C.L.B. III, Deprotonation by Dehydration: The Origin of Ammonium Sensing in the AmtB Channel, PLoS Comput Biol. 3 (2007) e22.
[7] R.S. Hutchison, J.J. Steenhuis, C.F. Yocum, M.R. Razeghifard, B.A. Barry, Deprotonation of the 33-kDa, Extrinsic, Manganese-stabilizing Subunit Accompanies Photooxidation of Manganese in Photosystem II, J. Biol. Chem. 274 (1999) 31987–31995.
[8] S. Taniguchi, M. Minamoto, M.M. Matsushita, T. Sugawara, Y. Kawada, D. Bethell, Electron transport in networks of gold nanoparticles connected by oligothiophene molecular wires, Journal of Materials Chemistry. 16 (2006) 3459.
[9] X. Yu, V.M. Rotello, Nanoparticle devices: Going with the electron flow, Nature Nanotechnology. 6 (2011) 693–694.
[10] A.A. Almulhem, The Effect of Ion Motion and Ion Neutralization at Metal Surfaces via Surface Plasmon-Excitation, Chinese Journal of Physics. 41 (2003).
[11] K.C.A. Smith, R.E. Alley, Electrical Circuits: An Introduction, Cambridge University Press, 1992.
[12] J.C. Kotz, P.M. Treichel, J. Townsend, Chemistry & Chemical Reactivity, Cengage Learning, 2011.
[13] J.G.R. Briggs, Longman A-level Course in Chemistry, Pearson Education South Asia, 2002.
[14] J. Morrison, Modern Physics: for Scientists and Engineers, Academic Press, 2010.
[15] G. Hegde, Mechatronics, Jones & Bartlett Publishers, 2009.
[16] A. Pytel, J. Kiusalaas, Mechanics of Materials: Si Edition, Cengage Learning, 2011.
[17] D. Blond, V. Barron, M. Ruether, K.P. Ryan, V. Nicolosi, W.J. Blau, et al., Enhancement of Modulus, Strength, and Toughness in Poly(methyl methacrylate)- Based Composites by the Incorporation of Poly(methyl methacrylate)- Functionalized Nanotubes, Advanced Functional Materials. 16 (2006) 1608–1614.
[18] J. Foroughi, G.M. Spinks, G.G. Wallace, High strain electromechanical actuators based on electrodeposited polypyrrole doped with di-(2-ethylhexyl)sulfosuccinate, Sensors and Actuators B: Chemical. 155 (2011) 278–284.
[19] Y. Li, X.Y. Cheng, M.Y. Leung, J. Tsang, X.M. Tao, M.C.W. Yuen, A flexible strain sensor from polypyrrole-coated fabrics, Synthetic Metals. 155 (2005) 89–94.
[20] K. Yamato, K. Tominaga, W. Takashima, K. Kaneto, Stability of electrochemomechanical strains in polypyrrole films using ionic liquids, Synthetic Metals. 159 (2009) 839–842.
[21] E. Smela, Conjugated Polymer Actuators for Biomedical Applications, Advanced Materials. 15 (2003) 481–494.
[22] Sutar, Dayanand, Aswal, D K, Gupta, S K, Yakhmi, J V, Electrochemical actuator from conductive electroactive polymer polypyrrole deposited on gold, IndianJournal of Pure & Applied Physics. 45 (2007) 345–357.
[23] M. Pyo, C.C. Bohn, E. Smela, J.R. Reynolds, A.B. Brennan, Direct Strain Measurement of Polypyrrole Actuators Controlled by the Polymer/Gold Interface, Chem. Mater. 15 (2003) 916–922.
[24] K. Idla, O. Inganäs, M. Strandberg, Good adhesion between chemically oxidised titanium and electrochemically deposited polypyrrole, Electrochimica Acta. 45 (2000) 2121–2130.
[25] G. Liu, K. Wang, N. Hoivik, H. Jakobsen, Progress on free-standing and flow-through TiO2 nanotube membranes, Solar Energy Materials and Solar Cells. 98 (2012) 24–38.

[26] S. Skaarup, Simultaneous anion and cation mobility in polypyrrole, Solid State Ionics. 159 (2003) 143–147.
[27] W. Takashima, S. Kawamura, K. Kaneto, Diffusion-limited characteristics of mechanically induced currents in polypyrrole/Au-membrane composites, Electrochimica Acta. 56 (2011) 4603–4610.
[28] A. Liu, W. Yuan, G. Shi, Electrochemical actuator based on polypyrrole/sulfonated graphene/graphene tri-layer film, Thin Solid Films. 520 (2012) 6307–6312.
[29] R. Temmer, I. Must, F. Kaasik, A. Aabloo, T. Tamm, Combined chemical and electrochemical synthesis methods for metal-free polypyrrole actuators, Sensors and Actuators B: Chemical. 166–167 (2012) 411–418.
[30] L. Qu, G. Shi, C. Liu, J. Yuan, W. Qian, Preparation, characterization and electrochemical properties of polypyrrole-polystyrene sulfonic acid composite film, Chinese Journal of Polymer Science. 23 (2005) 37–46.
[31] C. Hong, J.D. Nam, Y. Так, Enhanced Behaviors of Ionic-Polymer Metal Composite (IPMC) Actuator Coupled with Polymeric Anion-doped Polypyrrole Thin Film, Journal of the Korean Electrochemical Society. 9 (2006) 137–140.
[32] J. Kim, D. Sohn, Y. Sung, E.-R. Kim, Fabrication and characterization of conductive polypyrrole thin film prepared by in situ vapor-phase polymerization, Synthetic Metals. 132 (2003) 309–313.
[33] S. Prakash, Physics Vol (1 and 2), FK Publications, n.d.
[34] S. Roy, H. Kumar, R. Anderson, Efficient defrosting of an inclined flat surface, International Journal of Heat and Mass Transfer. 48 (2005) 2613–2624.
[35] J. Avloni, L. Florio, A.R. Henn, A. Sparavigna, Thermal electric effects and heat generation in polypyrrole coated PET fabrics, Arxiv Preprint arXiv:0706.3697. (2007).
[36] J.Y. Lee, D.W. Park, J.O. Lim, Polypyrrole-coated woven fabric as a flexible surface-heating element, Macromolecular Research. 11 (2003) 481–487.
[37] J. Mungkalasiri, L. Bedel, F. Emieux, J. Doré, F.N.R. Renaud, C. Sarantopoulos, et al., CVD Elaboration of Nanostructured TiO2-Ag Thin Films with Efficient Antibacterial Properties, Chemical Vapor Deposition. 16 (2010) 35–41.
[38] M. Guzman, J. Dille, S. Godet, Synthesis and antibacterial activity of silver nanoparticles against gram-positive and gram-negative bacteria, Nanomedicine: Nanotechnology, Biology and Medicine. 8 (2012) 37–45.
[39] V.C. Li, E. Herbert, Robust Self-Healing Concrete for Sustainable Infrastructure, Journal of Advanced Concrete Technology. 10 (2012) 207–218.
[40] G. Couégnat, G.L. Vignoles, V. Drean, C. Mulat, W. Ros, G. Perrot, et al., Virtual material approach to self-healing CMCs, in: 4th European Conference for AeroSpace Sciences (EUCASS), 2011: pp. 1–8.
[41] A. Miks, J. Novak, P. Novak, Third-order design of aspheric spectacle lenses, Optik - International Journal for Light and Electron Optics. 121 (2010) 2097–2104.
[42] G. Cao, Nanostructures & Nanomaterials: Synthesis, Properties & Applications, Imperial College Press, 2004.
[43] N.-T. Nguyen, Micro-optofluidic Lenses: A review, Biomicrofluidics. 4 (2010) 031501–031501–15.
[44] H. Li, C. Song, T.D. Luong, N.-T. Nguyen, T.N. Wong, An electrokinetically tunable optofluidic bi-concave lens, Lab Chip. (2012).
[45] S. Calixto, M.E. Sánchez-Morales, F.J. Sánchez-Marin, M. Rosete-Aguilar, A.M. Richa, K.A. Barrera-Rivera, Optofluidic variable focus lenses, Appl. Opt. 48 (2009) 2308–2314.
[46] McGraw-Hill, S.P. Parker, McGraw-Hill Dictionary of Scientific and Technical Terms, 6th ed., McGraw-Hill Professional, 2002.
[47] S.N. Piramanayagam, T.C. Chong, Developments in Data Storage: Materials Perspective, John Wiley & Sons, 2011.
[48] P. Rai-Choudhury, Handbook of Microlithography, Micromachining, and Microfabrication: Microlithography, SPIE Press, 1997.
[49] Y.-W. Su, C.-S. Wu, C.-C. Chen, C.-D. Chen, Fabrication of Two-Dimensional Arrays of CdSe Pillars Using E-Beam Lithography and Electrochemical Deposition, Advanced Materials. 15 (2003) 49–51.

Annex 1

Photo-CVD check list

- System without the bubbler connection -

1. Insert samples
2. Introduce liquid N_2 into the CVD trap
3. Open the N_2 trap
4. Open the N_2 carrier gas valve
5. Start pump
6. Open the pump's butterfly valve
7. Open vector gas valves
8. Open Mass Flow Controller (MFC) valve
9. Open the compressed air
10. Start injector/vector gas heating
11. Turn ON the UV lamps
12. Regulate UV chamber temperature by adjusting the compressed air opening valve
13. Adjust the total pressure by changing butterfly valve opening (pressure controller)
14. Start the injector main power unit
15. Start the injector software
16. Set the injector working parameters
17. Open the injector valves
18. Start the injector (by software)
19. At the end of the experiment, stop the injection (by software)
20. Close the injector valves
21. Close the injector software
22. Stop the injector main power unit
23. Open the butterfly valve at 100% to purge the system
24. Stop the pomp
25. Turn off the UV lamps
26. Close the compressed air valves when the UV laps cool down
27. Close MFM valve
28. Close the vector gas valves
29. Close the butterfly valve
30. Close the N_2 trap
31. Close the N_2 gas valve
32. Depressurize the sample chamber
33. Remove the samples

Annex 2

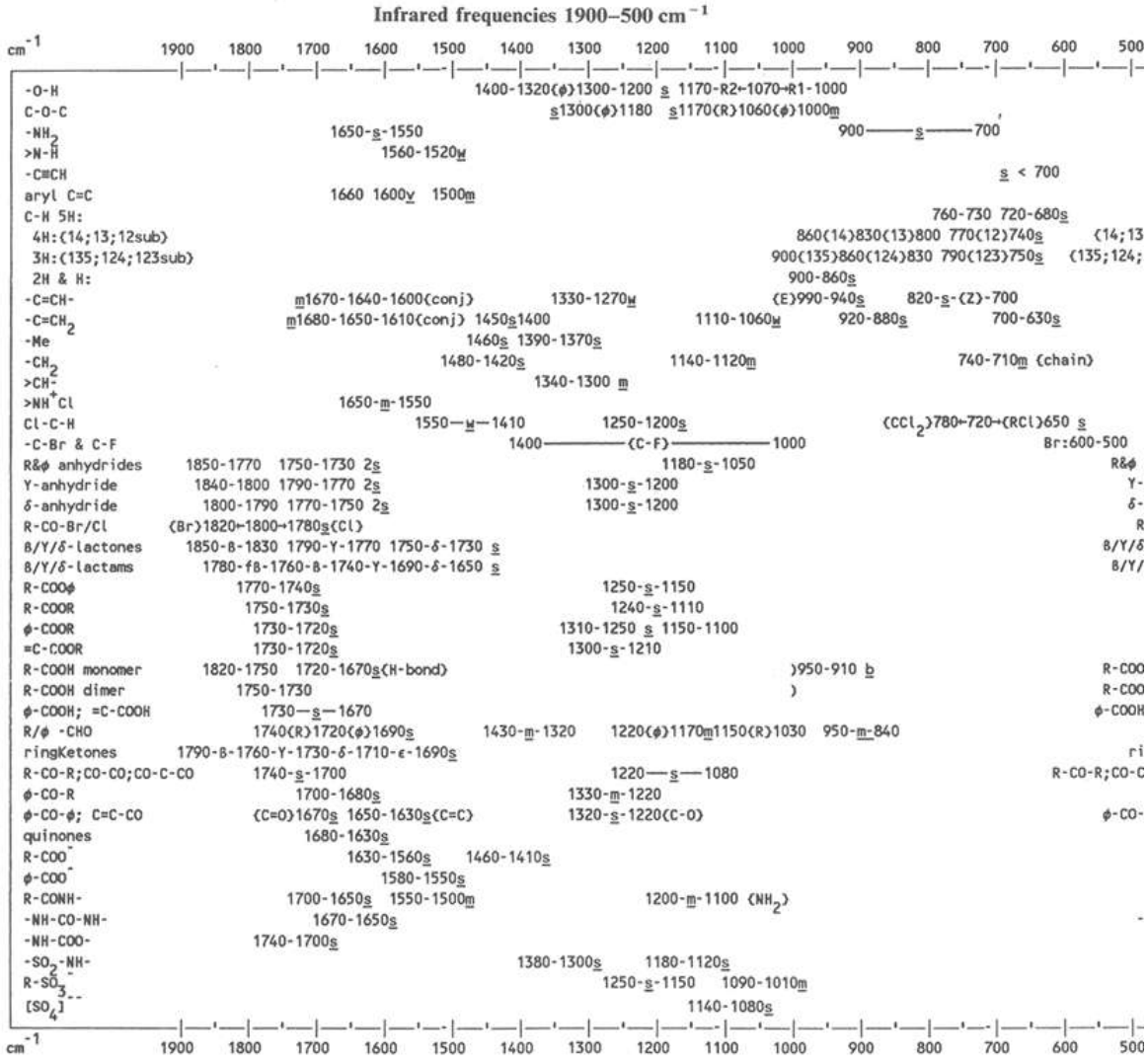

Infrared frequencies in 1900-500 cm^{-1} reproduced from Tables of Physical & Chemical Constants (16th edition 1995). 3.8.5 Infrared and Raman spectrophotometry. Kaye & Laby Online. Version 1.0, (1995), www.kayelaby.npl.co.uk

Annex 3

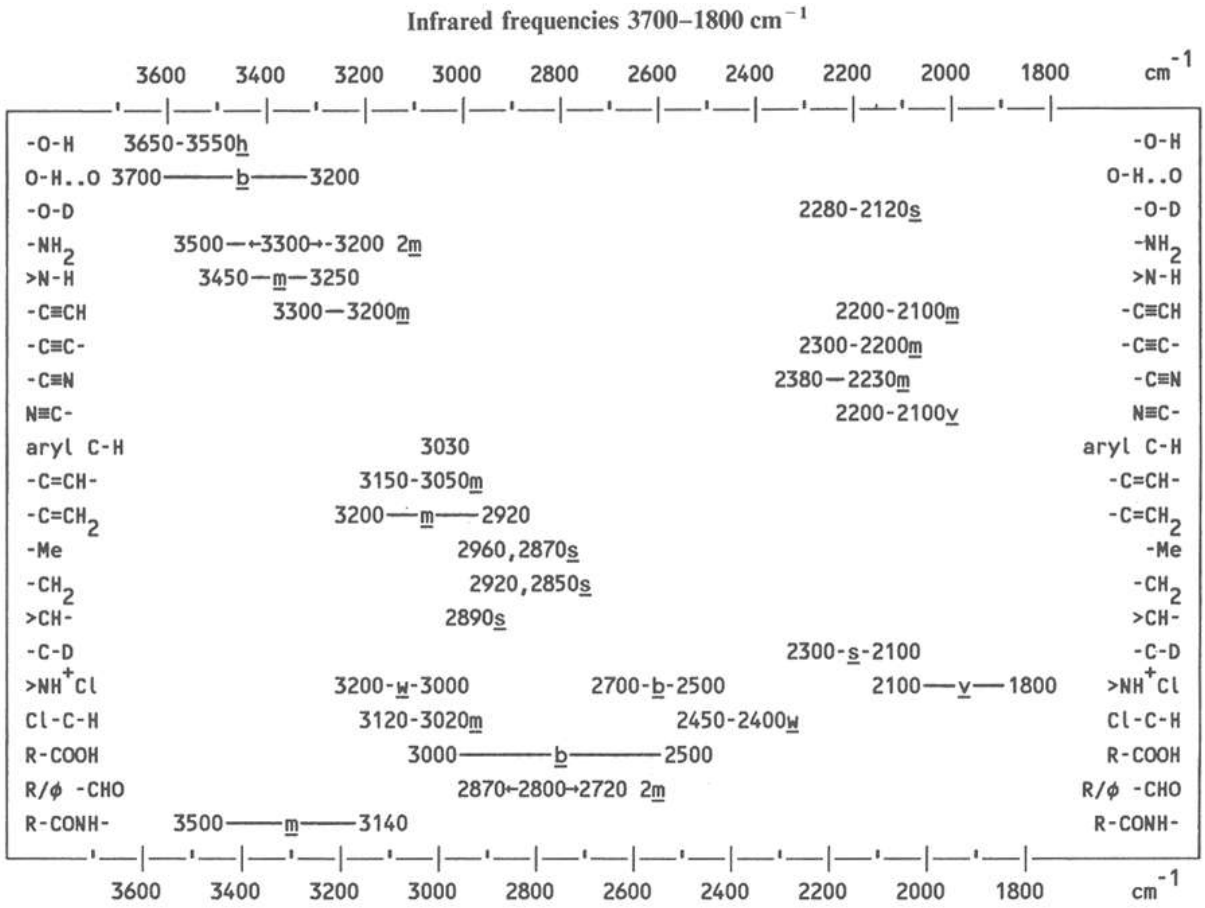

Infrared frequencies in 3700-1800 cm^{-1} reproduced from
Tables of Physical & Chemical Constants (16th edition 1995). 3.8.5 Infrared and Raman spectrophotometry. Kaye & Laby Online. Version 1.0, (1995) www.kayelaby.npl.co.uk

Annex 4

Ethanol Flow as Function of Injection Parameters

Ethanol / P_M = 1.8 bar N_2

1 ms - 5 Hz		
Time (Min)	Volume (ml)	Q (ml/min)
0	0	0
2,5	0,50	0,20000000
5	1,00	0,20000000
7,5	1,50	0,20000000
10	2,00	0,20000000
12,5	2,50	0,20000000
14,75	3,00	0,20338983
17,5	3,50	0,20000000
19,5	4,00	0,20512821
22	4,50	0,20454545
24,75	5,00	0,20202020
27	5,50	0,20370370
29,5	6,00	0,20338983
32	6,50	0,20312500
34,25	7,00	0,20437956
36,75	7,50	0,20408163
39	8,00	0,20512821
41,75	8,50	0,20359281
44	9,00	0,20454545
46,5	9,50	0,20430108
48,75	10,00	0,20512821
Average 1		0,20282296
Average 2		0,20368574

Ethanol / P_M = 2.8 bar N_2

1 ms - 1 Hz		
Time (Min)	Volume (ml)	Q (ml/min)
0	0	0
3,75	0,2	0,05333333
7,75	0,4	0,0516129
11	0,6	0,05454545
15,5	0,8	0,0516129
18,25	1	0,05479452
21	1,2	0,05714286
24,25	1,4	0,05773196
27,75	1,6	0,05765766
31,5	1,8	0,05714286
34,5	2	0,05797101
38,5	2,2	0,05714286
42,25	2,4	0,05680473
45	2,6	0,05777778
49	2,8	0,05714286
52,75	3	0,05687204
56	3,2	0,05714286
59,75	3,4	0,05690377
63,25	3,6	0,056917
66,75	3,8	0,05692884
70,5	4	0,05673759
Average 1		0,05619579
Average 2		0,05683356

Ethanol / P_M = 2.8 bar N_2

1 ms - 1 Hz		
Time (Min)	Volume (ml)	Q (ml/min)
0	0	0
3,75	0,2	0,05333333
7,75	0,4	0,0516129
11	0,6	0,05454545
14,5	0,8	0,05517241
18,5	1	0,05405405
22	1,2	0,05454545
25,5	1,4	0,05490196
29	1,6	0,05517241
32,75	1,8	0,05496183
37,25	2	0,05369128
39,75	2,2	0,05534591
43	2,4	0,05581395
47	2,6	0,05531915
50,25	2,8	0,05572139
53,75	3	0,05581395
57	3,2	0,05614035
60,5	3,4	0,05619835
63,5	3,6	0,05669291
67	3,8	0,05671642
70,25	4	0,0569395
Average 1		0,05513465
Average 2		0,05570292

Ethanol / P_M = 2.8 bar N_2

1 ms - 2 Hz		
Time (Min)	Volume (ml)	Q (ml/min)
0	0	0
2,15	0,2	0,09302326
3,75	0,4	0,10666667
5,75	0,6	0,10434783
7,5	0,8	0,10666667
9,25	1	0,10810811
11,25	1,2	0,10666667
13	1,4	0,10769231
14,75	1,6	0,10847458
16,75	1,8	0,10746269
18,5	2	0,10810811
20,5	2,2	0,10731707
22,25	2,4	0,10786517
24,25	2,6	0,10721649
25,75	2,8	0,10873786
27,75	3	0,10810811
29,5	3,2	0,10847458
31,25	3,4	0,1088
33,25	3,6	0,10827068
34,75	3,8	0,10935252
36,75	4	0,10884354
Average 1		0,10701014
Average 2		0,10806638

Ethanol / P_M = 2.8 bar N_2

1 ms - 5 Hz		
Time (Min)	Volume (ml)	Q (ml/min)
0	0	0
0,75	0,2	0,26666667
1,5	0,4	0,26666667
2,25	0,6	0,26666667
3	0,8	0,26666667
3,75	1	0,26666667
4,5	1,2	0,26666667
5,25	1,4	0,26666667
6	1,6	0,26666667
6,75	1,8	0,26666667
7,75	2	0,25806452
8,5	2,2	0,25882353
9,25	2,4	0,25945946
10	2,6	0,26
10,75	2,8	0,26046512
11,5	3	0,26086957
12,25	3,2	0,26122449
13,25	3,4	0,25660377
14	3,6	0,25714286
14,75	3,8	0,25762712
15,5	4	0,25806452
Average 1		0,26241725
Average 2		0,26046512

Ethanol / P_M = 3.8 bar N_2

1 ms - 5 Hz		
Time (Min)	Volume (ml)	Q (ml/min)
0	0	0
0,5	0,2	0,4
1,25	0,4	0,32
1,75	0,6	0,34285714
2,5	0,8	0,32
3	1	0,33333333
3,5	1,2	0,34285714
4,2	1,4	0,33333333
4,75	1,6	0,33684211
5,25	1,8	0,34285714
6	2	0,33333333
6,5	2,2	0,33846154
7	2,4	0,34285714
7,25	2,6	0,35862069
8,25	2,8	0,33939394
8,5	3	0,35294118
9,5	3,2	0,33684211
10	3,4	0,34
10,75	3,6	0,33488372
11,25	3,8	0,33777778
11,75	4	0,34042553
Average 1		0,34138086
Average 2		0,34021871

Ethanol / P_M = 2.8 bar N_2

5 ms - 1 Hz		
Time (Min)	Volume (ml)	Q (ml/min)
0	0	0
0,75	0,2	0,26666667
1,75	0,4	0,22857143
2,75	0,6	0,21818182
3,5	0,8	0,22857143
4,5	1	0,22222222
5,5	1,2	0,21818182
6,25	1,4	0,224
7,25	1,6	0,22068966
8	1,8	0,225
9	2	0,22222222
10	2,2	0,22
10,75	2,4	0,22325581
11,5	2,6	0,22608696
12,5	2,8	0,224
13,25	3	0,22641509
14,25	3,2	0,2245614
15,75	3,4	0,21587302
16	3,6	0,225
17,75	3,8	0,21408451
17,75	4	0,22535211
Average 1		0,22494681
Average 2		0,22251656

Ethanol / P_M = 2.8 bar N_2

10 ms - 1 Hz		
Time (Min)	Volume (ml)	Q (ml/min)
0	0	0
0,5	0,2	0,4
1	0,4	0,4
1,25	0,6	0,48
1,75	0,8	0,45714286
2,25	1	0,44444444
2,75	1,2	0,43636364
3,25	1,4	0,43076923
3,5	1,6	0,45714286
4	1,8	0,45
4,5	2	0,44444444
5	2,2	0,44
5,5	2,4	0,43636364
6	2,6	0,43333333
6,25	2,8	0,448
6,75	3	0,44444444
7,25	3,2	0,44137931
7,7	3,4	0,44155844
8	3,6	0,45
8,5	3,8	0,44705882
9	4	0,44444444
Average 1		0,4413445
Average 2		0,44350581

Annex 5

Deionized Water Flow as Function of Injection Parameters

Deionized Water / P_M = 2.8 bar N_2

1 ms - 1 Hz			
Time		Volume (ml)	Q (ml/min)
min	sec		
0	0	0	0
4	55	0,20	0,04067797
9	12	0,40	0,04347826
13	39	0,60	0,04395604
18	2	0,80	0,04436229
22	19	1,00	0,04480956
27	7	1,20	0,04425323
31	34	1,40	0,04435058
36	10	1,60	0,04423963
40	28	1,80	0,04448105
45	5	2,00	0,04436229
49	56	2,20	0,04405874
54	5	2,40	0,04437596
58	12	2,60	0,04467354
61	54	2,80	0,04523425
65	55	3,00	0,04551201
69	42	3,20	0,04591105
73	35	3,40	0,04620612
77	5	3,60	0,04670270
81	19	3,80	0,04673089
85	15	4,00	0,04692082
Average 1			0,04476485
Average 2			-

Deionized Water / P_M = 2.8 bar N_2

1 ms - 2 Hz			
Time		Volume (ml)	Q (ml/min)
min	sec		
0	0	0	0
1	56	0,20	0,10344828
4	3	0,40	0,09876543
5	55	0,60	0,10140845
7	47	0,80	0,10278373
9	41	1,00	0,10327022
11	40	1,20	0,10285714
13	33	1,40	0,10332103
15	27	1,60	0,10355987
17	24	1,80	0,10344828
19	28	2,00	0,10273973
21	3	2,20	0,10451306
23	7	2,40	0,10382120
25	19	2,60	0,10269914
27	22	2,80	0,10231425
29	7	3,00	0,10303377
31	4	3,20	0,10300429
33	1	3,40	0,10297829
35	9	3,60	0,10241821
37	15	3,80	0,10201342
39	9	4,00	0,10217114
Average 1			0,10272845
Average 2			-

Deionized Water / P_M = 2.8 bar N_2

1 ms - 5 Hz			
Time		Volume (ml)	Q (ml/min)
min	sec		
0	0	0	0
1	10	0,20	0,17142857
2	0	0,40	0,20000000
2	52	0,60	0,20930233
3	45	0,80	0,21333333
4	41	1,00	0,21352313
5	35	1,20	0,21492537
6	30	1,40	0,21538462
7	28	1,60	0,21428571
8	30	1,80	0,21176471
9	32	2,00	0,20979021
10	19	2,20	0,21324717
11	10	2,40	0,21492537
11	58	2,60	0,21727019
12	51	2,80	0,21789883
13	49	3,00	0,21712907
14	38	3,20	0,21867882
15	42	3,40	0,21656051
16	31	3,60	0,21796165
17	25	3,80	0,21818182
18	22	4,00	0,21778584
Average 1			0,21216886
Average 2			-

Deionized Water / P_M = 2.8 bar N_2

5 ms - 1 Hz			
Time		Volume (ml)	Q (ml/min)
min	sec		
0	0	0	0
0	55	0,20	0,21818182
1	47	0,40	0,22429907
2	40	0,60	0,22500000
3	46	0,80	0,21238938
4	32	1,00	0,22058824
5	41	1,20	0,21114370
6	27	1,40	0,21705426
7	25	1,60	0,21573034
8	25	1,80	0,21386139
9	26	2,00	0,21201413
10	16	2,20	0,21428571
11	8	2,40	0,21556886
12	10	2,60	0,21369863
13	0	2,80	0,21538462
14	10	3,00	0,21176471
15	3	3,20	0,21262458
16	10	3,40	0,21030928
17	13	3,60	0,20909971
18	5	3,80	0,21013825
18	49	4,00	0,21257750
Average 1			0,21478571
Average 2			-

Deionized Water / P_M = 2.8 bar N_2

10 ms - 1 Hz			
Time		Volume (ml)	Q (ml/min)
min	sec		
0	0	0	0
0	25	0,20	0,48000000
0	55	0,40	0,43636364
1	27	0,60	0,41379310
1	54	0,80	0,42105263
2	21	1,00	0,42553191
2	53	1,20	0,41618497
3	20	1,40	0,42000000
3	50	1,60	0,41739130
4	20	1,80	0,41538462
4	49	2,00	0,41522491
5	17	2,20	0,41640379
5	40	2,40	0,42352941
6	14	2,60	0,41711230
6	44	2,80	0,41584158
7	20	3,00	0,40909091
7	42	3,20	0,41558442
8	12	3,40	0,41463415
8	34	3,60	0,42023346
9	7	3,80	0,41681901
9	43	4,00	0,41166381
Average 1			0,42109200
Average 2			-

Deionized Water / P_M = 1.8 bar N_2

1 ms - 5 Hz			
Time		Volume (ml)	Q (ml/min)
min	sec		
0	0	0	0
1	16	0,20	0,15789474
2	15	0,40	0,17777778
3	18	0,60	0,18181818
4	18	0,80	0,18604651
5	19	1,00	0,18808777
6	45	1,20	0,17777778
7	59	1,40	0,17536534
8	53	1,60	0,18011257
10	4	1,80	0,17880795
11	15	2,00	0,17777778
12	32	2,20	0,17553191
13	48	2,40	0,17391304
15	4	2,60	0,17256637
16	5	2,80	0,17409326
17	19	3,00	0,17324350
18	14	3,20	0,17550274
19	10	3,40	0,17739130
20	11	3,60	0,17836499
21	47	3,80	0,17444529
23	6	4,00	0,17316017
Average 1			0,17648395
Average 2			-

Deionized Water / P_M = 3.8 bar N_2

1 ms - 5 Hz			
Time		Volume (ml)	Q (ml/min)
min	sec		
0	0	0	0
0	47	0,20	0,25531915
1	48	0,40	0,22222222
2	30	0,60	0,24000000
3	28	0,80	0,23076923
4	14	1,00	0,23622047
5	7	1,20	0,23452769
5	47	1,40	0,24207493
6	53	1,60	0,23244552
7	31	1,80	0,23946785
8	15	2,00	0,24242424
9	14	2,20	0,23826715
9	48	2,40	0,24489796
10	39	2,60	0,24413146
11	21	2,80	0,24669604
12	16	3,00	0,24456522
13	2	3,20	0,24552430
13	53	3,40	0,24489796
14	42	3,60	0,24489796
15	34	3,80	0,24411135
16	17	4,00	0,24564995
Average 1			0,24095553
Average 2			-

Annex 6

Published articles

[1] **C.C. Manole**, A.B. Stoian, C. Pirvu, Surface Perspective of a TiO_2 Nanoarchitecture, U.P.B. Scientific Bulletin 72 (2010) 245-248.

[2] C. Pirvu, **C.C. Manole**, A.B. Stoian, I. Demetrescu, Understanding of electrochemical and structural changes of polypyrrole/polyethylene glycol composite films in aqueous solution, Electrochimica Acta. 56 (2011) 9893–9903, *Thomson Reuters Impact Factor: 3.83, Relative Influence Score: 1.56.*

[3] **C.C. Manole**, C. Pirvu, Surface and electrochemical analysis for the understanding of TiO2 nanopores/nanotubes changes in post-elaboration treatment, Surface and Interface Analysis. 43 (2011) 1022–1029, *Thomson Reuters Impact Factor: 1.18, Relative Influence Score: 0.64.*

[4] **C.C. Manole**, C. Pirvu, I. Demetrescu, Evaluation of TiO_2 Nanotubes Changes after Ultrasonication Treatment, Molecular Crystals and Liquid Crystals. 521 (2010) 84–92, *Thomson Reuters Impact Factor: 0.58, Relative Influence Score: 0.37.*

[5] S. Popescu, C. Pirvu, M. Mindroiu, **C. Manole**, I. Demetrescu, Electrochemical Synthesis and Characterization of Ti Modified Electrodes with Polypyrrole – Polyethylene Glycol Hybrid Coating, Revista De Chimie. 61 (2010) 245–248, *Thomson Reuters Impact Factor: 0.59, Relative Influence Score: 0.13.*

[6] **C.C. Manole**, C. Pirvu, I. Demetrescu, TiO_2: From Nanotubes to Nanopores by Changing the Anodizing Voltage in Floride-Glycerol Electrolyte, Key Engineering Materials. 415 (2009) 5–8, *ISI/SCOPUS Indexed*.

[7] **C.C. Manole**, F. Maury, I. Demetrescu, Thermally Induced–Release of Internal Liquid Phase Encapsulated in a Polymer Membrane Grown by Photo-activated DLICVD, Journal Of Chemical Vapor Deposition, doi:10.1002/cvde.201206987, *Thomson Reuters Impact Factor: 1.8, Thomson Reuters Impact Factor: 1.16.*

[8] C. Pirvu, **C.C. Manole**, Electrochemical surface plasmon resonance for in-situ investigation of antifouling effect of ultra thin hybrid polypyrrole/PSS films, Electrochimica Acta, doi:10.1016/j.electacta.2012.11.045, *Thomson Reuters Impact Factor: 3.83, Thomson Reuters Impact Factor: 1.56.*

Total Thomson Reuters Impact Factor:11.36
Total Relative Influence Score: 5.42

Annex 7

Attended conferences

Authors	**Claudiu Constantin Manole**, Cristian Pîrvu
Presentation title	Electrochemical evaluation of a multilayer nanostructured coating
Presentation type	Oral Presentation
Presented at	4th International Conference "Biomaterials, Tissue Engineering & Medical Devices" – BioMedD'2010
Conference place	Sinaia, Romania
Conference date	23 – 25th September 2010

Authors	**Claudiu Constantin Manole**, Cristian Pîrvu, Mihaela Mîndroiu, Ioana Demetrescu
Presentation title	Monitoring Hydrophilic –Hydrophobic Character of a Surface Electrode via TiO_2 Nano Particles Addition as Aspect of Interface Phenomena
Presentation type	Poster Presentation
Presented at	9th ISE Spring Meeting - Electrochemical Sensors: from Nanoscale Engineering to Industrial Applications
Conference place	Turku, Finland
Conference date	8 – 11th May 2011

Authors	**Claudiu Constantin Manole**, Francois Senocq, Ioana Demetrescu, Francis Maury
Presentation title	Polypyrrole conductive thin fil ms deposited by Liquid Injection Photo-CVD
Presentation type	Poster Presentation
Presented at	European Workshop on Nano Transparent Conductive Materials
Conference place	Grenoble, France
Conference date	14 - 15th June 2012

Authors	**Claudiu Constantin Manole**, Olivier Marsan, Cedric Charvillat, Ioana Demetrescu, Francis Maury
Presentation title	Evidences for liquid encapsulation in PMMA ultra-thin film grown by liquid injection Photo-CVD
Presentation type	Poster Presentation
Presented at	8th Coatings Science International 2012 – COSI2012
Conference place	Noordwjik, Nederlands
Conference date	25 - 29th June 2012

Authors	**Claudiu Constantin Manole**, Cristian Pîrvu, Francis Maury, Ioana Demetrescu
Presentation title	Hybrid organic/inorganic thin film of TiO2/PPy grown through a single-step electrochemical process
Presentation type	Poster Presentation
Presented at	63rd Annual Meeting of the International Society of Electrochemistry
Conference place	Prague, Czech Republic
Conference date	19 - 24th August 2012